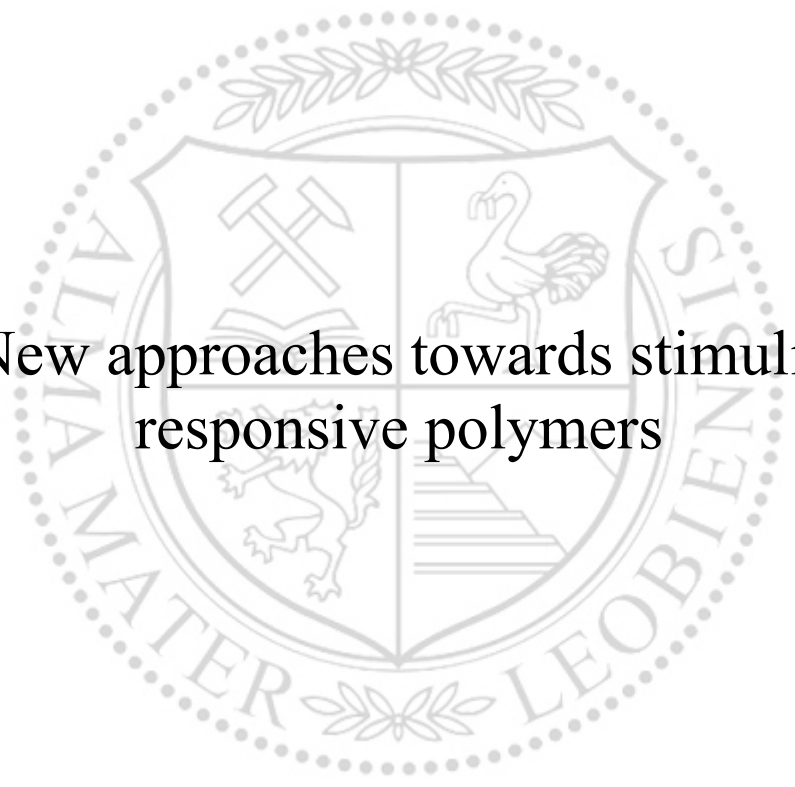Chair of Chemistry of Polymeric Materials

# Doctoral Thesis

# New approaches towards stimuli-responsive polymers

## Michael Giebler, M.Sc.

April 2021

**AFFIDAVIT**

I declare on oath that I wrote this thesis independently, did not use other than the specified sources and aids, and did not otherwise use any unauthorized aids.

I declare that I have read, understood, and complied with the guidelines of the senate of the Montanuniversität Leoben for "Good Scientific Practice".

Furthermore, I declare that the electronic and printed version of the submitted thesis are identical, both, formally and with regard to content.

Date  26.04.2021

Signature Author
Michael Giebler

# Acknowledgments

A scientific thesis like the following one can only be completed through a close and excellent cooperation of many people involved. In this chapter, I would like to thank all those who have supported and accompanied me during the preparation of this dissertation.

First of all, I would like to thank Priv.-Doz. DI Dr. Sandra Schlögl for her excellent supervision, endless patience, valuable help and encouragement throughout the duration of this thesis.

In addition, I would like to thank Univ. Prof. Mag. Dr. Wolfgang Kern for his scientific support and stimulating discussions.

I would also like to thank my mentor, Univ. Prof. DI Dr. Thomas Grießer, for the numerous constructive discussions and wise advices during e.g. our shared conferences.

Much of my gratitude is devoted to my colleagues at the PCCL and the chair of chemistry of polymeric materials. They not only enriched my time with their great help, but also ensured a perfect working atmosphere.

I would also like to thank my friends and companions from the bottom of my heart for their support over the past years.

I dedicate this work to my family, as I would not be writing these lines without their support. Thank you!

# Cooperation

This PhD thesis has been realized in cooperation with scientific organizations and institutions. They are listed below:

- Static water contact angles were measured out by **Elisabeth Rossegger**.

*Polymer Competence Center Leoben GmbH, Roseggerstraße 12, 8700 Leoben, Austria*

- White- light interferometry measurements were carried out by **Walter Alabiso** and **Thomas Ules**.

*Polymer Competence Center Leoben GmbH, Roseggerstraße 12, 8700 Leoben, Austria*

- Confocal microscopy measurements were carried out by **Simone Viola Radl** and **Simon Kaiser**.

*Polymer Competence Center Leoben GmbH, Roseggerstraße 12, 8700 Leoben, Austria*

- Remolding of grounded samples with a PVT-press was carried out by **Ivica Duretek**

*Chair of Polymer Processing, Montanuniversitaet Leoben, Otto-Glöckel-Straße 2, 8700 Leoben, Austria*

**The results of this thesis were published in peer-reviewed scientific publications and patents.**

**Publications in peer-reviewed journals**

(1) Giebler, M.; Radl, S.V.; Ast, M.; Kaiser, S.; Griesser, T.; Kern, W.; Schlögl, S. Dual-Responsive Polydimethylsiloxane Networks. *J. Polym. Sci. Part A Polym. Chem.* **2018**, *56*, 2319–2329, doi:10.1002/pola.29206.

(2) Giebler, M.; Radl, S.; Ules, T.; Griesser, T.; Schlögl, S. Photopatternable epoxy-based thermosets. *Materials (Basel).* **2019**, *12*, 2350, doi:10.3390/ma12152350.

(3) Giebler, M.; Alabiso, W.; Wieser, V.; Radl, S.; Schlögl, S. Photopatternable and Rewritable Epoxy-Anhydride Vitrimers. *Macromol. Rapid Commun.* **2021**, *42*, 2170005, doi:10.1002/marc.202170005.

(4) Giebler, M.; Sperling, C.; Kaiser, S.; Duretek, I.; Schlögl, S. Epoxy-anhydride vitrimers from aminoglycidyl resins with high glass transition temperature and efficient stress relaxation. *Polymers (Basel).* **2020**, *12*, 1–14, doi:10.3390/POLYM12051148.

**Patent**

Giebler; M; Wanghofer F.; Schlögl, M.; Wolfberger, M. Aushärtbare Zusammensetzung zur Herstellung eines Vitrimers und daraus erhältliches Vitrimer und Verfahren zu dessen Herstellung; A50332/2020

**Bachelor and Master Theses**

Markus Ast: performed part of his experimental studies on the topic of "*Dual-Responsive Polydimethylsiloxane Networks*". Some of the results are presented in section 3.1.

Clemens Sperling: performed his experimental studies on the topic of "*Epoxy-anhydride vitrimers from aminoglycidyl resins with high glass transition temperature and efficient stress relaxation*". Some of the results are shown in section 3.4.

Viktoria Feigl: performed her experimental studies on the topic of "*Influence of the transesterification catalyst on the network's properties of epoxy-anhydride vitrimers*". Some of the results are shown in section 3.5.

# Abstract

The aim of the present work was to develop new concepts towards "stimuli-responsive polymers". On the one hand, *ortho*-nitrobenzyl ester (*o*-NBE) chemistry was used to spatially control network properties by UV induced cleavage reactions. On the other hand, thermo-activated transesterifications were exploited to introduce dynamic properties in epoxy-based networks.

In particular, switchable polydimethylsiloxane networks were prepared, which were degraded in a controlled manner upon either UV exposure or in alkaline media. For this purpose, polydimethylsiloxane (PDMS) oligomers with terminal anhydride groups were thermally crosslinked with a bifunctional epoxy monomer containing a photolabile *o*-NBE-group. The sensitivity of the ester groups to hydrolytic cleavage reactions was used for pH-triggered network degradation. In addition, the photosensitivity of the *o*-NBE-group was employed for light-induced cleavage reactions. This allowed comparisons between the two cleavage mechanisms and a defined degradation of the network as a function of pH value and light intensity. Furthermore, it could be shown that by selective (over)-exposure and secondary photoreactions (leading to re-crosslinking of the networks), a switch between positive- and negative-tone photoresists is possible.

In a further study, *o*-NBE chromophores were introduced in epoxy-based thermosetting resins. Mechanical and degradation properties of the networks were adjusted by the applied anhydride hardeners. Thus, a wide range of glass transition temperature, chain mobility, hardness and contrast of positive-tone photoresists was established.

In the second part of this thesis, new covalent adaptable networks (e.g. vitrimers) were developed and investigated. By combining the chemistry of *o*-NBE with thermo-activated and reversible transesterification reactions, it was possible to generate a rewritable vitrimeric network. Positive-tone structures were inscribed by photolithography using the photoinduced degradation of the network across the *o*-NBE groups. Subsequently, a macroscopic reflow and erasing of the polymer patterns were induced by thermo-activated exchange reactions of the hydroxyl ester links at temperatures well above the topological freezing transition of the vitrimer. The regenerated film had a smooth surface topology and could be reused to inscribe new micropatterns via photolithography.

Parallel with the introduction of photo-responsive properties, further research was carried out to increase the glass transition temperature ($T_g$) of vitrimers for structural

applications. In particular, epoxy-anhydride vitrimers with a $T_g$ of up to 140 °C were prepared, which additionally exhibited efficient stress relaxation at elevated temperature. The networks were obtained by thermal curing of aminoglycidyl monomers with glutaric anhydride in various stoichiometric ratios. The tertiary amine groups in the structure of the aminoglycidyl derivatives enabled acceleration of the curing reaction and also catalyzed the transesterification reaction, which was presented in stress relaxation measurements. In addition, a remolding of milled samples was feasible demonstrating the recyclability of the high $T_g$ vitrimer networks. In subsequent work, the catalytic activity of selected amines for the transesterification of hydroxyl ester moieties was studied in a thermally cured epoxy- anhydride system using 3,4-epoxycyclohexylmethyl-3',4'-epoxycyclohexanecarboxylate as epoxy monomer and glutaric anhydride as hardener. The influence of the catalyst on the network density, the network mobility and the rate for the transesterification reactions within the polymer matrix was studied. Depending on the amine catalyst, networks with a $T_g$ ranging from 66 to 166 °C were obtained. Subsequent stress relaxation measurements demonstrated the activity of the compounds for catalyzing transesterification reactions.

The present thesis highlights the great potential of stimuli-responsive materials, whilst the newly developed material concepts and approaches pave the way towards future applications.

# Kurzfassung

Das Ziel der vorliegenden Arbeit war es, neue Konzepte im Bereich der "stimuli-responsiven Polymere" zu entwickeln. Einerseits wurde die Chemie von *ortho*-Nitrobenzylestern (*o*-NBE) verwendet, um Netzwerkeigenschaften durch UV-induzierte Spaltungsreaktionen gezielt zu steuern. Andererseits wurden thermoaktivierte Umesterungsreaktionen genutzt, um dynamische Eigenschaften in epoxidbasierten Netzwerken zu erzeugen.

Hierzu wurden schaltbare Polydimethylsiloxan (PDMS)-Netzwerke hergestellt, die entweder durch UV-Belichtung oder in alkalischen Medien kontrolliert degradiert werden können. Dabei wurden PDMS-Oligomere mit endständigen Anhydridgruppen thermisch mit einem bifunktionellen Epoxidmonomer vernetzt, das eine photolabile *o*-NBE-Gruppe enthielt. Die Empfindlichkeit der Estergruppen gegenüber hydrolytischen Spaltungsreaktionen wurde für den pH-gesteuerten Netzwerkabbau genutzt. Zusätzlich wurde die Photosensitivität der *o*-NBE-Gruppe für lichtinduzierte Spaltungsreaktionen genutzt. Dies ermöglichte einen definierten Abbau des Polymernetzwerks in Abhängigkeit des pH-Wertes und der Lichtintensität. Weiterhin konnte gezeigt werden, dass durch gezielte (Über-)Belichtung und sekundär auftretende Photoreaktionen (die zu einer Rückvernetzung der Netzwerke führte) ein Wechsel zwischen positiven und negativen Photolacken möglich ist.

In einer weiteren Studie wurden *o*-NBE-Chromophore in duromere Epoxidharze eingebracht. Die mechanischen und Abbau-Eigenschaften der Netzwerke wurden durch die eingesetzten Anhydridhärter beeinflusst. So konnte ein breiter Bereich von Glasübergangstemperaturen, Kettenbeweglichkeit, Härte und Kontrast von positiven Photolacken hegestellt werden.

Im zweiten Teil dieser Arbeit wurden neue kovalent adaptierbare Netzwerke (CANs, z.B. Vitrimere) entwickelt und untersucht. Durch die Kombination der *o*-NBE-Chemie mit thermoaktivierten und reversiblen Umesterungsreaktionen war es möglich, ein „wiederbeschreibbares" vitrimeres Netzwerk zu generieren. Durch den photoinduzierten Abbau des Netzwerks über die *o*-NBE-Gruppen wurden positive Photolacke mittels Photolithographie erzeugt. Anschließende, thermoaktivierte Austauschreaktionen der Hydroxyesterbindungen induzierten ein makroskopisches Fließen und die erzeugten Mikrostrukturen wurden bei erhöhter Temperaturen deutlich oberhalb des topologischen

Übergangs (eng. *topology freezing transition temperature,* $T_v$) des Vitrimers vollständig gelöscht. Die regenerierte Oberfläche hatte eine glatte Oberflächentopologie und konnte für neue Mikrostrukturen mittels Photolithographie wiederverwendet werden.

Die thermo-responsiven Eigenschaften wurden in weiteren Studien untersucht, um die Glasübergangstemperatur ($T_g$) von Vitrimeren für industriebasierende Anwendungen zu erhöhen. Insbesondere wurden Epoxy-Anhydrid Vitrimere mit einem $T_g$ von bis zu 140 °C hergestellt, die zusätzlich eine effiziente Spannungsrelaxation bei erhöhter Temperatur aufwiesen. Die Netzwerke wurden durch thermische Härtung von Aminoglycidylmonomeren mit Glutarsäureanhydrid in verschiedenen stöchiometrischen Verhältnissen erzeugt. Die in der Struktur der Aminoglycidylderivate vorhandenen tertiären Amingruppen beschleunigten nicht nur die Aushärtungsreaktion, sondern katalysierten auch die Umesterungsreaktionen, wie anschließende Spannungsrelaxationsmessungen zeigten. Darüber hinaus war eine Wiederverformung der pulverförmigen Proben möglich, was die Rezyklierbarkeit der Vitrimernetzwerke mit hohem $T_g$ zeigte. In weiteren Arbeiten wurde die katalytische Aktivität ausgewählter Amine für die Umesterung von Hydroxylester in einem thermisch gehärteten Epoxid-Anhydridsystem unter Verwendung von 3,4-Epoxycyclohexylmethyl-3',4'-Epoxycyclohexancarboxylat als Epoxidmonomer und Glutarsäureanhydrid als Härter untersucht. Hierbei wurde der Einfluss des Katalysators auf die Netzwerkdichte, die Netzwerkbeweglichkeit und die Rate für die Umesterungsreaktionen innerhalb der Polymermatrix untersucht. In Abhängigkeit des eingesetzten Aminkatalysators wurden Netzwerke mit einem $T_g$ von 66 bis 166 °C erhalten. Anschließende Spannungsrelaxationsmessungen zeigten die katalytische Aktivität bei Umesterungsreaktionen.

Die vorliegende Arbeit verdeutlicht das große Potenzial von stimuli-responsiven Polymeren, wobei mit den unterschiedlich entwickelten und angewendeten Materialkonzepten neue Anwendungsgebiete aufgezeigt werden.

# Table of content

# 1 Introduction

In 1907, the first synthetic polymer, a phenol-formaldehyde resin called Bakelite was developed and mass-produced by Leo Baekeland. [1] Since then a rapid development yielded a large variety of different polymeric materials in all forms and shapes and established this material in our society. To date, an estimated number of 8300 million metric tons of virgin plastics have been produced. [2] The largest market is packaging, an application area whose growth was accelerated by a global shift from reusable to single-use containers. [2] This high number illustrates the importance, but also the need of a sustainable mindset towards polymers in our life. Increasing ecological pollution and conservation of natural resources make it necessary to develop new material concepts. A paradigm shift is taking place, which will hopefully lead to a global improvement in waste management. In addition, the demands placed on polymer materials today are becoming more strict. Due to their unique properties, polymer materials developed from mass products into special products that made high-tech technologies possible in the first place. [3,4] Labels such as smart and stimuli-responsive show that these materials are finding an ever-increasing range of applications. The focus of this work is set on the structure, functionality and chemistry of stimuli-responsive polymers. Polymers that respond to stimuli are different from conventional polymers as they are able of undergoing a rapid physicochemical transition in the presence of various physical and/or chemical stimuli. This change in material properties can happen to a relative large extent and abrupt in response to an external environmental change. [5] These stimuli come in various forms, including pH [6,7], temperature [8,9], ionic [10–12], mechanical force [13], presence of biomolecules [14], electric/magnetic fields [15,16], light [17–19] or ultrasound [20] or a combination thereof. On-going research is aiming to transfer these material concept to numerous applications. Technological interest of stimuli-responsive polymers include reactive surfaces [21], drug-delivery and separation systems [22,23], chemo-mechanical actuators [24,25] or sensors [26]. For the design of stimuli-responsive polymers, one prominent approach relies on the controlled activation of chemical reactions within the polymer matrix. Possible reactions are crosslinking, cleavage reactions, changes in the individual polymer chain dimension or size, secondary structure, solubility, or in the number of crosslinks. [27–29]

The present thesis represents a comprehensive study on the development and characterization of new stimuli-responsive polymers. In particular, polymers that change their chemical and thermo-mechanical properties after temperature increase, or light irradiation are targeted at. The first part of this thesis covers the versatile interaction of UV-induced cleavage reactions of $o$-nitrobenzyl ester ($o$-NBE) links. This chemistry offers the possibility to specifically change mechanical properties of polymers and thus, facilitate recycling and/or recovery of embedded materials. The chemistry of $o$-nitrobenzyl ester derivatives has become a significant route to regulate selected physicochemical properties such as molecular weight, polarity or reactivity of polymers as a function of an optical stimulus. In the present work, it will be shown that the incorporation of $o$-nitrobenzyl ester groups into a polymer network can be applied to form dual-responsive networks, which degrade when exposed to either UV-light or alkaline environment. In addition, the dual-responsive nature of these cross linkers allowed for the introduction of positive- and negative-toned patterns by adjusting both the exposure dose and the solvent used in the development step. Expanding the concept to use of $o$-NBE chemistry for UV-induced change in solubility, photodegradable polymers with $o$-NBE links in the main chain and alternating the network composition and material properties were prepared.

The second part of the thesis deals with thermo-responsive networks, which consist of a dynamic network structures. These networks are able to rearrange their structure. The foundation of epoxy-based dynamic networks was first introduced by Leibler *et al.* in 2011, who termed this new class of materials as "vitrimers". [30] In vitrimers, bond exchange reactions, which are associative in nature, increase with rising temperature and lead to a change in the viscoelastic material properties. This salient feature can be used for a large variety of applications such as self-healing polymers. Vitrimers have a great potential in terms of scientific and technical applications. This is demonstrated by the lively scientific interest in this topic. Since the first mention of vitrimers in 2011 in connection with dynamic networks, 1,211 publications and 136 patents on this topic have been listed. [31] This confirms the great interest of the scientific community. In the present study, new approaches towards the development of stimuli-responsive polymers have been made. For that, different dynamic concepts were implemented in epoxy-based systems, which are able to respond to an external stimulus. Applying the salient features of the *ortho*-nitrobenzyl- chemistry ($o$-NB), photo-responsive properties were imparted into polymers,

which allowed for a well-defined cleavage of the network by light- exposure. With that, dual-responsive polymers, high-resolution resists and the photopatterning of epoxy-based thermosets as a function of network structure and network mobility were studied. By applying thermal stimuli in covalent adaptable networks (CANs), direct influence on the networks topology is possible, which in turn allowed a transition of classical thermosets with elastomeric properties. In the present thesis, vitrimers were developed, featuring a high glass-transition temperature ($T_g$) and rapid stress-relaxation. By varying the catalyst-system these properties could be tuned to enhance the utilization of these materials. Finally by imparting photo-responsive properties by introducing photo-sensitive $o$-NBE links into thermo-dynamic epoxy-based vitrimers new approaches towards photochemical repatternable materials could be introduced. The present thesis provides a comprehensive overview on stimuli- responsive polymers and established new approaches toward their development.

.
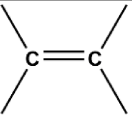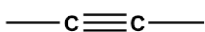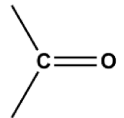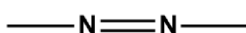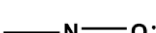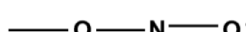
# 2 Theoretical Background

The following chapter sheds light on the basics of photochemistry and associated photoactive polymers. Moreover, it gives an introduction to the dynamic nature of covalent adaptable polymers and illustrates how to control and apply their chemistry.

## 2.1 Light absorption and emission

Excitation of a photoactive molecule leads to a distinct energy transfer. In this photophysical process, the absorbed photon energy of an excited luminophore (acceptor) is transferred to a chromophore (donor) by changing their energy states. [32] Examples for such chromophores are listed in Table 2-1:

**Table 2-1** Typical chromophoric groups [33]

| Chromophore | Typical compound | $\Lambda_{max}$ (nm) [a] | $E_{max}$ (L mol$^{-1}$cm$^{-1}$)[b] | Mode of electron transition |
|---|---|---|---|---|
| $C=C$ | Ethene | 193 | $10^4$ | $\pi \rightarrow \pi^*$ |
| $C\equiv C$ | Ethyne | 173 | $6 \cdot 10^3$ | $\pi \rightarrow \pi^*$ |
| $C=O$ | Acetone | 187 | $10^3$ | $\pi \rightarrow \pi^*$ |
|  |  | 271 | 15 | $n \rightarrow \pi^*$ |
| $N=N$ | Azomethane | 347 | 5 | $n \rightarrow \pi^*$ |
| $N=O^{\cdot}$ | t-Nitrosobutane | 300 | 100 | $\pi \rightarrow \pi^*$ |
|  |  | 665 | 20 | $n \rightarrow \pi^*$ |
| $O-N=O^{\cdot}$ | Amyl nitrite | 219 | 219 | $\pi \rightarrow \pi^*$ |
|  |  | 357 | 357 | $n \rightarrow \pi^*$ |

[a] Wavelength of maximum optical absorption [33]
[b] Decadic molar extinction coefficient ($\log I_0/I = \varepsilon \cdot c \cdot d$), where $\log I_0/I$ is the absorbance, $\varepsilon$ the molar attenuation coefficient, I the intensity, c the concentration of the attenuating species and d the optical length in cm [33]

In addition, a change in the charge distribution within the molecule is also triggering a change in its dipole moment. [34] The absorption of a photon is only allowed if the transition moment has a non-zero value i.e. the energy difference E between the ground state $E_1$ and the excited state $E_2$ has to be equal to the energy of the absorbed photon. [35] Photons have a specific energy E, which can be expressed by Planck's law [36]:

$$\Delta E = h \cdot \nu = \frac{hc}{\lambda}$$

(Equation 2-1)

Here $\Delta E$ is the difference in energy between the two states $E_1$ and $E_2$, h represents the Planck's constant, c the speed of light in vacuum, and v the frequency and $\lambda$ the wavelength of the absorbed light. [36] [37] If the photon does not match the energy criterion, it will not be absorbed and the irradiated material reflects, scatters or transmits the photon. For a more detailed picture, the molecular orbital model can be applied. [38] Linear combination of valence shell orbitals of an atom result in the formation of molecular orbitals. Combining two single orbitals, results in the formation of two molecular orbitals: one of lower (HOMO- highest occupied molecular orbital) and the other of higher energy (LUMO- lowest unoccupied molecular orbital). The HOMO, which is occupied by two electrons with an antiparallel spin, is responsible for the bonding of two atoms (bonding orbital). For the high-energy, antibonding orbital *vice versa* applies. In the ground state, the LUMO is unoccupied, but can be occupied by an electron upon electronic excitation of the molecule. [39] The electron is excited from the ground state $S_0$ to the excited singlet state $S_1$. [40] This process is presented in Figure 2-1.
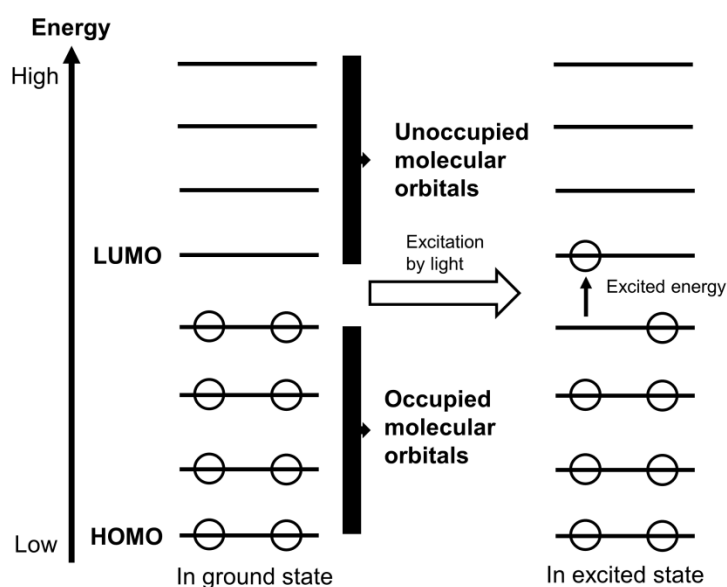


**Figure 2-1** Diagram of the HOMO and LUMO of a molecule (adapted from [40])]

In this excited state, the electron state is energetically unstable and returns to the ground state releasing excitation energy in various radiation and non-radiation processes. [41] These processes occur rapidly, whereas three different transitions/emissions can arise:

(1) Radiative relaxation in form of fluorescence or phosphorescence

(2) Non-radiative relaxation

(3) Photochemical reactions

In order to illustrate and understand these processes a Jablonski diagram (Figure 2-2) can be used. It illustrates molecular electronic energy levels, singlet and triplet, their vibrational levels, as well as photophysical processes.
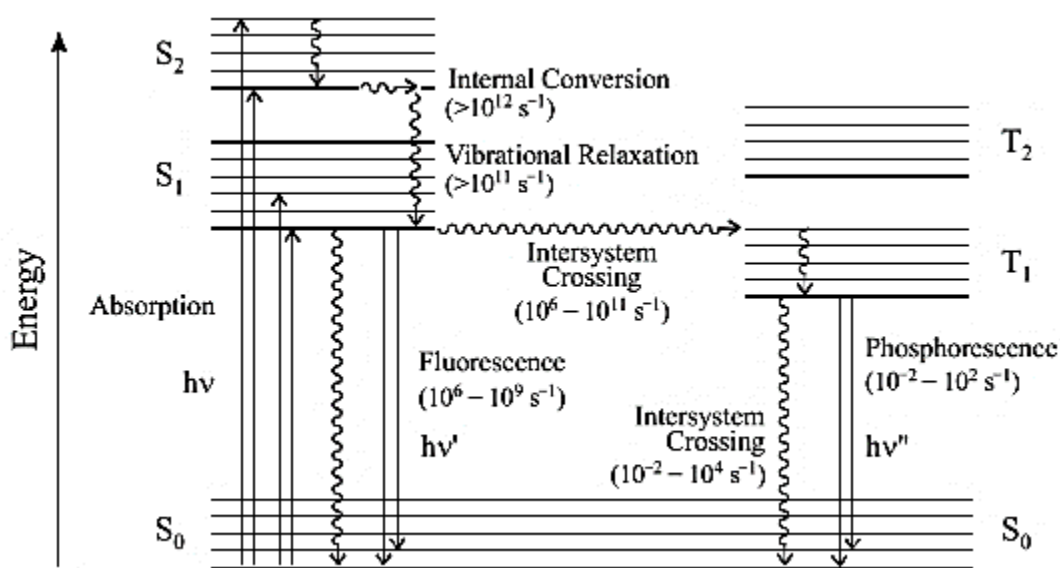


**Figure 2-2** Jablonksi diagram of an organic molecule [42]

In Figure 2-2, radiative transitions from one level to another are indicated by straight arrows and non-radiative ones by wavy arrows. [42] Kasha's rule broadens the understanding of the deactivation mechanism of excited states. [43] The rule states, that due to the rapid rate of deactivation to the lowest vibrational level of $S_1$ (or $T_1$), luminescence emission and chemical reaction by excited molecules will always originate from the lowest vibrational level of $S_1$ (or $T_1$). [34] [44] Regarding the kinetics of exited

states, the quantum yield of a species defines the number of moles of the species produced upon absorption of one mol of photons. [42]

(1) Radiative transitions

In this form of intramolecular deactivation processes of $S_1$ and $T_1$ states, two different types are distinguished. Both luminescence processes yield emission spectra with several bands instead of a single line:

- Fluorescence [35]: this form of deactivation involves emission of a photon between states of the same multiplicity, whereby it mostly occurs from the lowest vibrational level of the lowest excited state $S_1$. The maximum wavelength of fluorescence emission is shifted to lower energy (higher wavelengths) relative to the absorption maximum (Stokes shift). [35] Fluorescence proceeds in a period of $10^{-12}$ - $10^{-6}$ seconds.

$$S_1 \rightarrow S_0 + h \cdot v$$

- Phosphorescence [34]: after intersystem crossing of the excited electron and spin multiplicity change from singlet ($S_1$) to the triplet state ($T_1$), phosphorescence from the triplet state ($T_1$) occurs; also here the wavelength shifts to higher values. Although forbidden by the quantum mechanical selection rule, this process usually takes place in a period of $10^{-3}$ - $10^{-2}$ seconds. It is characteristic that phosphorescence occurs at higher wavelength, than fluorescence emission.

$$T_1 \rightarrow S_0 + h \cdot v$$

(2) Non-radiative transitions

In these transitions, return of the excited state and deactivation occurs without emission of radiation. Examples for such transitions are vibrational relaxations, intersystem crossing and internal conversion. [34]

Intersystem crossing includes intramolecular spin-forbidden and radiationless transitions between isoenergetic states of different multiplicity and has a timescale of $10^{-11} - 10^{-8}$ e.g.

$$S_2 \rightarrow T_1 \text{ [45]}$$

Internal conversion, on the other hand, involves relaxation from an upper excited electronic state such as $S_2$, $S_3$, etc. to a lower electronic excited state (e.g. $S_1$) with the same multiplicity e.g.

$$S_2 \rightarrow S_1 \text{ [45]}$$

Vibrational relaxations are transitions between a vibrationally excited state and the $v=0$ state within a given electronic state when excited molecules collide with other species, e.g. solvent molecules. The energy transfer can take place *via* quenching or molecular collisions. Different forms of quenching (e.g. static and dynamic quenching, perturbation) exist, whereas the excess of the vibrational energy is released in the form of heat. [37]

(3) Photochemical reactions

These forms of reactions require the absorption of photons and the resulting excitation of the reacting molecule to a higher energy level. During this process, the energy of the photon is transferred, whereas its energy becomes part of the total energy of the absorbing system. [35] Depending on the nature of the upper and lower electronic molecular state, different reactions occur. In order to understand photo-induced change through light absorption, two fundamental principles apply: [37]

(1) Grotthuss – Draper law: only light, which is absorbed by a chemical entity is active in causing photochemical change. [44]

(2) Stark – Einstein law: when a system is irradiated by light, each photon is absorbed only by one molecule (one-quantum process). This law applies for the large majority, but exceptions occur by intense light sources e.g. lasers, whereas absorption of two or more photons happen. [36] Examples for typical photochemical reactions are discussed in the next section.

## 2.2 Photo-induced reactions in polymers:

Over the past decades, polymers, which are capable of energy transfer and energy migration processes, have be studied extensively and numerous applications found their way in our daily life such as sensors, optics, medical devices, solar energy conversion, resist technologies, self-healing materials, and many more. [46,47] A large variety of stimuli-responsive materials are based on the interaction of macromolecules with light (e.g. photo-induced curing and cleavage reactions). The mechanism of excitation and deactivation were discussed in the previous chapter. In the following, two major polymer–light interactions are discussed in more detail.

### 2.2.1 Light-induced formation of covalent bonds

A prominent example for using light-induced reactions is photo-polymerization, in which solubility, adhesion, melting points, phases, and other chemical and physical properties are changing by network evolution. [48,49] Due to advantages, such as fast curing at room temperature, space and energy efficiency, high-resolution patterns, and solvent-free formulations, much attention has been devoted to these techniques. [47] In the recent decade, it became a powerful tool in various applications, such as coatings, inks, adhesives, varnishes, electronics, photolithography, and dyes. [50] [51] For curing applications, mostly Hg or Xe-lamps are used, whereas the development of more efficient curing equipment e.g. excimer lamps, spot lamps, light emitting diodes, radio frequency excited lamps, visible light sources, laser diodes gained increased attention. [52][53][54] Photopolymerization follows either a free radical or cationic mechanism as described in the following.

### 2.2.2 Free radical polymerization

In order to generate reactive species (free radicals, cations or anions), a photoinitiator absorbs (UV - VIS) light and generally gets excited from its ground singlet state $S_0$ to its first excited singlet state $S_1$ and is then converted into its triplet state $T_1$ via a fast intersystem crossing. [49] In many cases, this transient $T_1$ state yields the reactive radicals $R\cdot$. This reactive species react with the monomer molecule M and starts a chain reaction, which leads to the formation of a polymer. [50]

$$I \xrightarrow{h\nu} R\cdot \xrightarrow{M} RM\cdot \longrightarrow Polymer$$

A photoinitiating system often consists of at least a photoinitiator, a coinitiator, a radical scavenger and/or a photosensitizer [55,56].

Based on their reaction pathway radical creating photoinitiators are categorized in two main groups:

### 2.2.3  Type I photoinitiators [57]

In the photochemical reaction, the bond between the carbonyl group of a ketone (or aldehyde) and an α-carbon atom is cleaved. [58] This photoreaction is termed "Norrish-Type I" reaction. The resulting radicals 2 and 3 (Figure 2-3) can be converted to the corresponding products by recombination, decarbonylation or disproportionation.
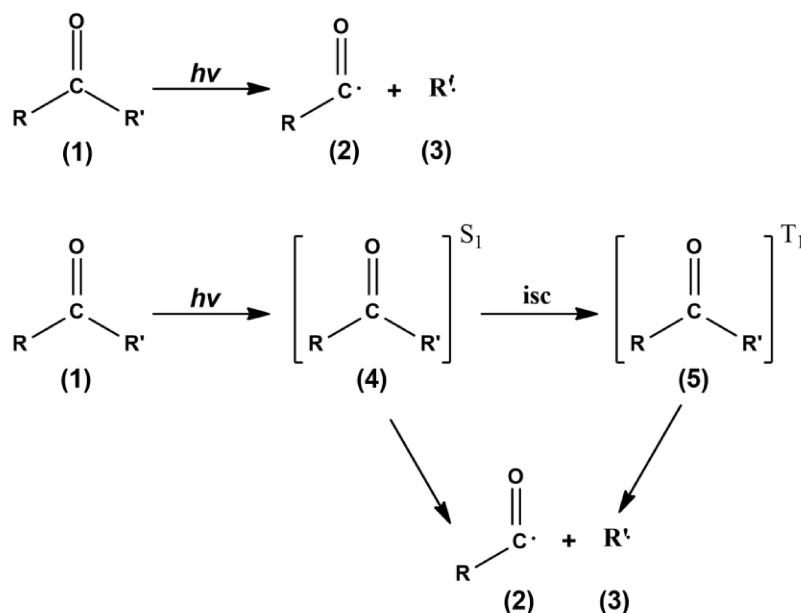


Figure 2-3 Norrish-Type I reaction - Part I [57]

By absorption of a photon, the ketone 1 (or aldehyde) is excited to the $S_1$ state (4), from which the $T_1$ state (5) can be reached by intersystem crossing. Norrish type 1 cleavage can start from both states and results in an acyl (2) and an alkyl radical (3). Aromatic ketones generally react from the triplet state due to fast intersystem crossing.

For asymmetric ketones, two different bonds are available. Which of the two breaks depends on the relative stability of the radicals R· and R'·.

Starting from the radical pair (2), (3) there are different reaction possibilities, the simplest being the back reaction to the starting material 1 (Figure 2-3):
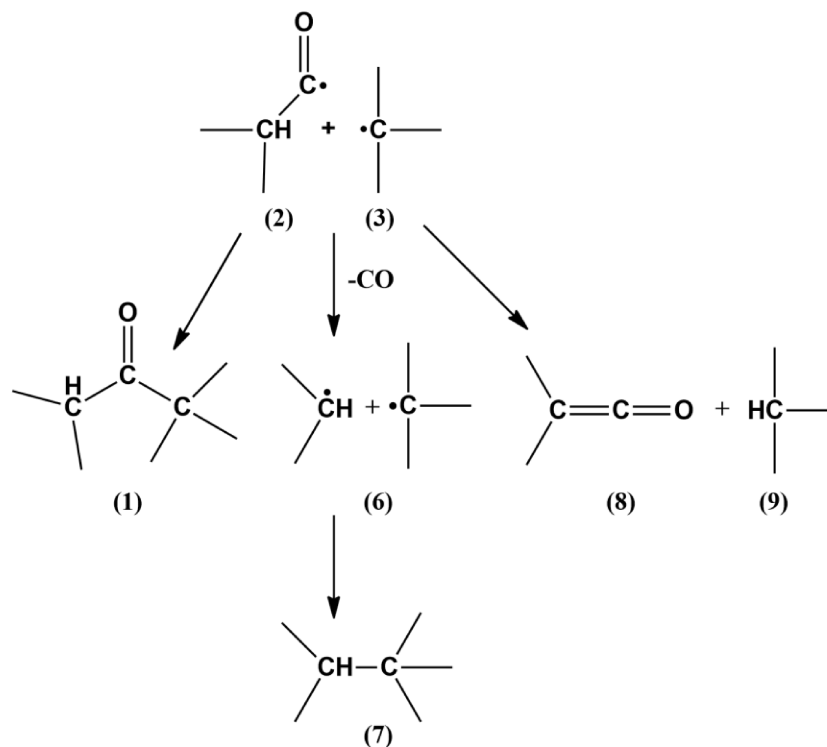


**Figure 2-4** Norrish-Type I reaction - Part II [57]

Furthermore, as illustrated in Figure 2-4, the acyl radical (2) can fragment by cleaving off carbon monoxide (CO), the two radicals (3) and (6) combine to form an alkane (7). A reaction to the symmetrical alkanes (R-R, R'-R') is largely prevented by the solvent cage. If the acyl radical (2) carries a hydrogen atom in the $\alpha$-position, it can be abstracted from the radical (3), resulting in the ketene (8) and the alkane (9).

A further reaction results from the abstraction of a (13) hydrogen atom of the radical (3) by the acyl radical (2), which leads to the formation of an aldehyde (10) and an alkene (11) (Figure 2-5). [57]. This reaction (H-abstraction) also occurs with solvent molecules- and matrix polymers.
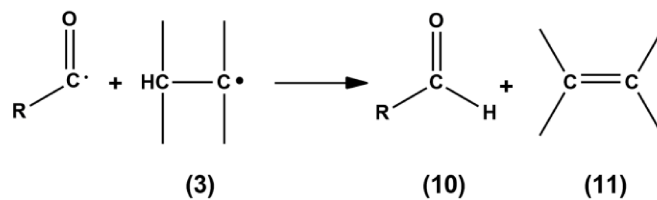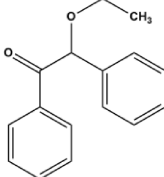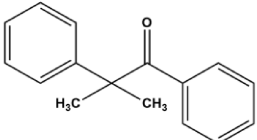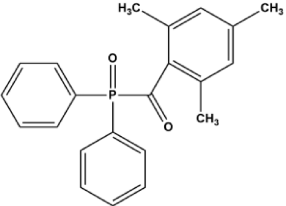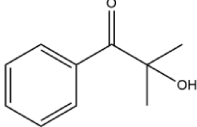
**Figure 2-5** Norrish-Type I reaction - Part III [57]

Some well established photoinitiators for radical polymerization, which are based on the Norrish-Type I reaction are listed in the following table [47]:

**Table 2-2** Example for photoinitiators based on Norrish-Type I reaction

| Class | Example | Chemical structure | Reference |
|---|---|---|---|
| Benzoin ethers | Benzoin ethyl ether |  | [49] |
| Benzil ketals | 2, 2-dimethoxy-2-phenylacetophenone |  | [59] |
| 2,4,6-trimethylbenzoyl)diphenyl-phosphine oxide | Acyl phosphine oxides |  | [60] |
| Aryl alkyl ketone | 2-hydroxy-2-methyl-1-phenylpropanone |  | [61] |

An particularly well-known example for such reactions is an aryl- alkyl ketone, which cleaves when irradiated with UV light and generates radicals (see Figure 2-6): [62,63]
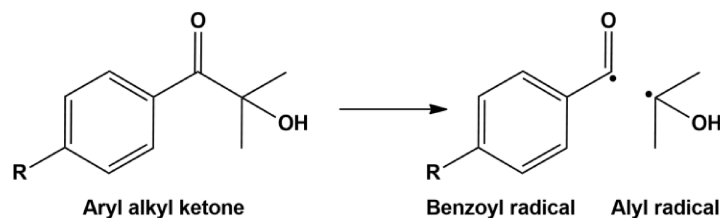
**Figure 2-6** Example for a photoinitiator, which cleaves in a Norrish-Type I reaction

## 2.2.4  Intramolecular abstraction of a γ-hydrogen ( Norrish-Type II) [57]

In this photochemical reaction, a transfer of γ-hydrogen atoms in aldehydes and ketones occurs after exposure to (UV)-light. [64,65]
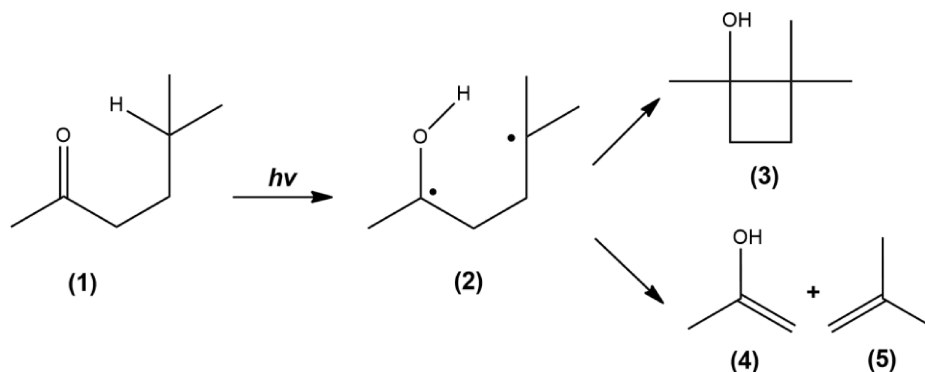


**Figure 2-7** Norrish-Type II reaction – Part I [27]

Photochemically excited aldehyde or ketone molecules, which carry a hydrogen atom in the γ-position, can undergo an intramolecular hydrogen abstraction reaction from both the $S_1$- and the $T_1$-state. [57] This reaction results in a cyclic six-membered transition state. The resulting 1,4-diradical (2) can either recombine to form a cyclobutanol (3) or fragment to form an enol (4), which tautomerizes to the related ketone (6), and yields an alkene concomitantly (5) (see Figure 2-7 and Figure 2-8): [57]
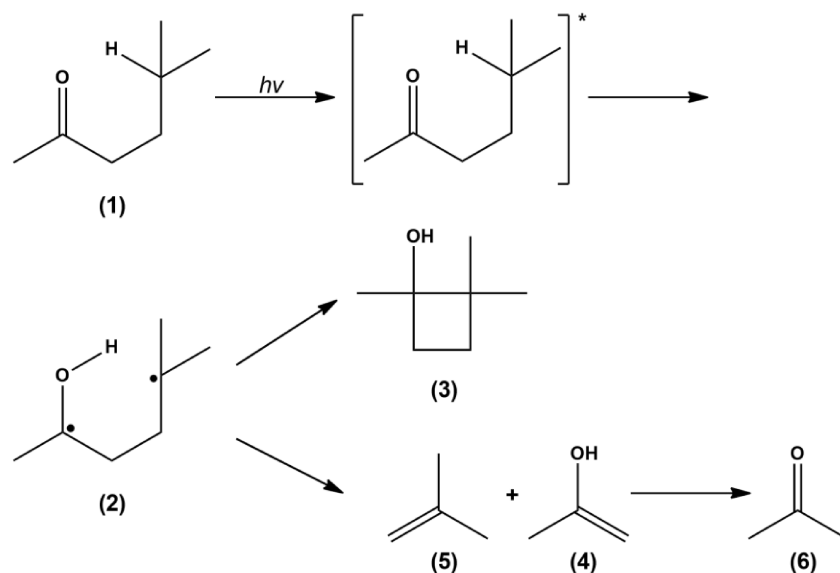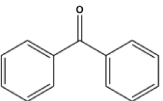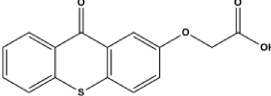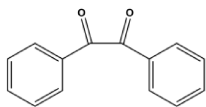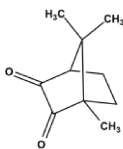
**Figure 2-8** Norrish-Type II reaction – Part II [27]

The ratio of fragmentation to cyclization is determined by the conformation of the diradical (2) in Figure 2-8 and consequently, by the orientation of the molecular orbitals to each other. [57]

### 2.2.5 Type II photoinitiators

Type II photoinitiators are based on aromatic ketones, which are photochemically excited to the T1 state. In the presence of hydrogen donors (such as methylene groups adjacent to nitrogen or oxygen), an exciplex is formed. In the next step, an electron is transferred to the aromatic ketone, followed by the transfer of a proton from the methylene group to the oxygen of the carbonyl group. [47,66] In the case of benzophenone and amines, ketyl radicals are formed, which rapidly dimerize to benzpinakol. The aminyl radicals, which is also formed, initiate radical polymerization. In photopolymerization science, the combination of the aromatic ketone and the hydrogen donor is also termed as "synergetic pair". Table 2-3 displays examples for aromatic ketones that can be applied as photoinitiators. Fig. 2-9 displays the reaction between benzophenone and an aliphatic (-aromatic) amine [69]. It should be mentioned that the well-established type II photoinitiator benzophenone has been discussed with respect to toxicity, and therefore benzophenone is no longer used e.g., in printing ink applications. Well established systems for Type II photoinitiators for radical polymerization are listed in the following table [47]:

14

**Table 2-3** Example for Type II photoinitiators

| Class | Example | Chemical structure | Reference |
|---|---|---|---|
| Benzophenone derivatives | Benzophenone | | [67] |
| Thioxanthone derivates | 2-((9-oxo-9H-thioxanthen-2-yl)oxy)acetic acid | | [67] |
| 1,2-diketones | Benzil | | radical |
| Camphor | Camphorquinone | | [68] |

An example for such reactions is a diaryl ketone, which abstracts hydrogen from a co-initiator (e.g. an aliphatic amino) and generates radicals (Figure 2-9):
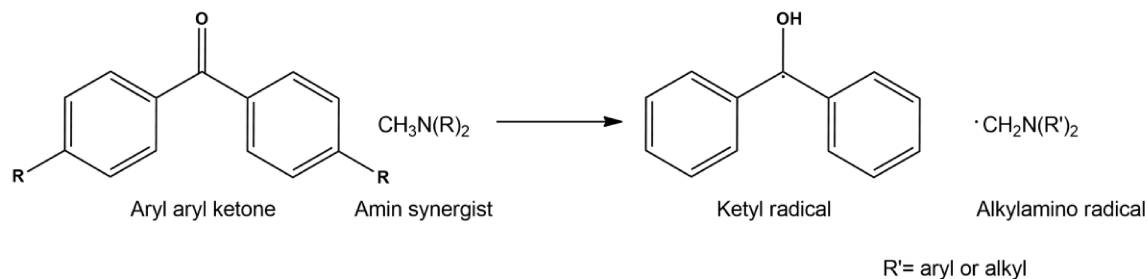


**Figure 2-9** Example for a photoinitiator based on hydrogen abstraction [69]

## 2.2.6  Limitations of Norrish reactions:

Due to the poor quantum yield in the Norrish-Type I reaction, it has long been suspected that primary fission is reversible. Barltrop *et al.* were able to prove this with erythro-2,3-dimethylcyclohexanone (1) with the photochemical isomerization to threo-2,3-dimethylcyclohexanone (2) (see Figure 2-10) [57,70] :
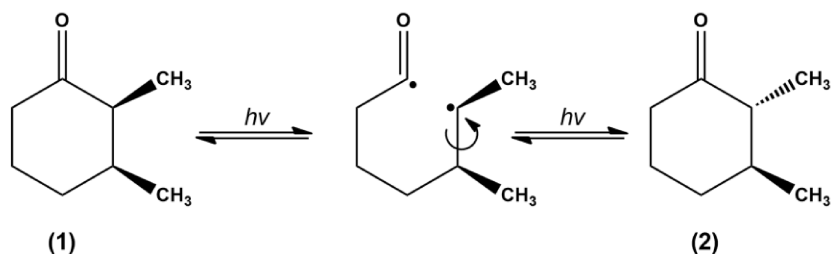
**Figure 2-10** Photochemical isomerization of erythro-2,3-dimethylcyclohexanone [70]

During the cleavage of cyclic saturated ketones (1) the radical pair has different reaction possibilities already described above, but the recombination after decarbonylation leads to a cycloalkane (3) narrowed down to one carbon atom (see Figure 2-11): [57]
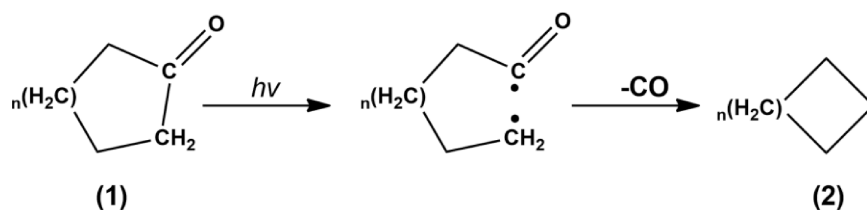


**Figure 2-11** Cleavage of cyclic saturated ketone and formation of a narrowed ring structure [57]

Regarding the Norrish Type II reaction, an explanation for the low quantum yield could be found in the racemization of optically active ketones (1) with chiral γ-carbon atoms. The diradical (2) can also react to the racemate (1) and (3) of the starting material in addition to the starting products mentioned above (see Figure 2-12): [57]
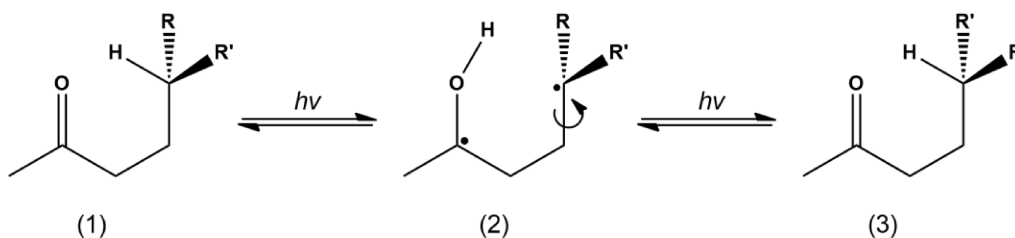


**Figure 2-12** Racemization of optically active ketones [57]

The Norrish-Type I reaction often occurs as a side reaction. The stability of the radicals formed by the α-cleavage is decisive for the ratio of Norrish-I to Norrish-II. Thus, aliphatic ketones (1) without an α-substituent react exclusively according to the type II mechanism, whereas aliphatic *tert*-butyl ketones (2) follow a type I reaction (see Figure 2-13). [57]
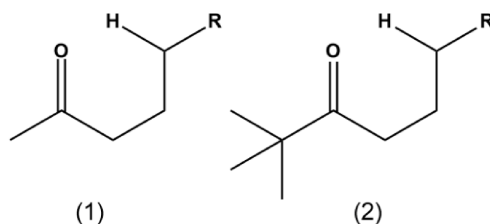
**Figure 2-13** Dependence of the α-substituent [57]

### 2.2.7 Considerations with respect to applications:

The polymerization involving a photoinitiator has some additional limitations, which have to be considered. Some limitations are listed below: [35]

- Oxygen inhibition: Cleavage products of the photoinitiator and radical chain products can react with atmospheric oxygen and form hydroperoxides, peroxides or carbonyl groups. Moreover, oxygen is able to quench the excited photoinitiators. In order to prevent oxygen inhibition, the reaction should be carried out under inert conditions. [45]

- Wavelength matching: The emission spectrum of the used lamp has to match with the absorption wavelength of the photoinitiator. This is illustrated in Figure 2-14. The wavelength range of the molecule (I) absorption has to match with the spectral emission range of the light source. [37] [50]
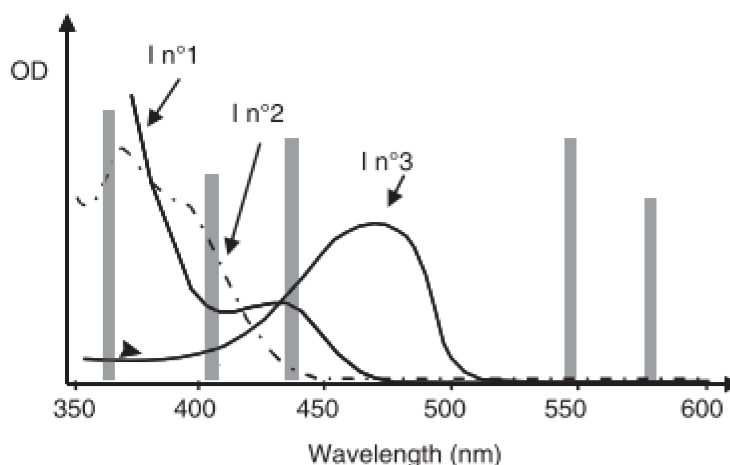


**Figure 2-14** Typical absorption spectra of photoinitiators that match with the emission of a Hg lamp [50]

- Pigments or colored compounds: In order to enhance the absorption of light, pigments can act as photosensitizers. The task of the photosensitizers is to absorb light and transfer the excess of energy to the photoinitiator through an energy transfer process, whereas the light scattering is important here. [71]

- Migration of low molecular weight compounds: Leaking and migration of low molecular weight substances can lead to unwanted odor. [72]

- Photobleaching of the photoinitiator: Photoinitiators, which absorb light in the visible region (> 400 nm) form cleavage products, which are transparent in the respective wavelength region. [73] Acylphosphine oxides are characteristic examples.

- Penetration depth of the light: The depth of light penetration increases as the wavelength of the light source rises. Therefore, in the case of a thick layer, a lamp emitting longer wavelengths and a photoinitiator absorbing in the long wavelength region should be applied. [35]

- Molar absorption coefficient ε: This parameter reflects the number of photons that are absorbed. A high molar absorption coefficient indicates a higher probability of the electronic transition and therefore, the amount of photoinitiator required for curing is lower. [37]

- Furthermore, ageing and a resulting yellowing and discoloration can occur, which can be decreased by additional absorbers and photo-oxidants. [74]

### 2.2.8 Cationic photopolymerization

Crivello and co-workers introduced diaryliodonium and triarylsulfonium salts as a starting point for optically triggered cationic curing of epoxy based resins. In this system, a photosensitive compound absorbs (UV- VIS) light and undergoes decomposition leading to an initiating species, namely a "super acid". This reactive species, a radical cation (R+·)

reacts with cationic polymerizable monomers (M corresponds to an epoxy monomer), and yield a polymer. [75–77] As illustrated in Figure 2-15 the photosensitive compound, namely Photoinitiator (PI) absorbs incident light and decomposes to form the initiating species. The active species, the radical cation (R$^+$), then reacts with the cationic polymerizable monomer (M), and yields the polymer. [50] Photoinitiators of this type are commonly termed "photoacid generators".

$$PI \xrightarrow{h\nu} H^+ \;+\; R^{\cdot +} \;+\; \text{Other products}$$

$$R^{\cdot +} \;+\; M \longrightarrow \text{Polymer}$$
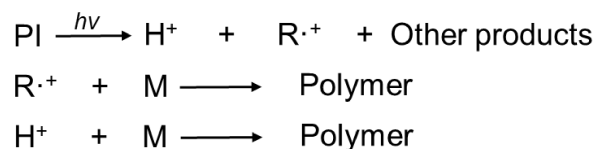
$$H^+ \;+\; M \longrightarrow \text{Polymer}$$

**Figure 2-15** General scheme of photoinitiated cationic polymerization [50]

Examples for photoinitiators for cationic polymerizations are onium salts. They consist of a chromophoric group as a light sensitive compound with heteroatoms as cationic centers. As a counterion, mostly inorganic metal complex anions are used. [50,78]

Frequently used onium salts are diaryl iodonium, triarylsulfonium, and tetra alkyl phosphonium salts with a non-nucleophillic counter ion such as $BF_4^-$, $PF_6^-$ and $SbF_6^-$. (see Figure 2-16). [79–81]
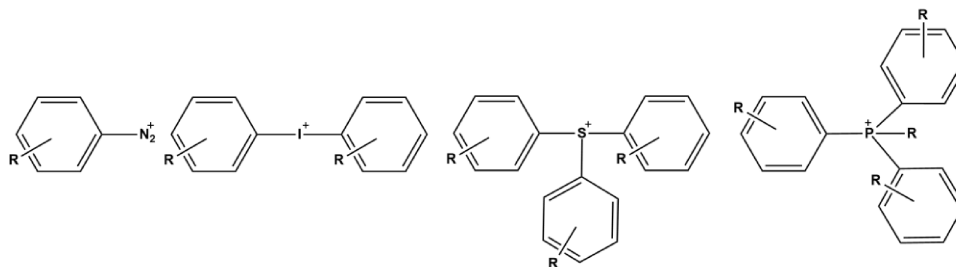


**Figure 2-16** Examples for photoinitiators used in cationic photopolymerization [50]

### 2.2.9  Comparison of both photo-induced curing mechanisms

One main difference between the two polymerization mechanisms are the different monomers. On the one hand, most monomers containing carbon–carbon double bond undergo radical polymerization, while ionic polymerizations are highly selective. Cationic

polymerization is mostly limited to electron-releasing substituents such as alkoxy, phenyl, vinyl, and 1,1-dialkyl. [82]

Further differences of both systems are listed in the following table [34,65]:

**Table 2-4** Comparison of radical vs. cationic photopolymerization

| Radical polymerization | Cationic photopolymerization |
|---|---|
| acrylates, unsaturated compounds | epoxides, tetrahydrofuran, vinylethers |
| Well- established, numerous photoinitiators and monomers available | Less- established, photoinitiator rather expensive |
| $O_2$- sensitive (inhibition) | Sensitive to bases |
| Waster- based systems possible | No water- based systems possible |
| No post reaction | Significant post reaction |
| acrylates can cause skin sensitization and skin irritation | |

## 2.3 UV-induced cleavage

Photo-induced cleavage of polymers is often of great interest regarding the specific degradation mechanism, when polymers are exposed to (UV-) light over a certain period. [74,83] In particular, research focused on the specific cleavage of polymers by photoactive groups. For that, different systems have been developed and especially applied for resist technologies. Some examples are the following:

- **Poly(methyl methacrylate)** (PMMA) [84–86] degrades by Norrish-Type I reaction, when exposed to light. As shown in Figure 2-17, PMMA splits off $CO_2$ and a $CH_3$- radical, and chain degradation proceeds *via* β- scission. [48]
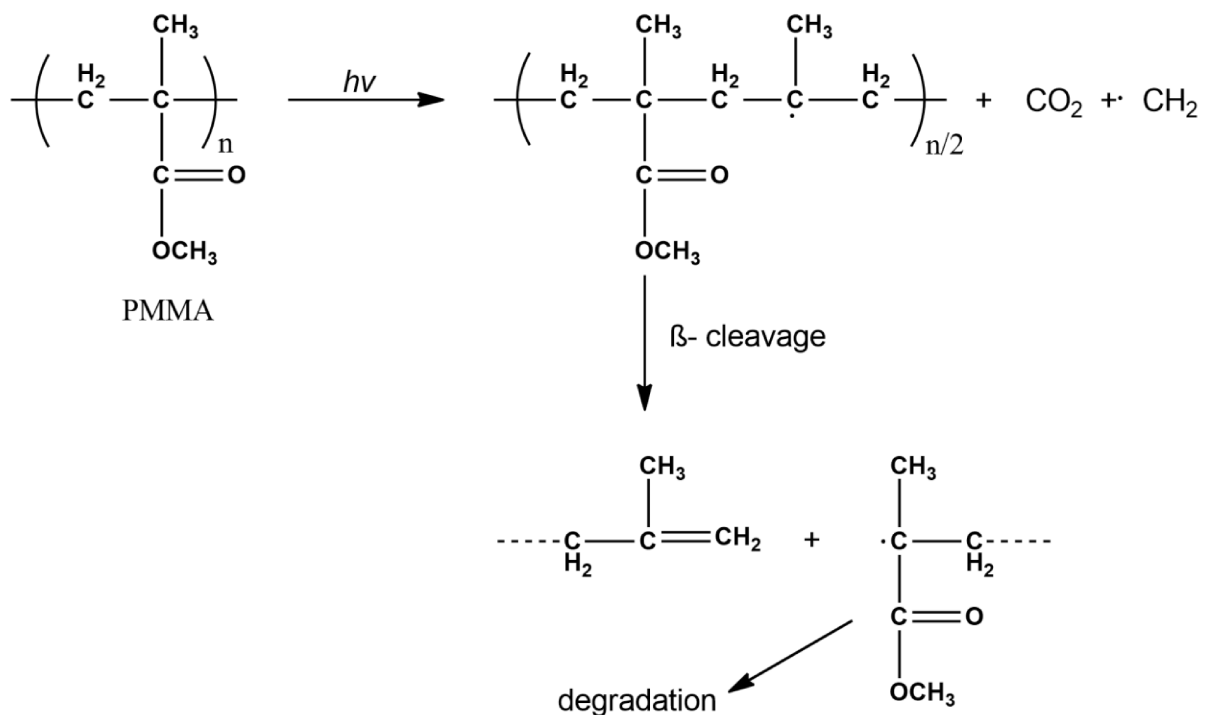


**Figure 2-17** Photodegradation of PMMA by Norrish-Type I reaction and subsequent chain scission [48]

- **Poly(2-butene sulfone) (PBS)** [87] undergoes a controlled decomposition by UV-radiation. As demonstrated in Figure 2-18, PBS degrades to monomers, 1-butene, and sulfur dioxide. This reaction mechanism is used for positive resists. [88]
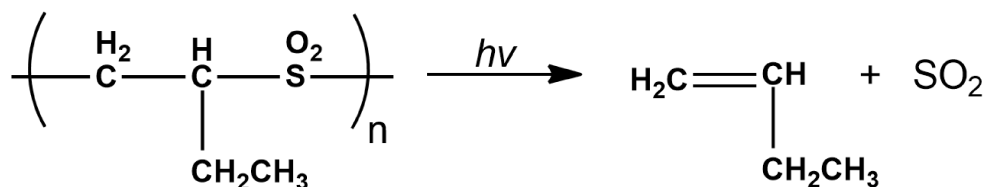


**Figure 2-18** Photodegradation of PBS [48]

For the manufacture of resists, change of the solubility of the resist polymer after exposure is essential. One example for a compound, which undergoes a significant polarity change after irradiation, is diazo- naphthoquinone (DNQ), which yields a carboxylic acid. Here, DNQ decomposes to indencarboxylic acid-4-sufonate, which is better soluble in alkaline conditions.
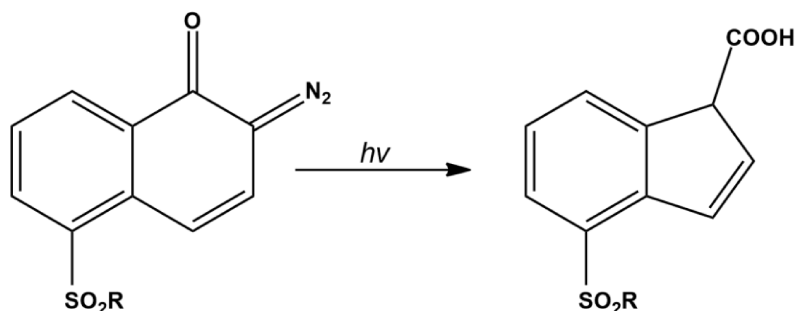


**Figure 2-19** Photodecomposition of NDQ [48]

The cleavage mechanism, which was used for this work is based on the chemistry of ortho-nitrobenzyl ester (o-NBE) compounds. It was first introduced by Schofield and co-workers in 1966 and first applied synthetically by Woodward *et al.* in 1970 as a protecting group for alcohols and carboxyl acids in organic chemistry. [89] [90] In addition, its chemistry was used in deprotecting phosphates, carbonates, carbanates, thiols, phenolates and alkoxides. [91] Once irradiated, the photo-cleavage follows a radical mechanism, based on a Norrish-Type II reaction. [92] The molecule absorbs energy in form of light to get excited and undergoes intersystem crossing from the singlet- to the

triplet state, where an n-π* transition takes place. Figure 2-20 illustrates the cleavage mechanism:



$R_2 = H, CH_3$
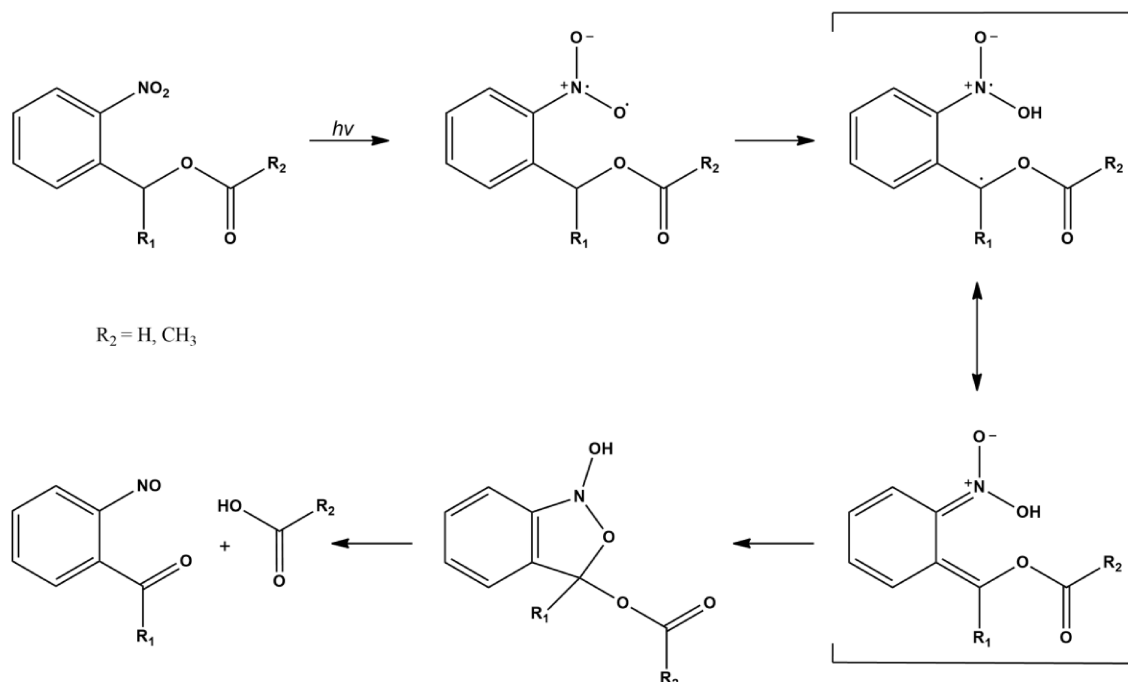
**Figure 2-20** Photoreactions of ortho-nitrobenzyl esters [93]

Upon radiation (200- 320 nm), an incident photon cleaves the N=O π- bond forming a diradical. [94] An intramolecular hydrogen abstraction of the benzylic C-H by the excited nitro groups forms an *aci*-nitro intermediate. Depending on the solvent and pH, the decay rate constant of the intermediate is ca. $10^2$- $10^4$ s$^{-1}$. The next step includes the irreversible cyclization of the *aci*-nitro intermediate and a subsequent formation of a further intermediate and a final ring- opening step, where 2-nitrosobenzalde and carboxylic acids are produced. [91,95,96] Upon longer dose, secondary photoreactions occure, involving the formation of azobenzene groups by dimerization of the o-nitrosobenzaldehyde. [94,97,98] The described mechanism is well-established in several applications, which will be discussed in the following chapter. [99] Regarding on-going scientific research, cleavage reactions driven by *o*-NBE can be found in drug releasing systems, functional coatings, optogenetics and photocages. [93,100–106] In order to increase the quantum yield and release rate of such compounds, a variety of modifications were studied in the past 30 years. Most variations target the aromatic chromophore and the substitution at the benzylic carbon atom. The aim of current research is the shift of the effective

absorbance to longer wavelengths. [107–109] [91] A further attempt in increasing the reaction and quantum yield is the addition of a second nitro group. [110] Examples for such modifications of *o*-NB analogues are listed in Figure 2-21. As leaving groups (LG) phosphates, carboxylates, carbonates, and carbamates to thiolates, phenolates, and alkoxides could be released. [91]
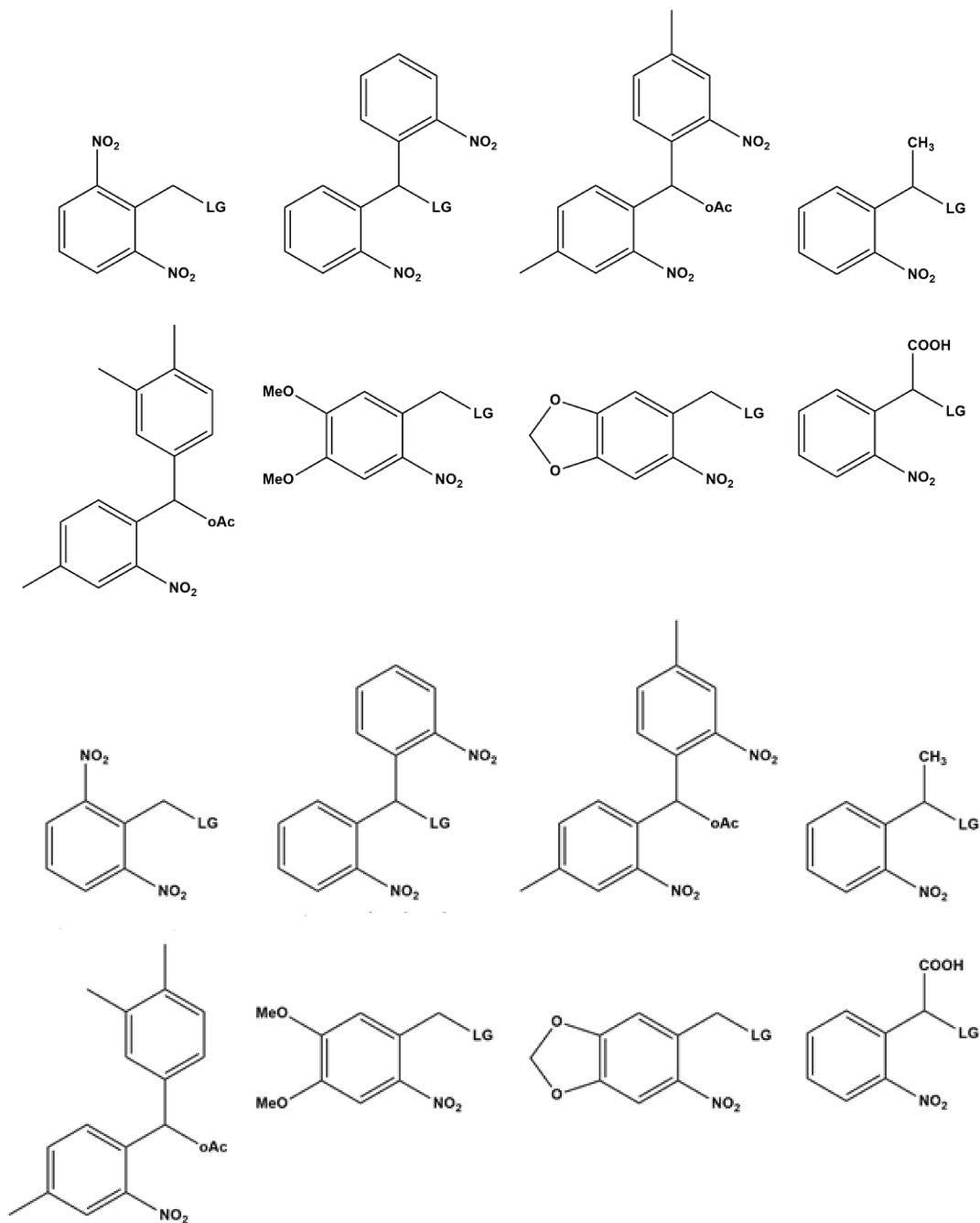


**Figure 2-21** *o*-NB analogues [91]

Moreover, due to the high quantum yields of the *o*-NBE isomerization, the reactions can be carried out with low exposure doses, which prevents damage of the photoresist matrix. [111] In the 1980s, first approaches were carried out to introduce *o*-NBE chemistry in methacrylate and acrylate photopolymers. Reichmanis *et al.* used *o*-NB alcohol derivatives with acrylate functions to produce thin polymer films for photoresists. [112] In another approach, *o*-nitrobenzyl cholate ester were introduced in a polymeric matrix of poly-co-(methyl methacrylate-methacrylic acid) to hinder the network's solubility. The *o*-nitrobenzylcholate ester could be cleaved upon radiation with UV light, yielding soluble cleavage products and allowed the selective removal of the irradiated area in an aqueous alkaline solution. [113]

## 2.4  Recent developments in the field of *o*-NBE chemistry

As described before, a large variety of different approaches that uses *o*-NBE chemistry have been introduced in the last decades. The majority of the studies report the design of methacrylate-, acrylate- or thiol-click networks with photosensitive *o*-NBE links. [114]

In more recent work, *o*-NBE-based photoresists were applied for the patterning of organic light-emitting diode (OLED) displays and organic thin-film transistors (OTFTs). [114,115] A photoresist, which is based on a co-polymer that contains monomers with highly fluorinated groups and methacrylic nitrobenzyl ester monomers is manufactured. [114,115] The copolymer became insoluble in hydrofluoroethers solvents, after photolysis of the *o*-nitrobenzyl ester groups, which allowed for selective network dissolution. With this approach sub-micrometer patterning was introduced, which showed higher performance compared to other chemically amplified techniques for PEDOT: PSS photo-patterning. [115] Another approach was the fabrication of protein microarrays, where a terpolymer (*o*-NBEMA-MMA-PEGMA) containing an *o*-nitrobenzyl methacrylate (*o*-NBEMA) was synthetized. Patterns were inscribed by photolithography using a phosphate buffer solution with a pH above 6.6 in the development step. Further binding of biotin to the hydroxyl end groups of PEGMA units enabled selective immobilization of streptavidin on the surface, allowing for multicomponent protein patterning. [88,114] In addition, *o*-NBE can be implemented in polyelectrolytes for the fabrication of PEMs (polyelectrolyte multilayers). Polyelectrolytes represent layers of polycations and layers of polyanions,

which change their charge interaction force among the layers, when exposed to an external trigger (e.g. pH, light or temperature). [114,116,117] For example, *o*-NBE containing methacrylate monomers were used in a photo-responsive PEM network to achieve an overlapping of two domains with different wavelength responsiveness. For that, two photolabile groups were used: dialkylamino-coumarin ester molecule (sensitive in the visible light region) and *o*-nitrobenzyl ester molecules (sensitive in the UV-light region). [116] Selective disassembly of the two PEMs domains was then obtained by light exposure.

## 2.5  Photolithography

Photolithographic methods are well-established techniques to produce computer chips, dynamic random access (DRAM) memories, optical sensors for digital cameras (CCD, CMOS image sensors), diode arrays, microelectro-mechanical systems (MEMS), photonics, transistors for LCD and OLED displays, silicon substrates for photovoltaic cells and many more. [50] [118] Several sources of electromagnetic radiation have been studied and introduced. Examples are X-ray lithography, ion beam lithography, electron beam lithography, and extreme ultraviolet lithography (EUV). [85,119,120] In addition, mercury lamps are often used with emission wavelengths at 365.4 nm (I-line), 404.7 nm (H-line) and 435.8 nm (G- line). [121] Reason to use UV-induced processes for lithographic process are, on the one hand, the shorter wavelength of UV than visible light and a higher ultimate feature resolution, and, on the other hand, the more efficiently controlled UV light source, without interference from visible light sources. [37] In optical photolithography, the overall structure of a resist contains a light-sensitive material in form of a thin layer (photoresist) deposited on a substrate (e.g. Si- wafer). A photo-mask, carrying e.g. circuit pattern information, is placed on the polymer layer and a subsequent transfer of that pattern by radiation is carried out. [122] Photolithography uses a set of parameters: the tone, the sensitivity, the resolution and the contrast, to define the appropriate resist for specific exposure conditions in order to achieve a desired pattern. [37] The thin layers are often applied by spin-casting on the substrate, and subsequently fixed by removal of the solvent by a baking or vacuum-step. [123] Several techniques for photolithography are applied in industry. In contact printing, a mask is placed on the wafer surface and visually aligned to the previous pattern on the wafer. After successful

alignment, the mask is pressed in hard contact on the resist coated wafer and exposed to radiation. [124] A modified version of this technique is proximity printing. Here a space between the wafer and the mask is maintained. [125] The main advantage of this method is the prevention of damage of mask and wafer, whilst the resolution decreases. [123] An additional approach for photolithography is projection lithography, in which the mask image is projected onto the wafer through an optical system. This method improves the lifetime of the wafer and decreases defect densities because intimate contact between the wafer and mask is not required. [122,126,127]

The general principle of photolithography is the selective expose of the photo-resist to light through a mask. The exposed regions undergo photo-chemically induced changes, which alter their solubility compared with the unexposed regions. The resist material mainly absorbs in the UV-region of the electromagnetic spectrum and either undergoes bond cleavage or creates radicals/cations, which induce crosslinking reactions (see section 2.2). [50] Based on the chemistry of the photo-sensitive resin two different forms of resists can be distinguished and illustrated in Figure 2-21. [123,128]

Positive-tone resist: in this system, the polymer cleaves through chain fragmentation and other fission reactions when exposed to light. Through rearrangement and/or formation of hydrophilic or hydrophobic groups, the polarity is changed. An additional washing step removes the soluble part of the resist and the unexposed areas remain unaltered, generating the structures. [129]

Negative-tone resist: through exposure with a light source, the thin polymer layer becomes insoluble. This is caused by an increasing rate of network formation and molecular weight. Usually photopolymerization, aided by photoinitiators, is used. Reactions, which utilize photopolymerization are described in section 2.2. [130]

Additional steps for e.g. the production of microelectronic components is etching or metallization. Here, the photoresist act as a protective layer or mask, whereas the uncovered areas of the metal, oxide, or silicon wafer are chemically etched (wet etch or dry etch under plasma). [50] One example for such a process is the etching of silicon dioxide layers, which are partly protected by a photo-resist. [131] For the etching

hydrofluoric acid is used, whereas photoresist covered areas are not attacked and *vice versa*. [37] In order to increase the photoresist's resistance against chemical etchants several methods can be used [37]:

1. Baking: This step induces a thermal cross- linking of the resist material. Thus, the resist becomes harder and less soluble in chemical etchants.
2. Resist thickness: By decreasing the acceleration time, the spin speed and the spin duration during the spin-coating process, thicker resist layer can be produced.

As illustrated in the following Figure 2-22, after the etching step, the stripping step follows place in which the remaining photoresist is completely removed. The result is a silicon wafer, whose surface contains lines and spaces on the nanometer scale. Furthermore, the spaces are filled with a conductor, usually copper, obtaining the complimentary metal-oxide semiconductor (CMOS). [50,125] The whole procedure is illustrated in the following figure:
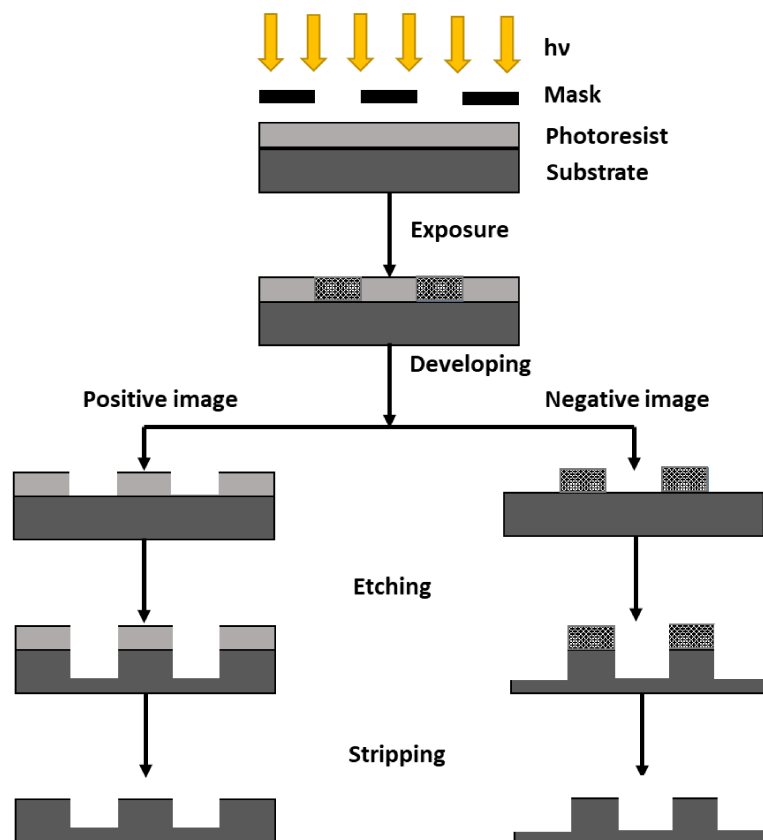


**Figure 2-22** Photolithographic process steps [35,124]

### 2.5.1 Key properties for the photolithographic quality

Regarding the quality of photolithographic processes several key elements have to be considered:

**Numerical aperture (NA):**

NA represents a dimensionless number of an optical system, that describes the ability to focus light through the accepted or emitted range of angles over the system [35].

$$NA = n \cdot \sin\theta \qquad \text{(Equation 2-2)}$$

n is the index of refraction of the medium in which a lens works and θ represents the maximum half-angle of the cone of light that can enter or exit the lens.

**Diffraction limit (d)**

Light cannot be focused to a smaller size than the diffraction limit, in which d is defined as the lowest spatial resolution, which can be resolved. [37]

$$d = \frac{\lambda}{2n \cdot \sin\theta} \qquad \text{(Equation 2-3)}$$

λ represents the wavelength of a light beam, that is travelling through a medium of a refractive index n, and converging to a spot with an angle θ. n·sinθ is termed the numerical aperture (NA).

d is in the order of 200-400 nm for wavelengths in the visible light region. [37] The result of d limits the spatial resolution of optical devices and the size of photolithographic pattering. New techniques in optical microscopy e.g. Scanning Near-field Optical Microscopy (SNOM) and Stimulated Depletion Emission Microscopy (STED) are able to overcome the diffraction limit. [37,132]

**Rayleigh equation/critical dimension**

The resolution limit of conventional optical lithography (instrument) is determined by the Rayleigh equation (Equation 2-4). It is directly proportional to the exposure wavelength (λ)

and inversely proportional to the numerical aperture (NA). $k_1$ represents a constant that depends on the equipment used and has values between 0.4 and 1.0. [37]

$$R = \frac{k_1 \cdot \lambda}{NA}$$ (Equation 2-4)

The equation shows, that the size of the features will decrease by decreasing the exposure wavelength or by increasing the numerical aperture.

**Depth of focus (DOF)**

One further key parameter for lithographic processes is the DOF. It is defined as the range of focus that can be tolerated, before the image quality is outside of its specifications. [125]

$$DOF = \frac{k_2 \cdot \lambda}{NA^2}$$ (Equation 2-5)

$k_2$ represents a second process-specific parameter with values <1. The DOF is proportional to the inverse of the square of NA. Generally, the resolution may improve by increasing NA, but it is only at the expense of depth of focus. [122]

**Standing wave effects**

In a fixed volume of space and without interference, only certain waveforms are stable, namely standing waves. All other wavelengths are destroyed by interference. This phenomenon occurs, when a light wave is trapped between two mirrors, separated by the length L, at the surface of the mirrors the wave displacement is zero, termed nodes. [37] Under these conditions, the only wavelengths that are stable over time can be defined by: [37]

$$\lambda = \frac{2L}{n}$$ (Equation 2-6)

n is an integer, with n=0,1,2...

### 2.5.2 Improvement of the key factors:

In order to improve key properties of optical instruments e.g. advancing the resolution limit, $k_1$ (III) or λ can be decreased and NA increased. However, change of the process factor $k_1$ is rather difficult, since an increase in NA also leads to a strong decrease in depth of focus. [37]

Another approach to adjust the capabilities of photolithographic systems is the selection of the lamp with a suitable wavelength. In the past decade, great effort has been taken in the development of excimer lamps, spot lamps, light emitting diodes, radio frequency excited lamps, visible light sources and laser diodes. [50] The list below illustrates some types of lamps with their characteristic values:

**Table 2-5** Correlation of radiation wavelength and minimum feature size in dynamic random access memory (DRAM) [35,125]

| $LW_{min}$ | Light source | Wavelength [nm] |
|:---:|:---:|:---:|
| 0.8 | Hg discharge lamps | 436 (g-line), 365 (i-line) |
| 0.5 | Hg discharge lamps | 436, 365, 250 |
| 0.35 | KrF excimer lasers | 248 |
| 0.25 | KrF excimer lasers | 248 |
|  | ArF excimer lasers | 193 |
| 0.18 | ArF excimer lasers | 193 |
| 0.090 | $F_2$ excimer lasers | 157 |
|  | ArF excimer lasers | 193 |
| 0.0065 | $F_2$ excimer lasers | 157 |
|  | ArF excimer lasers | 193 |
| 0.045 | EUV sources | 13.5 |

The prediction of Moore's law (number of transistors in a dense integrated circuit (IC) doubles every two years) has motivated the development of IC technologies to produce feature sizes down to 3 nm (2020). [133,134] In order to compensate for certain limitations in the lithographic processes resolution enhancement technologies (RET) were introduced.

To increase the contrast of the image formed at the wafer, manipulation of the wave front of the light passing through the photomask and into the imaging system is carried out. All techniques have the aim to control either the amplitude, the phase or the direction of a wave. Principal methods which are used are listed below: [135,136]

Phase-Shifting Masks: Feature of the mask are etched to create higher contrast trough interference effects.

Optical Process/Proximity Correction: For local exposure adjustment, the shapes of the polygons in the mask layout are changed.

Off-Axis Illumination: Light, which impinges on the photomask at higher angles, interacts with the diffraction pattern from the mask to increase particular high spatial frequencies.

### 2.5.3  Requirement to the resist material:

For the computer chip production, certain criteria are important to consider. In order to generate a uniform and thin film during the spin casting process, adhesion to various substrates e.g. metals is necessary. Moreover, the material must include high radiation sensitivity and high-resolution capability and withstand extremely harsh environments, for example, high temperature, strong acids, and plasmas. Progress has been made by using light of shorter wavelength and new materials with optical density less than 0.4. A high aspect (height-to-width) ratio of lines is limited by the risk of pattern collapse. Another approach is the control of the liquid of the resist material, whether for positive- or negative resists. Radiation induced conversion of additives can aid to control the solubility behavior of the polymer. [35,137,138]

**Sensitivity and contrast of a photoresist**

Sensitivity, S ($mJ\ cm^{-2}$) can be understood as the minimum light energy that is needed to produce a decent image. This is closely related to the energy at which the full thickness of negative resist remains, or all of the positive resist is removed, after development. [124] The sensitivity of a resist is related to the thickness d of the layer after exposure and development and can be determined from the spectral response curve (Figure 2-23). [139] For positive resists $S \equiv D_{exp}^{0.0}$ correlates to the exposure light dose necessary to completely remove the exposed polymer from the substrate, whereas for positive resists, there is some solubility, even at zero exposure. [140] $D_{exp}$ defines the product of light intensity and irradiation time. Here the normalized thickness of the resist layer is equal to zero, $d_{irr}/d_0 = 0$.

On the contrary, for the negative resist $S \equiv D_{exp}^{0.5}$, $D_{exp}^{0.8}$ or $D_{exp}^{0.9}$ corresponding to $d_{irr}$=0.5 $d_0$, $d_{irr}$= 0.8 $d_0$ or $d_{irr}$=0.9 $d_0$ can be used. [35]

High resist sensitivity correlates to a lower exposure dose and indicates a faster production rate. Furthermore, resists can be used for shorter UV wavelengths where the emission of conventional light-sources is reduced. A resist with a high sensitivity results, when the light source has strong emission lines, resulting in a shorter exposure time.[124,141,142]

The performance of a photoresist can be determined by its contrast curve, in which the remaining resist fraction of a uniformly illuminated resist is plotted versus the logarithm of the applied exposure dose. [143,144] The contrast curve characterizes the sharpness of the material transition from exposure to non-exposure. [143,144]
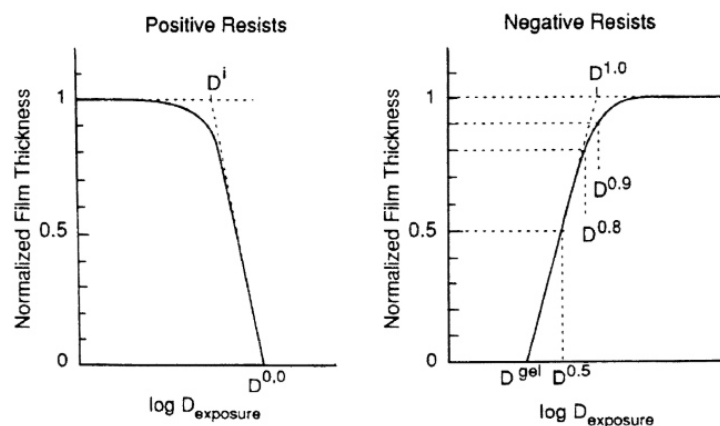


**Figure 2-23** Contrast curves showing resist thickness vs. exposure energy [35]

An important parameter is the contrast of a photoresist material, which characterizes the sharpness of the transition from exposure to non-exposure. It can be estimated from the slopes of the linear portions of the curves in Figure 2-23. [124] The contrast can be described as:

$$\gamma = \frac{1}{\log_{10}\frac{D_{100}}{D_0}}$$

(Equation 2-7)

$D_{100}$ and $D_0$ are obtained by extrapolating the linear portion of the normalized thickness versus energy plot to 1.0 normalized thickness. [124]

Other essential process parameters are: [124,144]

Viscosity: depending on the solid content and temperature, the viscosity has an impact on the flow properties and film thickness.

Adhesion: characterizes the strength of sticking of the film to a wide range of substrate materials e.g. silicon wafer or metals, whereas a weak adhesion can cause the loss of a pattern.

Thermal stability: a proper stability is necessary for plasma and UV treatment after the development step.

Photospeed: can be determined by the quantum efficiency of the resist.

Etch resistance:  describes the ability to protect the substrate from subsequent etching,

Shelf-life: describes the storage time, before the resists properties change over time.

## 2.6 Covalent adaptable networks (CANs)

In recent years a paradigm shift has occured. The strict classification of polymers according to their properties has been changed by the development of new materials. Examples for such classifications are thermosetting resins and thermoplastic polymers, which can be clearly characterized by their properties. On the one hand, thermosetting resins become hard and insoluble upon heating, whereas three-dimensional networks are formed bearing covalent bonds, which are typically strong and irreversible. On the other hand, thermoplastics can flow and be reshaped at ambient temperatures, consisting of linear polymer chains hold together by non-covalent intermolecular forces, making these polymers recyclable and reprocessable. Therefore, the main difference of these two classes is given by the nature of the bonds between the polymer chains. By implementation of exchangeable, reversible or adaptable covalent bonds into the polymer matrix, the physical properties of these two classes overlap and blur. [145] At this point the term dynamic refers to "dynamic" covalent bonds, which are reversible and can quickly reach thermodynamic equilibrium in response to a stimulus. [146]

Aims for the introduction of new polymeric materials are the need of an enhanced recyclability [147–149], shape memory [150,151], reversible polymerization [152,153], self-healing [154–157] and degradability. Regarding the special features of these polymeric materials, several applications have been introduced and were part of extensive studies in the last decade. External stimuli include heat [158–160], pressure [9], and light. [161,162] Along with dynamic covalent bonds, also non-covalent bonds such as hydrogen bonds [163], π-π stacking [164] and metal-ligand bonds [165] are used. Limitation of these approaches are often their weak binding energies. Non-covalent adaptive binding interactions typically range from 1 to 5 kcal/mol, contrary to the covalent binding energy of ≈50-150 kcal/mol. Thus, networks relying on non-covalent bonds are typically characterized by inferior mechanical properties. [166]

### 2.6.1 Rearrangement reaction pathways of covalent adaptable polymers

As described in the previous chapter, CANs can respond to an external trigger such as heat or light, and adapt their macromolecular structure by rearranging their covalent bonds to this response. [167] The nature of this response strongly depends on the rate and type of chemical bond exchange within the polymer matrix, which gets activated to is able to

flow and relax stress. [168] Limitations of such networks are partial reversibility owing to side reactions, which exclude certain thermoreversible cross-linking reactions. [169] Bowman and Kloxin distinguish between two different types of CANs, in which the dynamic structure is achieved either kinetically through bond exchange or by equilibrium shifts resulting in reversible depolymerization. [170]

Regarding rearrangement reactions within a macromolecular matrix, according to Winne *et al.* two molecular network rearrangements (MNRs) can be differentiated: [171]

1. Concerted (or single step) MNRs

2. Stepwise (or multistep) MNRs

For the concerted pathway (Figure 2-24), the new network connection can be formed simultaneously as the old network connection is interrupted, whilst no intermediate state is formed through an ordered transition state. Since all available network topologies have the same number of cross-links, the degree of connectivity or the cross-linking density of polymer networks that undergo concerted rearrangements will not change[171,172]
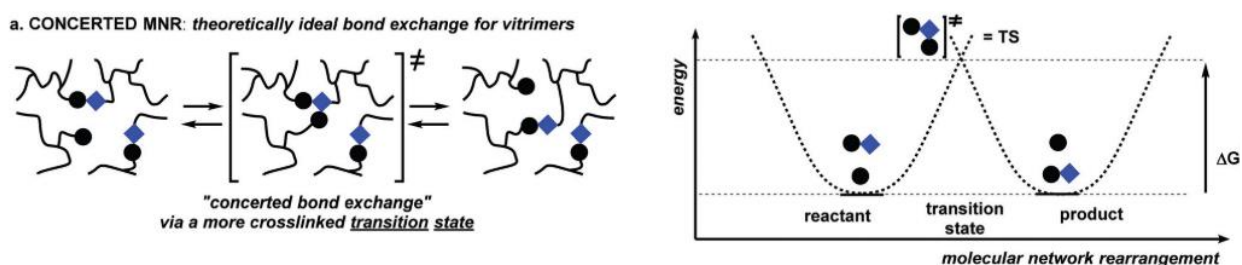


**Figure 2-24** Illustration of the concerted molecular network rearrangements (MNRs) within covalent networks and their energy profiles [171]

Examples for concerted pathways are polyionic polymer networks containing *N*-alkylated triazolium iodide moieties as cross-links [173] and polythioether networks including sulfonium sulfonate ion pair as alkylating cross-links.[174] Both reaction mechanism are illustrated in the following figure:

(a) Montarnal and Drockenmuller, 2015

(b) Winne and Du Prez, 2017
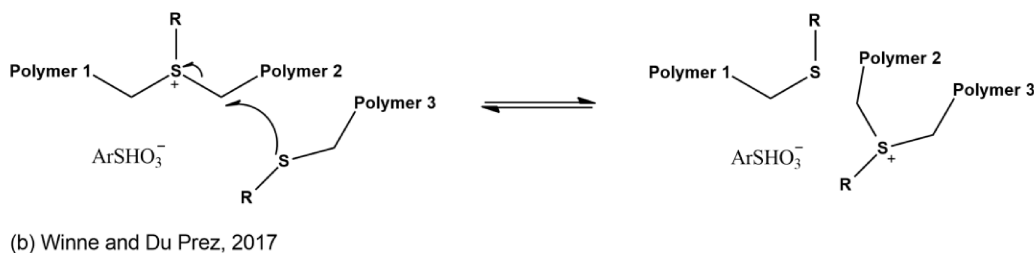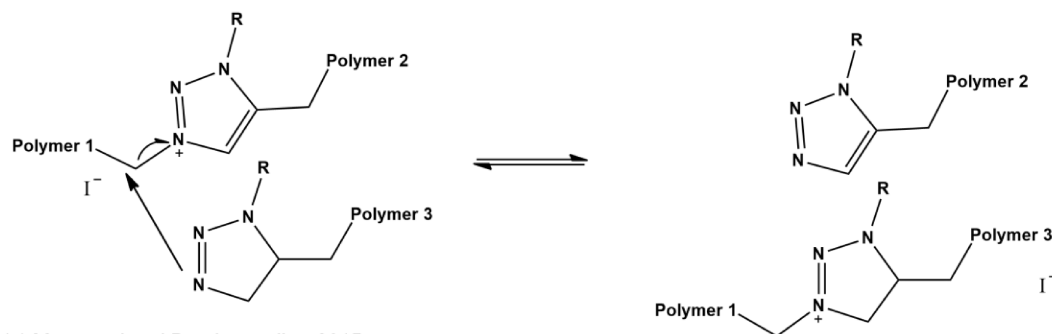
**Figure 2-25** Examples of (possible) concerted MNR-based networks [159,171,175,176]

In contrast to concerted MNR, for the non-concerted or stepwise reaction pathway two mechanism can be distinguished, which include a bond forming and a bond cleavage step (Figure 2-26). An addition/elimination or exchange-based pathway takes place in associative MNR. The previous association of two polymer chains is rearranged, resulting in a new covalent network bond and followed by an elimination step that fragments another network bond. [171] This involves the attack on defined functionalities along the backbone by an attached reactant, yielding a chemically identical product with a changed chain and crosslink configuration. [171,177]
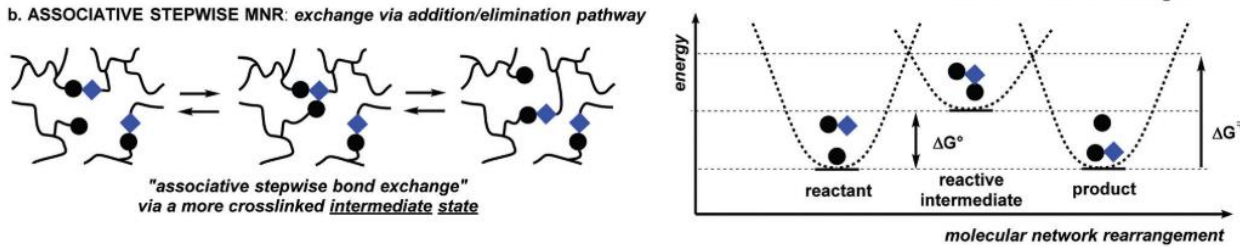
**Figure 2-26** Illustration of the associative molecular network rearrangements within dynamic covalent networks and their energy profiles [171]

As shown in Figure 2-26 there is a temporary increase in cross-linking density in the reactive (high-energy) <u>intermediate state</u> and the overall reaction rate depends on the proximity of the cross-links to be exchanged. [171] Examples for such reactions are the Diels-Alder cycloaddition [178], photo-induced radical addition–fragmentation reactions resulting in plasticity and a defined stress relaxation [171,179], (Lewis)- acid or base catalyst accelerated interchange of ester linkages between hydroxyl moieties inside an epoxy-based polyester resin [30], dynamic covalent chemistry of enaminone-moieties derived from amines and β-ketoesters [180], siloxanes as cross-linkers for hydroxy-functionalized polystyrene backbones undergoing rapid exchange reactions upon heating [181] and the dynamic exchange of thioesters with free thiols using a photobase to switch between dynamic and non-dynamic state [182]. These reactions are illustrated in Figure 2-27:
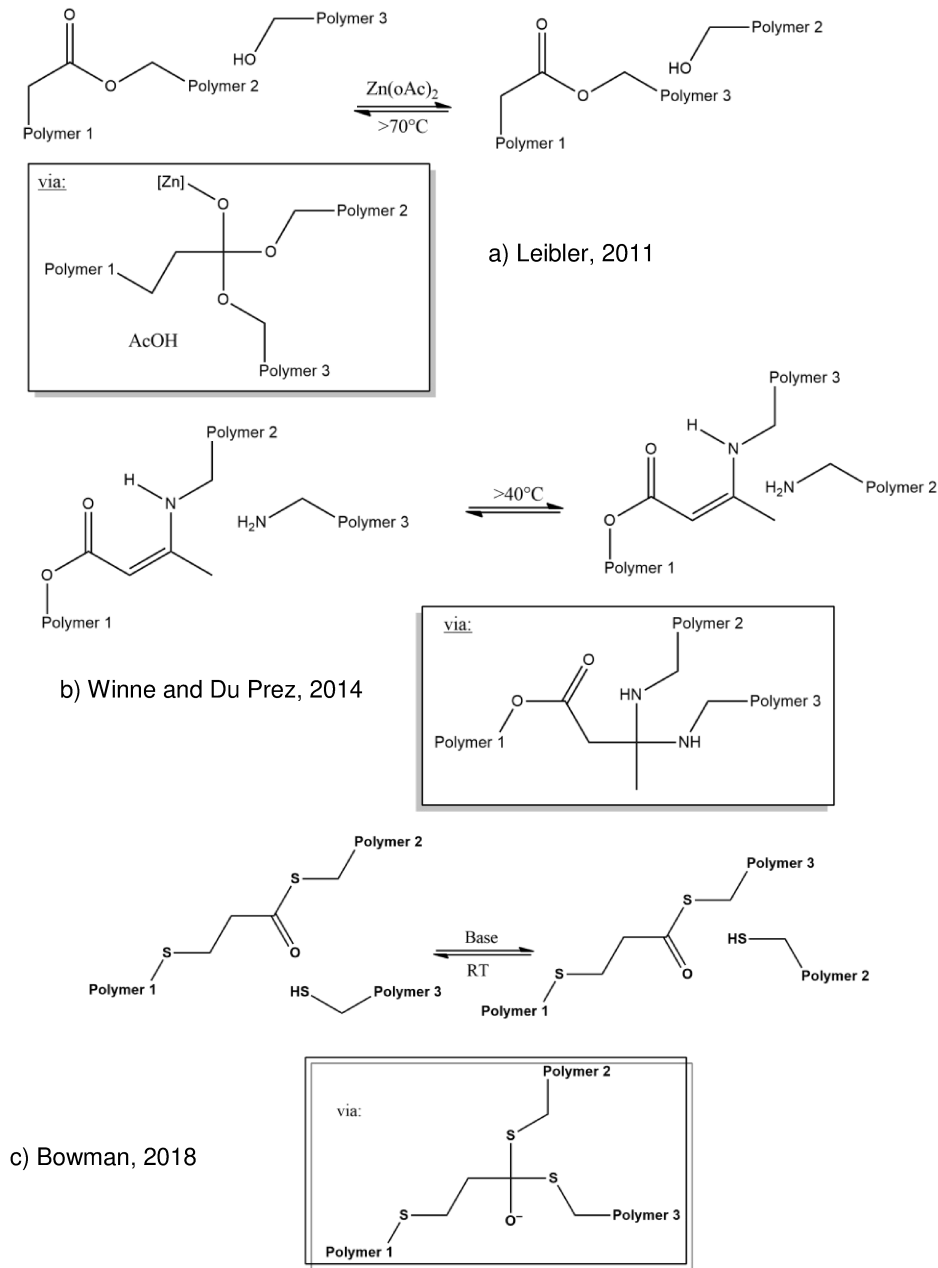
Figure 2-27 Examples of associative stepwise MNR-based dynamic covalent networks [30,159,171,182]

In contrast, the dissociative pathway follows and elimination/addition or reversible addition mechanism, in which a shift of the dynamic equilibrium between reactant groups and an adduct linkage structure occurs and a chain segment first fragments into two new chain ends.
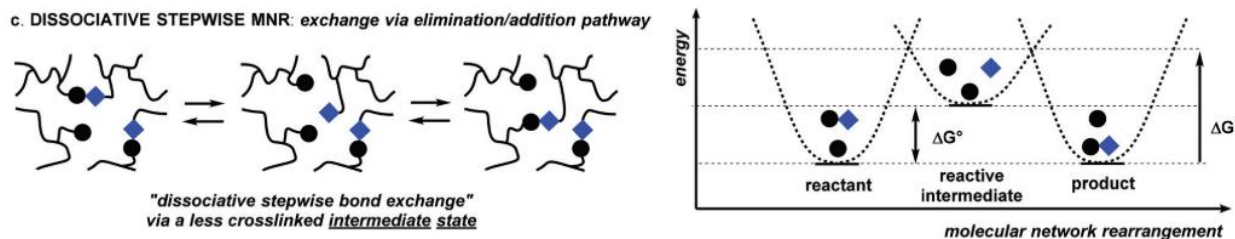
Figure 2-28 Illustration of the dissociative molecular network rearrangements within dynamic covalent networks and their energy profiles [171]

As illustrated in Figure 2-28, a temporarily uncross-linked <u>intermediate state</u> with the formation of reactive (higher energy) chain ends is formed. [171] However, no association of polymer chain segments occur as the polymer chain can fragment by itself. In a second step, a crosslinking can then be re-formed involving another polymer chain. [171] [183] Examples for the dissociative pathway are reversible Diels–Alder reaction between furanes and highly reactive acrylate-type dienophiles [184], hetero Diels-Alder reactions with dithioesters and cyclopentadienyl-functionalized (Cp) polymers [185] and the reaction between reversible bonds of isocyanates and hindered (secondary) amines as a dissociative stepwise MNR process for polymers with dynamic urea cross-links [186]. These reactions are illustrated in Figure 2-29.
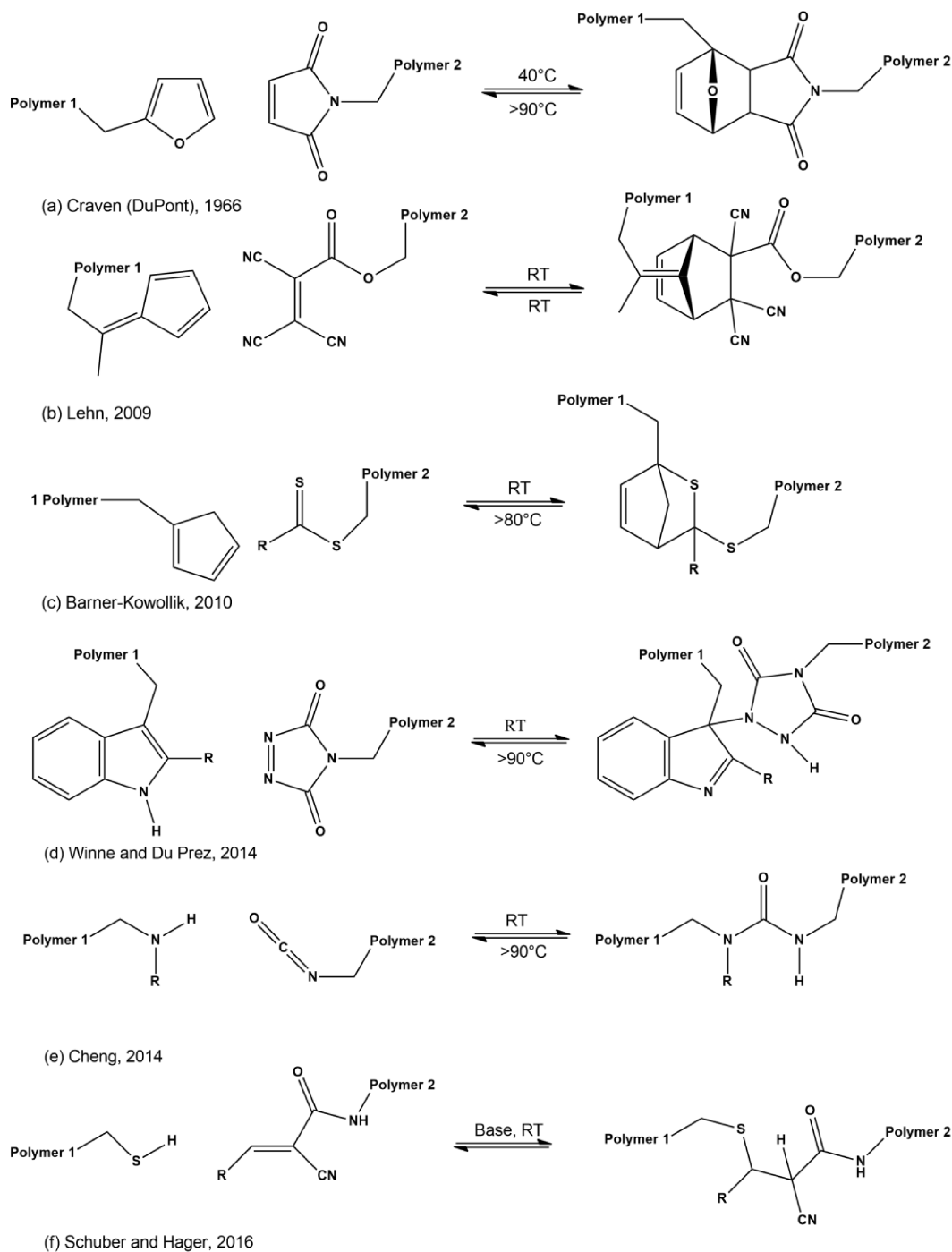
**Figure 2-29** Examples of dissociative stepwise MNR-based dynamic covalent networks [154,159,171,184–188]

According to Winne *et al.*, both mechanism do not meet the ideal requirements regarding their topology and connectivity fluctuations. They state, that the overall connectivity can be decreased upon heating in the dissociative pathway and can be increased upon

heating during the associative pathway as the equilibrium can shift to the endothermic side. [171]

### 2.6.2 Epoxy resins and the chemistry of epoxides

In the course of this thesis, mainly epoxy-based CANs were studied. Cured epoxy resins are thermosets and consist of closely cross-linked three-dimensional networks. There structures endow epoxy-based networks with insolubility in solvents, hindered macroscopic creep of the chains (flow), but also limited recyclability. [189] Material properties such as toughness, chemical resistance, mechanical properties ranging from extreme flexibility to high strength and hardness, high adhesive strength, good heat resistance, and high electrical resistance are dependent on the chemical structure of the curing agent and the curing conditions. [190] For more rigid materials, short-chain and stiffer monomers can be employed. Industrial applications of epoxy resins include coatings, adhesives, laminates, castings, encapsulations, mouldings and fibre reinforced plastics. [191] Compared to formaldehyde resins, no volatiles are released during curing, resulting in a minimum required pressure during the manufacture. In addition, the shrinkage is less pronounced in comparison to vinyl polymerizations used to cure unsaturated polyester resins. [190] Regarding the curing and the reactivity, due to the ring stress of the epoxy ring, these compounds are rather reactive. In general, epoxy resins can be produced either by step or chain-growth polymerization, or by a combination of both mechanism. [189]

Step-growth polymerisation (e.g. example c in Figure 2-28) proceeds by a series of elementary reaction steps between reactive sites. In each individual step, two reactive sites disappear and create a new covalent bond between the two functional groups. The reaction has to be reinitialized at each step; e.g. in the case of epoxides cured with amines. In order to control the polymer structure the main parameters consist of the sum of reactive monomer sites (functionality) and the used molar ratio between the co-reactive sites. [82,189] For instance, Figure 2-31 illustrates the reaction of an epoxy ring that is opened by a tertiary amine reacts.

In order to gain linear polymers, bifunctional reactants have to be used; monofunctional would disturb the polymer growth. The molar mass of the product gradually increases and the average molar mass becomes infinite at critical conversion (gelation). [189]

In contrast, chain growth polymerisation (represented in e.g. example e in Figure 2-29) includes steps such as initiation, propagation, transfer and chain termination. In prospect of epoxides, during the initiation stage, an ion (anion or cation) is generated either by a chemical reaction or by a suitable irradiation source and is called the active polymerisation centre. Once the active centres are formed, they form primary chains through the successive addition of monomers in the reproduction phase of the reaction. [192] Since the active centres are always present at the ends of the primary chains, the propagation reaction continues until it is determined by the chain transfer or termination step. [82,192] For both mechanisms, to control the structure of the polymer the functionality of the monomers, the molar ratio between the initiator and the monomers, the concentration of the species involved in the chain transfer steps and the temperature (thermal cycle), which influences the relative speed of the individual steps are the main parameters. [82,189]

The following Figure 2-30 a-e summarizes some common examples for reactions of epoxides:
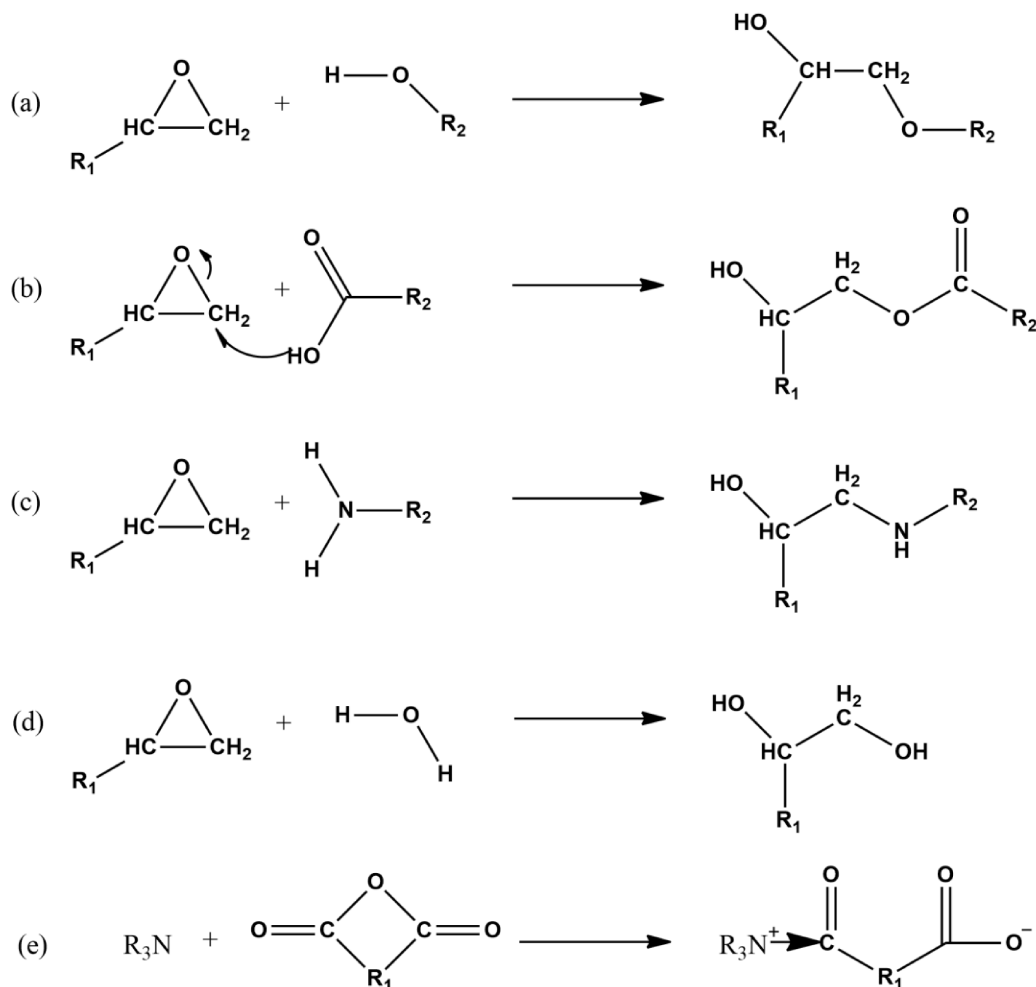
**Figure 2-30** Reactions of epoxies with (a) hydroxyl-groups, (b) carboxylic acids, (c) amines, (d) water and (e) a tertiary amine and the resulting ring-opening of an anhydride [190]

With regard to this thesis, cyclic anhydrides as hardeners were mostly used in the experiments. The reaction of the epoxy group with a cyclic anhydride initiated by a Lewis base follows a chain-growth copolymerisation. [189] The reaction of the Lewis base with the epoxy group includes the initiation, which results in the formation of a zwitterion containing a quaternary nitrogen atom (if the base used is a tertiary amine) and an alkoxide anion. [189] The so-formed alkoxide anion reacts rapidly with an anhydride group, leading to the formation of a species containing a carboxylic acid anion as the active centre. [189,193] The ammonium salt acts as the initiator of the chain wise copolymerization: [189]
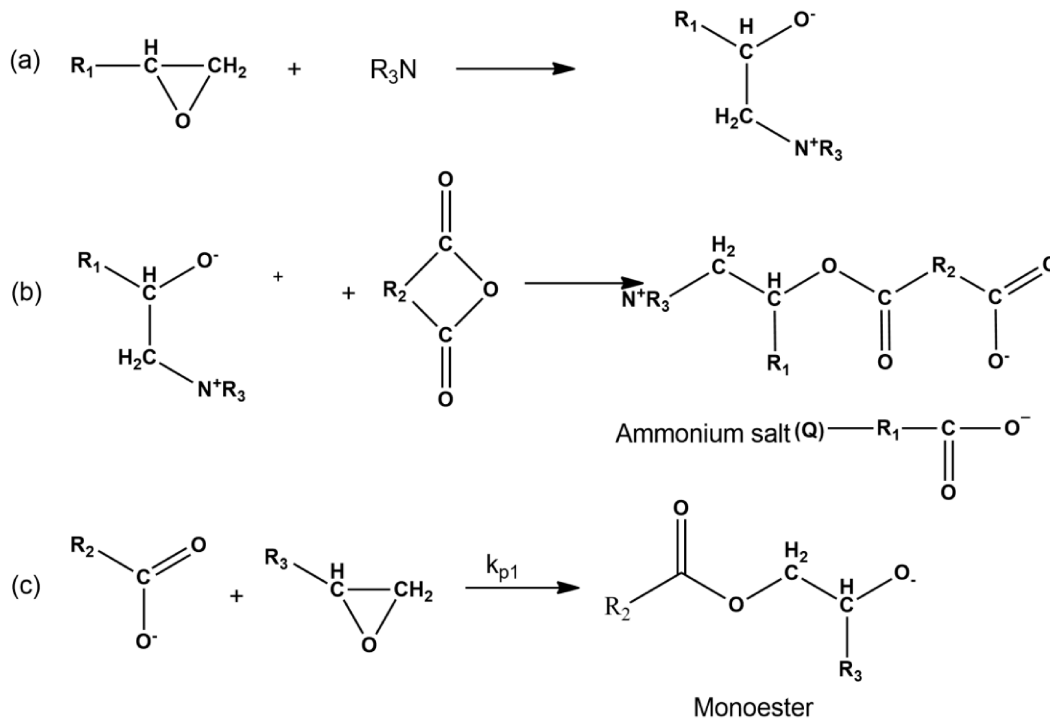
**Figure 2-31** Chain-growth reaction of an anhydride and an epoxide [189]

Propagation takes place by the reaction of the carboxylate anion with the epoxy group, renewing the alkoxide ion, which reacts rapidly with the anhydride group. [194] This leads to alternating chain copolymerisation of the epoxy and anhydride groups. [189,193,195]
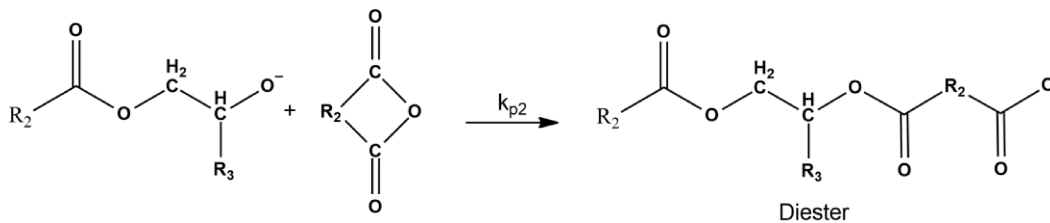


**Figure 2-32** Formation of a diester within the anhydride-epoxy reaction [189]

Regarding the calculation of the resin formulations, epoxy resins feature the specification of the epoxy equivalent weight per epoxy (WPE). WPE indicates the mass in g of the resin, which contains one mol of epoxy groups.

### 2.6.3 Vitrimers

As mentioned above, thermosetting polymeric materials such as epoxy resins are broadly used in paints and coatings, adhesives, electronic, industrial, aerospace industry tooling and offer unique mechanical and thermal properties, and good resistance to environmental degradation. [196]

Due their irreversible cross-linked nature, conventional epoxy materials are susceptible to failures after breakage or damage and hence cannot be easily reprocessed. The standard methods for disposing of epoxy materials are landfilling and incineration, which represent ecologically and economically inefficient processes. [197,198]

To meet the increasing demand of recyclable, reshapable and repairable polymers a constant search for new materials takes place. [199–202] In 2011, the group of Leibler introduced the new material class of vitrimers, which are covalent adaptable networks (CANs). [30] Vitrimers consist of covalently bound chains and are able to change their topology via exchange reactions. These reactions are associative in nature and thermally induced, resulting in the thermal malleability of the network. [172] At higher temperatures, the viscosity is mainly controlled by chemical exchange reactions while keeping the number of bonds and crosslinks constant. This results in a decrease of the viscosity, which follows the Arrhenius law and is typical of inorganic silica materials.[203] Which is contrary to thermosetting materials and dissociative CANs, which follow the Williams–Landel–Ferry model (WLF) for thermoplastic polymer melts. [172] This behavior can usually be found in silica, the archetype of glass, and few other inorganic compounds, which undergo a very gradual Arrhenius-like viscosity change near $T_g$ and gave vitrimer its name. [204,205]

In addition, a second transition temperature results from the cross-linking exchange reactions within the network. The network can rearrange its topology when the time scale of the bond exchange reactions becomes shorter than the time scale of material deformation. [172] Therefore, a transition from a viscoelastic solid to a viscoelastic liquid takes place at a temperature which is called the topology-freezing transition temperature $T_v$, which is conventionally chosen at the point where a viscosity of $10^{12}$ Pa s is reached according to Leibler *et al.* [30] The determination of this transition can be conducted by several methods, which can be found in section 2.4.6.

In order to enhance the understanding of vitrimer properties two distinct examples of the two transition temperature ranges are illustrated in Figure 2-32. [172]
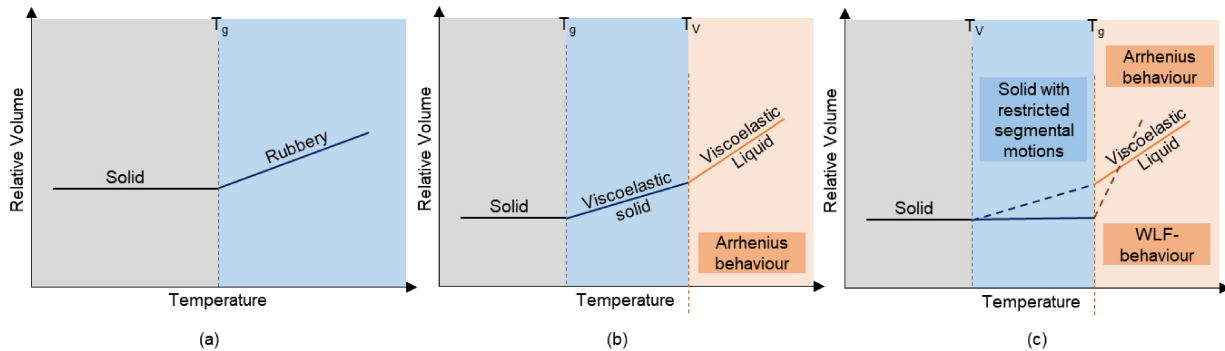


**Figure 2-33** Thermoplastic and dissociative covalent material phase transitions. Thermosetting vitrimer following (b) $T_g$ below $T_v$ and (c) $T_v$ below $T_g$ [166]

Two pathways can describe the occurring dynamics within the vitrimer matrix, whereas in both systems the $T_v$ is located in different regions. [166,172] In the first case, the $T_g$ of the vitrimer is well lower than the $T_v$. In a region between these two transition temperatures, the glassy solid initially changes to the rubber-like state or viscoelastic solid and behaves like a classical elastomer. Here, the exchange reaction is slow so that the network structure is basically fixed. Further heating accelerates the exchange reaction, which becomes macroscopically relevant at temperatures above $T_v$. Due to the exchange reactions the elastomer performs like a viscoelastic fluid whose flow is mainly controlled by the bond exchange kinetics. The change of the viscosity versus temperature follows the typical Arrhenius behavior. [166,172]

In the second case, the $T_g$ is higher than the $T_v$ of the network. Until reaching the $T_g$, the chain mobility is frozen due to the lack of segmental motions related with $T_g$ and no exchange reactions can occur. By increasing temperature and reaching the glass transition region, the segmental motion is steadily initiated while the exchange reactions are already activated. The kinetics of network rearrangement is diffusion controlled and network topology rearrangement is dominated by segmental movements, which lead to WLF viscosity behavior. [166,172]

With continuous heating, the system reaches a certain point where it shifts from a diffusion-controlled regime to an exchange reaction controlled regime and follows the Arrhenius law. Both regions can be influenced by the cross-link density, intrinsic rigidity of

monomers, the exchange reaction kinetics, and the density of exchangeable bonds and groups. [172]

Regarding the thermo-activated mechanism, some of them can take place in vitrimers, different exchange reactions can occur, whereas some are illustrated in Figure 2-27. In the course of this thesis, catalyzed transesterification will mostly be discussed.
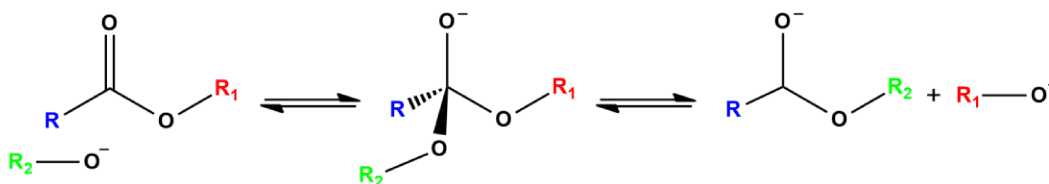


**Figure 2-34** Mechanism of a catalyzed transesterification reaction under basic conditions [206]

As illustrated in Figure 2-34 nucleophilic attack of an alkoxide on the carbonyl group occurs, whereas an ester leads to a tetrahedral intermediate, which in turn re-dissociates into a new alkoxide and a new ester. [206]

### 2.6.4  Catalysts for vitrimer systems

In order to increase the bond exchange rate and consequently enhance the stress-relaxation of a vitrimer system different catalyst systems have been introduced in the last couple of years. Moreover, to be able to tune the topology freezing temperature an appropriate catalyst is necessary. Since the systems presented in this thesis are mainly using transesterification reactions, the focus will be on transesterification catalysts.

In general, the number of published catalysts are rather small, due to several limitations. On the one hand, for classical transesterification reactions elevated temperatures are needed and therefore a good thermal stability of the catalyst compound is required. On the other hand, a homogenous mixing is necessary. Additionally, for future industry applications the cost factor is crucial. The two most common chemical groups, which are used as transesterification catalyst, are organometallic complexes and organic nitrogen-containing bases. [201]

Regarding organometallic complexes different types have been introduced. In a study by Liu *et al.* networks containing different dibutyltin salts as potential transesterification

catalysts were examined. By compression strength measurements and additional stress-relaxation studies, the authors could demonstrate the importance of the catalyst structure and its concentration. [207] This class of compounds also has been used in other studies and networks. [208,209] Another potential catalyst is stannous octoate (Sn(Oct)$_2$), which was added into a polylactide vitrimeric network and cross-linked with a diisocyanate, showing a distinct network rearrangement. [210] The by far most used organometallic complexes used as transesterification catalysts contain zinc as ionic center, such as Zn(acac)$_2$ or zinc acetate (Zn(OAc)). From those two compounds Zn(acac)$_2$ represents the most prominent one. The mechanism of the zinc catalysts proceeds in three main steps: (I) the reacting species are brought together directed by coordination bonds (II) polarization increases the electrophilicity of the carbonyl group in the esters and (III) shift of the alcohol/alkoxide equilibrium to the more nucleophilic alkoxide, whilst β-hydroxy-ester- formation and a resulting transesterification are occurring. [211,212] Due to its high efficiency, Zn(acac)$_2$ has been reported as catalyst in a multitude of publications. [203,213–217] Along with organic zinc salts, titanium-based compounds are able to catalyze transesterifications in epoxy/anhydride vitrimers. [208,218]

Regarding the organic nitrogen-containing bases, the most common example for a transesterification catalysts is the previously mentioned 1,5,7-Triazabicyclo[4.4.0]dec-5-ene (TBD). TBD is a strong guanidine base, which is capable to enhance the nucleophilicity of the alcoholic group via H-bond. [219,220] Due to its efficient transesterification properties, this compound can be found in numerous applications, such as thiol-ene vitrimers, acid/epoxy – vitrimers, nitrile-butadiene rubber vitrimers and photo-weldable carbon nanotube-reinforced materials. [162,221–223]

In addition, triphenylphosphine (TPP) is also applied as transesterification catalyst in epoxy-based vitrimers. [168,224] TPP catalyzes transesterification reactions across its lone pair at the phosphorous atom. [225]

So far, only a minor number of studies are comparing the individual catalysts and their performance on the same polymer network. Unterlass *et al.* studied the effect of three different catalysts and the influence of its concentration, namely triphenylphosphine (PPh$_3$) and triazabicyclodecene (TBD) and zinc acetate (Zn(acac)$_2$). [225]

a)                                          b)
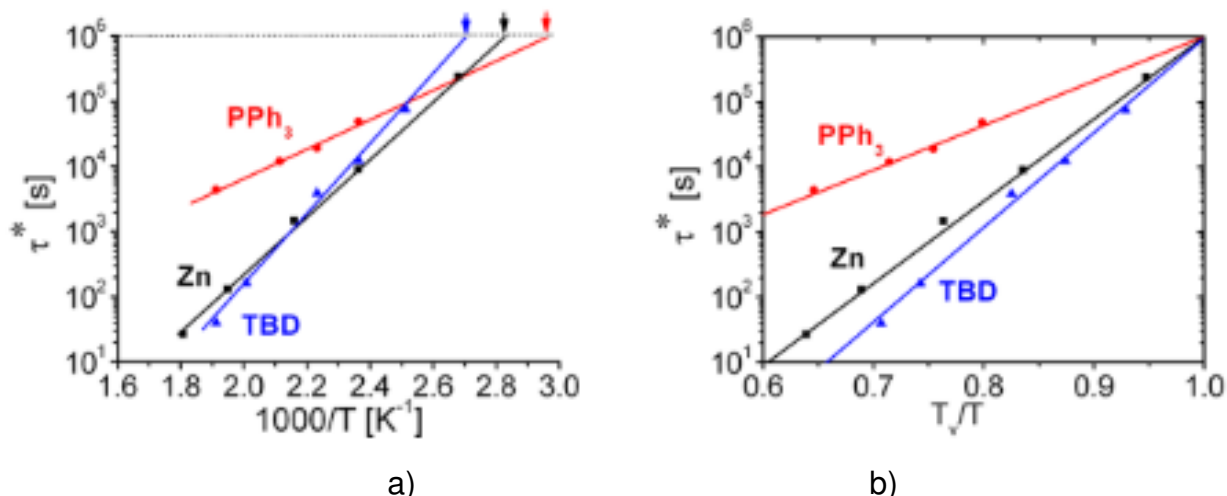
**Figure 2-35** a) Arrhenius plot of the relaxation times for Zn(oAc)$_2$, PPh$_3$, and TBD at 5 mol%, measured from shear stress relaxation experiments. (b) Angell fragility plot, normalized at T$_v$ for Zn(oAc)$_2$, PPh$_3$, and TBD at 5 mol% [225]

In a study by Capelot *et al.*, three catalysts, namely triphenylphosphine (PPh$_3$) and triazobicyclodecene (TBD), and zinc acetate [Zn(OAc)$_2$] were compared (Figure 2-35). The catalytic mechanisms are different and strongly depend on the activation energy. As shown in the figure, Zn(OAc)$_2$ and TBD represent the more efficient catalysts for transesterification and also had a shorter relaxation time at higher temperatures. The activation energies of the catalysts differ significantly, as shown in the "Angel Fragility Graph" in Figure 2-35b. [225]

### 2.6.5 "Hard" vitrimer networks (epoxy-anhydride networks)

One of the main limitations of vitrimer systems to date is to implement them in technically relevant applications. The obtained T$_g$s are mostly below RT and result in a softness of the material. For future applications of these materials, vitrimers should have T$_g$s comparable to classical thermosets and a controlled macroscopic flow well above the networks' T$_g$. [172] Different approaches have been carried out to overcome this limitation. [212] In industrial applications, epoxy/anhydride networks are typically obtained by curing resin with a monomer:hardener ratio ranging from 1:0.8 to 1:1. [226] In order to provide a sufficient number of free hydroxyl groups for transesterification, the ratio of epoxy to anhydride is often ~1:0.5 in vitrimers. [227] However, the reaction of anhydrides with epoxy monomers at this stoichiometric ratio tends to yield insufficiently cross-linked polymer networks with lower mechanical strength and stiffness compared to conventional

thermosets. [228] In general, a compromise has to be made between high network density/high $T_g$ and high chain mobility and viable $T_v$. In order to yield hard vitrimer networks, different strategies can be applied and a set of different reactions is needed to produce the OH- groups, which are necessary to promote transesterification. For instance, homopolymerization of excess epoxy groups or addition of alcohol or water to the original formulation could be an option for changing the networks structure to higher number of OH- groups and high network density. [229] As mentioned before, using an uncured system could provide (unreacted) OH- groups but obviously would lead to partly unpredictable vitrimer properties. [172] The most common approach to ensure a high crosslink density and hard network, is realized by the choice of the individual reactants and the individual monomer rigidity. A common example are anhydrides, which were successfully implemented in vitrimer systems. Succinic anhydride [216,228,230], glutaric anhydride [30], methylhexahydrophthalic anhydride (MHHPA) [227] and phthalic anhydride [231] show higher $T_g$s in comparison to normally used carboxylic acids. [232–234] Moreover, the addition of rigid co-monomers also showed a beneficial influence to the networks $T_g$. [221,235] Furthermore, previous studies have illustrated, that the $T_g$ can be influenced both by crosslink density and by the backbone rigidity of the epoxy monomer. [236] Another approach is the exploitation of the catalyst behavior. A synergy of fast curing rates, curing temperature, catalyst- concentration and activity could change the networks thermomechanical properties to higher network density and constant network dynamic. [236–238]

## 2.6.6 Determination of dynamic properties in vitrimer networks

In order to determine the specific topology freezing temperature of a vitrimer mainly three methods have been established so far:

**Stress-relaxation and rheological measurements**

Shear stress relaxation tests are used to characterize the viscoelastic properties of a polymer. This method is mostly used for non-crosslinked melts and solutions, but can be adapted to study chemically cross-linked polymers as well. [239] For the measurement, torsion to a certain percentage is applied to a sample and this deformation is kept constant for a predefined time. [240,241] The method can be applied to several rheometer geometries. Examples are plate-plate and solid rectangular fixtures (SRF) for rectangular specimens. For the evaluation the Maxwell model is used, which consists of a spring and a dashpot connected in series. This is illustrated in Figure 2-36.
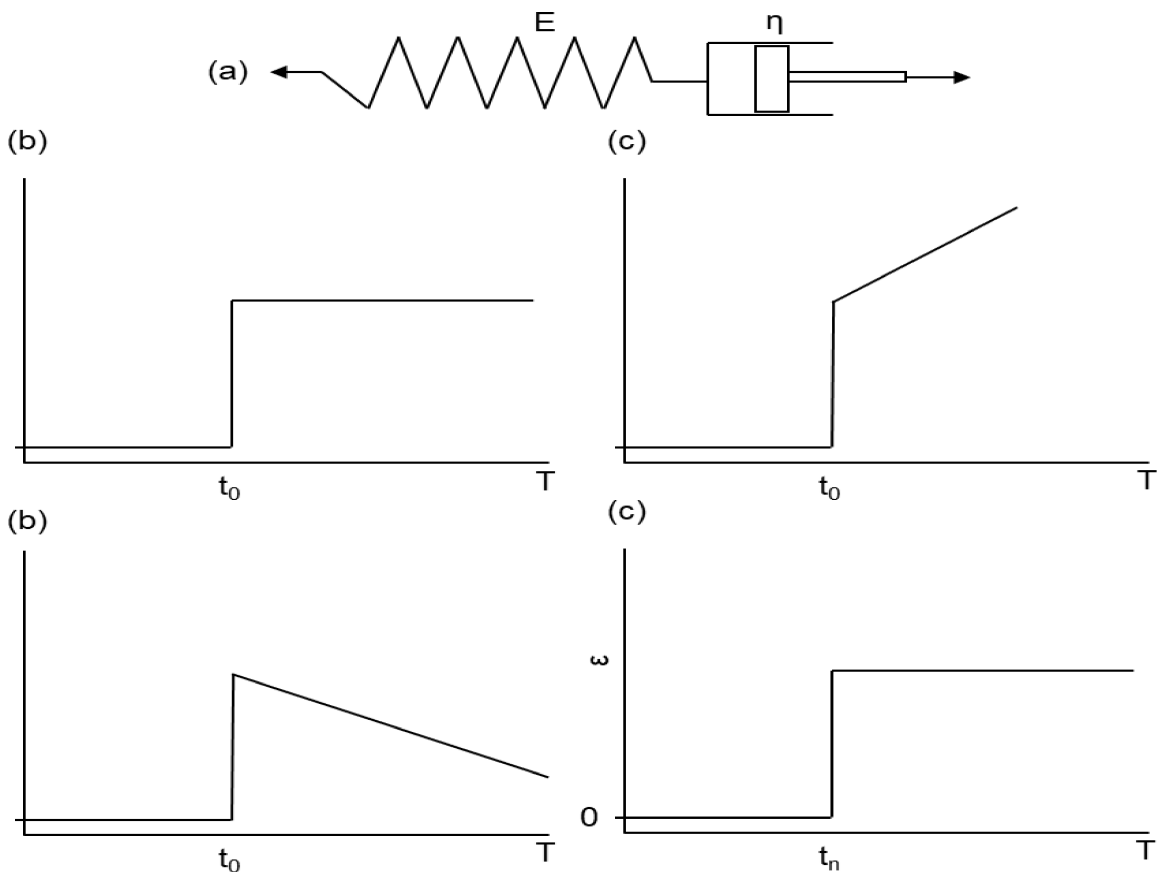


**Figure 2-36** (a) Illustration of the Maxwell model, (b) representation of a sudden deformation and the resulting stress curve, (c) representation of a sudden stress increase and the resulting deformation. [240]

For the calculation of the $T_v$ the following procedure is used:

Equation 2-8 shows the differential equation of the Maxwell model. $\eta$ and G are the material parameters of the elastic spring and damper. In equation 2-9, the boundary condition is given and after the deformation is constant, the stress asymptotically approaches zero and has its maximum at the beginning. At the relaxation time $\lambda$ or $\tau$, the exponent of the e-function becomes -1, which corresponds to a numerical value of 0.3678. This time can be determined by comparing the stress at the beginning and at any time of the measurement. With the help of Hooke's law in equation 2-13, the time-dependent relaxation modulus can be determined, which corresponds to G, the material constant of the spring, for the time zero. Since the relaxation time is defined as the viscosity of the damper divided by the shear modulus of the spring, the last material constant can be calculated. [242]

Differential equation of the Maxwell model:

$$\tau = \eta \frac{\delta \gamma}{\delta t} - \frac{\eta E \delta \tau}{\delta t} \qquad \text{(Equation 2-8)}$$

Boundary condition of relaxation:

$$\text{For relaxation: } \frac{\delta \gamma}{\delta t} = 0 \qquad \text{(Equation 2-9)}$$

Stress curve during a relaxation test:

$$\tau(t) = \tau_0 e - \frac{t}{\lambda} \qquad \text{(Equation 2-10)}$$

$$\lambda = \frac{\eta}{G} \qquad \text{(Equation 2-11)}$$

Determination of the relaxation time:

$$t{=}\lambda \text{ applies for } \tau(\lambda) = \tau_0 e^{-1} = \tau_0 \frac{1}{e} = \tau_0 * 0{,}3678 \qquad \text{(Equation 2-12)}$$

53

Determination of the time-dependent relaxation modulus:

$$G(t) = \frac{\tau(t)}{\gamma}$$

(Equation 2-13)

The master curve is generated by dividing the time of each data point by the shift factor at a certain temperature. The shift factor is calculated as described in the following Equation 2-14. For better understanding, Figure 2-37 (a) illustrates several relaxation curves obtained at different temperatures. The shear moduli were normalized to the initial shear modulus. Figure 2-37 (b) shows a master curve at a reference temperature of 160 °C. The shear moduli have been normalized to the initial shear modulus.

Shift factor according to the Arrhenius law:

$$aT = e^{\left(\frac{E_A}{R}\left(\frac{1}{T} - \frac{1}{T_{Ref}}f\right)\right)}$$

(Equation 2-14)

By superimposing relaxation modulus-time curves of the same material, but with different deformations, it can be seen whether the linear-viscoelastic range has been left.



(a)                                                                      (b)
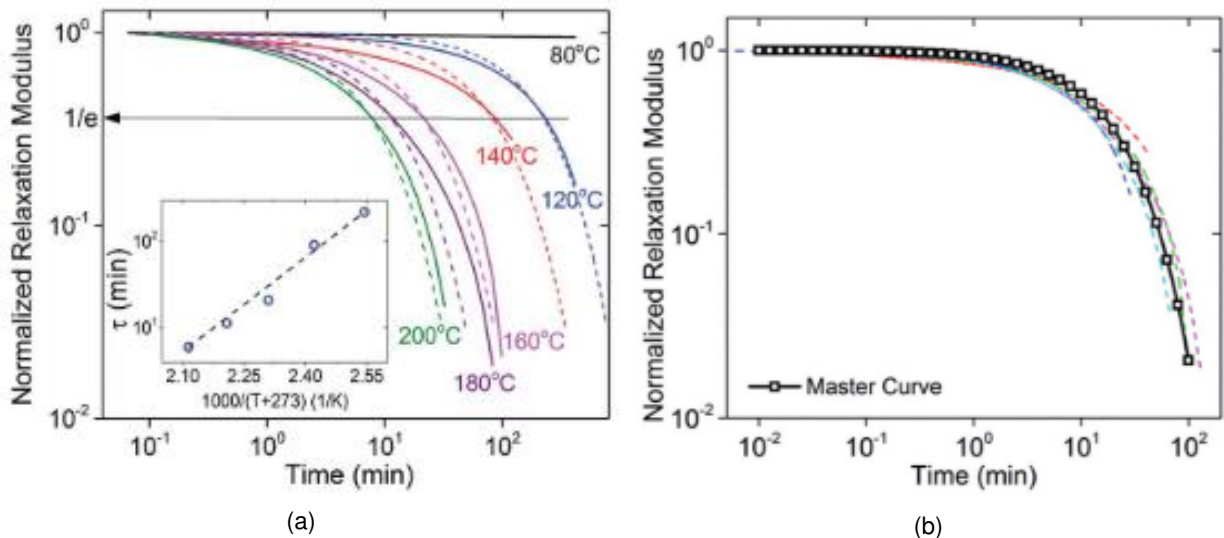
**Figure 2-37** (a) Relaxation curves at different temperatures, where the normalized shear modulus G/G0 was plotted against time t. (b) Master curve where all curves were referenced to 160 °C, where again the normalized shear modulus $G/G_0$ was plotted against time t divided by the displacement factor aT [233]

In order to determine the activation energy $E_A$, the relaxation times at different temperatures are plotted in an Arrhenius diagram. The natural logarithm of the relaxation times is calculated and plotted over 1/T or 1000/T, where T is the absolute temperature. The activation energy can be calculated by the slope k of the line. The mathematical background is illustrated in equation 2-15 - 2-17. The general Arrhenius equation gives a rate constant, in this case the relaxation time λ. Generally, the rate constant increases with increasing temperature. However, since vitrimers have shorter relaxation times with increasing temperature, negative activation energy is obtained. [242]

General Arrhenius-equation:

$$\lambda = A \cdot e^{\left(\frac{E_A}{RT}\right)}$$ 
(Equation 2-15)

Linear equation of the Arrhenius-diagra:

$$\ln(\lambda) = -\frac{E_A}{R} \cdot \frac{1}{T} + \ln(A)$$ 
(Equation 2-16)

Calculation of the activation energy from the slope of the straight line:

$$k = -\frac{E_A}{R} => E_A = |-k \cdot R|$$ 
(Equation 2-17)

The structural freezing transition temperature ($T_v$) can be calculated using the relationship given in formula 3.b to calculate the viscosity at each measurement point. Then the viscosity must be extrapolated up to $10^{12}$ Pa·s. The resulting temperature at this point represents the structural freezing transition temperature. [30,243]

**Dilatometry**

For this method, a constant tensile stress is applied to the sample. The temperature is constantly increased at a constant heating rate and the strain of the sample is recorded. With an increasing temperature, the sample expands, which becomes stronger when transesterification reactions become macroscopically relevant at the $T_v$. At this point, the material can flow due to the stress and the transesterification reactions and the elongation increases sharply. Therefore, the $T_v$ is set at the point where the material shows non-linear behavior. In order to illustrate this characteristic behavior Figure 2-38 shows dilatometry experiments for DGEBA-Pripol 1040 vitrimer comprising 5 mol% at different strains:
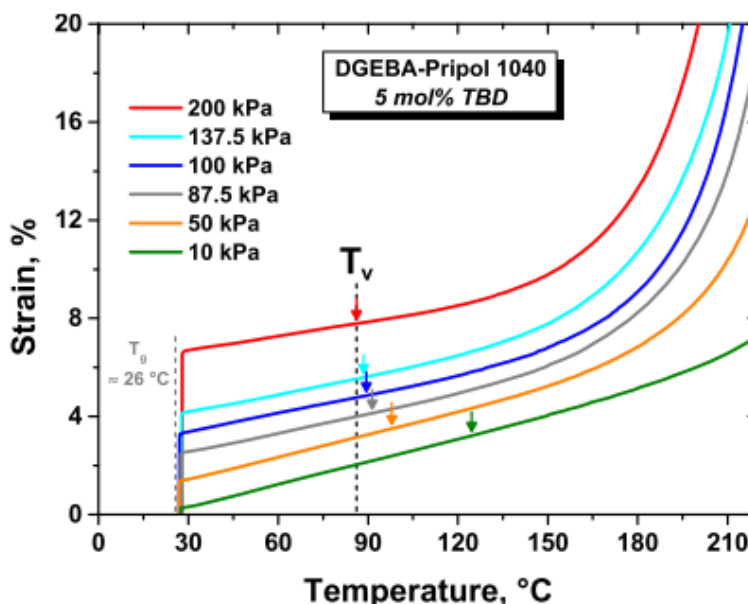


**Figure 2-38** Elongational creep curves of the DGEBA-Pripol 1040 vitrimer comprising 5 mol% (related to the COOH groups) of TBD as transesterification catalyst for various stresses at a heating rate of 3 K/min. The arrows indicate the respective onset of plastic flow [244]

Due to a softening of the system and an increase in elongation, the conventional $T_g$ can be observed as well. Above this temperature, a second effect can be observed. The increased mobility can now reduce tensions and orientations to a certain degree and the network can change into an entropically more favorable state and causes a contraction of the sample. [170,236,237]

The determination of the exact $T_v$ depends on several parameters such as the heating rate or the applied stress. A high stress causes an earlier non-linear strain and a higher

heating rate causes a later occurrence of the $T_v$. [235] A study by Kaiser *et al.* showed that with increasing stress, the $T_v$ of the system decreases to a minimum, which corresponds appropriately to the onset of bond exchange reactions of the network. This value is in fact the onset of rearrangement, which is exclusively dependent on the system's chemistry. Beyond this value, in the case of soft epoxy/acid networks, the effects of entropy-driven flexible coil insertion are superimposed on the creep, resulting in a return of the $T_v$ to a higher temperature. The $T_v$ shift is also less pronounced for stiffer epoxy/anhydride networks. [198,235]

**AIE luminogens**

In 2019, a new method to detect the topology freezing transition temperature was introduced by Yang *et al.* using aggregation-induced-emission luminogens in static condition without any external force, which was different from the above-mentioned dynamic characterizations. [166,245] The methods relies on doping of AIE fluorescent molecules in the vitrimer network, where the fluorescence of AIE luminogens changes below and above $T_v$. [166] Luminogens represent fluorescent organic compounds, which are emissive when restriction of intramolecular motions causes the dissipation of absorbed energy via radiation. [9] For vitrimers the luminogens, at the $T_v$, the luminogens permit significant molecular movement within the network. [9]
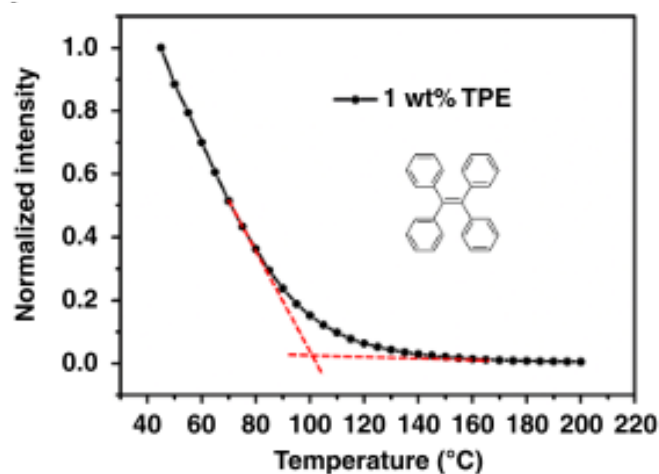


**Figure 2-39** Fluorescent intensity of AIE luminogens versus temperature in vitrimer networks [245]

# 3 Experimental

## 3.1 Materials

The following table lists the materials and substances used in this work. The chemicals were used as received:

**Table 3-1** Overview of the substances used

| Substance | Manufacturer/Brand | Purity |
|---|---|---|
| 1,5,7-Triazabicyclo(4.4.0)dec-5-en | Sigma Aldrich | n.a. |
| (2-Nitro-1,4-phenylene)dimethanol | TCI Europe | ≥95 % |
| 4,4′-methylenbis(N,N-diglycidylaniline) | Sigma Aldrich | n.a. |
| meta-Chloroperoxybenzoic acid | Sigma Aldrich | ≤77 % |
| Acetonitrile | Roth | ≥99.5 % |
| Ammonia solution | Roth | 30 %- |
| Bisphenol A Diglycidylether | Sigma Aldrich | n.a. |
| Chloroform | Roth | ≥99 % |
| Cyclohexane | Roth | ≥99.5 % |
| Dichloromethane | Roth | ≥99 % |
| Diethylether | Roth | ≥99.5 % |
| Dodecenylsuccinic anhydride | Sigma Aldrich | n.a. |
| Ethanol | Roth | ≥99.5 % |
| Ethylacetate | Roth | ≥99.5 % |
| Glutaric anhydride | Sigma Aldrich | 95% |
| Glycidyl-2-methylphenylether | Sigma Aldrich | 90 % |
| Guanine | Sigma Aldrich | 98% |
| Hexahydrophthalic anhydride | Sigma Aldrich | ≥95 % |
| Hexahydro-4-methylphthalic anhydride, mixture of cis and trans | Sigma Aldrich | 96 % |
| Potassium hydroxide | Roth | ≥85 % |
| N,N-diglycidyl-4-glycidyloxyaniline | Sigma Aldrich | n.a. |

| | | |
|---|---|---|
| N,N-Dimethylbenzylamine | Sigma Aldrich | ≥99 % |
| Sodium bicarbonate | Roth | ≥99 % |
| Succinic anhydride terminated polydimethylsiloxane | abcr | n.a. |
| Pyridine | Sigma Aldrich | 99.8 % |
| Tetrahydrofuran | Roth | ≥99.5 % |
| Zinc(II)-acetylacetonate hydrate | Sigma Aldrich | n.a. |

## 3.2  Equipment and characterization methods

Devices and equipment used for the experiments are listed below and explained in a brief description:

| | | |
|---|---|---|
| **Confocal microscopy** | MPR 1080, *Fries Research & Technology GmbH* | The confocal microscope by FRT provides information regarding the topography, structure, height, roughness, layer thickness etc. of the samples. The microscope has a resolution of 10 nm in height and laterally of < 2.5 nm. By adjusting the measuring rate (in Hz) and the measuring speed of the sensor, the quality of the recording can be adjusted. The evaluations and 3-D representation were carried out with the software Gwyddion 2.31. software. |
| **Contact angle measurement** | Drop Shaper Analyzer DSA *100, Krüss* | The surface contact angles were measured with the contact angle measuring device Krüss DSA 100 at 20-23°C at a relative humidity of 50-80% .The test liquids used were 2 µL of deionised water and diiodomethane deposited on the sample surfaces. The contact angle was determined from the arithmetic average of 5-10 droplets and by applying the Young & Laplace equation and using the software Drop Shape Analysis |
| **Dynamic Mechanical Analysis (DMA)** | DMA 8000, *Perkin Elmer* | The DMA 8000 is used to measure frequency- and temperature-dependent mechanical parameters of polymers. The determination limits for the storage modulus are $10^{-3}$ to $10^{10}$ MPa in a frequency range between 0.001 and 300 Hz. The maximum forces that can be applied are between 0.002 and 10 N with a resolution of |

|  |  | 0.002 N. The (theoretical) possible temperature range is between -190 and 400 °C. The measurements were used to determine the $T_g$ and storage modulus of the samples. |
| --- | --- | --- |
| **Differential scanning calorimetry (DSC)** | DSC 821e, *Mettler-Toledo* | The DSC 821e by Mettler-Toledo is used for the determination of the $T_g$. The measurements can be carried out in a temperature range from -50 to 700 °C with a heating rate of 0.02 - 300 K/min. STARe software was used. |
| **Fourier-transform infrared spectroscopy (FT-IR) measurement** | Vertex 70, *Bruker Optics,* USA | The VERTEX 70 is a fully digital FT-IR spectrometer designed for the (quantitative) characterization of the chemical structure of solid or liquid materials. The measurements can be performed in transmission and attenuated total reflection (ATR Platinum Diamond) mode. The detector used is a DLaTGS. The standard spectral resolution is $< 0.4$ cm$^{-1}$. The software used for the measurements is OPUS Version 7.0. The kinetics of the curing and photo-cleavage were determined via FT-IR. |
| **Nuclear magnetic resonance spectroscopy (NMR)** | Varian 400 MR, *Varia*n, USA | The Varian 400 MR spectrometer is operating at 399.66 MHZ. $^1$H- spectra were recorded for the structure analysis of the synthesis products, using ACD/NMR Processor (academic version). |
| **Optical light microscopy** | BX51, *Olympus,* Japan | The Olympus optical microscope, model BX51, was used for utilizing images of the resist materials. The images were taken by using the mounted camera ColorView IIIu and the analySIS software from Soft Imaging Solutions. |

| | | |
|---|---|---|
| **Radiometer** | Powerpuck II, S/N 18052 *EIT Instrument Markets*, USA | An integrated radiometer was used to determine the applied UV-exposure doses of the used light sources. |
| **Rheology** | MCR 501, *Anton Paar, Austria* | The rheometer was used to determine the stress-relaxation of the vitrimer networks. The service temperature of the device used for the experiments was between 70 and 250°C. For some of the experiments, the heating chamber was continuously purged with nitrogen at a volume flow of 1 m³/h. A constant elongational force of 0.1 N was applied to ensure a stable position of the sample and usually a deflection of 1% was applied. |
| **Spin coater** | Photo Resist *Spinner 4000 Electronic MicroSystems, USA* | The production of thin, uniform layers was carried out with rotation speeds of up to 4000 rpm of the dissolved or dispersed substances, which were applied to substrates ($CaF_2$- disk or Si- Wafer) fixed to the spin coater. The desired layer thickness results from the duration and speed of the rotation and is influenced by the viscosity of the liquid and solvent. |
| **UV lamp I** | Light Hammer 6, *Fusion UV Systems,* Heraeus Germany | For cleavage of the *o*-NBE functional polymers, a Light Hammer was used. The exposure took place via a microwave-assisted, electrodeless lamp with a maximum power of 200 W $cm^{-1}$. The irradiated substrates were transported via a LC6E laboratory conveyor belt with belt speeds of 0.1 - 75 m $min^{-1}$. |

| | | |
|---|---|---|
| **UV lamp II** | Omnicure S1000, *Lumen Dynamics*, Canada | The 100 W UV spotcure lamp achieves a spectral power density of up to 18 W/cm$^2$. The intensity of the exposure can be adjusted in 1% steps and was used for the cleavage kinetics of the *o*-NBE functional polymers. |
| **Nano-indentation** | Ultra Nanoindentation Tester, *Anton Paar*, Austria | For the experiments, a pyramidal-shaped Berkovich tip with an equivalent cone (semi-angle q = 70.3°) was used. The contact force was 50 µN, and the maximum indentation force was set to 1000 µN. Both loading and unloading rate amounted to 6000 µN/min. A 30 s hold segment was applied at the maximum load to obtain reliable stress-strain curves. Indentation hardness (H$_{IT}$) data were derived from the unloading-part of the load-displacement curve according to the "Oliver & Pharr Method". [246] |
| **Thermogravimetric measurements (TGA)** | TGA/DSC1 with STARe System and GC 200 gas controller, *Mettler Toledo*, Germany | In order to determine the thermal stability of the resins and the weight loss, TGA was carried out. For that, the samples were heated up to 900°C under nitrogen or oxygen atmosphere (10-20 mL/min) at a heating rate of 10 °C/min. For the determination STARe software was used. |
| **Vacuum press** | Collin, Ebersberg, Germany | The vacuum press was used for the remolding of vitrimers applying a pressure of 5 bar at 250°C in metal molds. |
| **White light interferometer (WLI)** | Leica DCM8 3D optical surface measurement system, *Leica Microsystems,* Germany | WLI was used for the imaging of the surface topography of the resist materials. The systems allows for a theoretical optical resolution of 0.35 µm and a vertical resolution better than 1 nm. |

## 3.3 Preparation of dual-responsive polydimethylsiloxane networks

The data and results given in this section have been published in the journal "Polymer Science Part A: Polymer Chemistry" under the title "*Dual-Responsive Polydimethylsiloxane Networks*", Volume 56, Issue 20, October 2018. Most of the following text, tables and figures have been taken from the respective publication. [247]

Markus Ast performed part of his experimental studies for his master thesis on the topic of "*Dual-Responsive Polydimethylsiloxane Networks*". Some of the results are presented in the following section.

### 3.3.1 Sample preparation and thermal curing of dual-responsive PDMS networks

In total three different formulation were prepared. The preparation of the PDMS-**1** network involved the dissolution of the photosensitive (2-nitro-1,4-phenylene) bis(methylene) bis(2-(oxiran-2-yl)acetate) (epoxy-**NBE**) in an excess of succinic anhydride terminated polydimethylsiloxane (2 epoxide equiv.). Epoxy-**NBE** as photosensitive monomer was synthesized as reported in the study by Radl *et al.* [93] As curing catalyst, N,N-dimethylbenzylamine (DMBA) (0.1% by weight of the total reaction mixture) was added to the formulation. The reaction mixture was then stirred at room temperature for 30 minutes. Thermal curing and subsequent annealing was carried out at 100°C for 168 hours.

In addition, the networks of PDMS-**2** and PDMS-**3** were prepared by dissolving different amounts of epoxy-**NBE** in the mono-functional glycidyl 2-methylphenyl ether (epoxy-**GME**). The epoxy formulations and DMBA (0.1% by weight of the total reaction mixture) were subsequently added to the succinic anhydride terminated polydimethylsiloxane (equimolar concentration of epoxy and anhydride moieties) and the reaction mixture was stirred at room temperature for 30 minutes. The samples were thermally cured at 100 °C for 12 hours to give solid films. The exact resin composition is given in the following table:

**Table 3-2** Composition of dual-responsive PDMS formulations [247]

| Sample | Bifunctional Crosslinker (Epoxy-**NBE**) (mol %)[a] | Mono-functional Chain Extender (Epoxy-**GME**) (mol %)[a] | Molar Ratio Epoxy Monomers[b] | Molar Ratio Epoxy Crosslinker[c] | Accelerator (wt %)[d] |
|---|---|---|---|---|---|
| PDMS-**1** | 33.3 | 0 | 2:1 | 1:0.5 | 0.1 |
| PDMS-**2** | 37.5 | 12.5 | 1:1 | 1:0.75 | 0.1 |
| PDMS-**3** | 25 | 25 | 1:1 | 1:0.5 | 0.1 |

[a] Molar concentration of the epoxy monomers in the formulation. [b] Molar ratio of anhydride-terminated PDMS to epoxy monomers in the formulation. [c] Molar ratio of anhydride-terminated PDMS to epoxy-based crosslinker (epoxy-NBE) in the formulation. [d] Weight percentage related to the total weight of the formulation.

### 3.3.2 Characterization of the curing of dual-responsive PDMS networks

Curing kinetics and the photocleavage of the stimuli-responsive PDMS formulation were monitored by FT-IR spectroscopy using a Vertex 70 spectrometer (Bruker, USA). Sixteen scans were accumulated at a resolution of 4 cm$^{-1}$ and the absorption peak areas were calculated using OPUS software. All spectra were recorded in transmission mode. For sample preparation, 2 µL of each formulation was drop-cast between a $CaF_2$ disk and a Si wafer. The curing (and annealing) reaction was monitored at 100 °C for 18-168 hours by recording FT-IR spectra after a predefined curing time.

Static water contact angles of the cured PDMS networks were determined using the DSA 100 Drop Shape Analysis System.

### 3.3.3 Characterization of the degradation of dual-responsive PDMS networks

In order to prepare test specimens, the PDMS formulations were poured into aluminum molds (2×5×1 mm). The thermal curing step was performed as stated in the previous section. The cured PDMS films were separated from the mold and 40-60 mg of each sample was immersed in 20 mL of aqueous NaOH solutions of varying basic concentration (1, 0.5, 0.05 and 0.025 M) at 21 °C. After the predefined reaction time, the decrease in sample weight was determined gravimetrically. The samples were then dried at 60°C to a constant weight, and the standardized gel fraction was calculated as follows:

Normalized gel fraction = $(w_0 - w_{t-h})/w_{t-h} \times 100$.

In this equation, $w_0$ and $w_{t-h}$ relates to the gel fractions of the cured PDMS network before and after the selected hydrolysis time in an alkaline medium.

The kinetics of the photocleavage reaction were studied by irritating the cured drop-cast films (between a $CaF_2$ disk and a Si wafer) with a medium pressure Hg lamp (Omnicure S1000 Lumen Dynamics, Canada) under a nitrogen atmosphere. The light density in the sample plane was measured with an integrating radiometer (Powerpuck II, EIT Instrument Markets) and was 51.55 mW $cm^{-2}$ between 250 and 470 nm. The depletion of the characteristic nitro groups was followed by FT-IR spectroscopy using a Vertex 70 spectrometer (Bruker). Sixteen scans with a resolution of 4 $cm^{-1}$ were accumulated.

Sol-gel analysis was used to determine the photoinduced changes in the solubility. Thin films were prepared by spin- casting of the PDMS formulations on Si wafer. The thermal curing of the samples was performed as described in the previous section. Quantitative FT-IR spectroscopy was carried out to characterize the insoluble gel fraction of the films during selected irradiation times. UV exposure was performed using an Omnicure S1000 lamp (51.55 mW $cm^{-2}$; $\lambda$ = 250-470 nm, $N_2$).

In order to produce micro-sized relief patterns on the PDMS-**1** films, photolithographic patterning was performed using a quartz chromium mask in contact mode. UV exposure was performed with an Omnicure S1000 lamp (51.55 mW $cm^{-2}$; $\lambda$ = 250-470 nm). Positive-tone structures were prepared with an irradiation dose of 0.26 J/$cm^{-2}$, and patterned films were developed by immersion in chloroform for 5 seconds. For the negative-tone patterns, the sample was exposed to a dose of 3.1 J $cm^{-2}$, then immersed in a NaOH solution (1 M) for 5 seconds to develop, and subsequently immersed in deionised water for 5 seconds to remove alkaline residues on the surface. The surface of the sample was purged in both cases with nitrogen to dry the resulting polymer pattern.

The inscribed patterns were characterized with a confocal microcopy (MicroProf®, Fries Research and Technology, Germany) at a measuring frequency of 3200 Hz. The height and lateral resolutions were 10 nm and 2.5 µm, respectively.

Differential scanning calorimetry (DSC) was performed using a Mettler-Toledo DSC 821e (USA) to characterize the thermal properties of the dual-responsive PDMS network before and after photocleavage. The cured and photochemically degraded PDMS samples were

heated to -20 to 50°C under nitrogen atmosphere (nitrogen flow rate of 20 mL min$^{-1}$) at a heating rate of -20 K min$^{-1}$. The glass transition temperature ($T_g$) was determined from the second heating run by taking the average point by heat capacity.

## 3.4 Preparation of photopatternable epoxy-based thermosets

The data and results shown in this section have been published in the journal "Materials" under the title "*Photopatternable Epoxy-Based Thermosets*", Volume 12, Issue 15, July 2019. Most of the following text, tables and figures have been taken from the respective publication. [246]

### 3.4.1 Preparation and thermal curing of photopatternable epoxy-based thermosets

For the preparation of the samples, epoxy-**NBE** was mixed with 1.0 epoxy equivalent of the respective anhydride hardener and 0.1 wt% DMBA. The composition of the resin formulations are shown in Table 3-3. For the formulations containing either dodecenylsuccinic anhydride (DDSA) or hexahydro-4-methylphthalic anhydride (HHMPA), the mixture was stirred for 30 minutes at room temperature in a glass vial. In addition, formulations containing hexahydrophthalic anhydride (HHPA) or glutaric anhydride (GA) were heated to 50 °C in a water bath (to dissolve the anhydride in epoxy-**NBE**) and stirred for 30 min. All formulations were cured at 100 °C for 18 hours, resulting in a solid sample.

**Table 3-3** Composition of photopatternable epoxy-based resin formulations

| Resin formulation | Type of anhydride | molar ratio[a] | accelerator [wt%] |
|---|---|---|---|
| epoxy-**NBE**/HHMPA | HHMPA | 1 | 0.1 |
| epoxy-**NBE**/HHPA | HHPA | 1 | 0.1 |
| epoxy-**NBE**/DDSA | DDSA | 1 | 0.1 |
| epoxy-**NBE**/GA | GA | 1 | 0.1 |

[a] Molar ratio of anhydride crosslinker to epoxy-**NBE** in resin formulation

### 3.4.2 Characterization of curing and cleavage kinetics

To monitor the thermally induced ring-opening reaction between epoxy-**NBE** and anhydride hardener and the subsequent photoinduced cleavage of the *o*-NBE links, FT-IR spectroscopy with a Vertex 70 spectrometer (Bruker, Billerica, USA) was used. Similar to the previous section, 16 scans were accumulated in transmission mode with a resolution of 4 cm$^{-1}$. IR absorption peaks were calculated using OPUS software (version 7.0, Bruker, Billerica, Massachusetts, USA). To prepare the samples, the resin formulation was drop-cast between a Si wafer and a CaF$_2$ substrate and cured at 100◦ C. The curing

rate was monitored for 18 h and FT-IR spectra were recorded at predetermined times. For the kinetics of the cleavage reaction, the films were irradiated with a medium pressure Hg lamp (Omnicure S1000, LumenDynamics, ON, Canada) under nitrogen atmosphere. The cleavage reaction was followed upon prolonged UV exposure. An integrated radiometer (Powerpuck II, EIT Instrument Markets, Leesburg, VA, USA) was used to determine the light intensity (power density P, in mW cm$^{-2}$) on the sample surface. The average power density was 114.4 mW cm$^{-2}$ (250 to 470 nm).

### 3.4.3 Characterization of network properties

Similar to the previous section, to determine the $T_g$ of the cured samples before and after UV irradiation, DSC was used. The cured samples were analyzed by heating at a rate of -20 °C to 120 °C min$^{-1}$. The $T_g$ was taken from the first heating step and was read as the midpoint in heat capacity. The preparation of the samples and subsequent UV irradiation was performed as described above. For the nanoindentation experiments, an Ultra Nanoindentation tester (Anton Paar, Graz, Austria) was applied, using Berkowitz pyramid tips with an equivalent cone semi-angle (q = 70.3°). The contact force was 50 µN and the maximum indentation force was 1000 µN. The loading and unloading speed was 6000 µN/min. A 30 s hold segment was applied to obtain a reliable stress-strain curve at maximum load. $H_{IT}$ data were taken from the unloaded part of the load-displacement curve according to the "Oliver and Pharr method". [248] In this method, the indentation hardness ($H_{IT}$) as a measure of surface hardness corresponds to the mean pressure supported by the sample at maximum load. The distance between the measuring points was 150 µm. In order to record the mechanical properties on a larger length scale and to obtain reliable results, nine indentations were performed over a total area of 300 x 300 µm.

### 3.4.4 Preparation and characterization of photopatterned films

For the sol-gel analysis, thin films were prepared between a Si wafer and a polypropylene foil. After curing at 100°C for 18 h, the polymer foil was removed and the cured films were irradiated with a medium pressure Hg lamp under nitrogen for predefined periods of time. FT-IR spectra of non-exposed and UV exposed samples were taken to study changes in the gel fraction after development in tetrahydrofuran for 10 min. Contrast curves were obtained by plotting the gel fractions versus the log function of the exposure dose.

The micropatterns were inscribed in the cured resin formulations by photolithography. The cured thin films were prepared as described in the previous paragraphs. Photolithographic patterning was then carried out using a quartz-chromium mask in contact mode with Omnicure S1000 (Lumen Dynamics, ON, Canada) as the light source. The exposure dose amounted to 22.3 $J/cm^2$ for cured epoxy-NBE/HHMPA, epoxy-NBE/HHPA and epoxy-NBE/DDSA systems. An exposure dose of 8.5 $J/cm^2$ was applied for the epoxy-NBE/GA network. Polymer films were developed by dipping the samples in tetrahydrofuran for a few seconds.

Surface topography measurements were conducted using a Leica DCM8 3D optical surface measurement system (Leica Microsystems, Wetzlar, Germany) with a Mirau 20× objective and ePSI (extended Phase Shift Interferometry) mode with blue light imaging. The images were acquired with blue light. This resulted in a theoretical optical resolution of 0.35 µm and a vertical resolution of >1 nm.

## 3.5 Photopatternable and rewritable epoxy-anhydride vitrimers

The data and results given in this section have been published in "Macromolecular Rapid Communications" under the title "*Photopatternable and Rewritable Epoxy-Anhydride Vitrimers*", Volume 42, Issue 2, 2021. Most of the following text, tables and figures have been taken from the respective publication. [249]

### 3.5.1 Preparation of photopatternable and rewritable epoxy-anhydride vitrimers

The preparation of the thin films was similar as described to the previous sections. In this approach, epoxy-NBE was mixed with HHPA at a stoichiometric ratio of 1:1 and 5 mol% (related to epoxy groups) of TBD as transesterification catalyst was added. In addition, DMBA (0.1 wt%) was applied to accelerate the curing reaction. The formulation was stirred in a glass vial at room temperature for 30 min. Thermal curing was carried out at 70 °C for 24 h yielding solid samples.

### 3.5.2 Writing and erasing of micropatterns

For the resin formulation, thin films were drop- cast on Si wafers. After thermal curing at 70 °C for 24 hours, the micropatterns were inscribed by photolithography using a quartz-chromium mask in contact mode. Irradiation was performed using an Omnicure S1000 (Lumen Dynamics, Canada) as a light source with an irradiation dose of 42.5 J/cm$^2$. Films were prepared as follows. The positive-tone structure was developed by immersing the sample in a mixture of tetrahydrofuran and ethanol in a 1:1 volume ratio for a few seconds. After development, thermal annealing at 120 °C for 24 hours under vacuum erased the positive-tone structures. A film with a smooth surface was obtained, which was again patterned by mask lithography.

### 3.5.3 Characterization of the photopatternable and rewritable films

The characterization was carried out in a similar manner, as previously described. The curing reaction was monitored by FT-IR spectroscopy using a Vertex 70 spectrometer. (Bruker, USA). Sixteen scans were accumulated in transmission mode with a resolution of 4 cm$^{-1}$. The area of the IR absorption peak was calculated using OPUS software. For

sample preparation, the resin formulation was drop-cast between Si and $CaF_2$ substrates and was cured at 70°C for 24h.

The curing rate was followed for 3 hours and FT-IR spectra were recorded at predetermined times. The cured drop-casted film was irradiated with a medium pressure Hg lamp to investigate the cleavage kinetics (Omnicure S1000, Lumen Dynamics, Canada) under nitrogen atmosphere. The cleavage reaction was monitored by FT-IR spectroscopy using a Vertex 70 spectrometer (Brucker, USA) as a function of exposure time. An integrated radiometer (Powerpuck II, EIT Instrument Markets, USA) was used to measure the light intensity (power density P; in mW $cm^{-2}$). The average power density was 114 mW $cm^{-2}$ (between 250 nm and 470 nm).

The conversion of the $o$-NBE group was estimated according to equation 3-1, in which $A_0$ and $A_t$ correspond to the peak area of the characteristic absorption band before and after the predefined UV exposure time. The absorption band at 2946 $cm^{-1}$ (C-$H_2$) was used as reference to normalize $A_0$ and $A_t$.

$$\% \text{ conversion} = \left[\frac{A_0 - A_t}{A_0}\right] \cdot 100$$

Equation 3-1

The $T_g$ was determined by differential scanning calorimetry (DSC) using a Mettler Toledo DSC 821e (USA). Samples were analyzed by heating from -20°C to 120°C at a heating rate of -20 °C $min^{-1}$. The $T_g$ was taken from the first heating run and was read as the midpoint in heat capacity.

TGA was carried out under a nitrogen atmosphere using a Mettler Toledo unit operated with a Star software. The nitrogen flow rate was 50 mL/min and the sample was heated from 25 °C to 900 °C with a heating rate 10 °C/min.

For sol-gel analysis, cured drop-cast films of the epoxy-anhydride resin were irradiated with an Omnicure S1000 (Lumen Dynamics, Canada) for predefined periods of time under nitrogen atmosphere. To determine the change in gel fraction, FT-IR spectra (Vertex 70

spectrometer, Brucker) of non-exposed and exposed samples were taken after development in a tetrahydrofuran/ethanol mixture at a 1:1 volume ratio for 5 minutes.

Surface topography measurements were carried out using the 3D optical surface metrology system Leica DCM8 (Leica Microsystems, Germany). Images were taken in ePSI (extended hase shift interferometry) mode using blue light with a Mirau 20x objective. For these parameters, the theoretical optical resolution is 0.35 μm and the vertical resolution is better than 1 nm.

The stress relaxation was characterized in torsion mode using an MCR 501 rheometer (Anton Paar, Graz, Austria) equipped with a rectangular torsion fixture. The heating chamber was continuously purged with nitrogen at a volumetric flow rate of 1 m³/h. A rectangular sample with a length of 30 mm and a width of 5 mm and a uniform thickness of 1.5 mm was heated to the required measuring temperatures (70, 100 and 120°C) and equilibrated for 20 min. A constant tensile force of 0.1 N was applied to ensure a stable position of the sample. After equilibrating the temperature, a deflection of 1% was applied and kept constant for the entire time and the torque was monitored over time.

$T_v$ and the activation energy of the transesterification reaction ($E_a$) were determined by taking the time required for the stress relaxation modulus to reach 37% (1/e) of its initial value as respective relaxation time ($\tau^*$). The stress relaxation modulus was measured at 70, 100 and 120 °C and plotted against 1000/T to fit the Arrhenius relationship (Equation 2-15). The calculation of the $T_v$ was carried out as described in section 2.6.6.

## 3.6 Epoxy-anhydride vitrimers from aminoglycidyl resins with high glass transition temperature and efficient stress relaxation

The data and results given in this section have been published in "Polymers" under the title "*Epoxy-anhydride vitrimers from aminoglycidyl resins with high glass transition temperature and efficient stress relaxation*", Volume 12, Issue 5, October 2020.Most of the following text, tables and figures have been taken from the respective publication. [250]

Moreover, parts of the following section have been filed at the Austrian Patent Office under the patent title „*Aushärtbare Zusammensetzung zur Herstellung eines Vitrimers und daraus erhältliches Vitrimer und Verfahren zu dessen Herstellung*"; A50332/2020.

Clemens Sperling performed his Bachelor thesis in the course of this topic. Selected results of his thesis are discussed within this section. [242]

### 3.6.1 Preparation of epoxy-anhydride vitrimers

To prepare the catalyzed vitrimer systems, either 4,4′-methylenebis(*N,N*-diglycidylaniline) or *N,N*-diglycidyl-4-glycidyloxyaniline were mixed with $Zn(acac)_2$-$H_2O$ (at a 5 mol% concentration related to the epoxy groups), placed in a PTFE beaker and heated to 100 °C. The formulation was stirred at 100 °C for 10 min to dissolve the catalyst. Glutaric anhydride was added stepwise and stirred at 100 °C for another 10 min. Air bubbles and low-molecular weight materials (e.g. acetylacetone from the catalyst) were removed under vacuum for 10 min. For non-catalytic systems, the samples were prepared without adding $Zn(acac)_2$-$H_2O$.

Table *3-4* summarizes the composition of the networks under investigation:

**Table 3-4** Composition of the investigated resin formulations. r denotes the stoichiometric ratio, which was defined as r = anhydride equiv. / epoxy equiv. [250]

| System | 3-DGOA [g] | 4-DGA [g] | Anhydride [g] | $Zn(acac)_2$-$H_2O$ [mg] | r |
| --- | --- | --- | --- | --- | --- |
| 3-DGOA-0.5-Zn | 5 | - | 5.7 | 658 | 0.5 |
| 3-DGOA-0.25-Zn | 5 | - | 2.9 | 658 | 0.25 |
| 3-DGOA-0.5 | 5 | - | 5.7 | - | 0.5 |
| 4-DGA-0.5-Zn | - | 5.7 | 5.7 | 658 | 0.5 |
| 4-DGA-0.25-Zn | - | 5.7 | 2.9 | 658 | 0.25 |
| 4-DGA-0.5 | - | 5.7 | 5.7 | - | 0.5 |

### 3.6.2 FT-IR spectroscopy of the vitrimer network

Similar to the previous sections, the thermally induced ring-opening reaction between the epoxide monomers and anhydride hardener was monitored by FT-IR spectroscopy using a Vertex 70 spectrometer (Bruker, Billerica, MA, USA). Sixteen scans were accumulated in transmission mode with a resolution of 4 cm$^{-1}$. The IR peak areas were calculated using OPUS software (Version 7.0, Brucker, Billerica, Massachusetts, USA). For sample preparation, thin films were spin-cast from chloroform solutions (1 mg/mL) of the resin formulations (Table 3-4) on Si wafer.

### 3.6.3 Dynamic-mechanical thermal Analysis (DMTA) of the vitrimer network

To prepare the sample, the resin formulation was poured in a preheated (120 °C) metal mold and cured at 120 °C for 20 hours. A cured sheet of 1.5 mm thickness was obtained from which rectangular samples (3×12 mm) were cut. DMTA experiments were carried out in tensile mode using a Mettler Toledo SDTA861e dynamic mechanical analyzer (Columbus, OH, USA). A clamp length of 9 mm was selected and measurements were performed with displacement-controlled oscillations of 2.5 µm amplitude at 1 Hz. The heating rate was 3 K/min from -50 °C to 230 °C.

### 3.6.4 TGA of the vitrimer network

TGA experiments were carried out using a Mettler Toledo (Columbus, Ohio, USA) TGA/DSC1 thermogravimetric analyzer. Measurements were performed from 25 °C to 900 °C at a heating rate of 10°C/min under nitrogen atmosphere. The data was analyzed using STAR software from Mettler Toledo (Columbus, Ohio, USA).

### 3.6.5  Stress relaxation measurements of the vitrimer network

Stress relaxation was characterized in torsion mode by a MCR 501 rheometer (Anton Paar, Graz, Austria), equipped with a rectangular torsion fixture. The heating chamber was continuously purged with nitrogen at a volumetric flow rate of 1 $m^3$/h. A rectangular sample of uniform thickness of 1.5 mm, a length 30 mm and width 5 mm was heated to the predefined temperature (160-280 °C) and equilibrated for 20 min. A constant elongation force of 0.1 N was applied to ensure a stable position of the sample. After temperature equilibration, a deflection of 1% was applied and kept constant during the measurement of the torque over time.

### 3.6.6  Recycling of the vitrimers networks

The cured 3-DHA-0.5-Zn and 4-DHA-0.5-Zn networks were grinded in a ball mill for 90 seconds and 30 Hz. The resulting powders were molded into 25 mm diameter discs using a vacuum press (Collin, Ebersberg, Germany) at 220 °C for 40 minutes at 5 bar pressure. In addition, molded test bars were prepared using a PVT 100 (SWO Polymertechnik, Krefeld, Germany) at 500 bar and at 250 °C for 5 minutes.

## 3.7 Influence of the transesterification catalyst on the network's properties

Viktoria Feigl performed her bachelor thesis in the course of this topic. Selected results of her thesis are discussed within this section. [251]

### 3.7.1 Preparation of epoxy-anhydride vitrimers

For sample preparation, 3,4-epoxycyclohexylmethyl-3',4'-epoxycyclohexane carboxylate (ECC) was mixed with the corresponding catalyst (at a 5 mol% concentration related to the epoxy groups), placed in a PTFE beaker and heated to 100 °C. The formulation was then slowly heated up to 120 °C and stirred for around 20 min to dissolve the individual catalyst. Glutaric anhydride was added stepwise and stirred at 100 °C for another 10 min. For all four systems, the stoichiometric ratio was 1:1 epoxy/anhydride. Air bubbles and low-molecular weight compounds (e.g. acetylacetone from the catalyst) were removed under vacuum for 10 min. The samples were cured for 20 h at 120 °C. Table 3-5 summarizes the composition of the networks under investigation.

**Table 3-5** Composition of the investigated resin formulations [251]

| System | ECC [g] | Anhydride [g] | Catalyst [mg] |
|---|---|---|---|
| ECC-0.5-Zn | 7 | 5.9 | 0.68 |
| ECC-0.5-TBD | 7 | 5.9 | 0.36 |
| ECC-0.5-Pyridine | 7 | 5.9 | 0.20 |
| ECC-0.5-Guanine | 7 | 5.9 | 0.39 |

### 3.7.2 FT-IR spectroscopy of the vitrimer network

Similar as in the previous sections, the thermally induced ring-opening reaction between the epoxide monomer and anhydride hardener was monitored by FT-IR spectroscopy using a Vertex 70 spectrometer (Bruker, Billerica, MA, USA). Sixteen scans were accumulated in transmission mode with a resolution of 4 cm$^{-1}$. The IR peak areas were calculated using OPUS software (Version 7.0, Brucker, Billerica, Massachusetts, USA). For sample preparation, thin films were drop-cast between a Si-wafer and CaF$_2$- disc and monitored at predefined times during the curing step.

### 3.7.3 Dynamic-mechanical thermal analysis (DMTA) of the vitrimer network

For sample preparation, the resin formulation was poured in a preheated (120 °C) metal mold and cured at 120 °C for 20 hours. A cured sheet of 1.5 mm thickness was obtained from which rectangular samples (3×12 mm) were cut. DMTA experiments were carried out in tensile mode using a Mettler Toledo SDTA861e dynamic mechanical analyzer (Columbus, OH, USA). A clamp length of 9 mm was selected and measurements were performed with displacement-controlled oscillations of 2.5 µm amplitude at 1 Hz. The heating rate was 3 K/min from -50 °C to 230° C.

### 3.7.4 TGA of the vitrimer network

In order to investigate the thermal stability of the networks, TGA experiments were carried out using a Mettler Toledo (Columbus, Ohio, USA) TGA/DSC1 thermogravimetric analyzer and were performed under nitrogen atmosphere. Samples were heated from 25 °C to 900 °C at a heating rate of 10 °C/min and data were analyzed using STAR software from METTLER TOLEDO (Columbus, Ohio, USA).

### 3.7.5 Stress relaxation stress measurements of the vitrimer network

Similar to previous studies, the stress relaxation of the vitrimer networks was determined using a MCR 501 rheometer (Anton Paar, Graz, Austria) in torsion mode, equipped with a rectangular torsion fixture. Due to the higher thermal stability of the networks the measurements were carried out under air. A rectangular sample of uniform thickness of 1.5 mm, a length 30 mm and a width 5 mm was heated to the predefined temperature (160 - 280 °C) and equilibrated for 20 min. A constant elongation force of 0.1 N was applied to ensure a stable position of the sample. After temperature equilibration, a deflection of 1% was applied and kept constant during the measurement of the torque over time.

### 3.7.6 Swelling experiments

When placing a crosslinked polymer in a suitable solvent, the outer structure of the material interacts with the solvent and solvent molecules migrate inside the network. After reaching an equilibrium between the elastic forces and free energy of mixing a steady state is achieved and the swelling process stops. During the swelling process unreacted

compounds (monomers, crosslinkers, etc.) and unattached polymer chains are dissolved. Swelling experiments can be applied to determine the fraction of soluble and insoluble parts, whereas the crosslinking density, molecular weight between crosslinking points and swelling degree can be calculated by equilibrium swelling measurements.

For the experimental part of this thesis, two properties were characterized by swelling experiments, namely the swelling degree and the gel fraction of the four networks.

For the calculation of the swelling degree, the initial and swollen weights of the polymer as shown in Equation 3-2 are used. For the preparation, five samples of the crosslinked polymer were weighted (75-85 mg) and immersed in 15 mL of a solvent (chloroform) in a separate vial, which initiates swelling of the network and solubilizes the unattached polymer and unreacted starting material. After 24 h at room temperature, the polymer was removed from the solvent, wiped off and weighted.

$$\text{Swelling degree} = \frac{\text{Swollen weight}}{\text{Initial weigt}} = \frac{m_{swollen}}{m_0} \qquad \text{(Equation 3-2)}$$

For the calculation of the gel fraction, the insoluble dried network as shown in Equation 3.3 is measured. A similar procedure is applied as previously described, whereas the insoluble part of the sample was taken out of the solvent and dried until constant weight was reached. The gel fraction was calculated according to Equation 3-3:

$$\text{Gel fraction} = \frac{\text{Dry weight}}{\text{Initial weight}} = \frac{m_{dry}}{m_0} \qquad \text{(Equation 3-3)}$$

# 4 Results and discussion

## 4.1 Dual-responsive polydimethylsiloxane networks

The data and results given in this section have been published in the "Journal of Polymer Science Part A: Polymer Chemistry" under the title "*Dual-Responsive Polydimethylsiloxane Networks*", Volume 56, Issue 20, October 2018. Most of the following text, tables and figures have been taken from the respective publication. [247]

Markus Ast performed part of his experimental studies for his master thesis on the topic of "*Dual-Responsive Polydimethylsiloxane Networks*". Some of the results are presented in the following section.
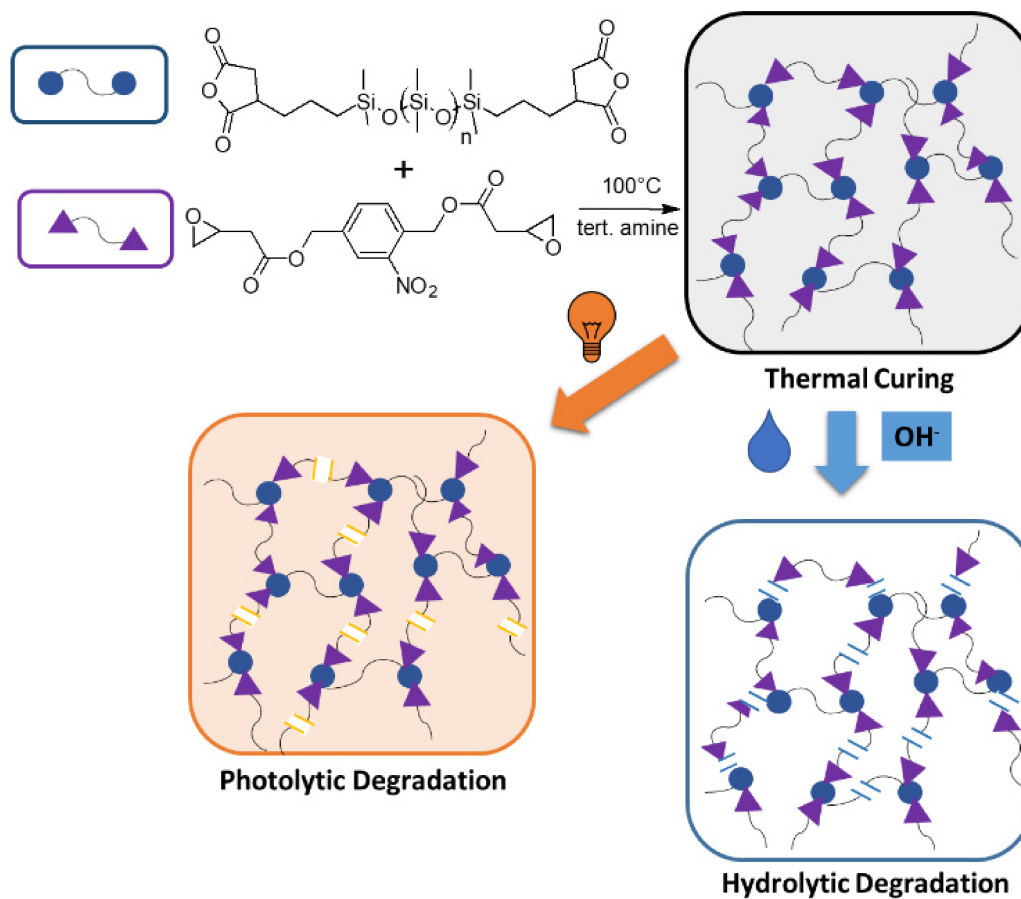


**Figure 4-1** Design and cleavage of dual-responsive PDMS networks [247]

In this study, *o*-nitrobenzyl ester (*o*-**NBE**) chromophores were introduced into polydimethylsiloxane (PDMS) networks to prepare photodegradable elastomer networks. Similar concepts have been rarely published and methods for controlled degradation of crosslinked PDMS generally require harsh conditions. [252,253]

Following the idea of a spatially controlled degradation of PDMS, a photocleavable crosslinker was incorporated into the polymer network, which is also sensitive to hydrolysis. The introduction of *o*-**NBE** linkers enables the preparation of dual-responsive PDMS network that degrades under UV light and/or alkaline media. In addition, the dual-responsive nature allowed switching of positive- and negative- tone patterns by adjusting both the exposure dose and the solvent used in the development step. The general scheme is shown in Figure 4-1.

### 4.1.1  Design and curing of dual-responsive PDMS networks

Dual-responsive elastomers were prepared by introducing a photosensitive *o*-NBE chromophore into the network, which is sensitive to hydrolysis in an alkaline milieu. For that, polydimethylsiloxane (PDMS) terminated with anhydride and epoxy monomers bearing photodegradable *o*-NBE chromophores were cured (Figure 4-1). The ring-opening reaction between the terminal anhydride groups of the polymer and the epoxy groups of the monomer yields ester crosslinks, which—along with the *o*-NBE groups—are expected to undergo hydrolysis when exposed to an alkaline environment (Figure 4-3).

Controlled network degradation can be obtained either by photocleavage of the *o*-NBE crosslinks or by hydrolysis of the ester bonds in aqueous alkaline media.

The degradation utilized by ester hydrolysis, enables a temporal control of network properties by adjusting the pH value of the aqueous solution to which the dual-responsive PDMS is exposed. The incorporation of the *o*-NBE chemistry allows spatial control of the crosslink density and solution properties in pH-responsive PDMS networks by well-defined cleavage of the covalent bonds upon UV irradiation.

In order, to prepare dual-responsive PDMS networks, anhydride-terminated PDMS and epoxy-**NBE** were mixed in stoichiometric ratios. However, the resin formulation was not stable and rapid phase separation occurred after mixing. Two different approaches were used to overcome this phase separation. Firstly, the amount of epoxy-**NBE** was gradually reduced to obtain a homogeneous and stable resin. This formulation (PDMS-**1**) consisted

of a 1:2 molar ratio of epoxy-**NBE** and anhydride-terminated PDMS, which was then drop-cast between two CaF$_2$ discs and cured at 100 °C. Figure 4-2 (a) illustrates the FT-IR spectra prior to and after thermal curing at 100 °C. The depletion of the two characteristic carbonyl peaks of the succinic anhydride group (1860 and 1778 cm$^{-1}$) and the appearance of the IR absorption band associated with the ester carbonyl group (1740 cm$^{-1}$) confirm the successful network formation by the ring opening reaction of the anhydride and epoxy groups.
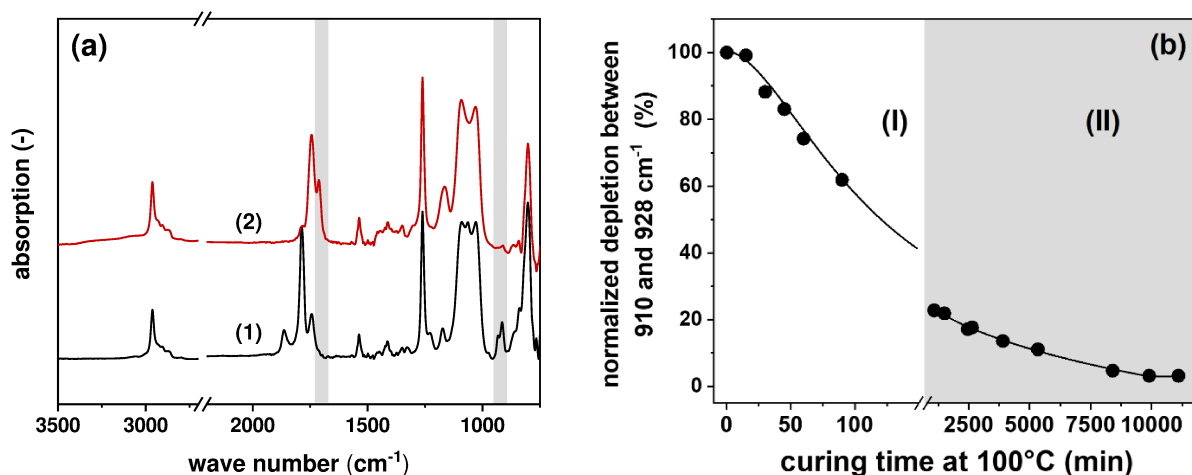


**Figure 4-2** (a) FT-IR spectra of PDMS-**1** (1) prior to and (2) after thermal curing and hydrolysis of the residual anhydride groups at 100 °C for 95 h. (b) Normalized conversion of the peak area between 910 and 928 cm$^{-1}$ versus curing time at 100 °C. Area I highlights the reaction progress due to the ring-opening reaction between the epoxy and anhydride moieties (curing) whilst area II illustrates the ring-opening reaction between the residual anhydride groups and moisture upon prolonged storage at 100 °C. [247]

The curing kinetics was studied by following the depletion of the epoxy peak at 910 cm$^{-1}$ [Figure 4-2 (b)]. A rapid depletion of the epoxy band was observed and after curing at 100 °C for 210 min, the conversion was 80%. However, no further depletion of the epoxy peak could be detected, as the epoxy signal partially overlapped with the absorption band of the succinic anhydride group at 920 cm$^{-1}$,

Since an excess of anhydride-terminated PDMS was used, additional thermal annealing of the cured PDMS network was performed to partially hydrolyze the remaining free anhydride groups in the presence of ambient moisture from the environment. The complete conversion of the anhydride groups is needed as the residues can react with the primary photocleavage products of the *o*-NBE compounds (e.g. aldehydes and free

carboxylic acids), which in turn can lead to a re-crosslinking of the network during photocleavage.

Through this additional thermal annealing the formation of free carboxylic acids was confirmed by FT-IR measurements. At 1712 cm$^{-1}$ a new signal appeared, which could be assigned to the C=O bond of the carboxylic acid, appeared, whilst the characteristic anhydride band gradually disappeared. By following the additional depletion of the anhydride band at 920 cm$^{-1}$, it can be concluded that the normalized peak area of the anhydride groups does not further decrease after thermal annealing at 100 °C for 7 days [see region II in Figure 4-2(b)]. The proposed curing and annealing mechanism of PDMS-**1** is shown in Figure 4-3:
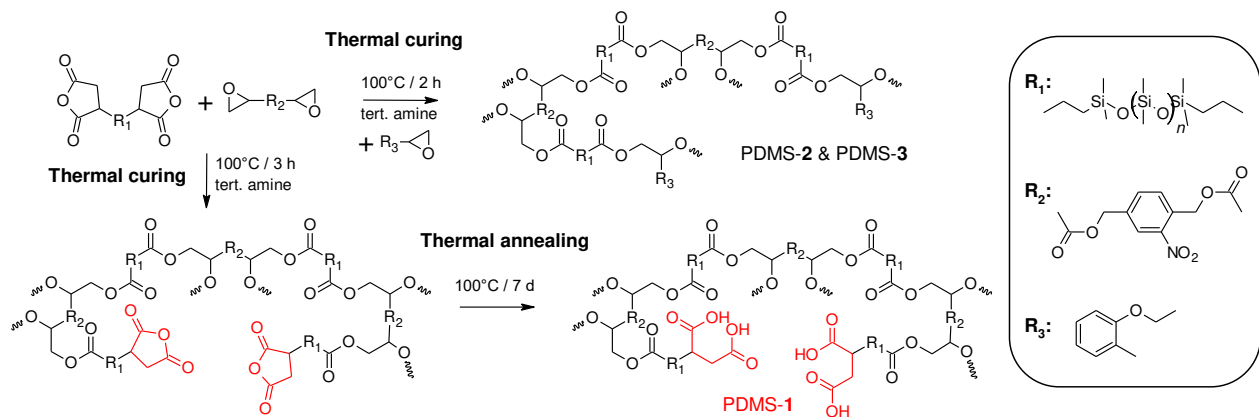


**Figure 4-3** Curing routes for the preparation of dual-responsive PDMS networks [247]

In the second approach, a mono-functional epoxy monomer (epoxy-**GME**) was added to epoxy-**NBE**, which acted as a compatibilizer and improved the dispersion of the cross-linker in the PDMS formulation (Figure 4-4). Equimolar mixtures of anhydride-terminated PDMS and epoxy monomers were previously prepared using 3:1 and 1:1 molar ratios of epoxy-**NBE** and epoxy-**GME** (PDMS-**2** and PDMS-**3**).

In these samples, the stoichiometric ratio of the epoxy to anhydride groups was 1:1. The curing kinetics was monitored by FT-IR spectroscopy following the changes in the characteristic absorption bands as described in the previous paragraph [Figure 4-4 (a)]. In both PDMS-**2** and PDMS-**3**, the depletion of the epoxide groups proceeded at a higher rate than in PDMS-**1** [Figure 4-4 (b)]. It is also evident that the curing rate increases with increasing epoxy-GME concentration, which is due to the higher mobility of the mono-

functional monomer. This also indicates that the curing kinetics of the dual-responsive PDMS is strongly dependent on the diffusion of the monomer.
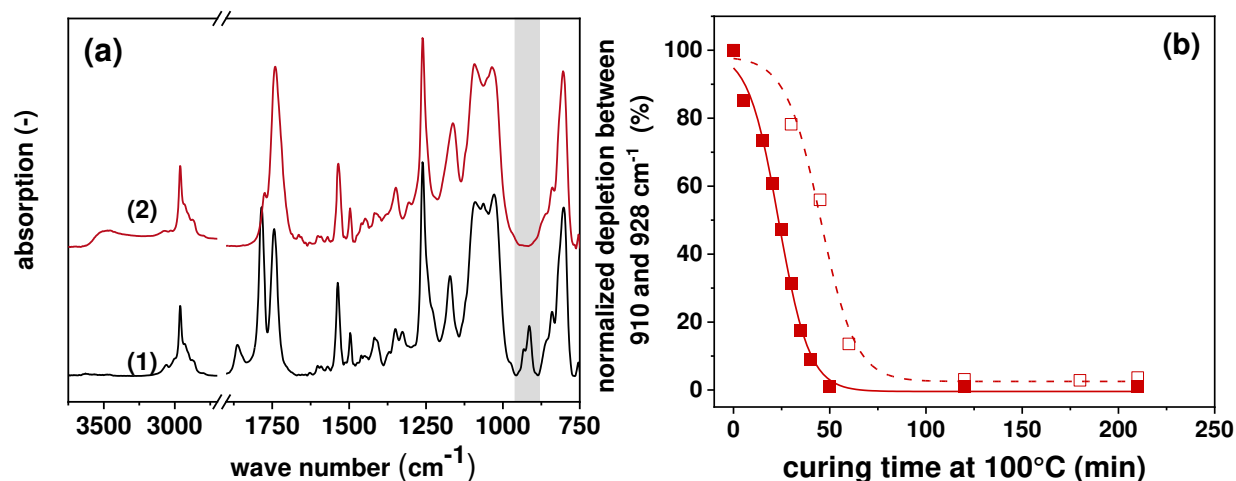


**Figure 4-4** (a) FT-IR spectra of PDMS-**2** (1) prior to and (2) after the thermal curing at 100 °C for 120 h. (b) Normalized conversion of the peak area between 910 and 928 cm$^{-1}$ related to the overlapping epoxy and anhydride signal versus curing time at 100 °C in PDMS-**2** (open squares) and PDMS-**3** (solid squares). [247]

With equimolar formulations, the reduction of the epoxide groups correlated well with the reduction of the anhydride signal and complete conversion of both groups was observed after 50 and 120 min for PDMS-**2** and PDMS-**3**, respectively. Since complete conversion of the oligomers and monomers was achieved, no additional thermal annealing step was required to hydrolyze the remaining anhydride groups.

### 4.1.2  Hydrolytic cleavage of dual-responsive PDMS networks

The cured networks were degraded across the ester bond linkers applying two different cleavage mechanisms. The hydrolysis of the ester groups was used to temporarily control the network cleavage [Figure 4-5 (a)]. In a study, Cichra and Adolph reported that the nitro group participates in the ester hydrolysis and they found accelerated hydrolysis rates for some nitro-substituted alkyl esters. [254]
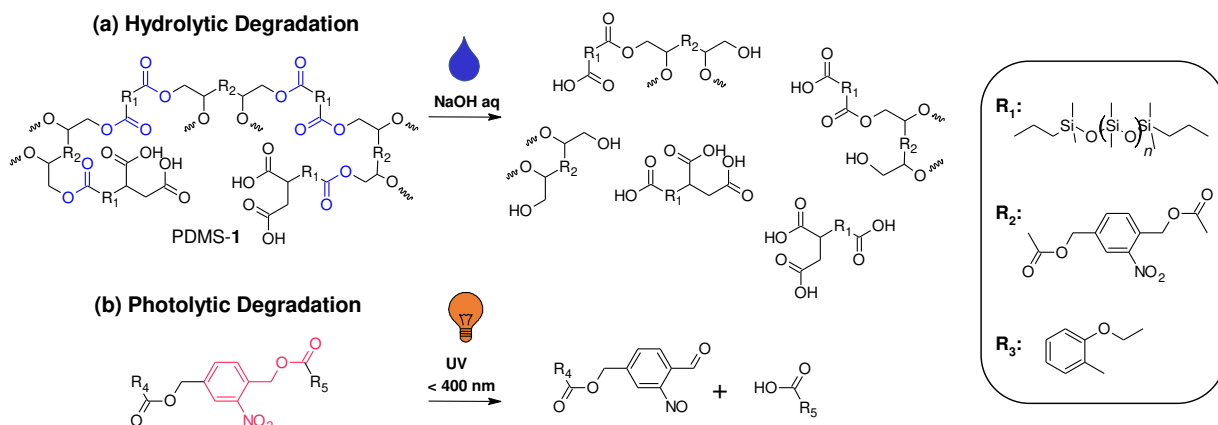
**Figure 4-5** (a) Hydrolytic and (b) photolytic cleavage routes of dual-responsive PDMS networks. [247]

The degradation kinetics at 21°C was quantified by monitoring the change in gel fraction over time for NaOH concentrations ranging from 0.025 to 1 M. Figure 4-6(a) shows a plot of the gel fraction of PDMS-**1** as a function of immersion time for different NaOH concentrations. The results indicate that the hydrolysis rate is strongly dependent on the pH value of the aqueous medium and increases significantly with an increasing NaOH concentration. In the PDMS-**1** network, a rapid hydrolysis of the ester bonds is observed in 1 M NaOH solution, with the elastomer being completely degraded within 2 h. A decrease of the NaOH concentration from 1 to 0.05 and 0.025 M extended the degradation time from 2 to 6 hours and 15 days, respectively. This behavior has been previously reported for a study by Göpferich *et al.*, in which the rate of hydrolysis of esters varies by several orders of magnitude due to the base catalysis. [255] The pH value has also been shown to be a useful parameter for the temporal control of network properties and has been used in the development of new materials for tissue engineering or drug release. [256]

In following experiments, the hydrolysis rates of the three different PDMS networks were compared at a given NaOH concentration of 0.05 M [Figure 4-6(b)]. The PDMS-**1** network was completely degraded within 120 h at 21 °C, while the gel contents of PDMS-**2** and PDMS-**3** amounted to around 90% under the same conditions. Even after 87 days of long-term storage, the gel content of PDMS-**2** and PDMS-**3** comprised 48% and 62%, respectively, suggesting that the higher hydrolysis rate of PDMS-**1** was not due to lower

crosslinking density, as PDMS-**1** and PDMS-**3** had the same molar ratio of epoxy to anhydride groups.
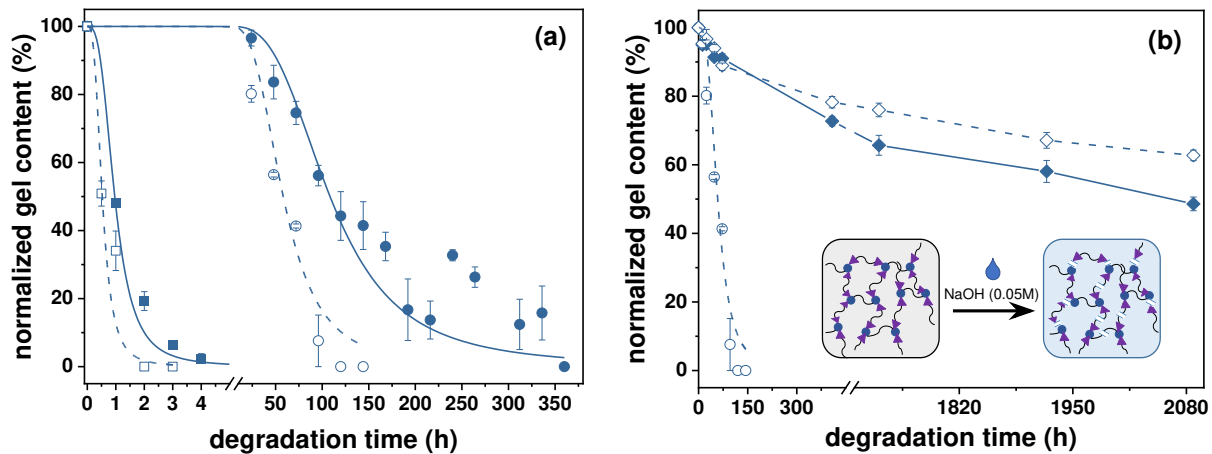


**Figure 4-6** (a) Relative gel fraction of PDMS-**1** networks versus degradation time at 21°C. The degradation was carried out in aqueous solutions with 1 (open squares), 0.5 (solid squares), 0.05 (open circles) and 0.025 M (solid circles) NaOH. (b) Relative gel fraction of PDMS-**1** (open circles), PDMS-**2** (solid diamonds) and PDMS-**3** (open diamonds) networks versus degradation time at 21 °C. The degradation was carried out in aqueous solutions with 0.05 M NaOH. Error bars represent standard deviations of three samples [247]

As reported by Göpferich, the reaction rate of ester hydrolysis is also a function of the network's water uptake. [255] Thus, hydrophilic polymers are usually characterized by a higher degradation rate, as more water molecules can migrate between the polymer chains, which induce bulk degradation of the network. [256]

Contrary, the degradation of hydrophobic polymers during ester hydrolysis occurs via a surface erosion mechanism as observed in polyanhydride networks. [257] For PDMS-**1**, it is noteworthy that part of the anhydride groups was not consumed by thermal curing with bifunctional crosslinkers, whereas the remaining anhydride moieties were hydrolyzed during a thermal post-annealing step. Thus, it is expected that dangling PDMS chains with terminal carboxylic acid groups are present in PDMS-**1** networks, which increase the polarity of the elastomer and hence affect the rate of hydrolysis in aqueous NaOH. However, the increase in polarity is less pronounced for PDMS-**1**, as evidenced by contact angle measurements. After curing PDMS-**2** and PDMS-**3** exhibited water contact angles of 109.0 ±3.67° and 105.4 ±1.73°, respectively, and the surface of the cured PDMS-**1** film was determined by a water contact angle of 102.8 ±0.8°.

The density of the network and the polarity of the surface did not appear to affect the hydrolysis rate of the dual-responsive network, but correlated well with the number of *o*-NBE groups incorporated into the network. The hydrolysis study showed that the formation of soluble species was more efficient in the highly crosslinked (cured with a larger amount of bifunctional epoxy crosslinker) PDMS-**2** than in the lower crosslinked PDMS-**3**.

The results indicate that the rate of hydrolysis of the PDMS-**2** network is mainly due to the large number of *o*-NBE groups, which are expected to undergo faster hydrolysis reactions than the ester groups formed by the thermal curing reactions.

The degradation of the network is not only related to the number of *o*-NBE groups, but also to the structure and polarity of the degradation products: the network structure of PDMS-**3** and PDMS-**1** consists of the same amount of epoxy anhydride, but the hydrolysis rate of PDMS-**1** is significantly higher. The PDMS-**1** network is expected to consist of dangling polymer chains with terminal carboxylic acid groups formed during thermal annealing.

On the other hand, the PDMS-**2** and PDMS-**3** network structures incorporate all terminal anhydride groups by stoichiometric amounts of epoxy-**GME**. Epoxy-**GME** affects the network properties, as the monofunctional epoxide does not lead to the formation of crosslink points but acts as a chain extender. [258]

Therefore, as the concentration of epoxy-**GME** rises, the molecular weight between the two cross-linked points increases and the molecular weight of the cleavage products increases, whilst the polarity of the cleavage products is expected to decrease. Cohen *et al.* demonstrated that the release of hydrophilic cleavage products increases the hydrophilicity of the network during hydrolysis. [259] This leads to an enhanced water uptake and a distinctive increase of the hydrolysis rate. Similar findings were observed by Pitt and Shah who showed that the hydrolysis cleavage reaction is accelerated when the polymer network becomes more hydrophilic during hydrolysis. [260]

It should be noted that PDMS is prone to chain scission reactions in hydroxylic solvents and under alkaline conditions. [261,262] Reactive chain ends are generated by the chain scission process, which undergo backbiting and related ring formation reactions. Both mechanisms—chain scission and backbiting—are reported to efficiently degrade PDMS and crosslinked PDMS networks. However, since PDMS-**2** and PDMS-**3** are relatively stable in 0.05 M NaOH solution (gel content 48-62% after 87 days), the degradation of Si-

O bonds in the polymer backbone does not appear to play a significant role in the hydrolytic degradation of the dual-responsive PDMS network.

Due to the efficient degradation of the PDMS-**1** network in an alkaline environment make PDMS-**1** an interesting material for nanoprint lithography (NIL) processes. Thermally cured PDMS formulations are widely used in soft imprinting processes as they have the advantages of good biocompatibility and high optical transparency in ultraviolet and visible light region.[137] Various approaches have been pursued to enable easy demolding without damaging the pattern structure and to ensure that no residues are left on the mold after multiple demolding steps. These involve appropriate surface modification of the mold and the development of low surface energy resists.[263] Due to the pH-sensitive nature of the dual-responsive elastomer network, residues can be conveniently removed from the mold by placing the mold in an alkaline aqueous solution at room temperature.

### 4.1.3  Photolytic cleavage of dual-responsive PDMS networks

Advancing from hydrolysis to photolysis, the photocleavage reaction of the dual-responsive PDMS networks was studied in thin films, which had been drop-cast on $CaF_2$ discs. The cured samples were irradiated with UV light to cleave the *o*-NBE groups [Figure 4-5(b)]. FT-IR spectra prior to and after UV illumination showed a decrease of the two characteristic $NO_2$ signals at 1537 cm$^{-1}$ (asymmetric stretching) and 1348 cm$^{-1}$ (symmetric stretching), which is associated with the conversion of nitro moieties to nitroso groups [Figure 4-5 (a)].
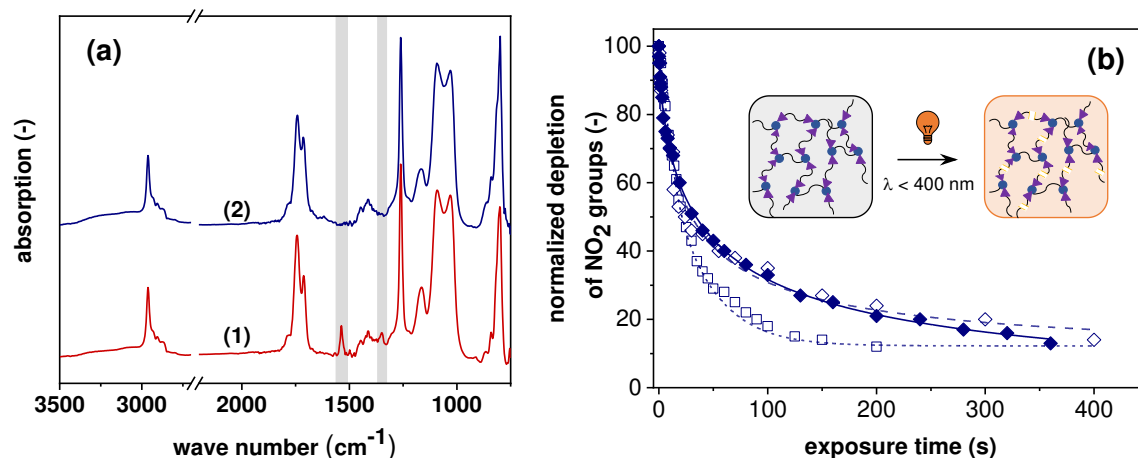
**Figure 4-7** (a) FT-IR spectra of cured PDMS-**1** (1) prior to and (2) after photocleavage (206.2 J/cm², λ < 400 nm, N₂). (b) Following the cleavage of the *o*-NBE links by FT-IR spectroscopy upon prolonged UV exposure: Depletion of the normalized intensity of the nitro band at 1537 cm⁻¹ in PDMS-**1** (open squares), PDMS-2 (solid diamonds) and PDMS-**3** (solid diamonds). [247]

In the PDMS-**2** and PDMS-**3** systems, the formation of characteristic cleavage products such as carboxylic acids and aldehydes is indicated by a slight broadening of the C=O signal (1635-1802 cm⁻¹). In PDMS-**1** the bands partly overlap with the signals of the carboxylic acid groups already present in the network structure [Figure 4-5 (a)].

The cleavage rates of the three different PDMS networks were then characterized by monitoring the decrease in the $NO_2$ signal at 1537 cm⁻¹ upon prolonged UV irradiation [Figure 4-5(b)]. The results reveal that the PDMS-**2** and PDMS-**3** networks show comparable cleavage rates, whereas the PDMS-**1** network is characterized by a faster photo-induced conversion of the nitro to the nitroso groups. For PDMS-**1**, the maximum conversion of nitro groups was achieved after 175 s of UV irradiation. In contrast, PDMS-**2** and PDMS-**3** required 400 s of UV irradiation to achieve full conversion. Although the $T_g$ of the three networks was comparable (Table 4-1), the differences in cleavage rates may be due to differences in the local mobility of the chromophore in the PDMS matrix.

**Table 4-1** Glass transition temperature ($T_g$) of dual-responsive PDMS networks prior to and after photocleavage. [247]

| Sample | $T_g$ (cured network) (°C) | $T_g$ (cleaved network) (°C) |
|--------|----------------------------|------------------------------|
| PDMS-**1** | -8 | -10[a] |
| PDMS-**2** | -8 | -11[b] |
| PDMS-**3** | -7 | -9[b] |

[a]Photocleavage was carried out with an exposure dose of 7.8 J/cm$^2$
[b]Photocleavage was carried out with an exposure dose of 15.6 J/cm$^2$

Tazuke *et al.* demonstrated, that the cleavage reaction in polymers with identical functional groups correlates directly with the $T_g$ of the material. In this case, the $T_g$ is influenced by main-chain rigidity and interpolymer interactions, which are both affected by segmental mobility. However, when comparing polymer systems with different functional properties, other interactions such as hydrogen bond formation and π-π stacking must also be taken into account. [264] It has to be considered that the isomerization and final conversion rates of the chromophores obtained by the FT-IR studies do not allow a direct correlation to network degradation and the formation of soluble products. Previous studies have shown that the presence of photodimerised by-products, such as azobenzene derivatives, can lead to the reformation of covalent bonds. [265,266]

In order to gain insight into the photo-induced degradation of the dual-response PDMS networks, the $T_g$ of the PDMS networks was compared prior to and after UV irradiation. The results showed that the $T_g$ of the networks decreased between 2 and 3 °C, indicating cleavage of covalent bonds (Table 4-1).

Besides the thermal properties, sol-gel analysis was used to study the light-induced changes in the solubility properties. It is interesting to note that the cleavage of PDMS-**1** was superior not only by alkaline hydrolysis but also by photolysis. In the case of PDMS-**2** and PDMS-**3,** the sol fraction did not exceed 5%, whilst in the case of PDMS-1, with a sol fraction of 67%, the photocleavage was considerably more effective
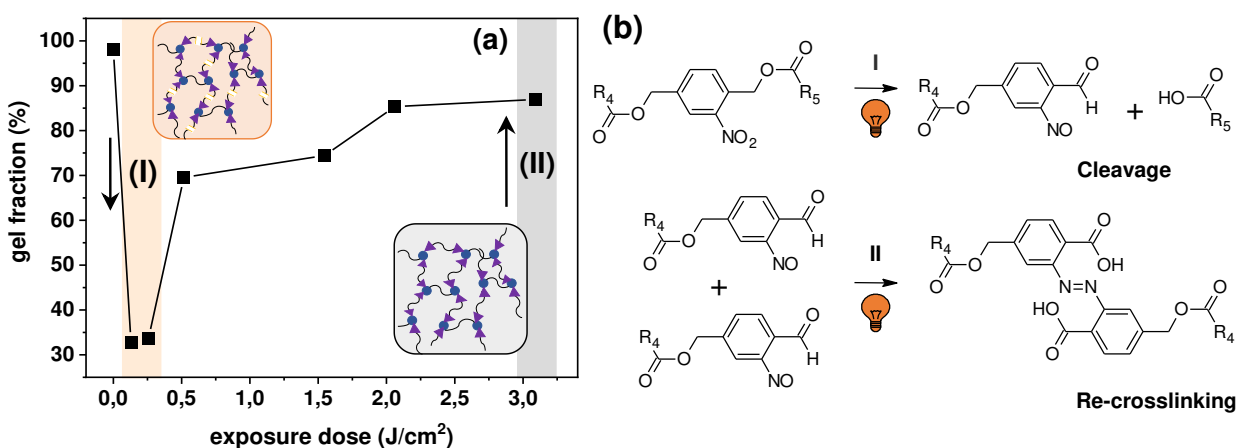
**Figure 4-8 (**a) Normalized gel fraction of PDMS-**1** as a function of the irradiation time (51.55 mW/cm$^2$, $\lambda$ < 400 nm, N$_2$) as obtained from FT-IR measurements. The line is a guide for the eye. Area I and II highlight the exposure time applied for the preparation of positive- and negative-tone micropatterns, respectively. (b) Proposed photoreactions that occur upon (I) 5 and (II) 60 s of UV exposure (51.55 mW/cm$^2$, $\lambda$ < 400 nm, N$_2$) as derived from sol gel analysis [247]

Since PDMS-**1** and PDMS-**2** have similar crosslinking densities (due to the equal content of the bifunctional epoxy-**NBE**), the superior cleavage in the PDMS-**1** network might be explained by differences in network structure (dangling chain ends in PDMS-**1**) and molecular weight between crosslinking points (lower molecular weight between two crosslinking points in PDMS-**1**).

Interestingly, during the photoinduced degradation of PDMS-**1** the ratio between the gel fraction and the exposure time followed the same trend as previously observed for photocleavable polyether networks. [267] In particular, the gel fraction underwent three different regimes. In the first step after UV irradiation, a characteristic decrease in the gel fraction from 98% to 33% at 0.13 J cm$^{-2}$ was observed. Even when the UV dose was increased from 0.13 J cm$^{-2}$ to 0.26 J cm$^{-2}$, the gel fraction did not decrease and remained at 34%. However, the gel fraction gradually increased when the UV dose exceeded 0.26 J cm$^{-2}$, and the gel fraction reached 87% at 3.1 J cm$^{-2}$ of UV exposure. The dual-responsive PDMS network was found to be susceptible to side reactions and the crosslinks in the network were regenerated by prolonged UV irradiation. In particular, it

was found that the dimerization of secondary photoproducts, such as azobenzene derivatives, were responsible for the increase in the gel fraction after prolonged irradiation In contrast to classical hydrolysis, photodegradation of the dual-response PDMS networks enabled spatial control of solubility properties, which is demonstrated by photolithographic patterning. In this experiment, thin films of PDMS-**1** were spin-cast onto Si wafers and thermally cured. Positive-tone relief structures were then inscribed in the cured elastomeric film by photolithography with a quartz-chromium mask. The exposed areas became partially soluble by photocleavage of the PDMS network, whilst the non-exposed areas remained insoluble and were not removed by development in chloroform [Figure 4-9 (a)]. After the development step, the inscribed relief structures were studied by confocal microscopy [Figure 4-9 (b,c)]. The micrographs showed that the relief structure, with a structure size of 100 µm, can be conveniently inscribed in the PDMS-**1** network.
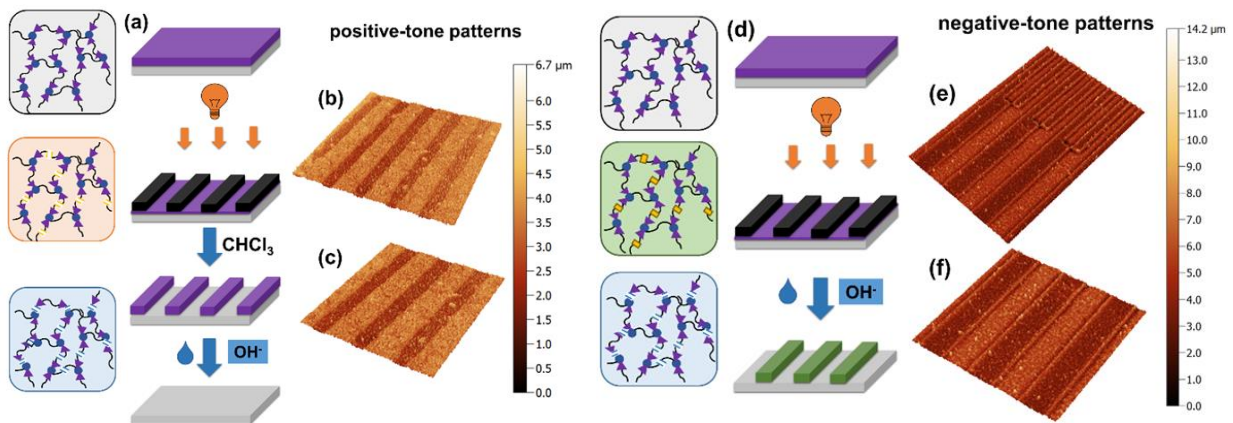


**Figure 4-9** (a) Schematic representation of the formation of positive-tone resist and subsequent removal of the resist by hydrolytic degradation of the PDMS network. (b and c) Confocal micrographs of positive-tone relief structures (100 µm lines and spaces) inscribed into PDMS-**1** by photolithography after the development in chloroform. (d) Schematic representation of the formation of negative-tone resists (e and f) Confocal micrographs of negative-tone relief structures (50 and 100 µm lines and spaces) inscribed into PDMS-**1** by photolithography after the development in 1 M aqueous NaOH. [247]

### 4.1.4 Conclusion to the study on dual-responsive polydimethylsiloxane networks

The dual responsive nature of the networks makes it an interesting candidate for microelectronics applications as the relief structures can be completely degraded by exposure to alkaline media in later steps. In addition to the positive-tone structures, the dual-responsive nature allows the fabrication of negative-tone structures. In particular, re-crosslinking of the PDMS network at higher exposure doses can be used to change the solubility of the network in the exposed areas. It is well known that nitrosobenzaldehyde is formed as the primary photoproduct by the cleavage of $o$-NBE links and is highly reactive and undergoes a secondary photoreaction. [266] Upon longer irradiation times, the nitroso species dimerize and form azobenzene groups. This reaction, along with other side reactions, leads to recrosslinking within the PDMS network, as confirmed by sol-gel analysis (Figure 4-8a). The hydrolysis-sensitive ester groups of the $o$-NBE links are converted into crosslinks with a higher stability in alkaline media (e.g., azobenzene groups). Thus, this crosslinking can be used to inscribe negative-tone patterns in the PDMS network. In this alternative approach, the development step is carried out, using an aqueous NaOH solution, which degrades the PDMS-**1** network in the unexposed area, while the exposed area (the re-crosslinked PDMS-**1** network) remains insoluble [Figure 4-9 (d)]. Confocal micrographs images of the inscribed negative tone micropatterns [Figure 4-9 (e,f)] confirm that this strategy is feasible.Comparing the two different cleavage routes in the dual-responsive PDMS network, it can be concluded that the hydrolytic network degradation benefits from high efficiency, is not limited by the film thickness and provides temporary control by adjusting the pH value of the medium.

In contrast, the photocleavage process does not lead to complete degradation of the network and is due to its nature limited to the film thickness in the micrometer range where UV light can penetrate. Nevertheless, photocleavage occurs rapidly, within seconds, and the spatial control of the cleavage process allows the elastomeric film to be inscribed with a well-defined positive relief structures. Based on the dual-responsive nature of the developed material, the two cleavage processes can be combined. This facilitates the formation of surface patterned PDMS materials, which can be fully degraded in an aqueous alkaline mdedium. In addition, by further utilizing photo-induced side reactions, it is possible to achieve a dual tone resists that switches between negative- and positive-tone structures by controlling the exposure and solvent in the development phase.

## 4.2 Photopatternable epoxy-based thermosets

The data and results given in this section have been published in "Materials" under the title "*Photopatternable Epoxy-Based* Thermosets", Volume 12, Issue 15, July 2019. Most of the following text, tables and figures have been taken from the respective publication. [246]
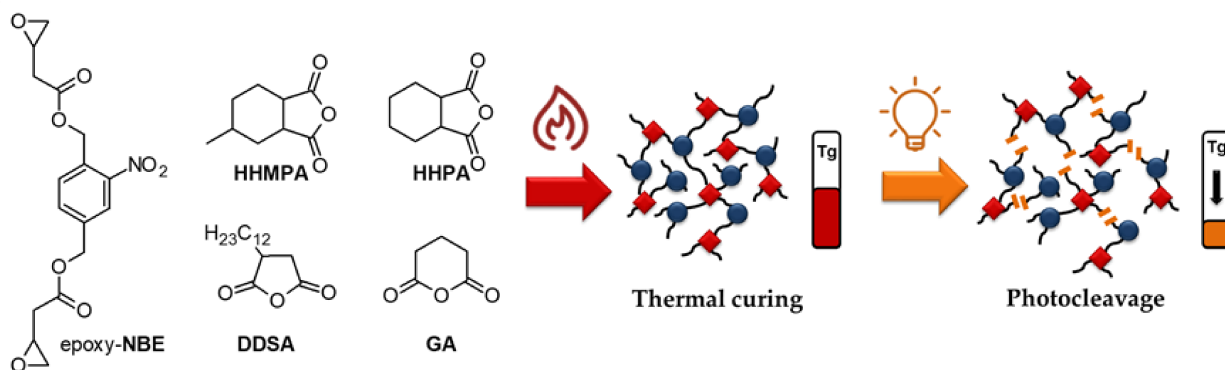


**Figure 4-10** Epoxy-NBE as photosensitive epoxy-based monomer and cycloaliphatic dicarboxylic acid anhydrides used in the preparation of photopatternable thermosets [246]

In this study, *o*-NBE chemistry was employed to produce positive-tone photoresists by controlled degradation of thermally cured epoxy-based networks upon UV irradiation. [93,267] Photosensitive links allowed the spatially controlled degradation of the covalent polymer networks when exposed to UV irradiation, enabling a switch in terms of solubility and thermomechanical properties. Photosensitive networks were prepared by thermal curing in the presence of anhydride hardeners and *o*-NBE derivatives with terminal epoxy groups. The aim of this work is to establish structure-property relationships between network composition and material properties (before and after photocleavage) to improve the performance of the photo-sensitive networks (Figure 4-10). By varying the anhydride hardener, networks with glass transition temperatures ranging from 16 to 72°C were obtained. The results revealed that the differences in network mobility significantly affect the efficiency of the cleavage reaction, the formation of soluble species, and, thus, the contrast curve of respective positive tone photoresists

### 4.2.1 Thermal curing of photopatternable epoxy-based thermosets

Photopatternable thermosets were prepared by thermal curing of epoxy-**NBE** with selected cycloaliphatic anhydrides (Figure 4-10). In order to reduce the curing reaction time and temperature, tertiary amines were added as accelerators. The accelerated curing mechanism follows the ring opening reaction of anhydrides by the amine under the formation of betaines. [268] The internal salt provides the carboxylate ions, which initiates the curing reaction to form the alkoxide ester with the epoxy group. Once formed, the alkoxide esters react with further anhydride groups to form carboxylate anion functional esters. They are able to open the epoxide moieties, leading to the perpetuation of the ring-opening reaction.
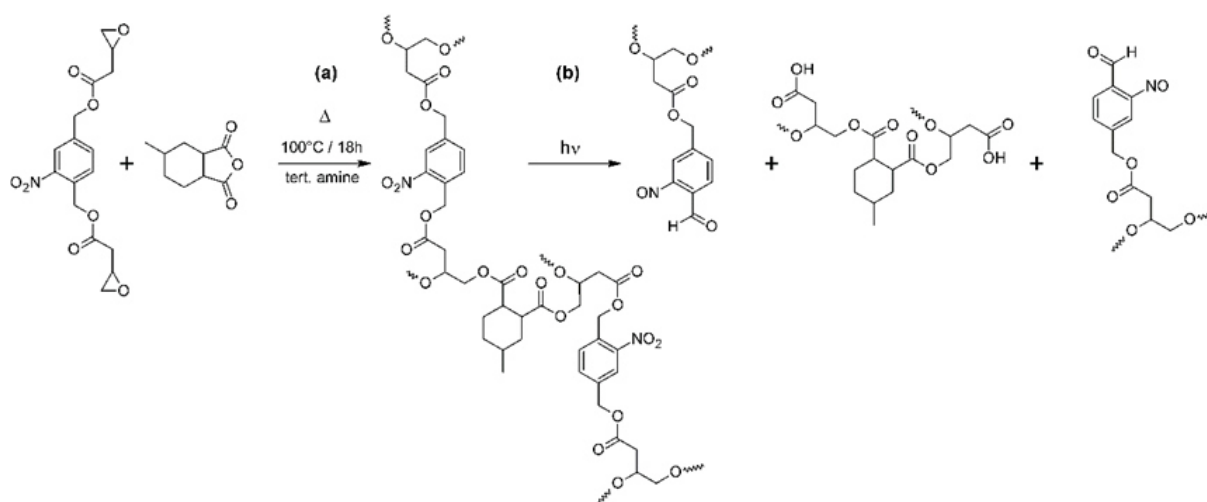


**Figure 4-11** (a) Thermal curing and (b) photocleavage of epoxy-based thermosets with photosensitive *o*-NBE links [246]

To determine the cure kinetics, resin formulations were drop-cast between a CaF$_2$ disc and a Si wafer. Figure 4-12a shows the FT-IR spectra of the epoxy-**NBE**/HHPA epoxy resin prior to and after thermal curing at 100 °C. In the cured state, the two carbonyl peaks (1860 and 1778 cm$^{-1}$) related to the anhydride group disappeared and a new band associated with the carbonyl group of the ester bond appeared at 1740 cm$^{-1}$. The epoxide peak at 910 cm$^{-1}$ disappeared, confirming the successful network formation by the nucleophilic ring-opening reaction.
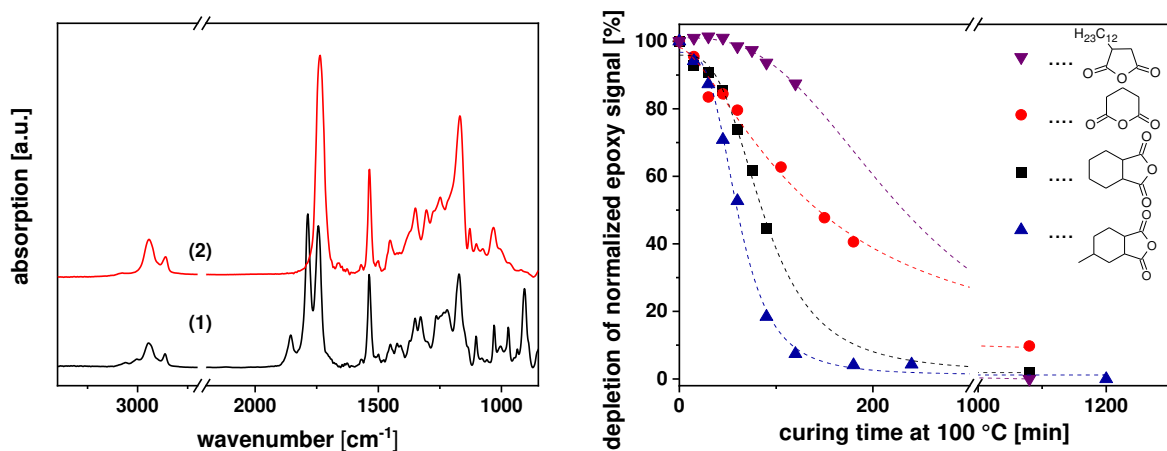
**Figure 4-12** (a) Fourier transform infrared (FT-IR) spectra of epoxy-**NBE**/HHPA (1) prior to and (2) after thermal curing at 100 °C. (b) Influence of the anhydride structure on the cure kinetics of photopatternable epoxy-based thermosets by following the normalized depletion of the peak area between 910 and 928 cm$^{-1}$. Thermal curing was performed at 100 °C. The lines are a guide for the eye. [246]

Similar observations were made for the other epoxy-anhydride formulations studied (see Figure 4-13).
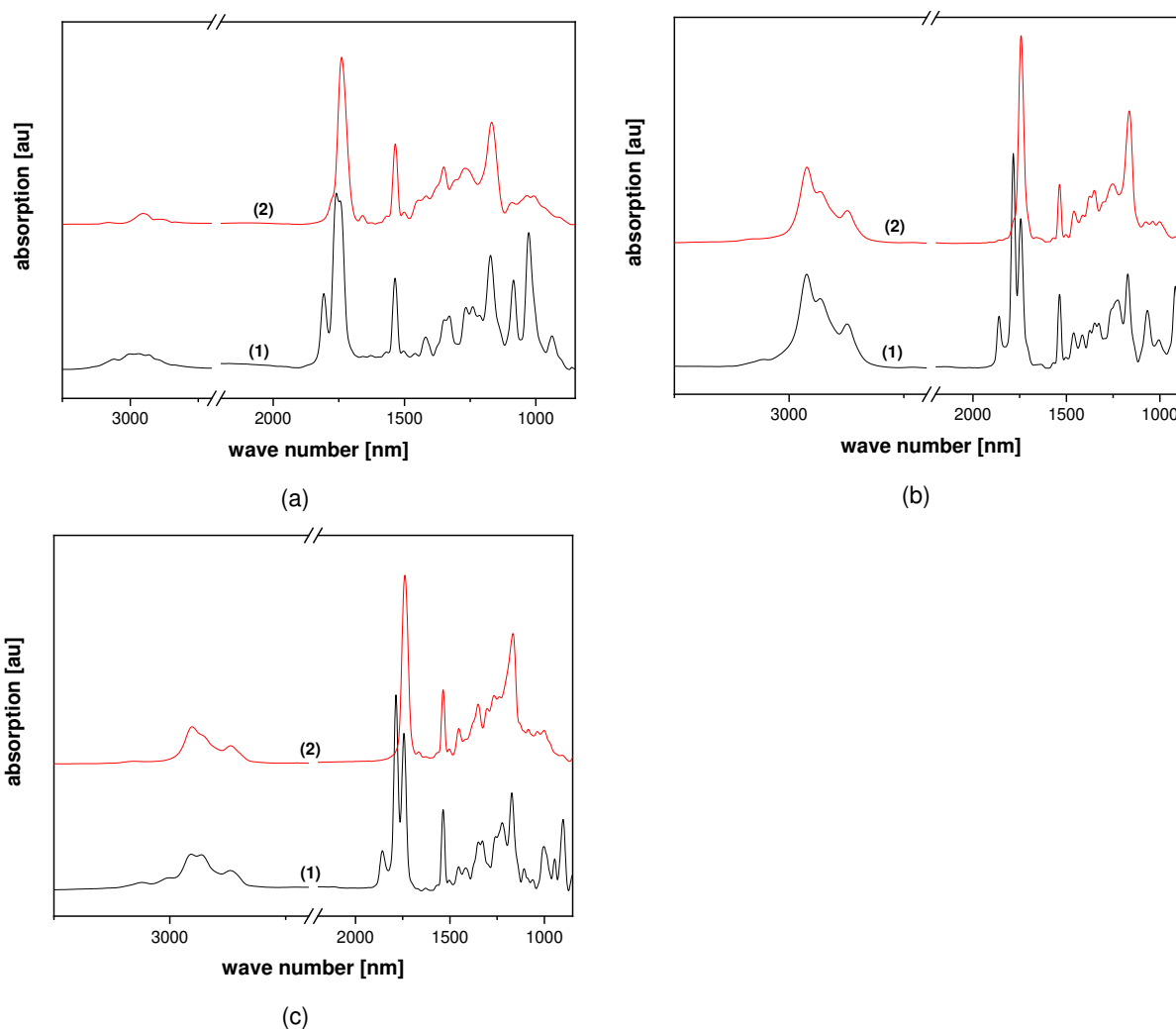
**Figure 4-13** FT-IR spectra of (a) epoxy-NBE/GA, (b) epoxy-NBE/DDSA and (c) epoxy-**NBE**/HHMPA (1) prior to after thermal curing at 100 °C. [246]

In order to investigate the effect of anhydride structures on the curing kinetics of the epoxy resin, the depletion of the epoxy peak at 910 cm$^{-1}$ was followed upon curing at 100 °C (Figure 4-12b). Since this epoxy band partially overlaps with the absorption band of the anhydride group at 920 cm$^{-1}$, the depletion of both signals was monitored. The results show that the curing rate decreases in the order HHMPA>HHPA>GA>DDSA. Almost complete conversion for HHMPA was observed after 180 min of curing. However, extended curing (> 1000 min) is necessary for both GA and DDSA to achieve > 90% conversion. The long alkyl chains in its structure may explain the low reactivity of DDSA. On the one hand, it may reduce the acidity of the anhydride group, and on the other hand, it may inhibit the reaction by steric action. For nonyl succinic anhydride, similar behavior was observed in the non-catalyzed cyclic ring-opening of epoxy resins. [269]

In contrast, the lower reactivity of GA compared to HHMPA and HHPA may be related to the higher stability of the six-membered ring system (lower ring strain). Previous studies on the ring-opening copolymerisation of epoxides and anhydrides have shown that a low ring strain (either epoxide or anhydride) results in lower reactivity of the monomer and lower molecular weight products. [270,271]

In addition to the curing kinetics, the anhydride structure also affects the thermo-mechanical properties and surface hardness, as shown in Table 4-2. DSC measurements demonstrate that the more rigid anhydrides (HHMPA and HHPA) produce networks with a $T_g$ of 72 and 46°C, respectively. In contrast, the epoxy-**NBE**/GA network exhibits a $T_g$ below room temperature, which is attributed to the flexibility of the anhydride in the open state. In contrast, curing with DDSA results in a $T_g$ that is slightly lower than that of the epoxy-**NBE**/HHPA system (44 °C). DDSA cured epoxy thermosets with $T_g$s in the range of 40 °C have also been reported by Webster and Pan, who established structure-property relationships for epoxy resins derived from renewable resources. [272]

The indentation hardness ($H_{IT}$) of the studied resins correlates well with the corresponding $T_g$ values and increases in the order GA>DDSA>HHPA>HMPA. Depending on the anhydride structure, the surface hardness varied by more than three orders of magnitude, ranging from soft epoxy-**NBE**/GA systems with a surface hardness of 8.6 ± 0.8 MPa to hard epoxy **NBE**/HHMPA systems with a surface hardness of 213.5 ± 19.8 MPa.

**Table 4-2** Glass transition temperature ($T_g$) and indentation hardness ($H_{IT}$) of cured photopatternable epoxy-based thermosets prior to and after UV exposure (74.5 mW cm$^{-2}$). [246]

| Resin formulation | $T_g$ [°C] | $H_{IT}$ [MPa] | $T_g$ [°C] | $H_{IT}$ [MPa] |
|---|---|---|---|---|
| | thermally cured | | photocleaved | |
| epoxy-**NBE**/HHMPA | 72 | 213.5 ± 19.8 | 48 | 110.9 ± 10.3 |
| epoxy-**NBE**/HHPA | 46 | 148.6 ± 13.8 | 32 | 83.0 ± 6.3 |
| epoxy-**NBE**/DDSA | 44 | 51.0 ± 4.7 | 30 | 41.3 ± 3.8 |
| epoxy-**NBE**/GA | 16 | 8.6 ± 0.8 | 12 | 1.3 ± 0.1 |

## 4.2.2 Photocleavage of photopatternable epoxy-based thermosets

The photocleavage of the epoxy-based networks was then monitored in the cured film. The film was drop-cast between a CaF$_2$ disc and a Si wafer. The samples were exposed with UV light at wavelengths below 400 nm to induce a cleavage reaction of the *o*-NBE links. As described in the previous section, during ester photolysis, nitroso compounds

and carboxylic acids are usually generated as primary cleavage products (Figure 4-11). [273] In this study, cleavage was monitored by the depletion of two characteristic $NO_2$ signals at 1537 $cm^{-1}$ and 1348 $cm^{-1}$ (conversion of nitro groups to nitroso groups). The corresponding spectra are shown in Figure 4-14. Furthermore, a characteristic broadening of the C=O absorption band (1646-1830 $cm^{-1}$) was observed, which is associated with the formation of carboxylic acids and other carbonyl-based cleavage products.
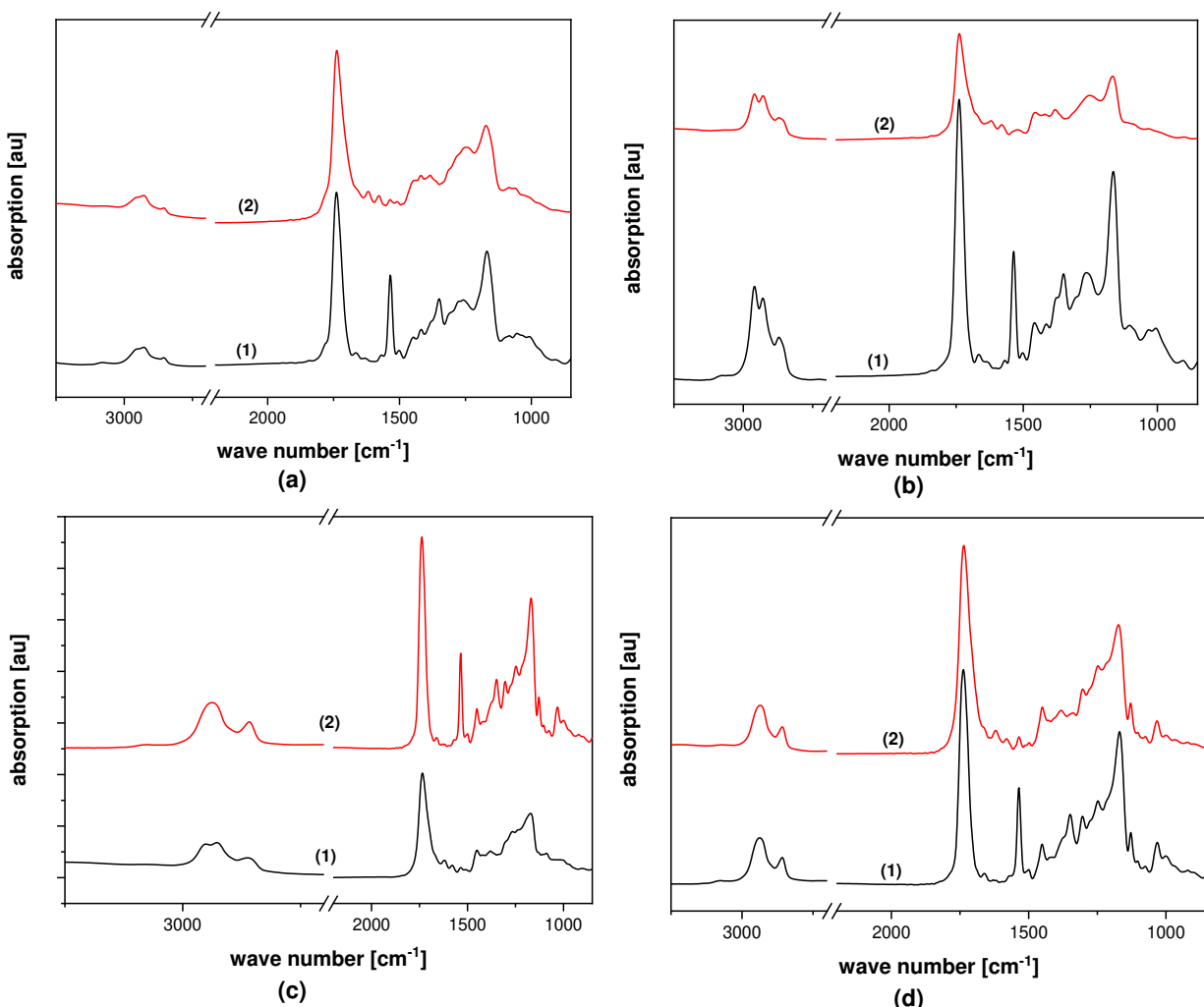


**Figure 4-14** FT-IR spectra of (a) epoxy-**NBE**/GA, (b) epoxy-**NBE**/DDSA and (c) epoxy-NBE/HHMPA and and (d) epoxy-**NBE**/HHPA (1) prior to and (2) after photocleavage (74.5 mW $cm^{-2}$). [246]

The cleavage kinetics was determined as a function of the employed anhydride by following the depletion of the absorption band at 1537 $cm^{-1}$ upon prolonged UV irradiation (Figure 4-15). For the epoxy-**NBE**/GA network, which had a low $T_g$, a rapid decrease in the nitro absorption band was observed. However, it is interesting to note that the $T_g$ of the epoxy-**NBE**/HHPA and epoxy-**NBE**/DDSA networks above room temperature (46 °C

and 44 °C, respectively) showed comparable cleavage ratios to the epoxy-**NBE**/GA system. This may be due to the sample's surface temperature, which increases to 38-40 °C during UV exposure. As a result, the UV exposure was carried out above or close to the $T_g$, which provides high network mobility and may result in comparable cleavage kinetics.
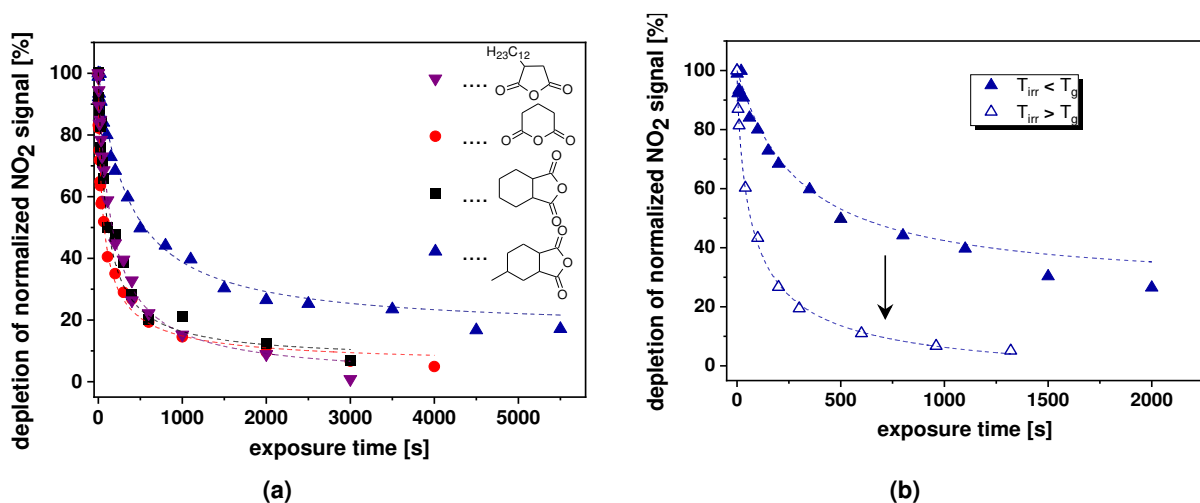


**Figure 4-15** (a) Cleavage kinetics of photopatternable epoxy-based thermosets versus anhydride structure. The normalized depletion of the nitro groups (at 1537 cm$^{-1}$) is followed upon prolonged UV irradiation (74.5 mW cm$^{-2}$). The lines are a guide for the eye. (b) Normalized depletion of the nitro groups (at 1537 cm$^{-1}$) in epoxy-**NBE**/HHMPA networks as a function of the reaction temperature: (full triangles) no additional heating of the sample during UV exposure ($T_{irr} < T_g$) and (open triangles) simultaneous heating of the sample to 80 °C ($T_{irr} > T_g$). The lines are a guide for the eye. [246]

In contrast, the high $T_g$ network (72 °C) the epoxy-**NBE**/HHMPA network had a lower cleavage rate due to the lower mobility of the chromophore under irradiation conditions. This can be easily overcome by simultaneously heating the sample to 80 °C ($T_{irr} > T_g$) during UV exposure. As shown in Figure 4-15b, the higher temperature accelerates the cleavage rate and results in higher nitro group conversion, confirming that the mobility of the network plays an important role in the cleavage kinetics. The photo-induced degradation of the network does not only decrease the $T_g$ but also the surface hardness (Table 2-1). The optically induced changes in material properties are more pronounced in networks containing rigid anhydrides such as HHMPA or HHPA. In particular, in the epoxy-**NBE**/HHMPA system, the $T_g$ decreases from 72 to 48 °C, whereas in the epoxy-**NBE**/GA

network the change in $T_g$ does not exceed 4 °C. A similar trend was observed for surface hardness.

In a further experiment, the influence of simultaneous heating was studied by measuring the surface hardness of the high-$T_g$ network epoxy-**NBE**/HHMPA as a function of the reaction temperature. Without additional heating, the surface hardness is almost halved due to the UV degradation of the network and the $H_{IT}$ value decreases from 213.5±19.8 to 110.9±10.3 MPa. Simultaneous heating of the samples to 50 °C or 70 °C reduces the $H_{IT}$ values to 40.6±3.8 MPa and 29.1 ±2.7 MPa, respectively. From the results obtained, it can be concluded that the cleavage of the $o$-NBE linkages contributes to the degradation of the network. In addition, the efficiency can be significantly improved by increasing the reaction temperature, thus increasing the mobility of the thermosets.

### 4.2.3  Photopatterning studies

For the successful positive-tone pattering of the epoxy-based networks, the photo-induced formation of soluble species is crucial. Therefore, sol-gel analysis was carried out on thin cured resins, which were irradiated with UV light at certain exposure doses and developed in tetrahydrofuran. The insoluble fractions were then determined by quantitative FT-IR spectroscopy. Figure 4-16a-d shows the gel fractions of the four thermosets versus exposure time.
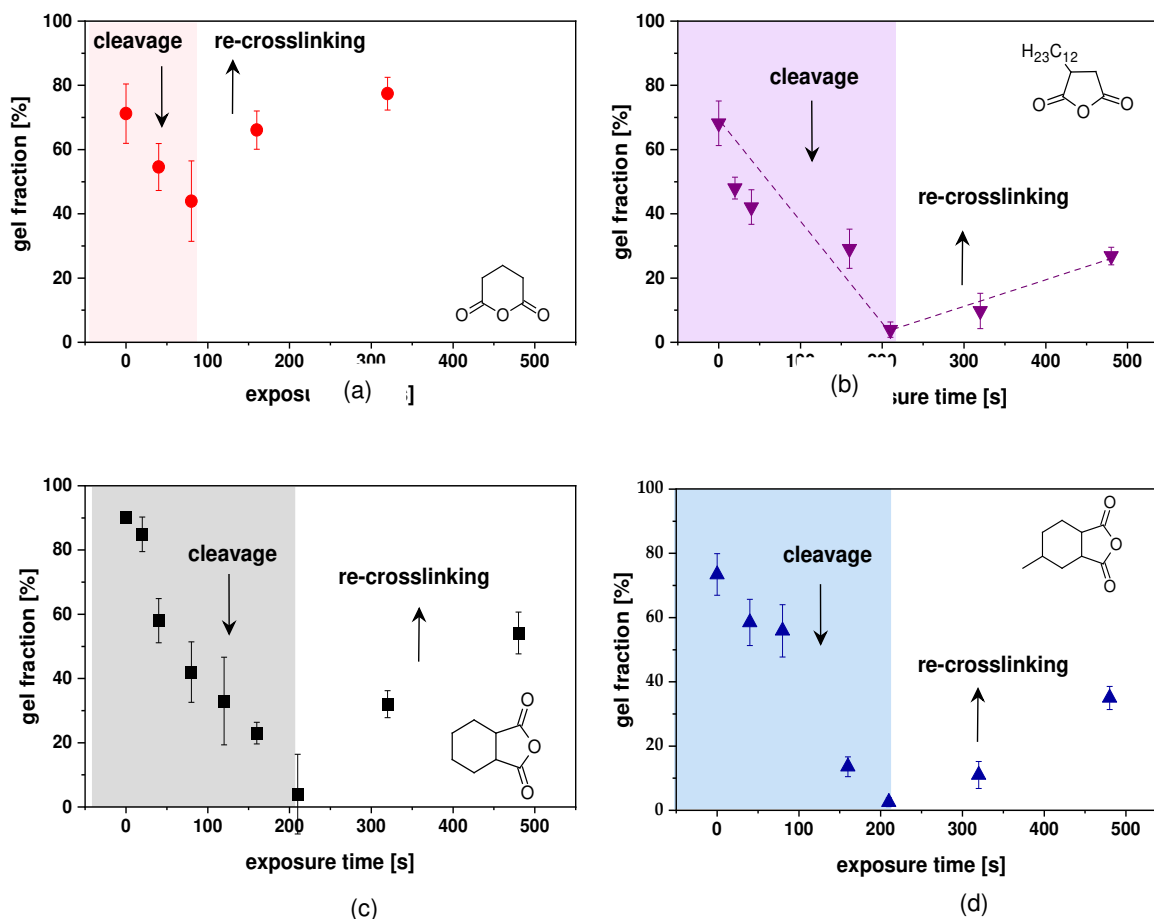
**Figure 4-16** Gel fraction of (a) epoxy-NBE/GA, (b) epoxy-NBE/DDSA, (c) epoxy-NBE/HHPA and (d) epoxy-NBE/HHMPA versus exposure time (75 mW/cm$^2$) as derived from quantitative FT-IR measurements. [246]

Epoxy-**NBE**/GA, epoxy-**NBE**/DSSA and epoxy-**NBE**/HHPA networks were characterized by comparable cleavage rates and yields (Figure 4-12a), but their ability to form soluble cleavage products was significantly different. For epoxy networks with low $T_g$, the gel fraction gradually decreases with increasing UV exposure to 42% of the minimum value (Figure 4-16a). With further increase in exposure time, the gel fraction increases, which is due to the reformation of covalent bonding. Previous studies have shown that secondary cleavage products are readily formed in highly mobile polymer networks (e.g. formation of azobenzene moieties), leading to a re-crosslinking of the networks. [267,273] On the other hand, epoxy-**NBE**/DDSA networks with a $T_g$ above room temperature dissolve completely after exposure for 200 s (Figure 4-16). Re-crosslinking of the cleaved polymer chains was again observed upon prolonged exposure to UV light (> 200 s). Networks with rigid anhydride network showed similar behavior (Figure 4-17c, d). This result confirms that the

mobile *o*-NBE network is more prone to side reactions than the rigid network. This correlates well with UV-induced changes in surface hardness and $T_g$, which are less pronounced in the flexible networks. A similar behavior has been observed in recent studies of photocleavable thiol-ene, thiol-ene and polydimethylsiloxane networks, which have a $T_g$ below room temperature and are very sensitive to crosslinking by secondary photoreactions. [92,103]



(a)                         (b)

(c)                         (d)
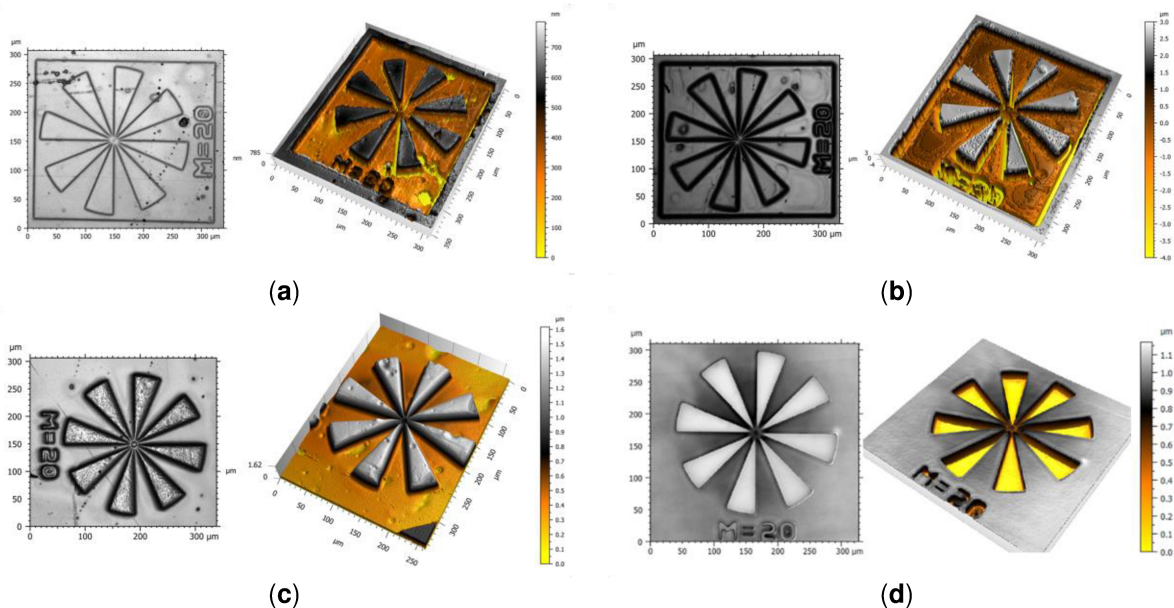
**Figure 4-17** Micrographs and surface profiles of photopatterned (a) epoxy-**NBE**/GA, (b) epoxy-**NBE**/DDSA, (c) epoxy-**NBE**/HHPA, and (d) epoxy-**NBE**/HHMPA systems as obtained from interference microscopy. [246]

**Table 4-3** Characteristics of positive tone photoresists based on photocleavable epoxy-based thermosets [246]

| Resin formulation | $D_0$ [J/cm$^2$] | $D_{100}$ [J/cm$^2$] | $\gamma$ | Resolution [µm] |
|---|---|---|---|---|
| epoxy-**NBE**/HHMPA | 16.3 | 2.27 | 1.17 | 8 |
| epoxy-**NBE**/HHPA | 19.5 | 0.26 | 0.53 | > 10 |
| epoxy-**NBE**/DDSA | 19.7 | 0.25 | 0.53 | > 10 |

Although the epoxy-**NBE**/GA resin system suffers from incomplete network degradation, the formation of soluble products is sufficiently efficient to allow inscribe positive-tone relief structures by mask lithography (Figure 4-17a). For the other three resin systems, which are completely soluble upon UV irradiation, characteristic photoresist properties such as contrast and resolution were determined (Table 4-3). Contrast is a measure of the change in resist solubility upon UV irradiation, and the contrast curve was determined by plotting

the gel fraction (corresponding to the thickness of the resist layer after the development step) as a logarithmic function of the irradiation dose (Figure 4-18a,b). The contrast (γ) was calculated using the equation 2-7 on page 33.

The contrast curves show that the exposure doses reaching full solubility ($D_{100}$) are in a similar range for the three networks studied. However, the $D_0$ values of the epoxy-**NBE**/HHMPA systems were significantly lower than those of the epoxy-**NBE**/DDSA and epoxy-**NBE**/HHPA networks, resulting in a higher contrast (1.17 versus 0.53). Topographic images of the positive tone patterns inscribed in epoxy-**NBE**/DDSA and epoxy-**NBE**/HHPA as well as in the epoxy-**NBE**/HHMPA system are shown in Figure 4-18 b-d. No significant swelling was observed in the crosslinked areas, while the exposed areas facilitated rapid development.



(a)                                                                 (b)
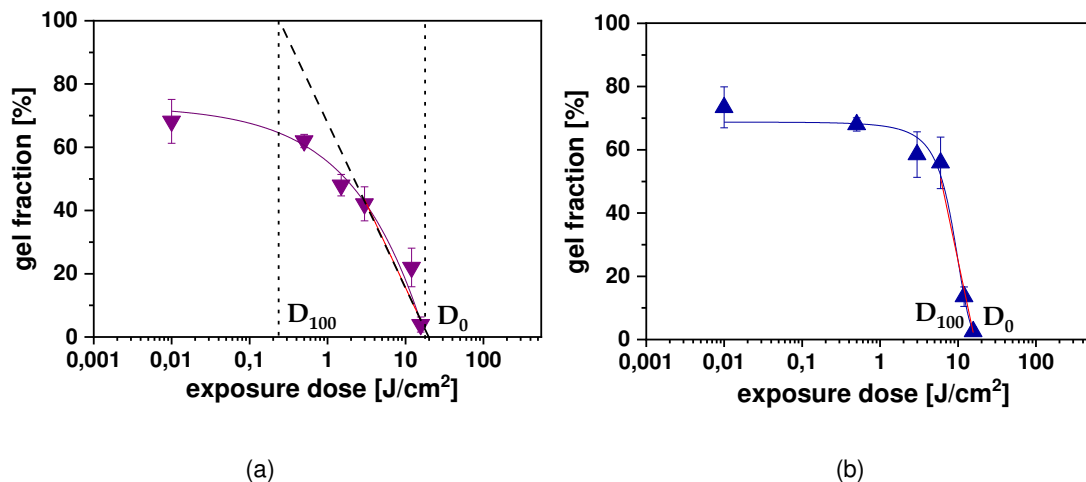
**Figure 4-18** Contrast curves of (a) epoxy-**NBE**/DDSA and (b) epoxy-**NBE**/HHMPA networks and calculation of the contrast (γ) from the slope of the linear area (dashed line) of the curve by extrapolating it to a gel content of 0% ($D_0$) and 100% ($D_{100}$), respectively. [246]

In the next step, the resolution was determined by pursuing a classical approach with patterns comprising lines and spaces with varying widths and by investigating the polymer patterns after the development step. For epoxy-**NBE**/HHMPA networks, separate lines and spaces of the positive- tone patterns were observed until a pattern width of 8 µm was reached. In contrast, the epoxy-**NBE**/HHPA and epoxy-**NBE**/DDSA networks were characterized by a lower resolution (>10 µm). This correlates well with the low contrast observed in these two thermosets. Furthermore, it should be noted that the contrast is

lower than that of resists used in the microelectronics industry. However, the photo-induced conversion of an insoluble thermoset to soluble cleavage products paves the way toward a versatile and convenient micropatterning of epoxy-based duromers.

### 4.2.4  Conclusion to the study on photopatternable epoxy-based thermosets

Structure–property relationships of photopatternable epoxy-based thermosets were established, showing the important role of network structure and network mobility on the cleavage kinetics, material properties, and related patterning performance of the photosensitive networks. The network mobility of the thermosets was tuned by changing the anhydride hardener or increasing the temperature during UV exposure. In addition to the curing kinetics, the anhydride hardener affects material properties such as $T_g$ and surface hardness. In particular, low $T_g$ (16 °C) networks (epoxy-**NBE**/GA) and high $T_g$ (72 °C) networks (epoxy **NBE**/HHMPA) were obtained. The mobility of the networks strongly affected the photocleavage of *o*-NBE linkages. The high $T_g$ network is characterized by a low cleavage rate, which can easily be overcome by heating the network above its $T_g$ during UV irradiation. However, sol-gel analysis shows that the flexible networks are prone to secondary photoreactions. These side reactions lead to a re-crosslinking of the network and incomplete formation of soluble species. On the other hand, networks with $T_g$ above room temperature became completely soluble by photolysis of the *o*-NBE chromophores. Thus, networks with high $T_g$ suffer from low cleavage rates, but can benefit from better patterning performance. In particular, the epoxy-**NBE**/HHMPA system achieved a resolution of 8 µm and a contrast of 1.17 without optimization.

## 4.3 Photopatternable and rewritable epoxy-anhydride vitrimers

The data and results given in this section have been published in "Macromolecular Rapid Communications" under the title "*Photopatternable and Rewritable Epoxy-Anhydride Vitrimers*", Volume 42, Issue 2, 2021. Most of the following text, tables and figures have been taken from the respective publication. [249]
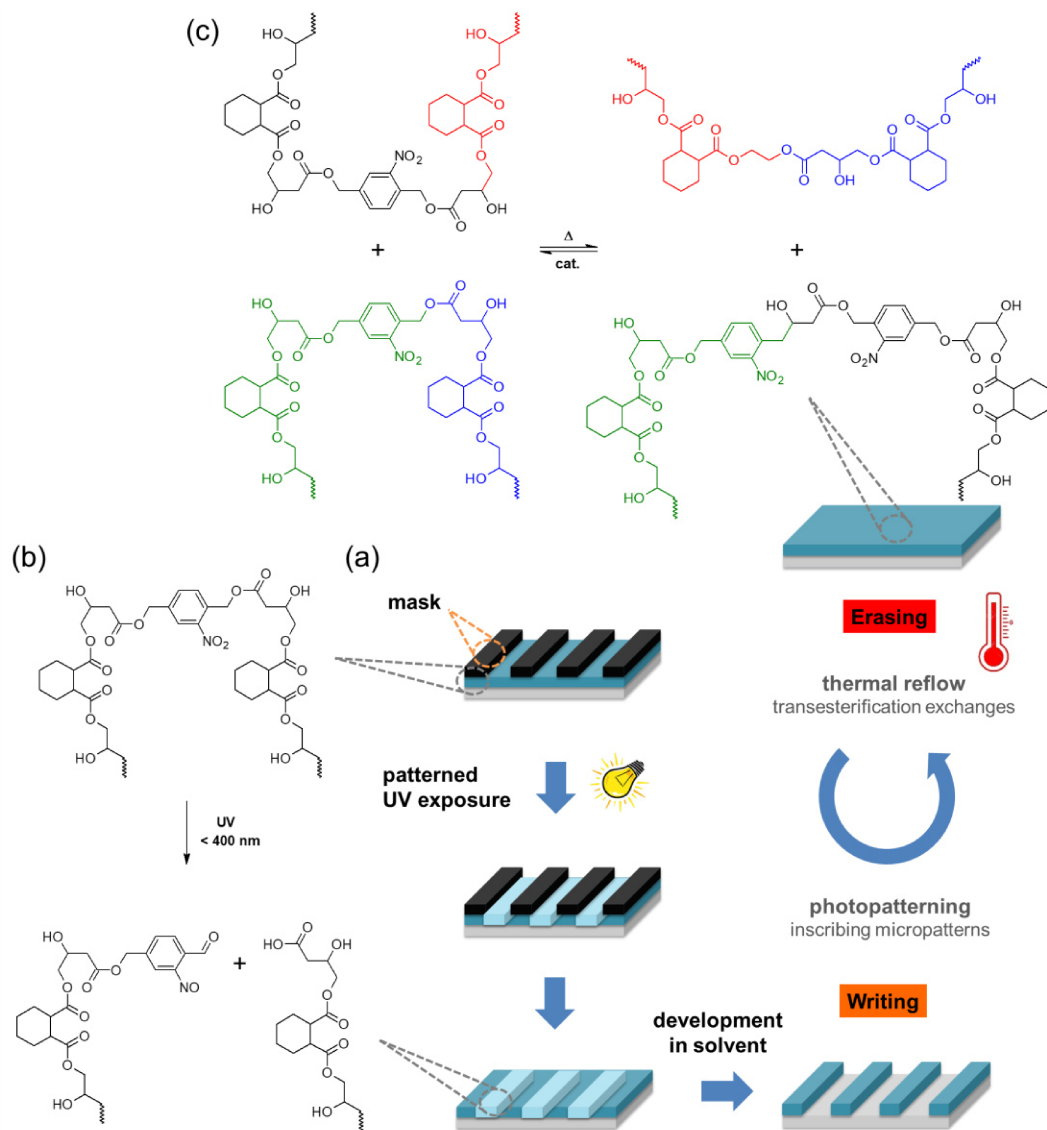


**Figure 4-19** Schematic representation of writing, erasing, and rewriting microstructures in photosensitive epoxy-anhydride vitrimers. a) The photopatterning was carried out by photolithography in contact mode using a quartz mask. b) Soluble cleavage products were generated in the exposed areas of the film by spatially controlled photolysis of the *o*-NBE links, which were removed during the development step by dipping the test specimen in a mixture of tetrahydrofuran and ethanol (volume ratio was 1:1). c) The microstructures were erased due to the thermal reflow of the network induced by catalyzed bond exchange reactions of the hydroxyl ester moieties. [249]

Combining the concept of photocleavage enabled by the *o*-**NBE** moieties and the dynamic nature of covalent adaptable networks, this study presents an approach of writing, erasing and re-writable micropatterns in vitrimer networks. A thermoset consisting of epoxy-terminated *o*-nitrobenzyl ester and hexahydrophthalic anhydride derivatives and in the presence of 1,5,7-triazabicyclo[4.4.0]dec-5-ene (TBD) resulted in a dynamic covalent network whose solubility was locally controlled by exposure to UV light. Using photo-induced solubility changes, micropatterns were inscribed into thin films using photolithographic techniques to achieve 20 µm positive-tone structures. The thermally activated exchange reaction of hydroxyl ester bonds allows the polymer sample to be completely erased at high temperatures and the recovered film can be reused to inscribe new micropatterns.

### 4.3.1  Curing and cleavage kinetics

In the presence of an organic base (TBD), the nucleophilic ring-opening reaction of the epoxy monomer across the anhydride was sufficiently fast. FT-IR studies showed a maximum conversion of the epoxide group (910 cm$^{-1}$) at 70 °C after 2 hours. The FT-IR spectra prior to and after thermal curing are shown in Figure 4-201b. With the depletion of the epoxy groups, the C=O bands of anhydride groups (1860, 1778 cm$^{-1}$) decreased and the C=O ester band (1739 cm$^{-1}$) appeared. Furthermore, a characteristic –OH band (3376-3608 cm$^{-1}$) appeared confirming the formation of hydroxyl ester bonds. The network benefits from a high cure rate, as sol-gel analysis revealed a gel content well above 90%.
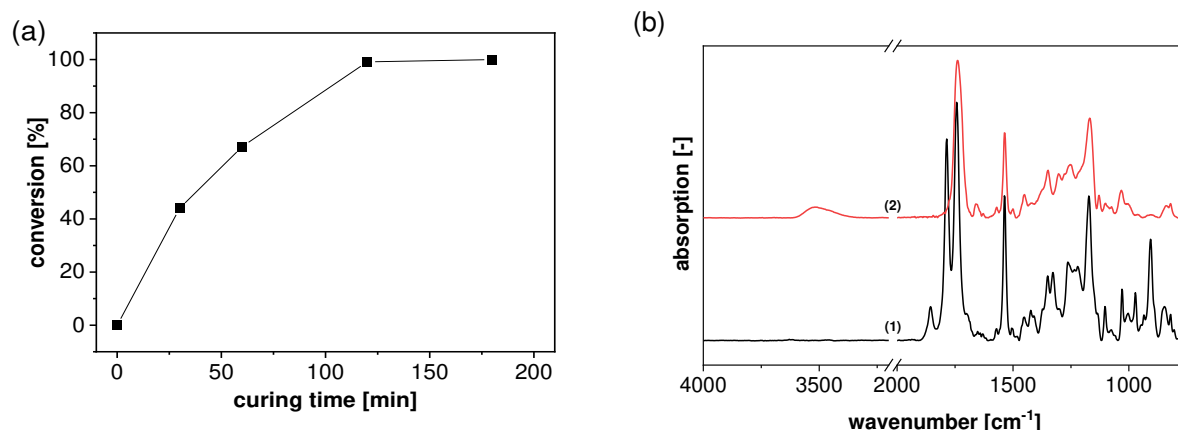
**Figure 4-20** (a) Cure kinetics of the photosensitive epoxy-anhydride vitrimer by following the normalized depletion of the peak area between 910 and 928 cm$^{-1}$. The lines are a guide for the eye. (b) FTIR spectra of the photosensitive epoxy-anhydride vitrimer (1) prior to and (2) after thermal curing at 70 °C. [249]

Light irradiation in the UVA spectral region lead to the cleavage of the *o*-NBE group and its conversion to nitroso compounds and carboxylic acid groups. For the cleavage kinetics, the characteristic NO$_2$ signal at 1537 cm$^{-1}$ was monitored by FT-IR. The photocleavage of the *o*-NBE bond results in a decrease of the NO$_2$ absorption band, and maximum conversion was obtained after 120 min exposure with UVA light (see Figure 4-21). As previously described, photocleavage of the *o*-NBE bond is directly related to the formation of soluble species, which in turn was used for the subsequent photopatterning step.
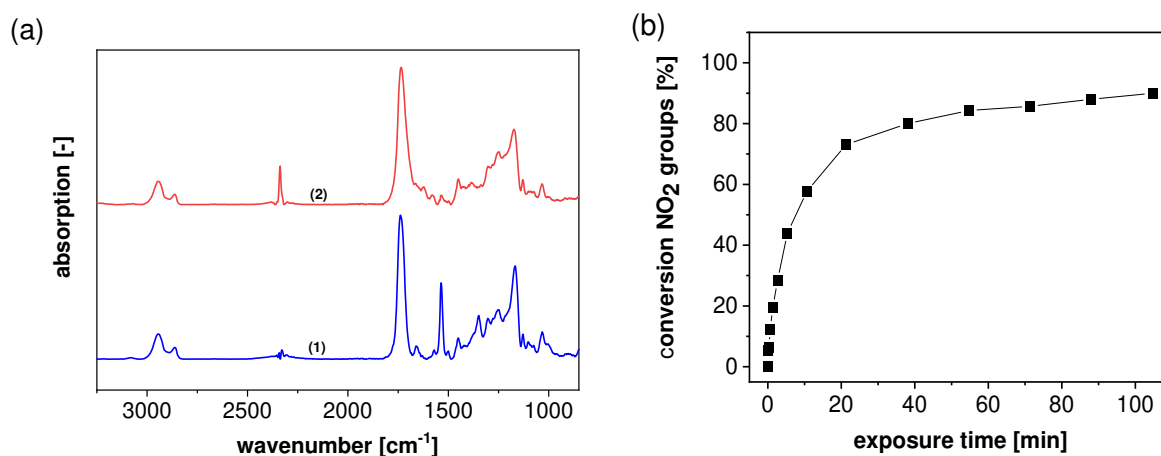


**Figure 4-21** (a) FT-IR spectra of the photosensitive epoxy-anhydride vitrimer prior to and after photocleavage (114 mW cm$^{-2}$). (b) Cleavage kinetics of the photosensitive epoxy-anhydride vitrimer. The normalized depletion of the nitro groups (at 1537 cm$^{-1}$) is followed upon prolonged UV irradiation (114 mW cm$^{-2}$). The lines are a guide for the eye. [249]

### 4.3.2 Sol-gel analysis and positive-tone pattering

The sol-gel analysis showed a gradual decrease in the insoluble fracture with increasing exposure dose (Figure 4-22). After 10 min of UV exposure, the network became fully soluble and positive-tone microstructures with a feature size of 20 μm were conveniently inscribed in thin drop-cast films of the epoxy-anhydride vitrimer by photolithography.
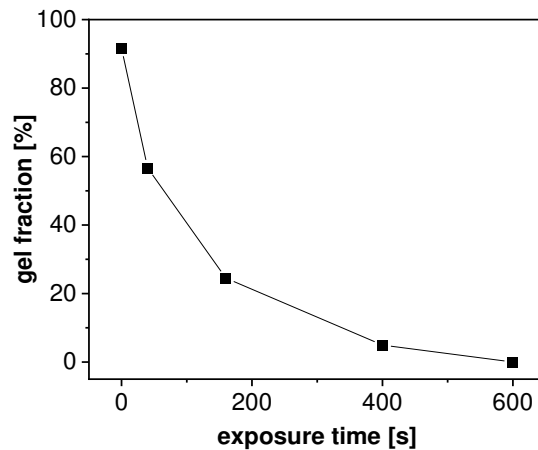


**Figure 4-22** Gel fraction of the photosensitive epoxy-anhydride vitrimer versus exposure time (114 mW/cm$^2$) as derived from quantitative FTIR measurements. The line is a guide for the eye. [249]

### 4.3.3 Thermo-mechanical properties

The cured network comprises a glass transition temperature (T$_g$) of 33 °C and is stable up to 180 °C as shown by dynamic scanning calorimetry (DSC) and thermal gravimetric analysis (TGA) measurements, respectively. The TGA is represented in the following figure:
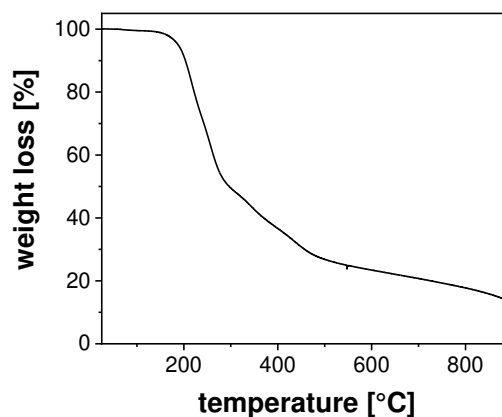


**Figure 4-23** TGA curve of the photosensitive epoxy-anhydride vitrimer. [249]

### 4.3.4 Stress-relaxation and self-healing ability of the network

The thermo-activated topology rearrangement of the network was determined by stress relaxation studies. Below $T_v$, the networks behave like thermosets since the exchange reaction rate is very slow and the dynamic bonds are essentially frozen. Increasing the temperature above $T_v$, the transition from an elastic solid to a viscoelastic liquid occurs. The viscosity gradually decreases with temperature and follows the Arrhenius law. Following the Maxwell model, the relaxation times ($\tau^*$) were determined as the time needed to relax to 1/e of the initial stress. Since the $\tau^*$ of vitrimers follows the Arrhenius law with the temperature, it can be expressed as $\tau_{(T)} = \tau_0 \exp(E_a/RT)$. $T_v$ values are obtained by extrapolation from the Arrhenius plot. [225] For more details regarding the calculation, see section 2.6.6. The measurements were carried out between 70 and 120 °C. In this temperature range, high mobility of the chain segments was ensured during the rheological experiments, as the studies were performed well above the network's $T_g$. The evolution of the relaxation modulus as a function of time and temperature is shown in Figure 4-24. The photosensitive network comprises a distinctive stress relaxation, whose rate increases with rising temperature.
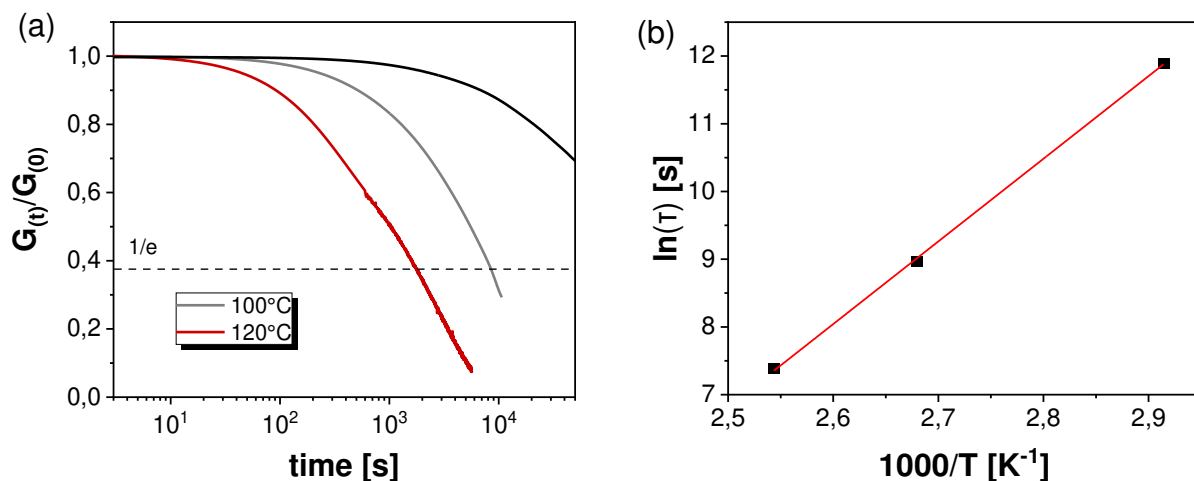


**Figure 4-24** a) Normalized stress relaxation curves of the photosensitive epoxy-anhydride network obtained at 70, 100, and 120 °C. b) Arrhenius plot derived from the measured relaxation times. [249]

The $T_v$ value was obtained by extrapolation from the Arrhenius plot and amounted to 49 °C (Figure 4-24b). It should be noted that the $T_v$ values of the catalyzed epoxy- anhydride vitrimers reported in the literature are usually in the range of 75-170 °C. [244] For photosensitive epoxy-anhydride vitrimers, the lower $T_v$ may by explained by the presence of the *o*-NBE groups, which are known to activate carboxyl groups. [274]

### 4.3.5  Writing and erasing of the microstructures

The thermo-activated macroscopic reflow of the epoxy-anhydride network leads to efficient healing and erasing of the micropatterns and the originally smooth surface morphology of the film is restored after thermal annealing at 120 °C for 24 h under vacuum (Figure 4-25b). Vacuum was applied to avoid oxidation reactions of the thin films during the healing process. Once healed, microstructures with a feature size of 20 μm were inscribed into the film by mask lithography again.
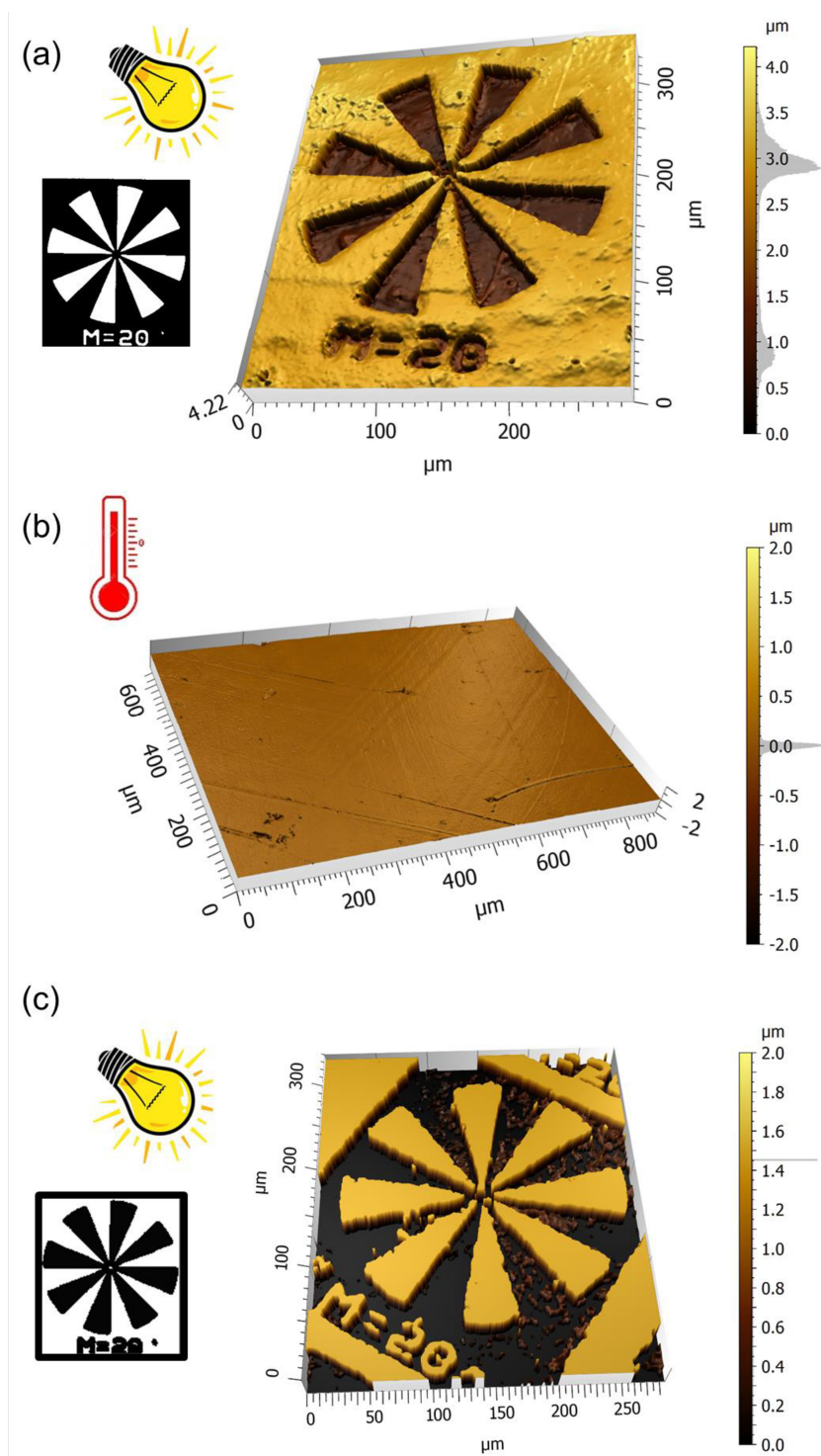
**Figure 4-25** Surface profiles from the photosensitive vitrimer after different treatments as obtained from interference microscopy: a) after the first photopatterning step and development in a mixture of tetrahydrofuran and ethanol (volume ratio was 1:1); b) after thermal annealing at 120 °C for 24 h under vacuum and c) after a second photopatterning (rewriting) step at the same region and development in a mixture of tetrahydrofuran and ethanol (volume ratio was 1:1) [249]

Compared to the first patterning step, the height of the microstructures is roughly halved (from 4 µm to 2 µm) due to the removal of material in the first development step. The number of writing cycles is therefore strongly influenced by the layer thickness and the size of the introduced patterns, as they determine the amount of material available to erase the patterns during the subsequent viscoelastic flow.

However, the depth of incident light limits the maximum thickness of this layer. *o*-NBE chromophores and their cleavage products are strongly absorbed in the UVA region and are responsible for the internal filtering effect, which reduces the light intensity in the deeper layers of the sample. [275] Studies of photo-responsive thiol-ene networks have shown that the cleavage reaction of the *o*-NBE groups is significantly slowed down by reducing the incident light intensity. As a result, thicker samples are expected to allow the introduction of relief patterns on the surface, rather than degrading the network across the entire cross-section of the test sample. [273] It should be noted that the cleavage efficiency decreases with increasing film thickness, but at the same time there is more material available for repeated erasing of the surface structure by the thermo-activated viscoelastic reflow.

To study the thermal stability of the network, FT-IR spectra were taken from the positive tone structures (non-exposed areas of the film), and from the healed sample after the subsequent thermal treatment Figure 4-26.
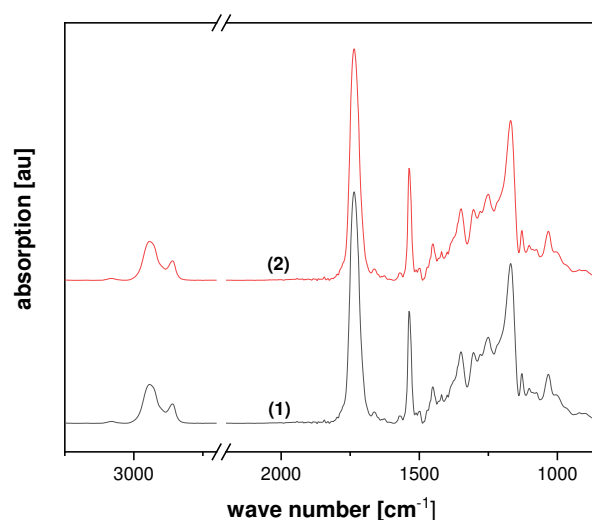


**Figure 4-26** FTIR spectra of the photopatterned photosensitive epoxy-anhydride vitrimer (1) prior to (2) and after thermal healing at 120 °C for 24 h (under vacuum). [249]

Erasing the structures at elevated temperature and under vacuum did not lead to any detectable material degradation, as the FT-IR spectrum of the thermally annealed network is comparable to the non-treated one.

### 4.3.6 Conclusion to the study on photopatternable and rewritable epoxy-anhydride vitrimers

In summary, repeated writing and erasing of positive tone patterns with a feature size of 20 µm has been demonstrated to be a promising approach to develop vitrimers with reversibly tunable surface topology. Micropatterns that are more complex can also be inscribed by varying the exposure dose during the pattering process. It is clear from the sol-gel analysis that the exposure time has a direct influence on the solubility and the amount of material removed during the development phase. Due to the photosensitivity of this vitrimer, it is possible to control the height of the microstructure more conveniently by locally or gradually varying the exposure dose during mask lithography.

Additional functions were imparted into covalent adaptable epoxy-anhydride networks by introducing photolabile $o$-NBE chromophores. The solubility was locally and temporarily controlled by UV- irradiation. Sol-gel analysis showed that the network is completely dissolved after 600 s of UV irradiation. The photosensitivity, which rendered the network microstructure with a feature size of 20 µm, can be inscribed into drop-cast films using mask lithography. The dynamic nature of the network was demonstrated by stress relaxation. At a temperature well above $T_v$ (49 °C), the thermally activated macroscopic flow of the network was used to completely erase the micropatterns. Interference microscopy of the healed surface revealed a smooth and defect-free surface topology. Using a second photolithographic step, the micropatterns were inscribed in the same area of the film, resulting in a rewritable photosensitive epoxy-anhydride vitrimer.

## 4.4 Epoxy-anhydride vitrimers from aminoglycidyl resins with high glass transition temperature and efficient stress relaxation

The data and results given in this section have been published in Polymers under the title "*Epoxy-anhydride vitrimers from aminoglycidyl resins with high glass transition temperature and efficient stress relaxation*", Volume 12, Issue 5, October 2020. Most of the following text, tables and figures have been taken from the respective publication. [250]

Moreover, parts of the following section have been filed at the Austrian Patent Office under the patent title „*Aushärtbare Zusammensetzung zur Herstellung eines Vitrimers und daraus erhältliches Vitrimer und Verfahren zu dessen Herstellung*"; A50332/2020

Clemens Sperling performed his Bachelor thesis in the course of this project. [242]



**Figure 4-27** Epoxy-anhydride vitrimers with varying $T_g$ prepared in the present study. r denotes the stoichiometric ratio, which was defined as r = anhydride equiv. / epoxy equiv. [250]

To date, the majority of the reported vitrimer systems are elastomeric networks at room temperature, having $T_g$s below 100 °C, which limits their applicability in structural components. [146] High-$T_g$ vitrimer systems often suffer from slow and insufficient transesterification reactions. [172] The aim of this study was the preparation of technically relevant vitrimer systems. For that, networks from 4,4′-methylenebis(*N,N*-diglycidylaniline) (4-DGA) and trifunctional *N,N*-diglycidyl-4-glycidyloxyaniline (3-DGOA) using glutaric anhydride as a hardener (Figure 4-27) were prepared. The two epoxy monomers do not only provide a rigid benzene ring to increase the network's $T_g$, but also contain tertiary amine moieties, which are able to catalyze curing and transesterification reactions in the epoxy-based vitimers. Without the addition of a conventional transesterification catalyst, networks with a high $T_g$ can be obtained, which exhibits significant stress relaxation and allow recycling and reprocessing.

### 4.4.1  Design and curing of high-$T_g$ epoxy-anhydride vitrimers

Epoxy anhydride networks were prepared by the reaction of N,N-diglycidyl-4-glycidyl oxyaniline (3-DGOA) or 4,4′-methylenebis(N,N-diglycidylaniline) (4-DGA) with glutaric anhydride at different stoichiometric ratios and catalyst contents (Table 3-4). The stoichiometric ratio r, defined as r = anhydride/epoxide equivalent, was either 0.5 or 0.25. In technical applications, r is usually in the range of 0.5 to 0.9 in order to obtain optimum mechanical and thermal properties of the cured resins. [276] However, to obtain hydroxyl ester networks with a large amount of free -OH groups, we also prepared epoxy-anhydride systems with an excess of epoxy groups (r = 0.25).

To prepare Zn(acac)$_2$-H$_2$O-catalysed epoxy-anhydride network, the transesterification catalyst was dissolved in the particular aminoglycidyl monomer and preheated at 100 °C. The anhydride was then added stepwise to obtain a homogeneous mixture, which was then cured at 120 °C. The curing rate was characterized by FT-IR spectroscopy. Figure 4-28 shows the FT-IR spectra of 3-DGOA-0.5-Zn prepared at r = 0.5 prior to and after thermal curing at 120 °C. After three hours curing, the two bands (1860 and 1778 cm$^{-1}$) associated with the carbonyl anhydride group disappeared and a new band at 1740 cm$^{-1}$ was observed, whereas this it was related to the carbonyl group.

A broad absorption band appeared at 3482 cm$^{-1}$, which was associated with the formation of the hydroxyl group. In addition, an epoxy band at 910 cm$^{-1}$ and the partially overlapping C-O absorption band (931 cm$^{-1}$) of the anhydride disappeared. Thus, this result indicates the successful formation of a hydroxyl ester linkages via a nucleophilic ring opening reaction between the aminoglycidyl epoxy monomer and glutaric anhydride. A complete conversion of the functional groups was obtained in less than 3 h and no significant changes in the bands were observed after 20 h of extended curing.

The rapid curing can be explained by the catalytic effect of Zn(acac)$_2$-H$_2$O. It is well known, that organic zinc salts as Lewis acids accelerate the curing reaction. [190,277] By dissolving zinc salts in epoxy monomers, Zn$^{2+}$ ions can substitute the organic ligands with the oxygen of the epoxide ring. Subsequently, ring opening of the epoxy group occurs and carboxylic acid ions are formed after the addition of anhydride (Figure 4-28 a), leading to a nucleophilic ring opening reaction with the epoxy moieties. Ester groups and additional carboxylate anions are formed, leading to a perpetuation of the ring-opening reaction. The reaction follows an anionic alternating copolymerization, yielding a polyester network. The ligand evaporates during solvation and curing, whereas the Zn$^{2+}$ ions remain in the cured network. In addition, at elevated temperatures water is released from the catalyst, which further accelerates the reaction by hydrolyzing the anhydride ring to form carboxylic acids. Moreover, it should be noted that homopolymerization of epoxy groups can occur as an alternative reaction pathway at an excess of epoxy monomer or at low curing temperatures. [278] A small band was observed at 1080 cm$^{-1}$, which might be related to the C-O absorption band of the esters. [279] However, the competition between esterification and etherification cannot be clearly identified since C–O bands of the ester moieties at 1250 cm$^{-1}$ overlap with ether bands (1200–1080 cm$^{-1}$) in the fingerprint area. With increasing excess of the epoxy moieties (catalyst formulation cured at r = 0.25), the IR absorption band from the -OH group (3482 cm$^{-1}$) increased significantly in the cured samples, whilst the band of the ester bond formed (1740 cm$^{-1}$) was less pronounced (Figure 4-29b). Full conversion was observed in the anhydride region, but the consumption of the epoxy groups was not complete, as indicated by the high intensity of the C-O band at 1234 cm$^{-1}$ and the remaining C-O band at 910 cm$^{-1}$. [278] The results clearly show the presence of unreacted epoxy groups (~6%), resulting in incomplete homopolymerization of 3-DGOA. This is mainly due to diffusion limitations of the

monomers above the gel point. This is typically observed in aromatic epoxies at high degrees of conversion (>90%) [195,280,281]. During the course of the curing reaction, the mobility of the monomers decreases due to the high viscosity of the matrix and the reaction becomes diffusion controlled since the diffusion of reactive species toward each other is hindered.

This behavior is even more pronounced in catalytic formulations with 4-DGA, since the epoxy monomers are highly functional and the rigid bi-functional aromatic structure reduces their mobility. Thus, even in the 4-DGA network cured at r = 0.5, a small amount of epoxy groups (~4%) remains unreacted after 20 hours of curing at 120 °C (Figure 4-28). The band region of -OH groups (3482 cm$^{-1}$) was smaller and lower than that of the cured 3-DGOA spectrum. Although it is possible to increase the number of -OH groups, the 4-DGA network is expected to be less effective in stress relaxation experiments, as a higher number of OH- groups favors the transesterification reaction. [210]
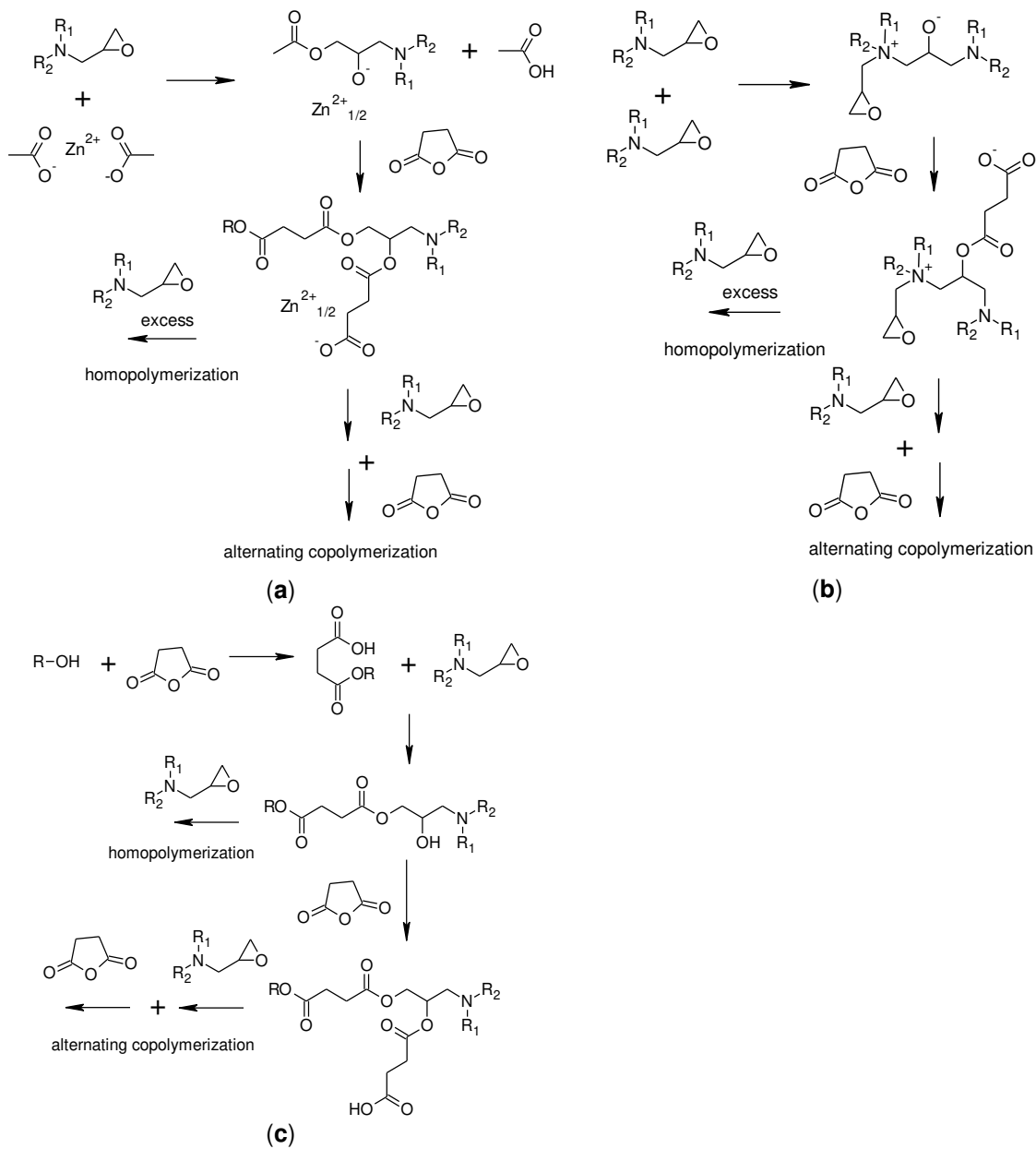
**Figure 4-28** Mechanism of the ring opening reaction of epoxies with anhydrides in the presence of (a) zinc salts and (b) tertiary amines as catalysts or (c) without catalyst. [250]

(a)



(b)



(c)
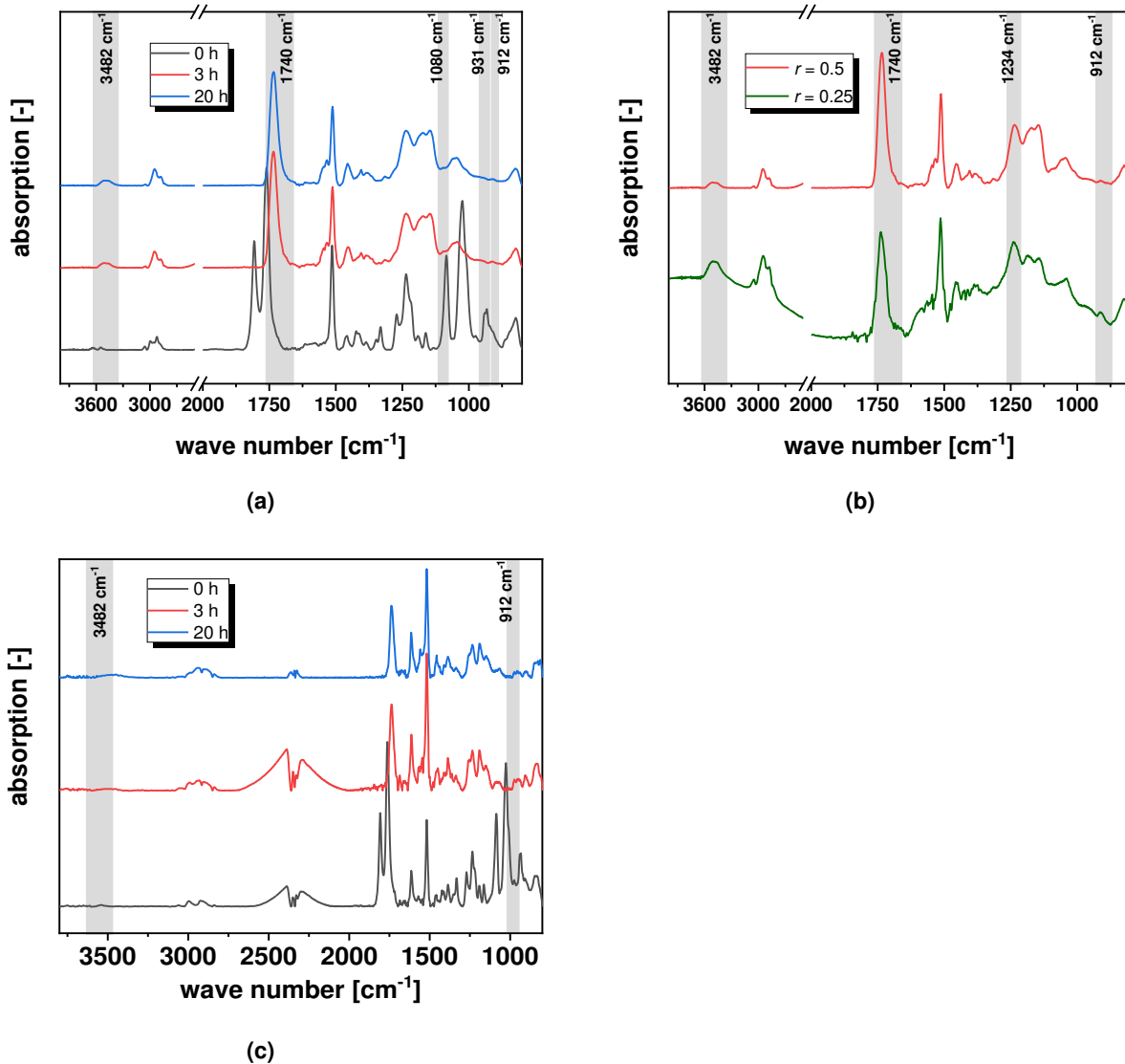
**Figure 4-29** (a) FT-IR spectra of catalysed 3- DGOA/glutaric anhydride systems cured with r = 0.5, prior to and after curing at 120 °C for 3 and 20 h. (a) FT-IR spectra of catalysed 3-DGOA/glutaric anhydride systems as a function of the stoichiometric ratio, after curing at 120 °C for 20 h. (a) FT-IR spectra of catalysed 4-DGA/glutaric anhydride systems cured with r = 0.5, prior to and after curing at 120 °C for 3 and 20 h  [250]

In addition, non-catalyzed networks were prepared from 3-DGOA and 4-DGA, with r = 0.5. In the absence of a catalyst, curing of the epoxy anhydride systems follows a step growth reaction Figure 2-28 c). [280] Traces of water or impurities with –OH groups initiate the reaction by opening the anhydride ring and forming a carboxylic acid group. After the carboxylic acid group is formed, a nucleophilic ring opening reaction with the epoxy group takes place yielding an -OH group, which then reacts with the anhydride moiety. [281] For

the curing of aminoglycidyl monomers, previous studies have shown that the tertiary amine groups of epoxy monomers can catalyze the reaction. [278] In the base-catalyzed ring opening reaction, the tertiary amine group opens the epoxy ring under the formation of an alkoxide (Figure 4-28 b). [278,281,282] The alkoxide reacts with the anhydride group to form a carboxylate anion, which can again open the epoxy group. The reaction also follows an anionic alternating copolymerisation to form a polyester network. Similar to the zinc-catalyzed system, homopolymerisation of epoxy monomers can occur in resin formulations with excess epoxy monomer. [283]

From the FT-IR data it could concluded that the final monomer conversions of the systems without $Zn(acac)_2$-$H_2O$ are comparable to those of the catalysed systems, although they are obtained at longer curing times. This is in good agreement with previous work on epoxy-anhydride systems, demonstrating that the catalyst mainly affects the curing kinetics but not the final monomer conversion. [281] In order to maximize the monomer conversion, all networks were cured at 120°C for 20 hours.

## 4.4.2 Thermal and thermomechanical properties of high-$T_g$ epoxy-anhydride vitrimers

Differences in the curing mechanism between catalyzed and non-catalyzed systems, together with varying degrees of homopolymerisation and residual monomer are expected to affect the thermomechanical properties of the networks. $T_g$ values were obtained by taking the maximum values of the tan δ curves in DMTA measurements and are given in Table 4-4. In particular, glutaric anhydride cured with 4-DGA results in a network with a higher $T_g$ than that with 3-DGOA. This can be explained by the higher functionality and rigidity of the tetra-functionalized epoxy monomer. Regardless of the epoxy monomer, the $T_g$ of the non-catalyzed network is higher than the $T_g$ of the catalyzed network. This behavior is also observed in other epoxy-anhydride networks and is associated with a faster cure of the resin in the presence of catalyst, which affects the network structure and leads to a lower crosslink density. [281,284] With increasing catalyst concentration, this effect becomes more pronounced and leads to a constant decrease in the obtained $T_g$ values. [285] Interestingly, the 3-DGOA catalyzed network cured with r = 0.25 shows a higher $T_g$ than the network with r = 0.5. This is due to the homopolymerization of the epoxy monomer, which is more pronounced at higher excesses of epoxy moieties and is

catalyzed by the -OH groups formed during the ring-opening reaction between the anhydride and epoxy moieties. [278] The additionally formed ether crosslinks further shift the $T_g$ of the networks to higher values. However, in the corresponding DMTA curve, only a one-step change in modulus and a single tan δ peak is observed, indicating a rather homogeneous network structure (Figure 4-30a).

**Table 4-4.** Characteristic properties of epoxy-anhydride vitrimers under investigation: $T_g$ values derived from dynamic-mechanical thermal analysis measurements and $T_v$ and $E_a$ data obtained from Arrhenius plots, in which $R^2$ denotes the coefficient of determination [250]

| System | $T_g$ [°C] | $T_v$ [°C] | $E_a$ [kJ/mol] | $R^2$ |
|---|---|---|---|---|
| 3-DGOA-0.25-Zn | 120 | 113 | 53 | 0.97 |
| 3-DGOA-0.5-Zn | 112 | 190 | 87 | 0.95 |
| 3-DGOA-0.5 | 125 | 241 | 154 | 0.99 |
| 4-DGA-0.25-Zn | 122 | 188 | 111 | 0.99 |
| 4-DGA-0.5-Zn | 130 | 227 | 158 | 0.96 |
| 4-DGA-0.5 | 140 | 238 | 161 | 0.99 |

This is in good agreement with previous work on epoxy anhydride vitrimers prepared from rigid epoxy monomers. [227] In contrast, the non-catalyzed 3-DGOA network prepared with r = 0.5 showed a significantly wider peak and a shift of the maximum tan δ towards higher values. The higher heterogeneity of the network is explained by the different curing mechanism of the non-catalyzed resin, which promotes homopolymerization of the epoxy monomer. Therefore, the non-catalyzed network is expected to have even more ether crosslinks than the catalyzed one, leading to additional transitions at higher temperatures. The results indicate that the degree of homopolymerisation increases in the order 3-DGOA-0.5-Zn < 3-DGOA-0.25-Zn < 3-DGOA-0.5. Similar behavior and a shift of maximum tan δ was observed for the DMTA curve of the 4-DGA networks (Figure 4-30b). However, the onset of the sub-glass transition is observed at around 20 °C. This indicates an incomplete curing of the network. The 4-DGA-0.5-Zn system also follows a similar trend with incomplete homopolymerisation of the epoxy monomer. This is also confirmed by FT-IR data, which show lower amount of -OH groups and high content of non-reactive epoxy monomers.
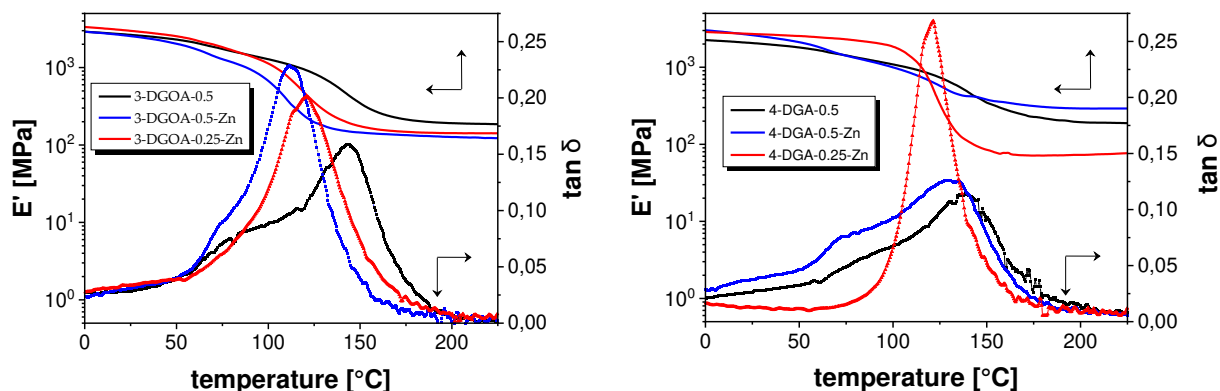
**Figure 4-30** Storage modulus (E') and tan δ curves of epoxy-anhydride vitrimers from (a) 3-DGOA and (b) 4-DGA. [250]

In addition to the thermodynamic properties, the thermal stability of the epoxy anhydride networks was determined using TGA as a function of stoichiometry, catalyst and epoxy monomer type (Figure 4-31). By adding $Zn(acac)_2$-$H_2O$ as catalyst, the 3-DGOA-0.5 system showed a decrease in initial weight loss temperature ($T_i$) from 320 °C to 280 °C and an increase in weight loss from 11% to 23% at 900 °C ($w_{900}$). This is mainly related to the higher number of ether crosslinks, formed at an excess of epoxy monomers in the resin formulations.

The higher thermal stability of the non-catalysed system is due to the higher degree of homopolymerisation as observed in the DMTA experiments. The ether groups are more thermally stable than the ester moieties, thus improving the thermal properties of the respective networks [23]. This is also confirmed by the even higher thermal stability of the catalytic network prepared with r = 0.25 (3-DGOA-0.25-Zn). Both $T_i$ (~280 to 300 °C) and $w_{900}$ were further increased to 23% and 28%, respectively. This is due to the formation of a large amount of ether crosslinks. In contrast to the catalyst and stoichiometry, the type of diglycidylaniline derivative used in this study does not significantly affect the thermal stability of the epoxy hydride network. Although DMTA curves indicate a higher heterogeneity in 4-DGA-anhydride networks, the weight loss curves of networks from 4-DGA and 3-DGOA are comparable and exhibit a one-stage decomposition process. As an example, Figure 4-31b compares the weight loss curves of catalyzed networks from 4-DGA and 3-DGOA, and both networks have nearly identical $T_i$ and $w_{900}$ values.
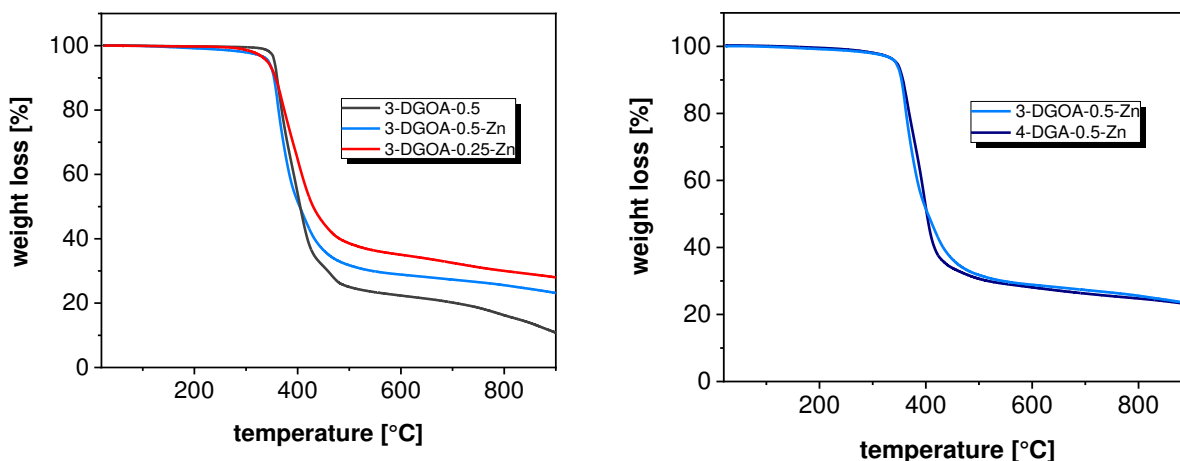
**Figure 4-31 .** TGA curves of epoxy-anhydride vitrimers. (a) Influence of catalyst and stoichiometry on the thermal stability of vitrimers from 3-DGOA and glutaric acid and (b) influence of the type of epoxy monomer (3-DGOA vs. 4-DGA) on the thermal stability of catalysed vitrimers (epoxy and anhydride groups in stoichiometry). [250]

### 4.4.3 Thermally adaptable properties and reprocessability of high-$T_g$ epoxy-anhydride vitrimers

Thermally induced topological rearrangements of the network were studied using stress relaxation experiments. Since the epoxy-anhydride vitrimers under investigation display a $T_g$ in the range between 113 and 140 °C and were stable at least up to 280 °C, the stress relaxation experiments were carried out between 160 and 280 °C. As a result, thermal degradation of the network was avoided during the rheological measurements, whilst a high mobility of the chain segments was ensured as the studies were carried out above the networks' $T_g$.

Figure 4-32a,b shows the time-dependent evolution of the relaxation modulus at 220 °C for 3-DGOA and 4-DDGA networks, respectively. All the networks present a characteristic relaxation, even the network without $Zn(acac)_2$-$H_2O$, albeit at a lower relaxation rate. Thus, this result demonstrates that a tertiary amine can catalyze the transesterification exchange reaction in the network. As expected, the relaxation rate increases with the addition of $Zn(acac)_2$ −$H_2O$ giving rise to acceleration of the bond exchange reactions in the presence of the catalyst. In In addition, the network prepared with r = 0.25 has a higher relaxation rate than the network with a lower excess of epoxy groups (r = 0.5). This is mainly due to the high degree of homopolymerisation of the epoxy, which is known to

increase the number of terminal -OH groups in the network, contributing to stress relaxation. [210] In contrast, the limited availability of -OH groups leads to a reduced relaxation rate as observed in 4-DGA networks. FT-IR experiments have already shown that 4-DGA networks have a lower content of -OH groups, which clearly affects the exchange rate of bonding reactions at high temperature.

After determining the stress relaxation curves at different temperatures, the topological freezing temperature ($T_v$) was calculated as previously shown from the corresponding Arrhenius graph (see page 55). The $T_v$ values of the epoxy-anhydride networks under investigation are shown in Table 4-4, and the related Arrhenius plots of the relaxation times are provided in Figure 4-32c,d.
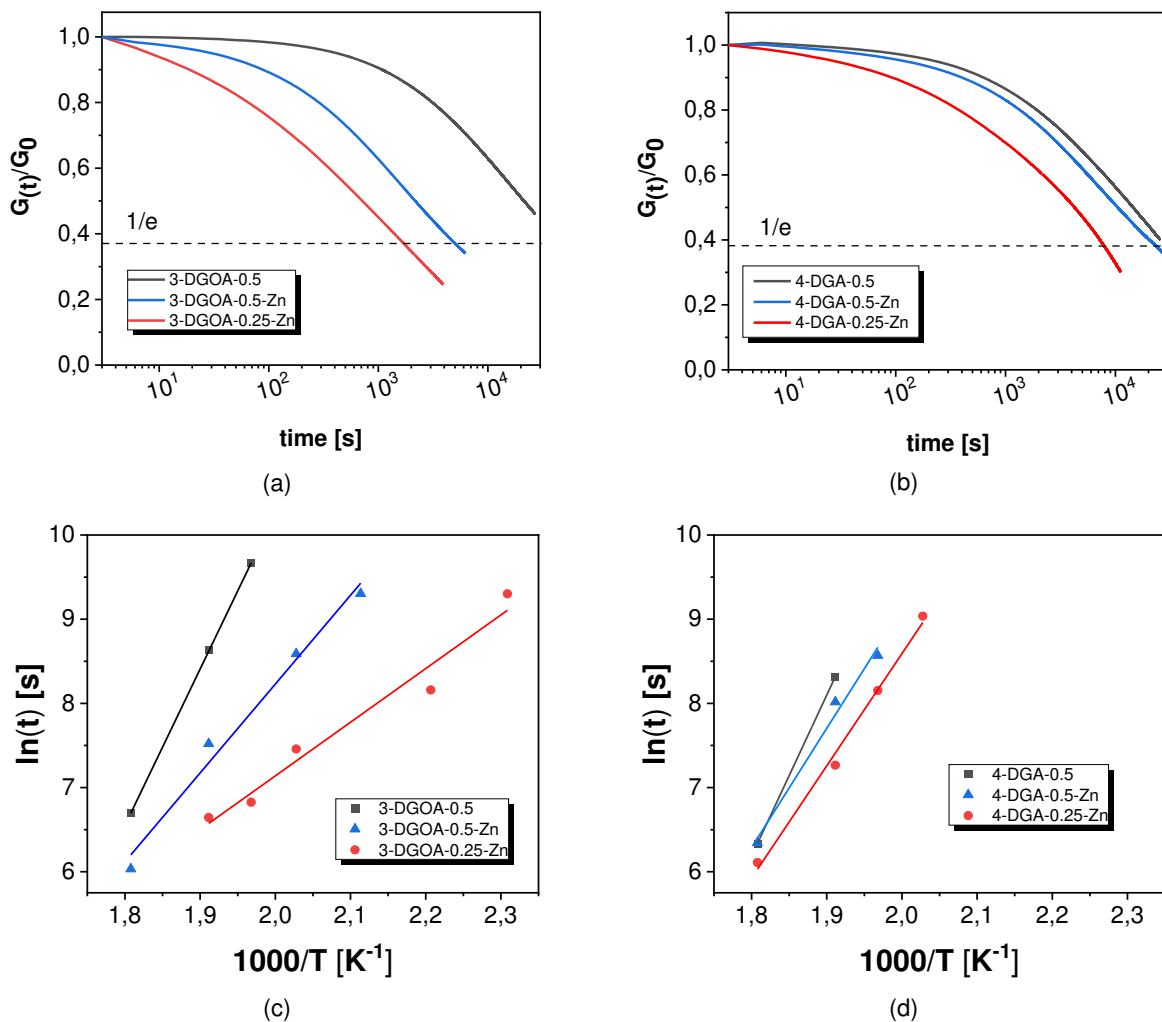


**Figure 4-32** Normalised stress relaxation curves of epoxy-anhydride networks from (a) 3-DGOA and (b) 4-DGA obtained at 220 °C. Arrhenius plot of the measured relaxation times from epoxy-anhydride networks obtained with (c) 3-DGOA and (d) 4-DGA [250]

The activation energy ($E_a$) and the $T_v$ values significantly differ for the networks under investigation. As already observed for the stress relaxation curves at 220 °C, the bond exchange reactions are accelerated by $Zn(acac)_2−H_2O$ and an increasing number of –OH groups in the network, which leads to a decrease in both $T_v$ and $E_a$. The high number of –OH groups might also explain the comparatively low $T_v$ of the 3-DGOA-0.25-Zn network, which is in the range of the $T_g$ of the network. In contrast, all other networks comprise a $T_v$ well above the $T_g$. This can be attributed to differences in the degree of homopolymerisation of the epoxy monomer in the network. On the one hand, homopolymerisation leads to the formation of polymer chains with terminal -OH groups, which promote transesterification. On the other hand, the higher number of ether bonds formed through homopolymerisation, the more the $T_g$ of the network is shifted towards higher values. In 3-DGOA-0.25-Zn network this effect is particularly pronounced and the $T_v$ value is lower than the $T_g$. In contrast, in the 4-DGA-0.25-Zn network the number of -OH groups are significantly lower, as indicated by the FT-IR data. Therefore, the $T_v$ value (188 °C) turns out to be higher than the $T_g$ of the network (122 °C). Although the non-catalyzed network had a higher degree of homopolymerization than the catalyzed network, significantly higher $T_v$ values were obtained (238°C for 4-DGA-0.5 and 241°C for 3-DGOA-0.5. The significant increase in $T_v$ is mainly due to the different catalytic reactivity of organic zinc salts in the transesterification reaction compared to tertiary amines. Thus, even if the non-catalyzed networks are characterized by the highest $T_g$ (up to 140 °C), the values are not able to exceed the corresponding $T_v$ data. Similar behavior of vitrimers was previously discussed by Du Prez and co-workers in their study on the material characteristics of vitrimers. [172] The dynamic nature of the network was used to thermally reprocess the epoxy-anhydride network. In order to demonstrate the recyclability of the network, cured test plates of 3-DGOA-0.5-Zn and 4-DGOA-0.5-Zn were grinded to a fine powder (Figure 4-33a and Figure 4-34a), which were remoulded in a press at 5 bar pressure and 220 °C. The grain boundaries of the resin particles were still visible (Figure 4-33b and Figure 4-34b). However, when the samples were molded at high temperature (250°C) and high pressure (500 bar), most of the grain boundaries disappeared (Figure 4-33c, d and Figure 4-34c, d).
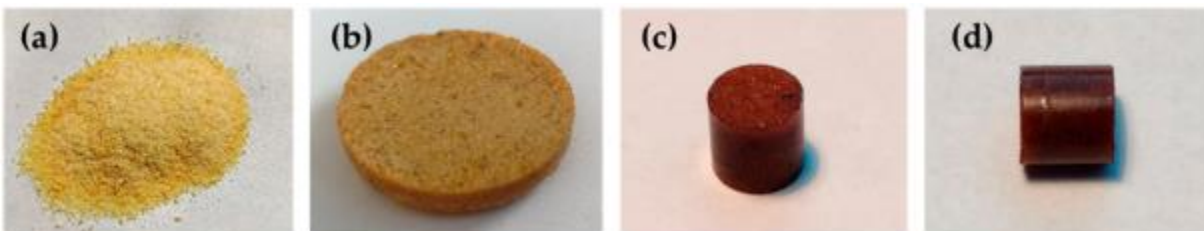
**Figure 4-33** (a) Grinded powder from 3-DGOA-0.5-Zn networks. (b) Remolded test specimen obtained by applying 5 bar at 220 °C. The diameter of the disc is 25 mm. (c,d) Remolded test specimen obtained by applying 500 bar at 250 °C. The diameter of the cylinder is 7 mm. [250]
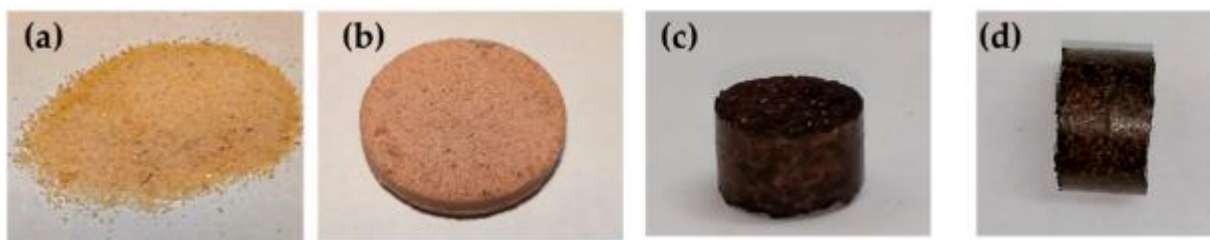


**Figure 4-34** (a) Grinded powder from 4-DGA-0.5-Zn networks. (b) Remolded test specimen obtained by applying 5 bar at 220 °C. The diameter of the disc is 25 mm. (c,d) Remolded test specimen obtained by applying 500 bar at 250 °C. The diameter of the cylinder is 7 mm. [250]

### 4.4.4 Conclusion to the study on epoxy-anhydride vitrimers from aminoglycidyl resins with high glass transition temperature and efficient stress relaxation

Epoxy anhydride vitrimers were prepared by thermal curing of tri- and tetra-functional aminoglycidyl epoxy monomers with glutaric anhydride. Cured networks were obtained at 120 °C without the addition of a catalyst, since the tertiary amine groups present in the structure of the epoxy monomers were able to accelerate the nucleophilic ring-opening reaction. Final monomer conversions decreased with rising functionality of the epoxy monomers due to diffusion limitations of the monomers at high degrees of conversion. By adding $Zn(acac)_2-H_2O$ as transesterification catalyst, the curing was significantly accelerated. However, incomplete conversion of the epoxy groups was observed in networks with a high excess of epoxy monomer (r = 0.25). A higher content of epoxy monomer gave rise to the formation of ether linkages via homopolymerisation, which shifted the $T_g$ and the thermal stability of the networks to higher values. The highest $T_g$ (140 °C) was obtained with non-catalyzed 4-DGA/glutaric anhydride systems, which were also able to relax stresses adequately. The results evidence that the tertiary amine groups within the structure of the epoxy monomers catalyze the transesterification exchange

reaction, albeit at lower rates than networks with $Zn(acac)_2 - H_2O$. Along with the zinc salt, the relaxation rate increased with rising degree of homopolymerisation, which is related to a higher number of terminal –OH groups in the networks. In particular, fast stress relaxation at a low $T_v$ (113 °C) was obtained in catalyzed 3-DGOA/glutaric anhydride networks prepared with r = 0.25. Furthermore, the thermally activated bond exchange reactions were exploited to reprocess the cured networks. Successful remoulding of a grinded powder was demonstrated. The high $T_g$ paired with the efficient stress relaxation and ability towards reprocessing makes this type of epoxy-anhydride vitrimers interesting candidates for structural applications operating at high service temperature.

## 4.5 Influence of the transesterification catalyst on the properties of epoxy-anhydride vitrimers

Viktoria Feigl performed her bachelor thesis in the course of this project. Selected results of her thesis are discussed within this section. [251]
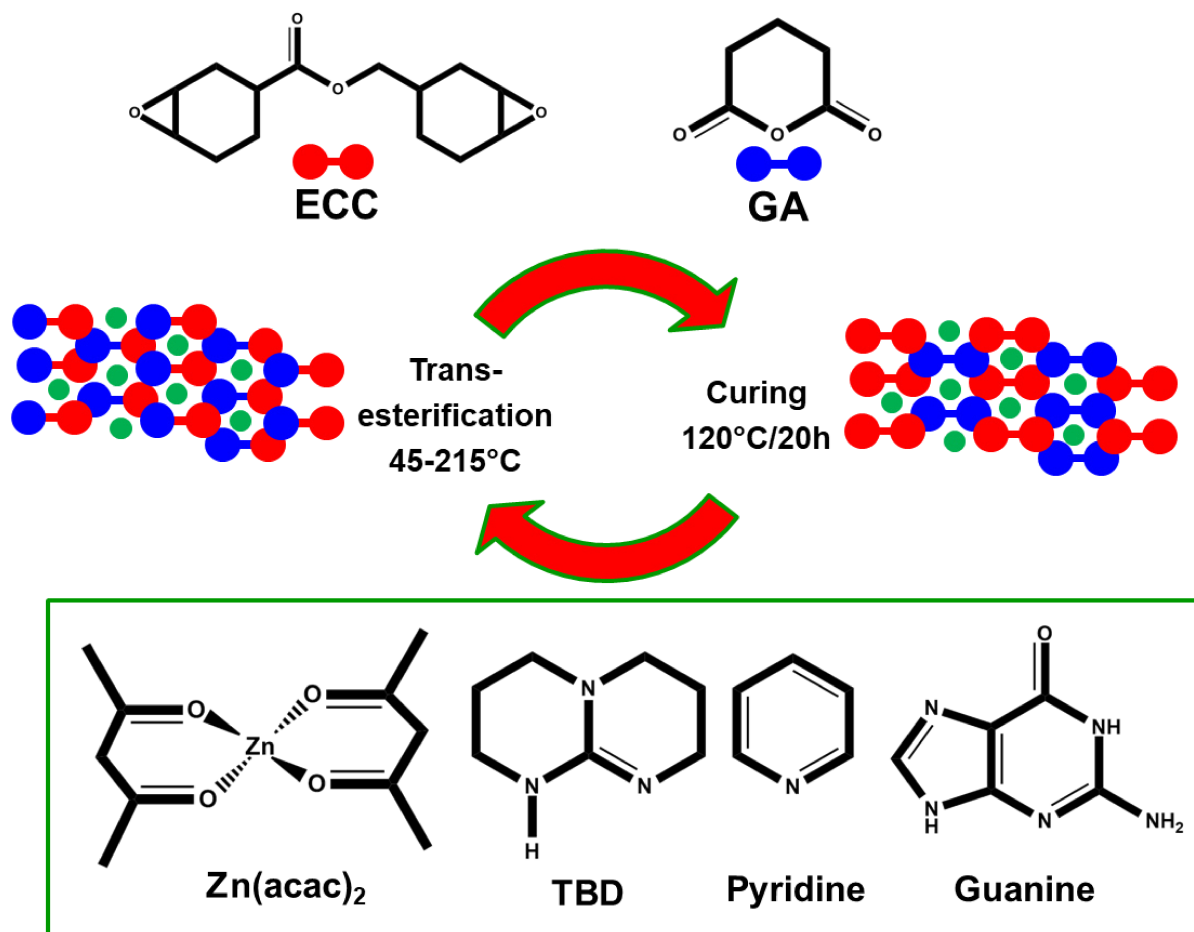


**Figure 4-35** Epoxy-anhydride vitrimers and the studied catalysts

As the previous studies demonstrated, the selection of the catalyst is crucial for tailoring the properties of a vitrimer network (either for curing or for transesterification). On the one hand, the catalyst influences the curing speed and network structure and on the other hand, bond exchange reactions within the polymer network are strongly affected by the activity of the catalyst. To broaden the development of vitrimeric systems, research on efficient catalysts is essential, as to date, the number of available transesterification

catalysts is limited. Moreover, the established systems are lacking in bringing economic aspects, efficiency and environmental compatibility together. As previously mentioned, catalysts such as $Zn(acac)_2$ have the additional disadvantage that volatile compounds are released at higher temperatures. In order to increase the industrial relevance of vitrimer materials, networks should exhibit a high efficiency in catalyzing transesterification reactions. In the following study, the influence of selected catalysts on a predefined vitrimeric network was investigated. A further goal of these experiments was to produce a high-$T_g$ vitrimer network ($T_g$ > RT), as this allows a wider range of use for industrial applications. The basic network consisted of an epoxy monomer and an anhydride hardener. A commercially available epoxy monomer was chosen, which is branded under the name Uvacure 1500 and already contains an ester group in its structure, which is essential for the transesterification reaction. Glutaric anhydride was used as crosslinker, which is known in literature to give high-$T_g$ vitrimer networks. [224,286] For the experiments, the catalytic effect of two established and two new catalysts were compared. The two established catalysts were $Zn(acac)_2$ and TBD. Both compounds are known to enable ring opening (for curing) and for catalysing transesterification reactions. The two new catalysts tested were pyridine and guanine.

### 4.5.1  Preparation of the network

Epoxy-anhydride networks consisting of four different catalysts were prepared by reacting the epoxy monomer, namely 4-epoxycyclohexylmethyl-3',4'-epoxycyclohexane carboxylate (ECC) with glutaric anhydride (GA). For this, the stoichiometric ratio of the formulation was kept constant, whilst the type of catalysts was varied (Table 3-5). For the preparation, in all of the four networks, the transesterification catalyst was first dissolved in the ECC, which was preheated between 100 and120 °C. After full solvation, the anhydride was added stepwise and after obtaining a homogeneous mixture, curing was carried out at 120 °C for 20 h. For the preparation of the individual networks, different strategies were pursued. This was caused by the different material properties (e.g. solid or liquid) and the solubility of the catalysts. With TBD and $Zn(acac)_2$ it was possible to dissolve them in the resin in a homogenous way. Similar behavior applies for the liquid catalyst pyridine. In order to obtain a homogenous intermixing of the catalyst with the epoxide and anhydride, the preparation of the guanine involved an additional dissolving

of the guanine in few mL of pyridine. To ensure only a minor influence of the pyridine, the solvent was removed under vacuum for approximately 30 min at 50°C. After curing, a homogenous formulation was obtained. Without this treatment, a precipitation of the guanine catalyst was observed.

The curing kinetics was monitored using FT-IR spectroscopy. Figure 4-36 illustrates the FT-IR spectra of the four networks prepared with the individual catalysts, prior to and after thermal curing at 120 °C. Similar to the previously studied anhydride/epoxy networks, the two bands at 1860 and 1778 cm$^{-1}$ related to carbonyl of the anhydride groups disappeared after a cure time of 5 h. In contrast, the carbonyl group of the newly formed ester linkages was observed at 1740 cm$^{-1}$. At 3482 cm$^{-1}$, the hydroxyl groups appeared with a broad absorption band. In addition, the epoxy band at 910 cm$^{-1}$ and the partly overlapping C–O absorption band at 931 cm$^{-1}$ of the anhydride hardener disappeared. The results of the FT-IR experiments demonstrate a successful formation of hydroxyl ester linkages via the nucleophilic ring-opening reaction between ECC and glutaric anhydride hardener. Full conversion of the functional groups is obtained within 5 h, whereas no significant change in the bands was detected for extended curing (20 h).
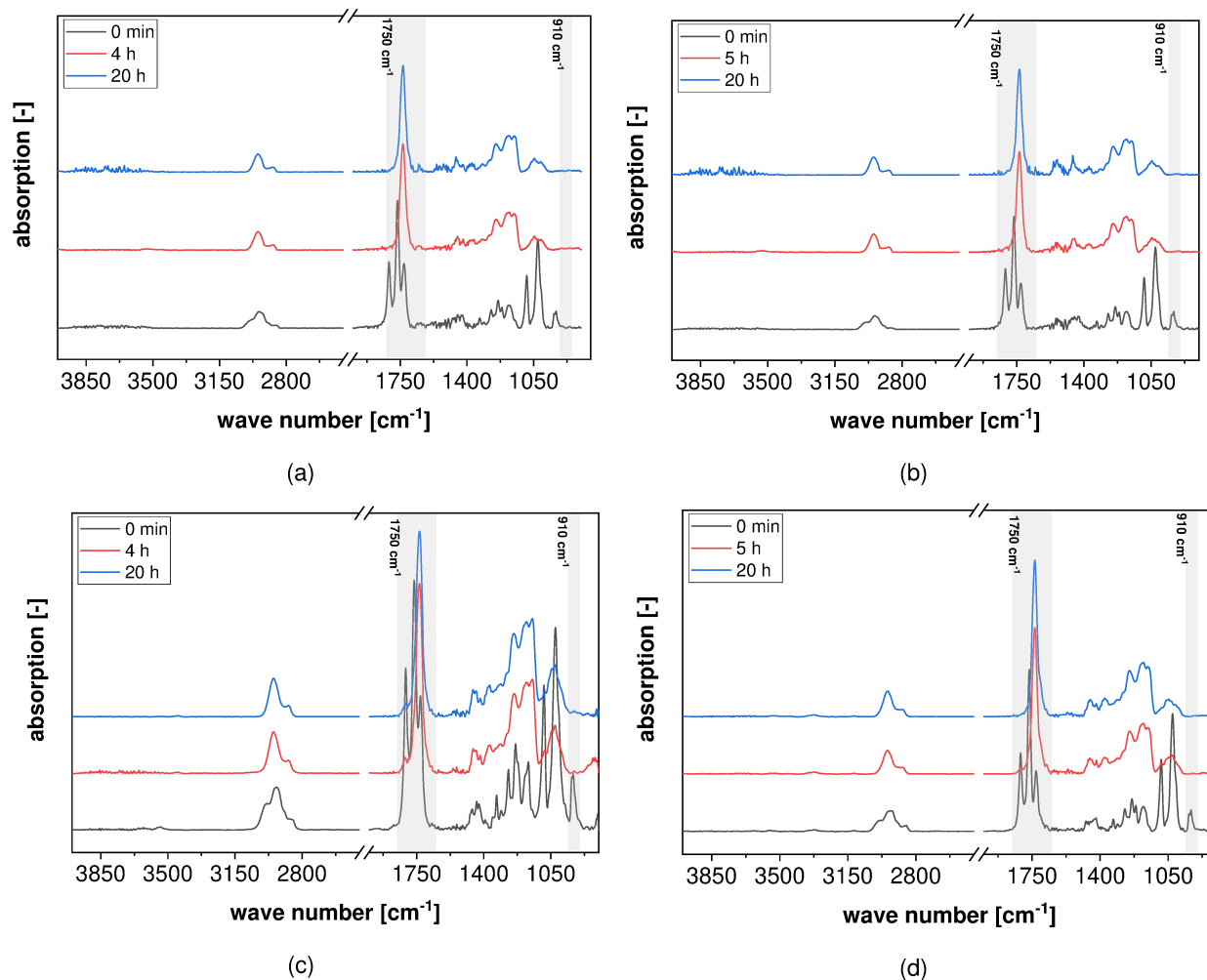
**Figure 4-36 (**a) FT-IR spectra of TBD catalyzed ECC/glutaric anhydride systems cured at 120 °C for 0.4 and 20 h. (b) FT-IR spectra of Zn(acac)$_2$ catalyzed ECC/glutaric anhydride systems cured at 120 °C for 0.5 and 20 h. (c) FT-IR spectra of pyridine catalyzed ECC/glutaric anhydride systems cured at 120 °C for 0.4 and 20 h. (d) FT-IR spectra of guanine catalyzed ECC/glutaric anhydride systems cured at 120 °C for 0.5 and 20 h.
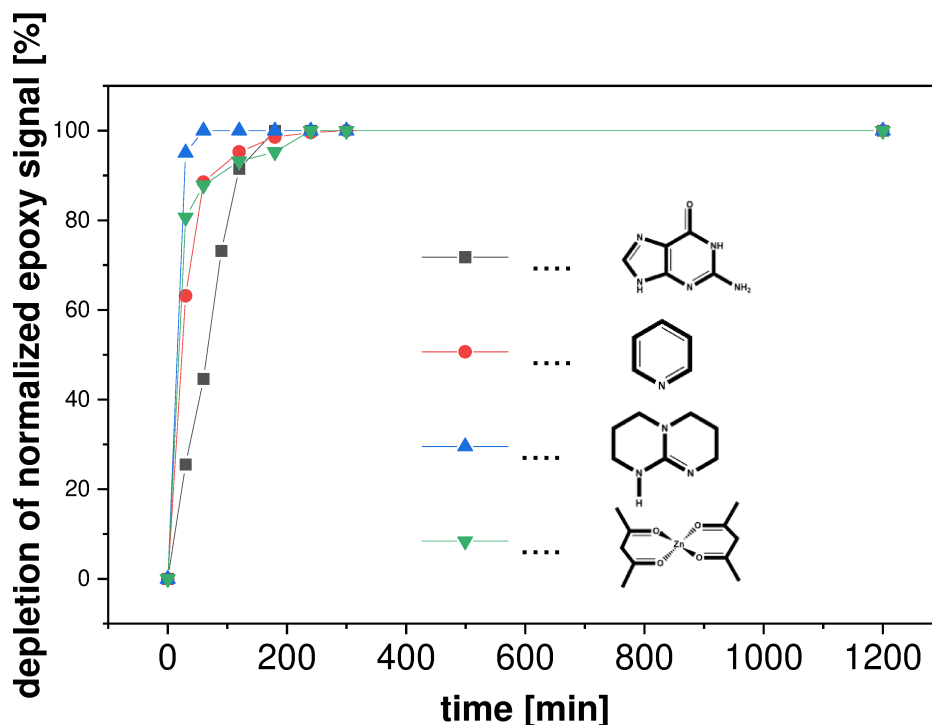
**Figure 4-37** Cure kinetics of ECC/glutaric anhydride systems containing different transesterification catalysts by following the normalized depletion of the peak area between 910 and 928 cm$^{-1}$. Thermal curing was performed at 120 °C. The lines are a guide for the eye.

The cure kinetics of the four catalyzed vitrimer systems is shown in Figure 4-37. Comparing the four systems, TBD showed the fastest depletion of the epoxy groups. TBD represents a strong amidine base and has a high nucleophilic activity to promote the ring-opening reactions. [220] With a pK$_a$ of 15 (pK$_a$ of conjugate acid in water) it allows a rapid polymerization of cyclic esters via bifunctional nucleophilic mechanism. [287,288] In contrast, the reaction of pyridine (pK$_a$ of 5) with the epoxy-groups probably follows an anionic addition polymerization, which resulted in a significantly slower curing rate. [190,289] As described in the previous section, Zn salts catalysis follows an anionic alternating copolymerization, yielding polyester networks. The results in Figure 4-37 show the cure rate of pyridine and the organic Zn salt. Guanine on the other hand represents a heterocyclic aromatic system, bearing a secondary aromatic amine and a primary amine functionality. In a recent study, adenine (similar functionalities as guanine) was tested as a potential hardener with DGEBA. The study showed a faster reactivity of the imidazole N-H and that the primary amine appears unable to complete the curing reaction and forms the three-substituted product under the applied conditions, probably because of steric

133

hindrance. This effect might also explain the observed lack of reactivity of the three aromatic nitrogen atoms present in the guanine molecule. [290,291] These observations are also found in the present curing kinetics, showing an order of TBD > pyridine = Zn(acac)$_2$ > guanine.

### 4.5.2 Thermal and thermo-mechanical properties of the catalyzed epoxy-anhydride vitrimers

As indicated in the previous section, the individual catalysts result in a different cure mechanism, which most likely affect the thermomechanical properties of the networks. The T$_g$ values were determined from DMTA measurements by taking the maxima of the tan δ curve and are provided in Table 4-5. It is well known that the T$_g$ of a fully cured epoxy resin depends on the molecular stiffness and average functionality of the reagents. [227] In particular, curing of ECC with glutaric anhydride in the presence of pyridine yields networks with higher T$_g$ than the other catalysts. This result would indicate that catalyzing this system with pyridine affects the network structure and leads to a higher cross-linking density. Similar to the previous section, one possible explanation for the higher network density could be the affinity to react with epoxy monomers and a higher possibility for homopolymerization of the epoxy moieties. Resulting in additionally formed ether crosslinks and further shift of the T$_g$. [278] In a study by Dell'Erba *et al.* a pyridine derivate, namely 4-(dimethylamino)pyridine (DMPA) generated a higher crosslink density associated with the longer primary polyether chains resulting from the use of DMAP as initiator, in comparison to typical tertiary amines. [292] The presence of a second network could be indicated by a second peak in the tan δ curve of the pyridine system. The results show, that the pyridine effectively contributed in the curing reactions and therefore led to an enhanced completion of cross-linking reaction, resulting in high cross-link density and T$_g$. TBD on the other hand, has already demonstrated to act as an efficient curing agent and follows the pyridine network with a T$_g$ of 132 °C. Same applies for the Zn(acac)$_2$ catalyzed network. In regard to guanine, the networks exhibits a rather low T$_g$ of 63 °C, which is nearly 100 °C lower, than the network containing pyridine. The low network density could be the result of an inefficient curing reaction and the presence of side reactions. [290] Moreover, the primary amine group of the guanine could also react with an epoxy group and terminate the curing reaction. [190] As shown in Figure 4-38, a broad

peak for the tan δ of the guanine network was obtained. This could indicate the occurrence of side reactions such as homopolymerizations.
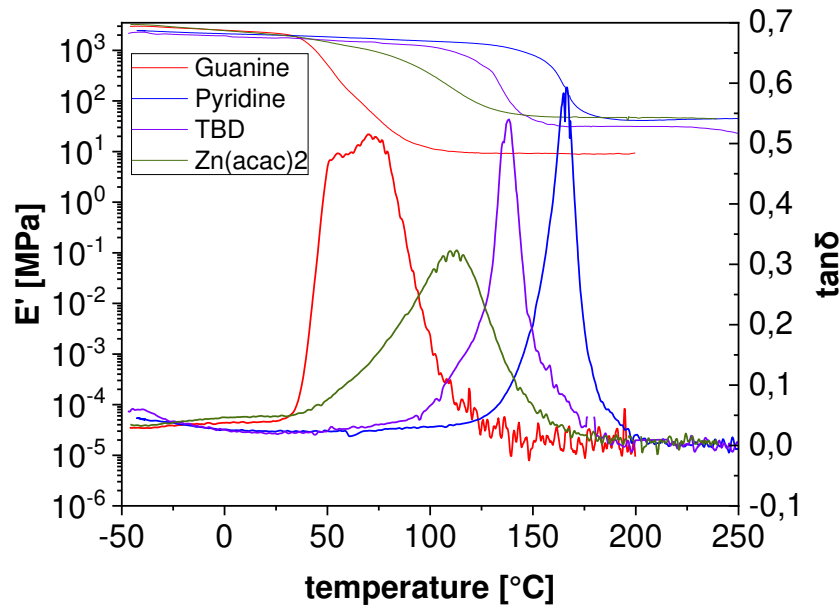


**Figure 4-38** Young's modulus (E') and tan δ curves of epoxy-anhydride vitrimers

The thermal stability of the networks as a function of the employed catalyst was determined by using TGA. As illustrated in Figure 4-39, the addition of the individual catalysts had different effects on the thermal stability, showing a decrease in initial weight loss temperature ($T_i$) from ~315 to 205 °C together with an increase in weight loss at 900 °C ($w_{900}$) from 2% to 4%. The pyridine-catalyzed network showed the highest thermal stability, whereas this result probably relates to the higher degree of homopolymerization, as observed in DMTA experiments. Ether groups are thermally more stable and therefore improve the thermal properties of the corresponding networks. The TBD and $Zn(acac)_2$ – catalyzed networks feature a similar thermal stability, which correlates well with the network density observed in the DMTA experiments. Regarding the guanine-catalyzed network, the low network density was confirmed by the lower thermal stability of 205 °C. All of the four networks display a one-stage decomposition process.
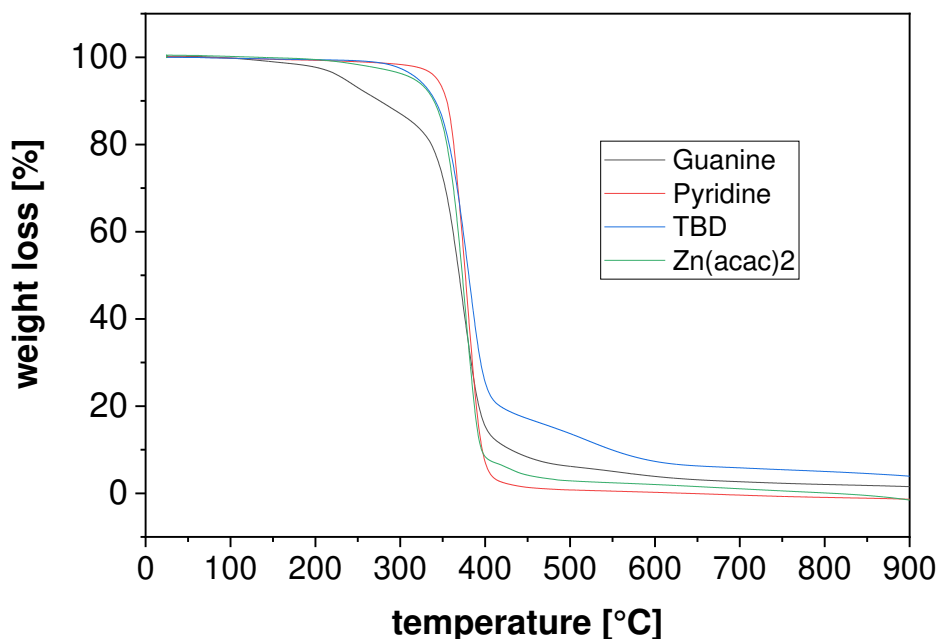
**Figure 4-39** TGA curves of epoxy-anhydride vitrimers.

### 4.5.3 Thermally adaptable properties of the catalyzed epoxy-anhydride vitrimers

The thermally triggered topology rearrangements of the networks were characterized using stress relaxation experiments via rheometer. TGA measurements showed a short-term thermal stability up to 250 °C for all networks and the DMTA experiments $T_g$ values between 63 and 166 C. As a result, thermal degradation of the network are avoided during the rheological measurements avoided. In addition, the study was carried out over the networks' $T_g$, which ensured high mobility of the chain segments. The relaxation time ($\tau^*$) was determined as described in the previous section. Figure 4-40 illustrates the results of the individual systems. The two well-established transesterification catalysts, TBD and Zn(acac)$_2$, showed a distinctive temperature-dependent stress-relaxation. However, the two new catalyst could also efficiently catalyze transesterification reactions within the network. Due to the large difference in their network density, both systems showed a rather different stress-relaxation behavior. On the one hand, the pyridine-catalyzed network had the highest $T_g$ and consequently the lowest chain mobility. On the other hand, the guanine-based system with a $T_g$ of 66 °C already had a flexible structure at a starting temperature of 180 °C and facilitates a fast stress-relaxation.

(a)

(b)

(c)

(d)
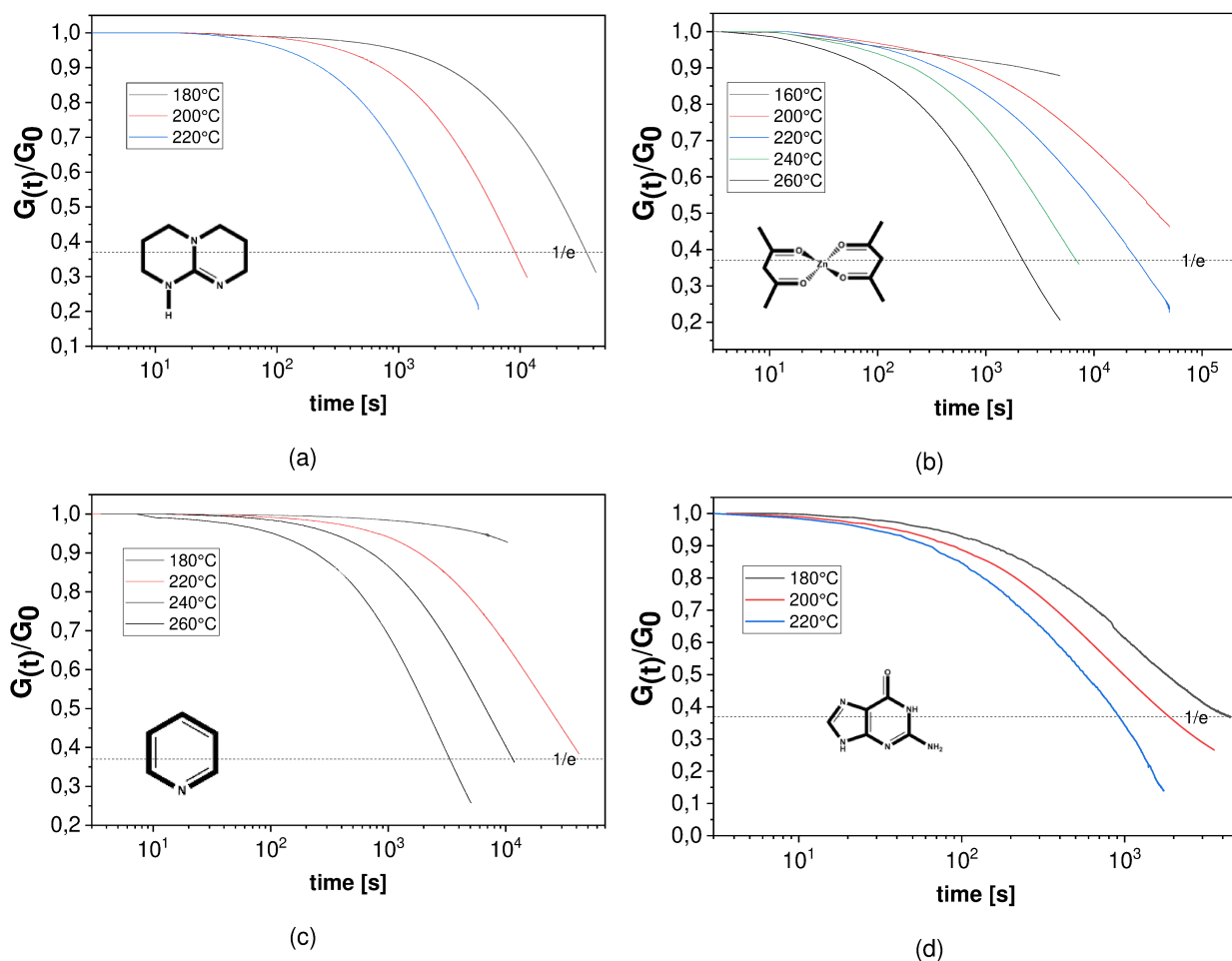
**Figure 4-40** Normalized stress relaxation curves of epoxy-anhydride networks catalyzed **(a)** with TBD **(b)** Zn(acac)$_2$ **(c)** pyridine and **(d)** guanine

In order to compare the stress relaxation of the four different networks, Figure 4-40 illustrates the stress relaxation curves of the individual networks at 220 °C. The results reveal that the guanine-catalyzed networks results in the fastest stress relaxation, which can be explained by the lower crosslink density and higher mobility of the network. In contrast, networks catalyzed with TBD or Zn(acac)$_2$ exhibit a slower exchange kinetics. Pyridine, introduced as new catalyst, is also able to accelerate bond exchange reactions, albeit at a much lower rate, which is related to the high crosslink density of the network and the low catalyst activity.

Subsequently, the $T_v$ was calculated as previously described from the respective Arrhenius plots. The $T_v$ values of the epoxy-anhydride networks are shown in Table 4-5, and the related Arrhenius plots of the relaxation times are provided in Figure 4-42.

137
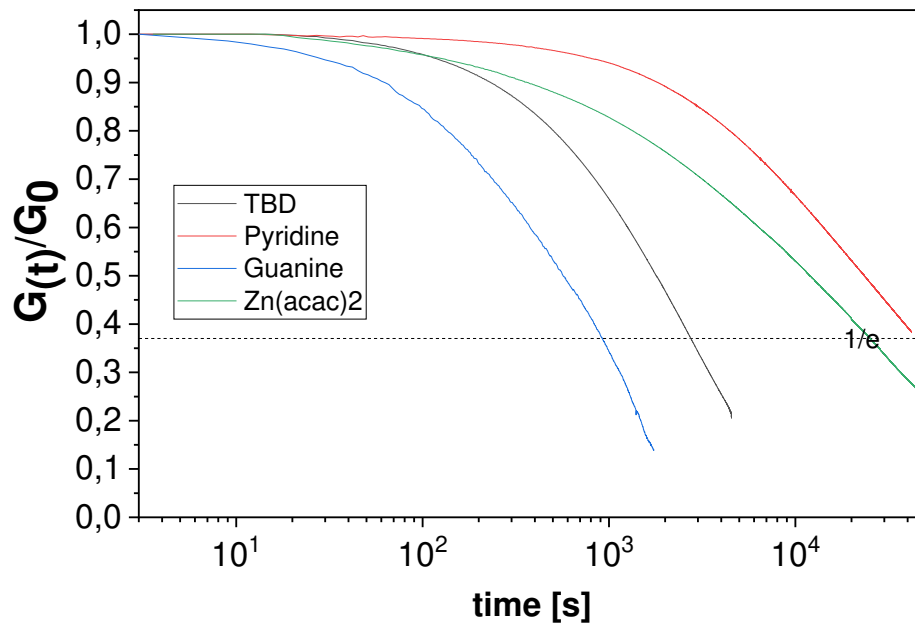
**Figure 4-41** Normalized stress- relaxation curves of the individual networks at 220°C
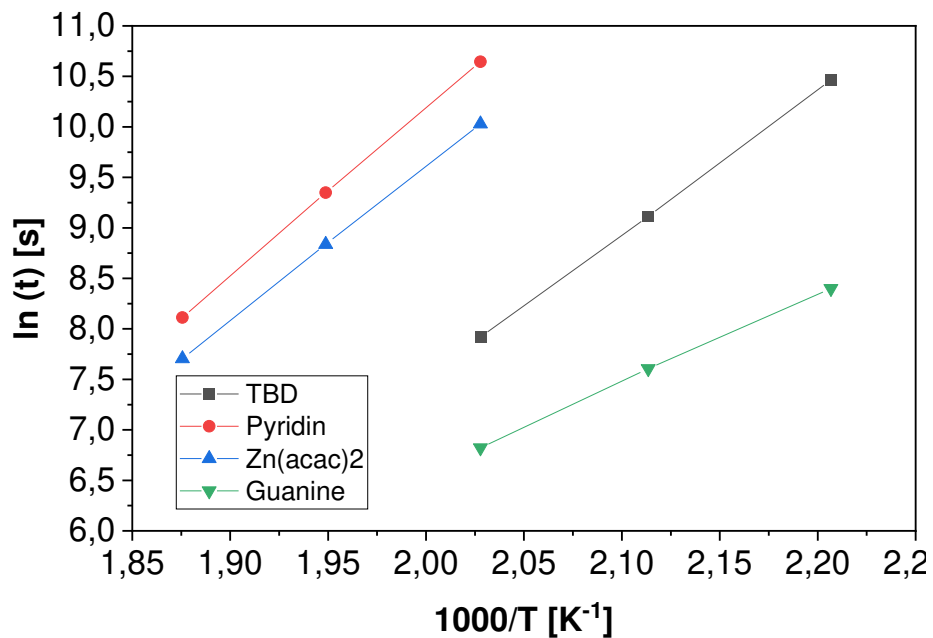


**Figure 4-42** Arrhenius plot of the measured relaxation times from epoxy-anhydride networks obtained with the individual catalysts

The activation energy for the exchange reactions and the $T_v$ values significantly differ for the individual catalyzed networks. As already observed for the stress relaxation curves at 220 °C, the bond exchange reactions are differently accelerated. [201]

**Table 4-5** Characteristic properties of epoxy-anhydride vitrimers under investigation: $T_g$ values derived from dynamic-mechanical thermal analysis DMTA measurements and $T_v$ and $E_a$ data obtained from Arrhenius plots, in which $R^2$ denotes the coefficient of determination

| System | $T_g$ [°C] | $T_v$ [°C] | $E_a$ [kJ/mol] | $R^2$ |
|---|---|---|---|---|
| ECC-GA-Zn | 110 | 198 | 127 | 0.99 |
| ECC-GA-TBD | 132 | 167 | 118 | 0.99 |
| ECC-GA-Pyridine | 166 | 215 | 138 | 0.99 |
| ECC-GA-Guanine | 63 | 45 | 73 | 0.99 |

The rather low activation energy and $T_v$ of the guanine-catalyzed system can be explained by the high chain mobility and the low network density. In addition, the calculated $T_v$ is significantly lower than the determined $T_g$. One possible explanation could be the shift of the $T_g$ by the higher number of ether bonds formed by homopolymerization.

Moreover, the guanine molecule has three functionalities with $pK_a$- values (in water) of 3.3 (amide), 9.2 (secondary), 12.3 (primary), which most likely are influencing the transesterification and curing behavior as well. [293]

The rather high $E_a$ and $T_v$ of the pyridine- catalyzed network can be explained by the high network density and inefficiency of the catalyst for transesterification. Comparing the two networks with the highest $T_g$; TBD and pyridine-catalyzed networks the activation energy differs of 20 kJ/mol. Regarding the catalyst activity, TBD as a strong guanidine base enhances the nucleophilicity of the alcoholic group via H-bonding. [201] On the other hand, pyridine has a moderate nucleophilicity for carbonyl groups. The nitrogen atom of pyridine is nucleophilic because the lone pair of electrons cannot be delocalized around the ring. [294] Comparing the curing and transesterification results, the different affinities can be confirmed. The pyridine-catalyzed network had a higher $T_g$ and probably a better curing rate, whereas the TBD-catalyzed network facilitates the faster transesterification rate. Similar to previous studies, $Zn(acac)_2$ demonstrated to be an efficient transesterification catalyst, but only slightly faster than pyridine, which is interesting when comparing the distinctive difference in the $T_g$ (Δ56°).

### 4.5.4 Swelling measurements

As previously described in section 3.7.6, five samples of each system were prepared and the swelling degree and gel fraction were calculated as defined in Equation 3-2 and 3-3:
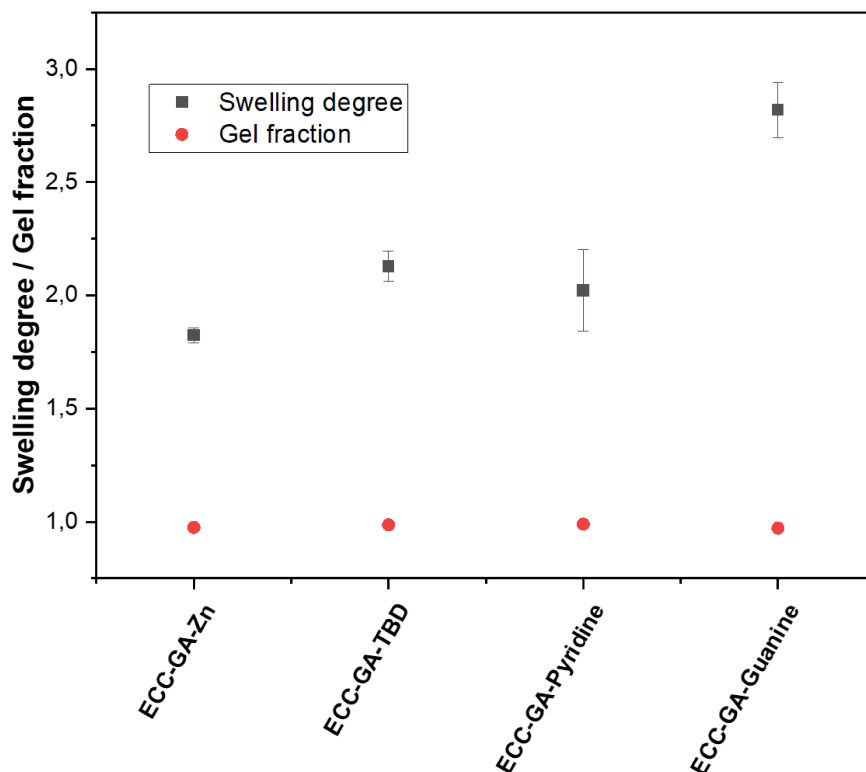


**Figure 4-43** Swelling degree and gel fraction of the four vitrimer systems under investigation

As illustrated in Figure 4-43, three of the networks showed similar swelling behavior, whereas the $Zn(acac)_2$ catalyzed network exhibited the lowest swelling degree. Contrary, the guanine-catalyzed network had the highest swelling degree, which is associated with a lower crosslink density. The results are in good agreement with the data obtained from DMA and relaxation experiments. Regarding the solvent removal within the polymer networks, the process took one week at 85 °C under vacuum to dry the samples until constant weight. The gel content amounted to 0.99 ±0.09 for the pyridine-catalyzed network and 0.97 ±0.004 for the guanine-catalyzed one giving rise to a high cure degree of the vitrimer networks under investigation.

### 4.5.5 Conclusion to the study on the activity of transesterification catalysts

Epoxy-anhydride vitrimers formed by the ring-opening reaction of ECC with GA were prepared using four different catalysts for the curing and subsequent thermo-activated transesterifications. Cured networks were obtained at 120 °C, whereas FT-IR measurements showed a full conversion of the epoxy groups after 300 min curing time. DMTA measurements indicate side reactions and homopolymerization in different degrees depending on the applied catalyst. Moreover, by varying the type of catalysts, different network densities were obtained, resulting in a $T_g$ range from 66 to 166 °C. Formation of ether linkages and a resulting shift of the $T_g$ can be an explanation. Moreover, the reaction of the primary amine function of guanine with the epoxy moieties is expected to terminate the curing reaction yielding networks with lower crosslink density. Regarding the stress relaxation, all of the four catalyzed systems showed the ability to accelerate bond exchange reactions within the network. The distinctive difference in the relaxation times are attributed to the different network densities and the activity of the individual catalyst. This was confirmed by swelling measurements of the networks. The highest transesterification activity was shown by guanine.

Although the polymer networks are based on the same type and amount of epoxy monomer and anhydride hardener, the ability towards curing and transesterification is largely influenced by the choice of catalyst. This enables a convenient tailoring of network density, mobility and stress relaxation of respective vitrimer systems. For future studies, the influence of the number and type of amine functionalities should be studied and the activation energy of the individual catalysts determined to get a deeper insight into the mechanisms of amine-based catalysts                                    .

# 5  Summary and outlook

In the present thesis, strategies towards the preparation of new stimuli-responsive polymers have been introduced. The network evolution, mechanical properties, thermal and photochemical behavior of different polymer networks have been studied in detail to establish new approaches towards stimuli-responsive polymers.

In the first part of this thesis, the salient features of $o$-NBE chemistry have been imparted to selected polymer networks. PDMS networks undergoing controlled bond cleavage in response to either UV radiation or different pH values as external triggers were prepared by thermally crosslinking PDMS oligomers with terminal anhydride groups in the presence of bifunctional epoxy monomers containing $o$-NBE groups. The susceptibility of ester groups towards hydrolytic cleavage reactions is used to degrade the network under alkaline conditions. Sol-gel analysis confirmed that the degradation time can be controlled by the concentration of the base and amounts to different time scales ranging from a few hours to several weeks. In addition, photoinduced degradation of the elastomeric networks was achieved by cleavage of $o$-NBE links by UV irradiation. Using photolithographic techniques, positive-tone patterns with a structural size of 100 µm were obtained, confirming the spatial control of solubility properties. However, re-crosslinking of the network was observed with increasing exposure dose due to side reactions of the primary photocleavage products. Since the reformed cross-links were less susceptible to ester hydrolysis, this side reaction could be used to form negative-tone microstructures in the PDMS network. [247]

In a further study, photopatternable epoxy-based thermosets were prepared and the cleavage properties were studied as a function of network structure and network mobility. By exploiting the $o$-NBE-chemistry, local switching of solubility by light at specific wavelengths was achieved. An $o$-NBE derivative with terminal epoxy groups was thermally cured with different types of cycloaliphatic anhydrides via a nucleophilic ring-opening reaction. By varying the anhydride structure, the glass transition temperature ($T_g$) and surface hardness could be adjusted over a wide range. After network formation, the photolability of the $o$-NBE groups enabled a well-defined photocleavage of the network. FT-IR studies showed that the cleavage rate and cleavage yield increased with rising

network mobility, which is facilitated by the inherent network properties ($T_g$ below room temperature) or by simultaneous heating of the thermosets above their $T_g$. The formation of soluble species was confirmed by sol-gel analysis, which showed that networks with lower $T_g$ were more prone to secondary photoreactions at higher exposure dose, leading to a re-crosslinking of the cleaved polymer chains. This change in solubility properties was used to inscribe positive-tone micropatterns into thin films of the thermosets using photolithographic techniques. The contrast curve showed that the resist properties of the rigid network are superior compared to those of the flexible network with a contrast of 1.17 and a resolution of 8 µm. [246]

In a subsequent study, a novel method for writing, erasing and rewriting micropatterns was developed. For that, the *o*-NBE chemistry was combined with the dynamic nature of vitrimers. Thermal curing of an epoxide monomer comprising an *o*-NBE group and hexahydrophthalic anhydride was carried out in the presence of TBD yielding a dynamic covalent network whose solubility was locally controlled by UV irradiation. The photolysis of *o*-NBE chromophores enabled a well- defined cleavage of the epoxy anhydride network to form soluble photolysis products, which was verified by sol-gel analysis. The photo-induced change in solubility was exploited to inscribe micropatterns by photolithographic techniques and, after development in organic solvents, positive-tone structures with a feature size of 20 µm were obtained. Due to the thermally activated exchange reaction of the hydroxyl ester links and the associated macroscopic reflow, the polymer patterns were completely erased at temperatures well above the $T_v$ of the vitrimer network. The regenerated film had a smooth surface topology and could be reused to write new micropatterns using mask lithography. [249]

Further work on vitrimers involved the design of an epoxy-anhydride network with a high $T_g$ that comprised an efficient stress relaxation at elevated temperature. The vitrimer was prepared by thermal curing of aminoglycidyl monomer and glutaric anhydride in different stoichiometric ratios. The tertiary amine groups present in the structure of the aminoglycidyl derivative did not only accelerated the curing reaction, but also catalyzed the transesterification reaction above $T_v$ as shown by stress relaxation measurements. [250]The topology of the rearrangements enabled a reprocessing of the network suitable, which was demonstrated by pressing the grinded powder of the cured material in a hot press. Epoxy-anhydride vitrimers were characterized by a high $T_g$ (up to 140 °C) and a

high storage modulus at 25 °C (~2.5 GPa).The obtained materials are interesting candidates for structure applications operating at high temperatures. [250]

Finally, the four amine bases were studied towards their activity in catalyzing transesterifications in vitrimers. The individual catalysts were added into an epoxy-anhydride system, which was cured at 120 °C for 20 h. Depending on the catalyst, the $T_g$ varied between 66 and 166 °C. The networks were stable well above 200 °C and distinctive stress relaxation was observed at elevated temperature. The $T_v$ of the dynamic network varied between 45 °C (guanine as catalyst) and 215 °C (pyridine as catalyst).

The results of this thesis confirm the great scientific and industrial potential of stimuli-responsive polymers. On the one hand, light-induced systems were developed that allow a convenient switching between positive- and negative-tone resists. On the other hand, the dynamic nature of vitrimeric systems was applied to obtain high $T_g$ duromeric network with improved recyclability. In addition, the combination of these two concepts enabled the fabrication and reuse of resist materials.

With the introduction of vitrimers, a third main class has been added to the classical polymer classes (thermosets and thermoplastics). The unique viscoelastic properties, based on thermally triggered associative exchange reactions enable the materials to flow at the topology freezing transition temperature. This behavior makes them reprocessable and a potential candidate for industrial applications such as adhesives, resin substitutes or even thermosetting copolyesters for in-space assemblies. [295,296] As vitrimers lose their resistance to creep, one of the main challenges in research is to control the kinetics of the exchange reaction for the applications. [172] For future industrial applications, systems need to be developed that have high hardness and high dynamics at low induced temperatures. Further research should focus on the development of materials with controllable kinetics, which are stable towards harsh conditions, are upscalable, easily introduced in polymeric networks and do not degrade over time. [172] In addition, the number of effective, economic and ecological catalyst systems is limited so far. Further developments of efficient catalysts could broaden that subject. Since vitrimers, in principle, can be similar (re)processed as glass and metals, synthetic organic polymers may also evolve toward a new recognition as versatile, lightweight raw materials with high intrinsic value. [172]

As previously mentioned, *o*-NBE compounds have a great potential for various applications, such as acting as protecting groups for oligosaccharides synthesis, in biological fields as cell microarrays or as photoresponsive biomaterials for targeted drug delivery. [297,298] Regarding the development of photoresists by *o*-NBE chemistry, the resolution and mechanical stability could be improved to ensure the full performance of this methodology. For future studies, the introduction of monomers such as methacrylic *o*-NBE- monomers could enhance such properties. Further challenges, which arise due to the nature of these compounds, are the difficulties in thicker coatings due to the presence of byproducts that act as inner filter and the low penetration of UV light. [114] Possible solutions to overcome this limitation involves the use of two photons emission source or with the use of photobleaching compounds. [114,299]

In addition, in the last years 3D printing became one of the most studied fields in polymer engineering. Due to the low polymerization kinetics of the NB- monomers, the applicability in radical controlled polymerization for 3D printing is limited. [114] For future development in this flied in regard to NB-chemistry, the RAFT method and single electron transfer– living radical polymerization could be a promising candidate. [300,301]

As demonstrated in this thesis, the combination of these two areas could be a promising candidate for the recycling of photoresists. However, the mechanical properties have to be improved. For that, further studies should focus on improving the process parameters and a variety of monomers could be implemented.

The present work demonstrates the great potential of stimuli-responsive polymers and an outlook on the direction they could take to enable the vision of smart polymers in our everyday life. As shown, various stimuli can be applied to enable a change on a macroscopic and microscopic scale. Future research will need to focus on the combination of different stimuli, new mechanisms, enhancement of the efficiency and environmental aspects to accomplish the full potential of these materials and to establish them as part of the commonly used polymers.

# References

1.  Baker, I. *Fifty Materials That Make the World*; Springer International Publishing: Cham, 2018; ISBN 978-3-319-78764-0.

2.  Geyer, R.; Jambeck, J.R.; Law, K.L. Production, use, and fate of all plastics ever made. *Sci. Adv.* **2017**, *3*, e1700782, doi:10.1126/sciadv.1700782.

3.  Pohl, G. *Textiles, polymers and composites for buildings*; Woodhead Publishing Limited, 2010; ISBN 978-1-84569-397-8.

4.  Koltzenburg, S.; Maskos, M.; Nuyken, O. *Polymer Chemistry*; Springer Berlin Heidelberg: Berlin, Heidelberg, 2017; ISBN 978-3-662-49277-2.

5.  Ashutosh, T.; Hisatoshi, K. *Responsive Materials and Methods*; Tiwari, A., Kobayashi, H., Eds.; John Wiley & Sons, Inc.: Hoboken, NJ, USA, 2013; ISBN 9781118842843.

6.  Dai, S.; Ravi, P.; Tam, K.C. pH-Responsive polymers: synthesis, properties and applications. *Soft Matter* **2008**, *4*, 435, doi:10.1039/b714741d.

7.  SCHMALJOHANN, D. Thermo- and pH-responsive polymers in drug delivery. *Adv. Drug Deliv. Rev.* **2006**, *58*, 1655–1670, doi:10.1016/j.addr.2006.09.020.

8.  Jochum, F.D.; Theato, P. Temperature- and light-responsive smart polymer materials. *Chem. Soc. Rev.* **2013**, *42*, 7468–7483, doi:10.1039/c2cs35191a.

9.  Podgórski, M.; Fairbanks, B.D.; Kirkpatrick, B.E.; McBride, M.; Martinez, A.; Dobson, A.; Bongiardina, N.J.; Bowman, C.N. Toward Stimuli-Responsive Dynamic Thermosets through Continuous Development and Improvements in Covalent Adaptable Networks (CANs). *Adv. Mater.* **2020**, *32*, 1906876, doi:10.1002/adma.201906876.

10. Magnusson, J.P.; Khan, A.; Pasparakis, G.; Saeed, A.O.; Wang, W.; Alexander, C. Ion-Sensitive "Isothermal" Responsive Polymers Prepared in Water. *J. Am. Chem. Soc.* **2008**, *130*, 10852–10853, doi:10.1021/ja802609r.

11. Ueki, T. Stimuli-responsive polymers in ionic liquids. *Polym. J.* **2014**, *46*, 646–655, doi:10.1038/pj.2014.37.

12. García, M.C. Ionic-strength-responsive polymers for drug delivery applications. In *Stimuli Responsive Polymeric Nanocarriers for Drug Delivery Applications*;

Elsevier, 2019; pp. 393–409 ISBN 9780081019955.

13. Davis, D.A.; Hamilton, A.; Yang, J.; Cremar, L.D.; Van Gough, D.; Potisek, S.L.; Ong, M.T.; Braun, P. V.; Martínez, T.J.; White, S.R.; et al. Force-induced activation of covalent bonds in mechanoresponsive polymeric materials. *Nature* **2009**, *459*, 68–72, doi:10.1038/nature07970.

14. Colson, Y.L.; Grinstaff, M.W. Biologically responsive polymeric nanoparticles for drug delivery. *Adv. Mater.* **2012**, *24*, 3878–3886, doi:10.1002/adma.201200420.

15. Tanaka, T.; Sun, S.-T.; Hirokawa, Y.; Katayama, S.; Kucera, J.; Hirose, Y.; Amiya, T. Mechanical instability of gels at the phase transition. *Nature* **1987**, *325*, 796–798, doi:10.1038/325796a0.

16. TANAKA, T.; NISHIO, I.; SUN, S.-T.; UENO-NISHIO, S. Collapse of Gels in an Electric Field. *Science (80-. ).* **1982**, *218*, 467–469, doi:10.1126/science.218.4571.467.

17. Cui, J.; Del Campo, A. Photo-responsive polymers: properties, synthesis and applications. In *Smart Polymers and their Applications*; Elsevier, 2014; pp. 93–133 ISBN 9780857096951.

18. ter Schiphorst, J.; Saez, J.; Diamond, D.; Benito-Lopez, F.; Schenning, A.P.H.J. Light-responsive polymers for microfluidic applications. *Lab Chip* **2018**, *18*, 699–709, doi:10.1039/C7LC01297G.

19. Jochum, F.D.; zur Borg, L.; Roth, P.J.; Theato, P. Thermo- and Light-Responsive Polymers Containing Photoswitchable Azobenzene End Groups. *Macromolecules* **2009**, *42*, 7854–7862, doi:10.1021/ma901295f.

20. Kost, J.; Leong, K.; Langer, R. Ultrasonic Modulated Drug Delivery Systems. In *Polymers in Medicine II: Biomedical and Pharmaceutical Applications*; Chiellini, E., Giusti, P., Migliaresi, C., Nicolais, L., Eds.; Springer US: Boston, MA, 1986; pp. 387–396 ISBN 978-1-4613-1809-5.

21. Yakushiji, T.; Sakai, K.; Kikuchi, A.; Aoyagi, T.; Sakurai, Y.; Okano, T. Graft architectural effects on thermoresponsive wettability changes of poly(N-isopropylacrylamide)-modified surfaces. *Langmuir* **1998**, *14*, 4657–4662, doi:10.1021/la980090+.

22. Matsumura, S.; Hlil, A.R.; Lepiller, C.; Gaudet, J.; Guay, D.; Shi, Z.; Holdcroft, S.; Hay, A.S. Stability and Utility of Pyridyl Disulfide Functionality in RAFT and

Conventional Radical Polymerizations. *J. Polym. Sci. Part A Polym. Chem.* **2008**, *46*, 7207–7224, doi:10.1002/pola.

23.     Bajpai, A.K.; Shukla, S.K.; Bhanu, S.; Kankane, S. Responsive polymers in controlled drug delivery. *Prog. Polym. Sci.* **2008**, *33*, 1088–1118, doi:10.1016/j.progpolymsci.2008.07.005.

24.     Kuckling, D.; Richter, A.; Arndt, K.-F. Temperature and pH-Dependent Swelling Behavior of Poly(N-isopropylacrylamide) Copolymer Hydrogels and Their Use in Flow Control. *Macromol. Mater. Eng.* **2003**, *288*, 144–151, doi:10.1002/mame.200390007.

25.     Ma, M.; Guo, L.; Anderson, D.G.; Langer, R. Bio-inspired polymer composite actuator and generator driven by water gradients. *Science (80-. ).* **2013**, *339*, 186–189, doi:10.1126/science.1230262.

26.     Hu, J.; Liu, S. Responsive Polymers for Detection and Sensing Applications: Current Status and Future Developments. *Macromolecules* **2010**, *43*, 8315–8330, doi:10.1021/ma1005815.

27.     Quan, L. *Intelligent Stimuli-Responsive Materials*; Li, Q., Ed.; John Wiley & Sons, Inc.: Hoboken, NJ, USA, 2013; ISBN 9781118680469.

28.     Khutoryanskiy, V. V.; Georgiou, T.K. *Temperature-Responsive Polymers: Chemistry, Properties, and Applications*; Wiley-VCH, 2018; ISBN 978-1-119-15780-9.

29.     Wei, M.; Gao, Y.; Li, X.; Serpe, M.J. Stimuli-responsive polymers and their applications. *Polym. Chem.* **2017**, *8*, 127–143, doi:10.1039/c6py01585a.

30.     Montarnal, D.; Capelot, M.; Tournilhac, F.; Leibler, L. Silica-Like Malleable Materials from Permanent Organic Networks. *Science (80-. ).* **2011**, *334*, 965–968, doi:10.1126/science.1212648.

31.     Dimensions https://app.dimensions.ai Available online: https://app.dimensions.ai/discover/publication?search_mode=content&search_text =vitrimer&search_type=kws&search_field=full_search.

32.     Brown, B. *Excited states and photochemistry of organic molecules*; 1997; Vol. 53; ISBN 1560815884.

33.     Becker, Heinz G O H. Böttcher, F.D.; D. Rehorek, G. Roewer, K. Schiller, H.-J.T. *Einführung in die Photochemie*; 3rd ed.; Deutscher Verlag der Wissenschaften:

Berlin, 1991; ISBN 3136337026.

34. Wardle, B. *Principles and Applications of Photochemistry*; Wiley: Hoboken, 2009; ISBN 978-0-470-71013-5.

35. Schnabel, W. *Polymers and Light: Fundamentals and Technical Applications*; 2007; ISBN 9783527318667.

36. Vincenzo Balzani, Paola Ceroni, A.J. *Photochemistry and Photophysics: Concepts, Research, Applications*; Wiley-VCH: Weinheim, 2014; ISBN 978-3-527-67104-5.

37. Davies, M.L.; Douglas, P.; Evans, R.C.; Burrows, H.D. *Applied Photochemistry*; Evans, R.C., Douglas, P., Burrow, H.D., Eds.; Springer Netherlands: Dordrecht, 2013; Vol. 9789048138; ISBN 978-90-481-3829-6.

38. Fasani, E.; Albini, A. *Photochemistry: Volume 43*; 2015; Vol. 43; ISBN 978-1-78262-125-6.

39. Horspool, W.M.; Allen, N.S.; Cox, A.; Pratt, A.C.; Dunkin, I.; Harriman, A. (Tony) *Photochemistry*; Gilbert, A., Ed.; SPR - Photochemistry; The Royal Society of Chemistry, 1998; Vol. 29; ISBN 978-0-85404-415-3.

40. Clayden, J.; Greeves, N.; Warren, S.; Wothers, P. Organic Chemistry. *Am. Nat.* **2001**, *40*, 1990–1992, doi:10.1086/278635.

41. Bredas, J.L. Mind the gap! *Mater. Horizons* **2014**, *1*, 17–19, doi:10.1039/c3mh00098b.

42. Montalti, M.; Credi, A.; Prodi, L.; Gandolfi, M.T. *Handbook of Photochemistry: Third edition*; CRC Press, 2006; ISBN 9780824723774.

43. Chen, M.; Zhong, M.; Johnson, J.A. Light-Controlled Radical Polymerization: Mechanisms, Methods, and Applications. *Chem. Rev.* **2016**, *116*, 10167–10211, doi:10.1021/acs.chemrev.5b00671.

44. Persico, Maurizio; Granucci, G. *Photochemistry A Modern Theoretical Perspective*; 1st ed.; Springer: Heidelberg, 2018; ISBN 3319899716.

45. Andrew, G. *Photochemistry*; Gilbert, A., Ed.; Photochemistry; Royal Society of Chemistry: Cambridge, 1998; Vol. 31; ISBN 978-0-85404-415-3.

46. Bertrand, O.; Gohy, J.-F. Photo-responsive polymers: synthesis and applications. *Polym. Chem.* **2017**, *8*, 52–73, doi:10.1039/C6PY01082B.

47. Mendes-Felipe, C.; Oliveira, J.; Etxebarria, I.; Vilas-Vilela, J.L.; Lanceros-Mendez,

S. State-of-the-Art and Future Challenges of UV Curable Polymer-Based Smart Materials for Printing Technologies. *Adv. Mater. Technol.* **2019**, *4*, 1–16, doi:10.1002/admt.201800618.

48. Nakamura, K. *Photopolymers: Photoresist Materials, Processes, and Applications*; CRC Press, 2014; ISBN 9781466517318.

49. Fouassier, J.P.; Lalevée, J. *Photoinitiators for Polymer Synthesis: Scope, Reactivity and Efficiency*; 2012; ISBN 9783527332106.

50. Allen, N.S. *Photochemistry and Photophysics of Polymer Materials*; Allen, N.S., Ed.; John Wiley & Sons, Inc.: Hoboken, NJ, USA, 2010; ISBN 9780470594179.

51. Decker, C. Kinetic study and new applications of UV radiation curing. *Macromol. Rapid Commun.* **2002**, *23*, 1067–1093, doi:10.1002/marc.200290014.

52. Al Mousawi, A.; Garra, P.; Dumur, F.; Graff, B.; Fouassier, J.P.; Lalevée, J. Flavones as natural photoinitiators for light mediated free-radical polymerization via light emitting diodes. *J. Polym. Sci.* **2020**, *58*, 254–262, doi:10.1002/pol.20190044.

53. Stansbury, J.W.; Idacavage, M.J. 3D printing with polymers: Challenges among expanding options and opportunities. *Dent. Mater.* **2016**, *32*, 54–64, doi:10.1016/j.dental.2015.09.018.

54. Lee, H.; Lim, C.H.J.; Low, M.J.; Tham, N.; Murukeshan, V.M.; Kim, Y.J. Lasers in additive manufacturing: A review. *Int. J. Precis. Eng. Manuf. - Green Technol.* **2017**, *4*, 307–322, doi:10.1007/s40684-017-0037-7.

55. Corrigan, N.; Xu, J.; Boyer, C. A Photoinitiation System for Conventional and Controlled Radical Polymerization at Visible and NIR Wavelengths. *Macromolecules* **2016**, *49*, 3274–3285, doi:10.1021/acs.macromol.6b00542.

56. Vitale, A.; Trusiano, G.; Bongiovanni, R. UV-Curing of Adhesives: A Critical Review. *Prog. Adhes. Adhes.* **2018**, *3*, 101–154, doi:10.1002/9781119526445.ch4.

57. Uhl, W.; Kyriatsoulis, A. *Namen- und Schlagwortreaktionen in der Organischen Chemie*; B. G. Teubner Verlag: Wiesbaden, 1994; ISBN 978-3-663-02003-5.

58. Swenton, J.S. Photochemistry of organic compounds. I, Selected aspects of olefin photochemistry. *J. Chem. Educ.* **1969**, *46*, 7, doi:10.1021/ed046p7.

59. Tehfe, M.-A.; Dumur, F.; Graff, B.; Morlet-Savary, F.; Gigmes, D.; Fouassier, J.-P.;

Lalevée, J. Design of new Type I and Type II photoinitiators possessing highly coupled pyrene–ketone moieties. *Polym. Chem.* **2013**, *4*, 2313, doi:10.1039/c3py21079k.

60.     Sumiyoshi, T.; Schnabel, W.; Henne, A. The photolysis of acylphosphine oxides. *J. Photochem.* **1986**, *32*, 191–201, doi:10.1016/0047-2670(86)87008-3.

61.     Jiang, F.; Drummer, D. Curing Kinetic Analysis of Acrylate Photopolymer for Additive Manufacturing by Photo-DSC. *Polymers (Basel).* **2020**, *12*, 1080, doi:10.3390/polym12051080.

62.     Crivello, J. V.; Kong, S. Synthesis and Characterization of Second-Generation Dialkylphenacylsulforiium Salt Photoinitiators. *Macromolecules* **2000**, *33*, 825–832, doi:10.1021/ma991661n.

63.     Allen, N.S. Photoinitiators for UV and visible curing of coatings: Mechanisms and properties. *J. Photochem. Photobiol. A Chem.* **1996**, *100*, 101–107, doi:10.1016/S1010-6030(96)04426-7.

64.     Norrish, R.G.W. On the principle of primary recombination in relation to the velocity of thermal reactions in solution. *Trans. Faraday Soc.* **1937**, *33*, 1521, doi:10.1039/tf9373301521.

65.     Coyle, J.D. Introduction to organic photochemistry. *Photochemistry* 1986, 1–176.

66.     Alvarez-Dorta, D.; León, E.I.; Kennedy, A.R.; Martín, A.; Pérez-Martín, I.; Riesco-Fagundo, C.; Suárez, E. Sequential Norrish Type II Photoelimination and Intramolecular Aldol Cyclization of α-Diketones: Synthesis of Polyhydroxylated Cyclopentitols by Ring Contraction of Hexopyranose Carbohydrate Derivatives. *Chem. - A Eur. J.* **2013**, *19*, 10312–10333, doi:10.1002/chem.201301230.

67.     Arsu, N.; Aydin, M.; Yagci, Y.; Jockusch, S.; Turro, N.J. One component thioxanthone based Type II photoinitiators in Photochemistry and UV Curing: New Trends. *Res. Signpost* **2006**, 20–32.

68.     Kamoun, E.A.; Winkel, A.; Eisenburger, M.; Menzel, H. Carboxylated camphorquinone as visible-light photoinitiator for biomedical application: Synthesis, characterization, and application Carboxylated camphorquinone as visible-light photoinitiator. *Arab. J. Chem.* **2016**, *9*, 745–754, doi:10.1016/j.arabjc.2014.03.008.

69.     Monroe, B.M.; Weed, G.C. Photoinitiators for free-radical-initiated photoimaging

systems. *Chem. Rev.* **1993**, *93*, 435–448, doi:10.1021/cr00017a019.

70. Barltrop, J.A.; Giles, D. Studies in organic photochemistry. Part X. The photochemical addition of cyclohexene-1,4-diones to olefins and acetylenes. *J. Chem. Soc. C Org.* **1969**, *49*, 105, doi:10.1039/j39690000105.

71. Jamalullail, N.; Mohamad, I.S.; Norizan, M.N.; Baharum, N.A.; Mahmed, N. Short review: Natural pigments photosensitizer for dye-sensitized solar cell (DSSC). In Proceedings of the 2017 IEEE 15th Student Conference on Research and Development (SCOReD); IEEE, 2017; Vol. 2018-Janua, pp. 344–349.

72. Wypych, G. *Handbook of Odors in Plastic Materials*; Secound Ed.; ChemTec Publishing: Toronto, Canada, 2017; ISBN 978-1-895198-98-0.

73. Ehrenstein, G.W.; Pongratz, S. *Resistance and Stability of Polymers*; Carl Hanser Verlag GmbH & Co. KG: München, 2013; ISBN 978-3-446-41645-1.

74. Lu, T.; Solis-Ramos, E.; Yi, Y.; Kumosa, M. UV degradation model for polymers and polymer matrix composites. *Polym. Degrad. Stab.* **2018**, *154*, 203–210, doi:10.1016/j.polymdegradstab.2018.06.004.

75. Fouassier, J.P.; Lalevée, J. Photochemical production of interpenetrating polymer networks; Simultaneous initiation of radical and cationic polymerization reactions. *Polymers (Basel).* **2014**, *6*, 2588–2610, doi:10.3390/polym6102588.

76. Javadi, A.; Mehr, H.S.; Sobani, M.; Soucek, M.D. Cure-on-command technology: A review of the current state of the art. *Prog. Org. Coatings* **2016**, *100*, 2–31, doi:10.1016/j.porgcoat.2016.02.014.

77. Crivello, J.V.; Reichmanis, E. Photopolymer materials and processes for advanced technologies. *Chem. Mater.* 2014, *26*, 533–548.

78. Crivello, J.V. The Discovery and Development of Onium Salt. *J. Polym. Sci.* **1999**, *37*, 4241–4254.

79. Crivello, J. V.; Lam, J.H.W. Diaryliodonium Salts. A New Class of Photoinitiators for Cationic Polymerization. *Macromolecules* **1977**, *10*, 1307–1315, doi:10.1021/ma60060a028.

80. Li, M.; Wang, S.; Li, F.; Zhou, L.; Lei, L. Organocatalyzed atom transfer radical polymerization (ATRP) using triarylsulfonium hexafluorophosphate salt (THS) as a photocatalyst. *Polym. Chem.* **2020**, *11*, 2222–2229, doi:10.1039/C9PY01742A.

81. Banerjee, S.; Paira, T.K.; Kotal, A.; Mandal, T.K. Room temperature living cationic

polymerization of styrene with HX-styrenic monomer adduct/FeCl3 systems in the presence of tetrabutylammonium halide and tetraalkylphosphonium bromide salts. *Polymer (Guildf).* **2010**, *51*, 1258–1269, doi:10.1016/j.polymer.2010.01.051.

82.    Odian, G. *Principles of Polymerization*; John Wiley & Sons, Inc.: Hoboken, NJ, USA, 2004; Vol. 37; ISBN 0471274003.

83.    Guillet, J.E. Fundamental processes in the uv degradation and stabilization of polymers. *Pure Appl. Chem.* **1972**, *30*, 135–144, doi:10.1351/pac197230010135.

84.    Arulkashmir, A.; Bhosale, M.E.; Krishnamoorthy, K. Cleavable and removable polymer thermosets for organic field effect transistor packaging. *RSC Adv.* **2013**, *3*, 22591, doi:10.1039/c3ra43320j.

85.    MacDonald, S.A.; Willson, C.G.; Fréchet, J.M.J. Chemical Amplification in High-Resolution Imaging Systems. *Acc. Chem. Res.* **1994**, *27*, 151–158, doi:10.1021/ar00042a001.

86.    Nechifor, C.D.; Dorohoi, D.O.; Ciobanu, C. The influence of gamma radiations on physico-chemical properties of some polymer membranes. *Rom. Reports Phys.* **2009**, *54*, 349–359, doi:10.1007/12.

87.    Zhang, Z.P.; Rong, M.Z.; Zhang, M.Q. Polymer engineering based on reversible covalent chemistry: A promising innovative pathway towards new materials and new functionalities. *Prog. Polym. Sci.* **2018**, *80*, 39–93, doi:10.1016/j.progpolymsci.2018.03.002.

88.    Doh, J.; Irvine, D.J. Photogenerated Polyelectrolyte Bilayers from an Aqueous-Processible Photoresist for Multicomponent Protein Patterning. *J. Am. Chem. Soc.* **2004**, *126*, 9170–9171, doi:10.1021/ja048261m.

89.    Barltrop, J.A.; Plant, P.J.; Schofield, P. Photosensitive protective groups. *Chem. Commun.* **1966**, *92*, 822, doi:10.1039/c19660000822.

90.    Patchornik, A.; Amit, B.; Woodward, R.B. Photosensitive protecting groups. *J. Am. Chem. Soc.* **1970**, *92*, 6333–6335, doi:10.1021/ja00724a041.

91.    Wang, P. Photolabile protecting groups: Structure and reactivity. *Asian J. Org. Chem.* **2013**, *2*, 452–464, doi:10.1002/ajoc.201200197.

92.    Romano, A.; Roppolo, I.; Giebler, M.; Dietliker, K.; Možina; Šket, P.; Mühlbacher, I.; Schlögl, S.; Sangermano, M. Stimuli-responsive thiol-epoxy networks with photo-switchable bulk and surface properties. *RSC Adv.* **2018**, *8*, 41904–41914,

doi:10.1039/c8ra08937j.

93. Radl, S.; Kreimer, M.; Manhart, J.; Griesser, T.; Moser, A.; Pinter, G.; Kalinka, G.; Kern, W.; Schlögl, S. Photocleavable epoxy based materials. *Polymer (Guildf).* **2015**, *69*, 159–168, doi:10.1016/j.polymer.2015.05.055.

94. Il'ichev, Y. V.; Schwörer, M.A.; Wirz, J. Photochemical Reaction Mechanisms of 2-Nitrobenzyl Compounds: Methyl Ethers and Caged ATP. *J. Am. Chem. Soc.* **2004**, *126*, 4581–4595, doi:10.1021/ja039071z.

95. Bamford, C.H.; Norrish, R.G.W. 359. Primary photochemical reactions. Part VII. Photochemical decomposition of isovaleraldehyde and di-n-propyl ketone. *J. Chem. Soc.* **1935**, 1504, doi:10.1039/jr9350001504.

96. Kim, M.S.; Diamond, S.L. Photocleavage of o-nitrobenzyl ether derivatives for rapid biomedical release applications. *Bioorganic Med. Chem. Lett.* **2006**, *16*, 4007–4010, doi:10.1016/j.bmcl.2006.05.013.

97. Guillier, F.; Orain, D.; Bradley, M. Linkers and cleavage strategies in solid-phase organic synthesis and combinatorial chemistry. *Chem. Rev.* **2000**, *100*, 2091–2157, doi:10.1021/cr980040+.

98. Pelliccioli, A.P.; Wirz, J. Photoremovable protecting groups: reaction mechanisms and applications. *Photochem. Photobiol. Sci.* **2002**, *1*, 441–458, doi:10.1039/b200777k.

99. Zhao, H.; Sterner, E.S.; Coughlin, E.B.; Theato, P. O-Nitrobenzyl alcohol derivatives: Opportunities in polymer and materials science. *Macromolecules* 2012, *45*, 1723–1736.

100. Kamatham, N.; Raj, A.M.; Givens, R.S.; Da Silva, J.P.; Ramamurthy, V. Supramolecular photochemistry of encapsulated caged: Ortho -nitrobenzyl triggers. *Photochem. Photobiol. Sci.* **2019**, *18*, 2411–2420, doi:10.1039/c9pp00260j.

101. Romano, A.; Angelini, A.; Rossegger, E.; Palmara, G.; Castellino, M.; Frascella, F.; Chiappone, A.; Chiadò, A.; Sangermano, M.; Schlögl, S.; et al. Laser-Triggered Writing and Biofunctionalization of Thiol-Ene Networks. *Macromol. Rapid Commun.* **2020**, *2000084*, 1–7, doi:10.1002/marc.202000084.

102. Rossegger, E.; Nees, D.; Turisser, S.; Radl, S.; Griesser, T.; Schlögl, S. Photo-switching of surface wettability on micropatterned photopolymers for fast transport

of water droplets over a long-distance. *Polym. Chem.* **2020**, doi:10.1039/d0py00263a.

103. Rossegger, E.; Hennen, D.; Griesser, T.; Roppolo, I.; Schlögl, S. Directed motion of water droplets on multi-gradient photopolymer surfaces. *Polym. Chem.* **2019**, *10*, 1882–1893, doi:10.1039/c9py00123a.

104. Choi, S.K. Photocleavable linkers. In *Photonanotechnology for Therapeutics and Imaging*; Elsevier, 2020; pp. 243–275 ISBN 9780128178409.

105. Cabane, E.; Zhang, X.; Langowska, K.; Palivan, C.G.; Meier, W. Stimuli-responsive polymers and their applications in nanomedicine. *Biointerphases* **2012**, *7*, 1–27, doi:10.1007/s13758-011-0009-3.

106. Dcona, M.M. Applications of ortho-Nitrobenzyl photocage in cancer-biology. **2018**.

107. Milburn, T.; Matsubara, N.; Billington, A.P.; Udgaonkar, J.B.; Walker, J.W.; Carpenter, B.K.; Webb, W.W.; Marque, J.; Denk, W. Synthesis, photochemistry, and biological activity of a caged photolabile acetylcholine receptor ligand. *Biochemistry* **1989**, *28*, 49–55, doi:10.1021/bi00427a008.

108. Houlihan, F.M.; Shugard, A.; Gooden, R.; Reichmanis, E. An Evaluation Of Nitrobenzyl Ester Chemistry For Chemical Amplification Resists. In Proceedings of the Advances in Resist Technology and Processing V; MacDonald, S.A., Ed.; 1988; Vol. 0920, p. 67.

109. Cameron, J.F.; Frechet, J.M.J. Photogeneration of organic bases from o-nitrobenzyl-derived carbamates. *J. Am. Chem. Soc.* **1991**, *113*, 4303–4313, doi:10.1021/ja00011a038.

110. Foote, R.S.; Cornwell, P.; Isham, K.R.; Gigerich, H.; Stengele, K.-P.; Pfleiderer, W.; Sachleben, R.A. Photolabile Protecting Groups for Nucleosides:synthesis and Photodeprotection Rates. *Tetrahedron* **1997**, *53*, 4247–4264.

111. Schwalm, R. Lithographic Evaluation of One-Component Deep-UV Resists Containing o-Nitrobenzyl Ester Moieties. *J. Electrochem. Soc.* **1989**, *136*, 3471–3476, doi:10.1149/1.2096487.

112. Reichmanis, E.; Smith, B.C.; Gooden, R. O-nitrobenzyl photochemistry: Solution vs. solid-state behavior. *J. Polym. Sci. Polym. Chem. Ed.* **1985**, *23*, 1–8, doi:10.1002/pol.1985.170230101.

113. Reichmanis, E.; Gooden, R.; Wilkins, C.W.; Schonhorn, H. A study of the

photochemical response of o-nitrobenzyl cholate derivatives in P(MMA-MAA) matrices. *J. Polym. Sci. Polym. Chem. Ed.* **1983**, *21*, 1075–1083, doi:10.1002/pol.1983.170210415.

114. Romano, A.; Roppolo, I.; Rossegger, E.; Schlögl, S.; Sangermano, M. Recent Trends in Applying Ortho-Nitrobenzyl Esters for the Design of Photo-Responsive Polymer Networks. *Materials (Basel).* **2020**, *13*, 2777, doi:10.3390/ma13122777.

115. Taylor, P.G.; Lee, J.-K.; Zakhidov, A.A.; Chatzichristidi, M.; Fong, H.H.; DeFranco, J.A.; Malliaras, G.G.; Ober, C.K. Orthogonal Patterning of PEDOT:PSS for Organic Electronics using Hydrofluoroether Solvents. *Adv. Mater.* **2009**, *21*, 2314–2317, doi:10.1002/adma.200803291.

116. Gumbley, P.; Koylu, D.; Pawle, R.H.; Umezuruike, B.; Spedden, E.; Staii, C.; Thomas, S.W. Wavelength-Selective Disruption and Triggered Release with Photolabile Polyelectrolyte Multilayers. *Chem. Mater.* **2014**, *26*, 1450–1456, doi:10.1021/cm403979p.

117. Jiang, X.; Zheng, H.; Gourdin, S.; Hammond, P.T. Polymer-on-Polymer Stamping: Universal Approaches to Chemically Patterned Surfaces. *Langmuir* **2002**, *18*, 2607–2615, doi:10.1021/la011098d.

118. Crivello, J. V.; Reichmanis, E. Photopolymer materials and processes for advanced technologies. *Chem. Mater.* **2014**, *26*, 533–548, doi:10.1021/cm402262g.

119. Kemp, K.; Wurm, S. EUV lithography. *Comptes Rendus Phys.* **2006**, *7*, 875–886, doi:10.1016/j.crhy.2006.10.002.

120. Ronse, K. Optical lithography-a historical perspective. *Comptes Rendus Phys.* **2006**, *7*, 844–857, doi:10.1016/j.crhy.2006.10.007.

121. Burns, K.; Adams, K.B.; Longwell, J. Interference Measurements in the Spectra of Neon and Natural Mercury. *J. Opt. Soc. Am.* **1950**, *40*, 339, doi:10.1364/JOSA.40.000339.

122. Thompson, L.F.; Willson, C.G.; Bowden, M.J. *Introduction to microlithography*; 1994; ISBN 0841228485.

123. Feuer, M.D.; Prober, D.E. Projection Photolithography-Liftoff Techniques for Production of 0.2-μm Metal Patterns. *IEEE Trans. Electron Devices* **1981**, *28*, 1375–1378, doi:10.1109/T-ED.1981.20616.

124. El-Kareh, B. *Fundamentals of Semiconductor Processing Technology*; Springer US: Boston, MA, 1995; ISBN 978-1-4613-5927-2.

125. Mack, C. *Fundamental Principles of Optical Lithography*; John Wiley & Sons, Ltd: Chichester, UK, 2007; ISBN 9780470723876.

126. Moreau, W.M. *Semiconductor Lithography*; Springer US: Boston, MA, 1988; ISBN 978-1-4612-8228-0.

127. Seisyan, R.P. Nanolithography in microelectronics: A review. *Tech. Phys.* **2011**, *56*, 1061–1073, doi:10.1134/S1063784211080214.

128. Shaw, J.M.; Gelorme, J.D.; LaBianca, N.C.; Conley, W.E.; Holmes, S.J. Negative photoresists for optical lithography. *IBM J. Res. Dev.* **1997**, *41*, 81–94, doi:10.1147/rd.411.0081.

129. Yeh, W.-M.; Noga, D.E.; Lawson, R.A.; Tolbert, L.M.; Henderson, C.L. Comparison of positive tone versus negative tone resist pattern collapse behavior. *J. Vac. Sci. Technol. B, Nanotechnol. Microelectron. Mater. Process. Meas. Phenom.* **2010**, *28*, C6S6-C6S11, doi:10.1116/1.3518136.

130. Brunner, T.A.; Fonseca, C.A. Optimum tone for various feature types: positive versus negative. *Adv. Resist Technol. Process. XVIII* **2001**, *4345*, 30, doi:10.1117/12.436866.

131. Huang, Z.; Geyer, N.; Werner, P.; de Boor, J.; Gösele, U. Metal-Assisted Chemical Etching of Silicon: A Review. *Adv. Mater.* **2011**, *23*, 285–308, doi:10.1002/adma.201001784.

132. Hell, S.W. Far-Field Optical Nanoscopy. *Science (80-. ).* **2007**, *316*, 1153–1158, doi:10.1126/science.1137395.

133. Moore, G.E. Cramming more components onto integrated circuits, Reprinted from Electronics, volume 38, number 8, April 19, 1965, pp.114 ff. *IEEE Solid-State Circuits Soc. Newsl.* **2006**, *11*, 33–35, doi:10.1109/N-SSC.2006.4785860.

134. Das, U.K.; Bhattacharyya, T.K. Opportunities in Device Scaling for 3-nm Node and Beyond: FinFET Versus GAA-FET Versus UFET. *IEEE Trans. Electron Devices* **2020**, *67*, 2633–2638, doi:10.1109/TED.2020.2987139.

135. Schellenberg, F.M. A History of Resolution Enhancement Technology. *Opt. Rev.* **2005**, *12*, 83–89, doi:10.1007/s10043-004-0083-6.

136. Schellenberg, F.M. Resolution enhancement technology: the past, the present,

and extensions for the future. *Opt. Microlithogr. XVII* **2004**, *5377*, 1, doi:10.1117/12.548923.

137. Guo, L.J. Nanoimprint Lithography: Methods and Material Requirements. *Adv. Mater.* **2007**, *19*, 495–513, doi:10.1002/adma.200600882.

138. Alexander Liddle, J.; Gallatin, G.M.; Ocola, L.E. Resist Requirements and Limitations for Nanoscale Electron-Beam Patterning. *MRS Proc.* **2002**, *739*, H1.5, doi:10.1557/PROC-739-H1.5.

139. Griffing, B.F.; West, P.R. Contrast enhanced photoresists—processing and modeling. *Polym. Eng. Sci.* **1983**, *23*, 947–952, doi:10.1002/pen.760231706.

140. Arthur B. Glaser, G.E.S.-S. *Integrated Circuit Engineering: Design, Fabrication and Application*; Addison Wesley Longman: New York, United States, 1978; ISBN 9780201074277.

141. Wake, R.W.; Flanigan, M.C. A Review Of Contrast In Positive Photoresists. In Proceedings of the Journal of Chemical Information and Modeling; Thompson, L.F., Ed.; 1985; Vol. 53, p. 291.

142. Oldham, W.G. The Use of Contrast Enhancement Layers to Improve the Effective Contrast of Positive Photoresist. *IEEE Trans. Electron Devices* **1987**, *34*, 247–251, doi:10.1109/T-ED.1987.22914.

143. Campbell, Stephen, A. *The Science and Engineering of Microelectronic Fabrication-Oxford University Press*; 1st ed.; Oxford University Press: New York, United States, 1996;

144. Kirchauer, H. Photolithography Simulation, Technical University Vienna, 1998.

145. Zou, W.; Dong, J.; Luo, Y.; Zhao, Q.; Xie, T. Dynamic Covalent Polymer Networks: from Old Chemistry to Modern Day Innovations. *Adv. Mater.* **2017**, *29*, doi:10.1002/adma.201606100.

146. Van Zee, N.J.; Nicolaÿ, R. Vitrimers: Permanently crosslinked polymers with dynamic network topology. *Prog. Polym. Sci.* **2020**, *104*, 101233, doi:10.1016/j.progpolymsci.2020.101233.

147. Ruiz de Luzuriaga, A.; Martin, R.; Markaide, N.; Rekondo, A.; Cabañero, G.; Rodríguez, J.; Odriozola, I. Epoxy resin with exchangeable disulfide crosslinks to obtain reprocessable, repairable and recyclable fiber-reinforced thermoset composites. *Mater. Horizons* **2016**, *3*, 241–247, doi:10.1039/C6MH00029K.

148. Takahashi, A.; Ohishi, T.; Goseki, R.; Otsuka, H. Degradable epoxy resins prepared from diepoxide monomer with dynamic covalent disulfide linkage. *Polymer (Guildf).* **2016**, *82*, 319–326, doi:10.1016/j.polymer.2015.11.057.

149. Kuang, X.; Zhou, Y.; Shi, Q.; Wang, T.; Qi, H.J. Recycling of Epoxy Thermoset and Composites via Good Solvent Assisted and Small Molecules Participated Exchange Reactions. *ACS Sustain. Chem. Eng.* **2018**, *6*, 9189–9197, doi:10.1021/acssuschemeng.8b01538.

150. Rousseau, I.A.; Xie, T. Shape memory epoxy: Composition, structure, properties and shape memory performances. *J. Mater. Chem.* **2010**, *20*, 3431, doi:10.1039/b923394f.

151. Lewis, C.L.; Dell, E.M. A review of shape memory polymers bearing reversible binding groups. *J. Polym. Sci. Part B Polym. Phys.* **2016**, *54*, 1340–1364, doi:10.1002/polb.23994.

152. Bowman, C.; Du Prez, F.; Kalow, J. Introduction to chemistry for covalent adaptable networks. *Polym. Chem.* **2020**, *11*, 5295–5296, doi:10.1039/d0py90102d.

153. Chao, A.; Zhang, D. Investigation of Secondary Amine-Derived Aminal Bond Exchange toward the Development of Covalent Adaptable Networks. *Macromolecules* **2019**, *52*, 495–503, doi:10.1021/acs.macromol.8b02654.

154. Amamoto, Y.; Otsuka, H.; Takahara, A.; Matyjaszewski, K. Self-Healing of Covalently Cross-Linked Polymers by Reshuffling Thiuram Disulfide Moieties in Air under Visible Light. *Adv. Mater.* **2012**, *24*, 3975–3980, doi:10.1002/adma.201201928.

155. Amamoto, Y.; Kamada, J.; Otsuka, H.; Takahara, A.; Matyjaszewski, K. Repeatable Photoinduced Self-Healing of Covalently Cross-Linked Polymers through Reshuffling of Trithiocarbonate Units. *Angew. Chemie Int. Ed.* **2011**, *50*, 1660–1663, doi:10.1002/anie.201003888.

156. Li, Q.; Liu, C.; Wen, J.; Wu, Y.; Shan, Y.; Liao, J. The design, mechanism and biomedical application of self-healing hydrogels. *Chinese Chem. Lett.* **2017**, *28*, 1857–1874, doi:10.1016/j.cclet.2017.05.007.

157. Wu, Y.; Wang, L.; Zhao, X.; Hou, S.; Guo, B.; Ma, P.X. Self-healing supramolecular bioelastomers with shape memory property as a multifunctional

platform for biomedical applications via modular assembly. *Biomaterials* **2016**, *104*, 18–31, doi:10.1016/j.biomaterials.2016.07.011.

158. Yang, H.; Yu, K.; Mu, X.; Shi, X.; Wei, Y.; Guo, Y.; Qi, H.J. A molecular dynamics study of bond exchange reactions in covalent adaptable networks. *Soft Matter* **2015**, *11*, 6305–6317, doi:10.1039/C5SM00942A.

159. Jourdain, A.; Asbai, R.; Anaya, O.; Chehimi, M.M.; Drockenmuller, E.; Montarnal, D. Rheological Properties of Covalent Adaptable Networks with 1,2,3-Triazolium Cross-Links: The Missing Link between Vitrimers and Dissociative Networks. *Macromolecules* **2020**, *53*, 1884–1900, doi:10.1021/acs.macromol.9b02204.

160. Xu, C.; Cui, R.; Fu, L.; Lin, B. Recyclable and heat-healable epoxidized natural rubber/bentonite composites. *Compos. Sci. Technol.* **2018**, *167*, 421–430, doi:10.1016/j.compscitech.2018.08.027.

161. Chatani, S.; Kloxin, C.J.; Bowman, C.N. The power of light in polymer science: Photochemical processes to manipulate polymer formation, structure, and properties. *Polym. Chem.* **2014**, *5*, 2187–2201, doi:10.1039/c3py01334k.

162. Lyon, G.B.; Cox, L.M.; Goodrich, J.T.; Baranek, A.D.; Ding, Y.; Bowman, C.N. Remoldable Thiol-Ene Vitrimers for Photopatterning and Nanoimprint Lithography. *Macromolecules* **2016**, *49*, 8905–8913, doi:10.1021/acs.macromol.6b01281.

163. Campanella, A.; Döhler, D.; Binder, W.H. Self-Healing in Supramolecular Polymers. *Macromol. Rapid Commun.* **2018**, *39*, 1–19, doi:10.1002/marc.201700739.

164. Thakur, V.K.; Kessler, M.R. Self-healing polymer nanocomposite materials: A review. *Polymer (Guildf).* **2015**, *69*, 369–383, doi:10.1016/j.polymer.2015.04.086.

165. Fischer, H. Self-repairing material systems—a dream or a reality? *Nat. Sci.* **2010**, *02*, 873–901, doi:10.4236/ns.2010.28110.

166. Krishnakumar, B.; Sanka, R.V.S.P.; Binder, W.H.; Parthasarthy, V.; Rana, S.; Karak, N. Vitrimers: Associative dynamic covalent adaptive networks in thermoset polymers. *Chem. Eng. J.* **2020**, *385*, 123820, doi:10.1016/j.cej.2019.123820.

167. Greenland, B.W.; Hayes, W. *Healable Polymer Systems*; 2013; ISBN 978-1-84973-626-8.

168. Liu, T.; Zhao, B.; Zhang, J. Recent development of repairable, malleable and recyclable thermosetting polymers through dynamic transesterification. *Polymer*

*(Guildf).* **2020**, *194*, 122392, doi:10.1016/j.polymer.2020.122392.

169. Kloxin, C.J.; Scott, T.F.; Adzima, B.J.; Bowman, C.N. Covalent Adaptable Networks (CANs): A Unique Paradigm in Cross-Linked Polymers. *Macromolecules* **2010**, *43*, 2643–2653, doi:10.1021/ma902596s.

170. Bowman, C.N.; Kloxin, C.J. Covalent adaptable networks: Reversible bond structures incorporated in polymer networks. *Angew. Chemie - Int. Ed.* **2012**, *51*, 4272–4274, doi:10.1002/anie.201200708.

171. Winne, J.M.; Leibler, L.; Du Prez, F. Dynamic Covalent Chemistry in Polymer Networks: A Mechanistic Perspective. *Polym. Chem.* **2019**, *10*, 6091–6108, doi:10.1039/c9py01260e.

172. Denissen, W.; Winne, J.M.; Du Prez, F.E. Vitrimers: permanent organic networks with glass-like fluidity. *Chem. Sci.* **2016**, *7*, 30–38, doi:10.1039/C5SC02223A.

173. Obadia, M.M.; Mudraboyina, B.P.; Serghei, A.; Montarnal, D.; Drockenmuller, E. Reprocessing and Recycling of Highly Cross-Linked Ion-Conducting Networks through Transalkylation Exchanges of C-N Bonds. *J. Am. Chem. Soc.* **2015**, *137*, 6078–6083, doi:10.1021/jacs.5b02653.

174. Obadia, M.M.; Jourdain, A.; Cassagnau, P.; Montarnal, D.; Drockenmuller, E. Tuning the Viscosity Profile of Ionic Vitrimers Incorporating 1,2,3-Triazolium Cross-Links. *Adv. Funct. Mater.* **2017**, *27*, 1–10, doi:10.1002/adfm.201703258.

175. Montarnal, D.; Delbosc, N.; Chamignon, C.; Virolleaud, M.-A.; Luo, Y.; Hawker, C.J.; Drockenmuller, E.; Bernard, J. Highly Ordered Nanoporous Films from Supramolecular Diblock Copolymers with Hydrogen-Bonding Junctions. *Angew. Chemie Int. Ed.* **2015**, *54*, 11117–11121, doi:10.1002/anie.201504838.

176. Hendriks, B.; Waelkens, J.; Winne, J.M.; Du Prez, F.E. Poly(thioether) Vitrimers via Transalkylation of Trialkylsulfonium Salts. *ACS Macro Lett.* **2017**, *6*, 930–934, doi:10.1021/acsmacrolett.7b00494.

177. Zhang, Z.; Chen, Q.; Colby, R.H. Dynamics of associative polymers. *Soft Matter* **2018**, *14*, 2961–2977, doi:10.1039/c8sm00044a.

178. Marref, M.; Mignard, N.; Jegat, C.; Taha, M.; Belbachir, M.; Meghabar, R. Epoxy-amine based thermoresponsive networks designed by Diels-Alder reactions. *Polym. Int.* **2013**, *62*, 87–98, doi:10.1002/pi.4287.

179. Scott, T.F.; Schneider, A.D.; Cook, W.D.; Bowman, C.N. Chemistry: Photoinduced

plasticity in cross-linked polymers. *Science (80-. ).* **2005**, *308*, 1615–1617, doi:10.1126/science.1110505.

180. Denissen, W.; Rivero, G.; Nicolaÿ, R.; Leibler, L.; Winne, J.M.; Du Prez, F.E. Vinylogous urethane vitrimers. *Adv. Funct. Mater.* **2015**, *25*, 2451–2457, doi:10.1002/adfm.201404553.

181. Nishimura, Y.; Chung, J.; Muradyan, H.; Guan, Z. Silyl Ether as a Robust and Thermally Stable Dynamic Covalent Motif for Malleable Polymer Design. *J. Am. Chem. Soc.* **2017**, *139*, 14881–14884, doi:10.1021/jacs.7b08826.

182. Worrell, B.T.; McBride, M.K.; Lyon, G.B.; Cox, L.M.; Wang, C.; Mavila, S.; Lim, C.H.; Coley, H.M.; Musgrave, C.B.; Ding, Y.; et al. Bistable and photoswitchable states of matter. *Nat. Commun.* **2018**, *9*, doi:10.1038/s41467-018-05300-7.

183. Chakma, P.; Konkolewicz, D. Dynamic Covalent Bonds in Polymeric Materials. *Angew. Chemie - Int. Ed.* **2019**, *58*, 9682–9695, doi:10.1002/anie.201813525.

184. Reutenauer, P.; Buhler, E.; Boul, P.J.; Candau, S.J.; Lehn, J.M. Room temperature dynamic polymers based on Diels-Alder chemistry. *Chem. - A Eur. J.* **2009**, *15*, 1893–1900, doi:10.1002/chem.200802145.

185. Inglis, A.J.; Nebhani, L.; Altintas, O.; Schmidt, F.G.; Barner-Kowollik, C. Rapid bonding/debonding on demand: Reversibly cross-linked functional polymers via diels-alder chemistry. *Macromolecules* **2010**, *43*, 5515–5520, doi:10.1021/ma100945b.

186. Ying, H.; Zhang, Y.; Cheng, J. Dynamic urea bond for the design of reversible and self-healing polymers. *Nat. Commun.* **2014**, *5*, 1–9, doi:10.1038/ncomms4218.

187. Craven, J.M. Cross-linked thermally reversible polymers produced from condensation polymers with pendant furan groups cross-linked with maleimides 1966.

188. Kuhl, N.; Geitner, R.; Vitz, J.; Bode, S.; Schmitt, M.; Popp, J.; Schubert, U.S.; Hager, M.D. Increased stability in self-healing polymer networks based on reversible Michael addition reactions. *J. Appl. Polym. Sci.* **2017**, *134*, 2541–2550, doi:10.1002/app.44805.

189. Pascault, J.-P.; W.R.J.J. *Epoxy Polymers: New Materials and Innovations*; Pascault, J., Williams, R.J.J., Eds.; Wiley, 2009; ISBN 9783527324804.

190. May, C. *Epoxy resins: chemistry and technology (2nd edition)*; CRC Press, 1987;

ISBN 9780824776909.

191. Blank, W.J.; He, Z.A.; Picci, M. Catalysis of the epoxy-carboxyl reaction. *J. Coatings Technol.* **2002**, *74*, 33–41, doi:10.1007/BF02720158.

192. *Epoxy Resins and Composites I*; Advances in Polymer Science; Springer Berlin Heidelberg: Berlin, Heidelberg, 1985; Vol. 72; ISBN 978-3-540-15546-1.

193. Mauri, A.N.; Galego, N.; Riccardi, C.C.; Williams, R.J.J. Kinetic Model for Gelation in the Diepoxide−Cyclic Anhydride Copolymerization Initiated by Tertiary Amines. *Macromolecules* **1997**, *30*, 1616–1620, doi:10.1021/ma9614048.

194. Pascault, J.-P.; Williams, R.J.J. General Concepts about Epoxy Polymers. In *Epoxy Polymers*; Wiley-VCH Verlag GmbH & Co. KGaA: Weinheim, Germany, 2010; pp. 1–12 ISBN 9783527324804.

195. Leukel, J.; Burchard, W.; Krüger, R.-P.; Much, H.; Schulz, G. Mechanism of the anionic copolymerization of anhydride-cured epoxies – analyzed by matrix-assisted laser desorption ionization time-of-flight mass spectrometry (MALDI-TOF-MS). *Macromol. Rapid Commun.* **1996**, *17*, 359–366, doi:10.1002/marc.1996.030170512.

196. Jin, F.L.; Li, X.; Park, S.J. Synthesis and application of epoxy resins: A review. *J. Ind. Eng. Chem.* **2015**, *29*, 1–11, doi:10.1016/j.jiec.2015.03.026.

197. Ignatyev, I.A.; Thielemans, W.; Vander Beke, B. Recycling of polymers: A review. *ChemSusChem* **2014**, *7*, 1579–1593, doi:10.1002/cssc.201300898.

198. Overcash, M.; Twomey, J.; Asmatulu, E.; Vozzola, E.; Griffing, E. Thermoset composite recycling – Driving forces, development, and evolution of new opportunities. *J. Compos. Mater.* **2018**, *52*, 1033–1043, doi:10.1177/0021998317720000.

199. Palmer, J.; Ghita, O.R.; Savage, L.; Evans, K.E. Successful closed-loop recycling of thermoset composites. *Compos. Part A Appl. Sci. Manuf.* **2009**, *40*, 490–498, doi:10.1016/j.compositesa.2009.02.002.

200. Yang, Y.; Urban, M.W. Self-healing polymeric materials. *Chem. Soc. Rev.* **2013**, *42*, 7446–7467, doi:10.1039/c3cs60109a.

201. Alabiso, W.; Schlögl, S. The Impact of Vitrimers on the Industry of the Future: Chemistry, Properties and Sustainable Forward-Looking Applications. *Polymers (Basel).* **2020**, *12*, 1660, doi:10.3390/polym12081660.

202. Zhang, P.; Li, G. *Advances in healing-on-demand polymers and polymer composites*; Elsevier Ltd, 2016; Vol. 57; ISBN 0012255785.

203. Capelot, M.; Montarnal, D.; Tournilhac, F.; Leibler, L. Metal-catalyzed transesterification for healing and assembling of thermosets. *J. Am. Chem. Soc.* **2012**, *134*, 7664–7667, doi:10.1021/ja302894k.

204. Bottinga, Y.; Richet, P. Silicate melts: The "anomalous" pressure dependence of the viscosity. *Geochim. Cosmochim. Acta* **1995**, *59*, 2725–2731, doi:10.1016/0016-7037(95)00168-Y.

205. Saika-Voivod, I.; Poole, P.H.; Sciortino, F. Fragile-to-strong transition and polyamorphism in the energy landscape of liquid silica. *Nature* **2001**, *412*, 514–517, doi:10.1038/35087524.

206. Demongeot, A.; Mougnier, S.J.; Okada, S.; Soulié-Ziakovic, C.; Tournilhac, F. Coordination and catalysis of Zn 2+ in epoxy-based vitrimers. *Polym. Chem.* **2016**, *7*, 4486–4493, doi:10.1039/C6PY00752J.

207. Liu, W.; Schmidt, D.F.; Reynaud, E. Catalyst Selection, Creep, and Stress Relaxation in High-Performance Epoxy Vitrimers. *Ind. Eng. Chem. Res.* **2017**, *56*, 2667–2672, doi:10.1021/acs.iecr.6b03829.

208. Snyder, R.L.; Fortman, D.J.; De Hoe, G.X.; Hillmyer, M.A.; Dichtel, W.R. Reprocessable Acid-Degradable Polycarbonate Vitrimers. *Macromolecules* **2018**, *51*, 389–397, doi:10.1021/acs.macromol.7b02299.

209. Zhao, W.; Feng, Z.; Liang, Z.; Lv, Y.; Xiang, F.; Xiong, C.; Duan, C.; Dai, L.; Ni, Y. Vitrimer-Cellulose Paper Composites: A New Class of Strong, Smart, Green, and Sustainable Materials. *ACS Appl. Mater. Interfaces* **2019**, *11*, 36090–36099, doi:10.1021/acsami.9b11991.

210. Brutman, J.P.; Delgado, P.A.; Hillmyer, M.A. Polylactide Vitrimers. *ACS Macro Lett.* **2014**, *3*, 607–610, doi:10.1021/mz500269w.

211. Claude, U.; Lyon, B.; Lyon, C.P.E. Formation of Cross-Linked Films from Immiscible Precursors through Sintering of Vitrimer Nanoparticles. **2018**, 6–10, doi:10.1021/acsmacrolett.8b00173.

212. Demongeot, A.; Mougnier, S.-J.; Okada, S.; Soulié-Ziakovic, C.; Tournilhac, F. Coordination and Catalysis of Zn2+ in Epoxy-Based Vitrimers. *Polym. Chem.* **2016**, *7*, 4486–4493, doi:10.1039/C6PY00752J.

213. Demongeot, A.; Groote, R.; Goossens, H.; Hoeks, T.; Tournilhac, F.; Leibler, L. Cross-Linking of Poly(butylene terephthalate) by Reactive Extrusion Using Zn(II) Epoxy-Vitrimer Chemistry. *Macromolecules* **2017**, *50*, 6117–6127, doi:10.1021/acs.macromol.7b01141.

214. Xu, C.; Huang, X.; Li, C.; Chen, Y.; Lin, B.; Liang, X. Design of "Zn2+ Salt-Bondings" Cross-Linked Carboxylated Styrene Butadiene Rubber with Reprocessing and Recycling Ability via Rearrangements of Ionic Cross-Linkings. *ACS Sustain. Chem. Eng.* **2016**, *4*, 6981–6990, doi:10.1021/acssuschemeng.6b01897.

215. Jeske, R.C.; DiCiccio, A.M.; Coates, G.W. Alternating copolymerization of epoxides and cyclic anhydrides: An improved route to aliphatic polyesters. *J. Am. Chem. Soc.* **2007**, *129*, 11330–11331, doi:10.1021/ja0737568.

216. Han, J.; Liu, T.; Zhang, S.; Hao, C.; Xin, J.; Guo, B.; Zhang, J. Hyperbranched Polymer Assisted Curing and Repairing of an Epoxy Coating. *Ind. Eng. Chem. Res.* **2019**, *58*, 6466–6475, doi:10.1021/acs.iecr.9b00800.

217. Zhang, B.; Kowsari, K.; Serjouei, A.; Dunn, M.L.; Ge, Q. Reprocessable thermosets for sustainable three-dimensional printing. *Nat. Commun.* **2018**, *9*, doi:10.1038/s41467-018-04292-8.

218. Duquenne, Christophe Mougnier, Sebastien-jun Tournilhac, Francois-genes Leibler, L. Titanium-based catalyst for vitrimer resins of expoxy/anhyride type 2015, 39.

219. Kiesewetter, M.K.; Scholten, M.D.; Kirn, N.; Weber, R.L.; Hedrick, J.L.; Waymouth, R.M. Cyclic guanidine organic catalysts: What is magic about triazabicyclodecene? *J. Org. Chem.* **2009**, *74*, 9490–9496, doi:10.1021/jo902369g.

220. Simón, L.; Goodman, J.M. The mechanism of TBD-catalyzed ring-opening polymerization of cyclic esters. *J. Org. Chem.* **2007**, *72*, 9656–9662, doi:10.1021/jo702088c.

221. Chen, J.H.; An, X.P.; Li, Y.D.; Wang, M.; Zeng, J.B. Reprocessible Epoxy Networks with Tunable Physical Properties: Synthesis, Stress Relaxation and Recyclability. *Chinese J. Polym. Sci. (English Ed.* **2018**, *36*, 641–648, doi:10.1007/s10118-018-2027-9.

222. Yang, Y.; Pei, Z.; Zhang, X.; Tao, L.; Wei, Y.; Ji, Y. Carbon nanotube–vitrimer composite for facile and efficient photo-welding of epoxy. *Chem. Sci.* **2014**, *5*, 3486–3492, doi:10.1039/C4SC00543K.

223. Kaiser, S.; Wurzer, S.; Pilz, G.; Kern, W.; Schlögl, S. Stress relaxation and thermally adaptable properties in vitrimer-like elastomers from HXNBR rubber with covalent bonds. *Soft Matter* **2019**, *15*, doi:10.1039/C9SM00856J.

224. Altuna, F.I.; Hoppe, C.E.; Williams, R.J.J. Shape memory epoxy vitrimers based on DGEBA crosslinked with dicarboxylic acids and their blends with citric acid. *RSC Adv.* **2016**, *6*, 88647–88655, doi:10.1039/c6ra18010h.

225. Capelot, M.; Unterlass, M.M.; Tournilhac, F.; Leibler, L. Catalytic control of the vitrimer glass transition. *ACS Macro Lett.* **2012**, *1*, 789–792, doi:10.1021/mz300239f.

226. Yue, L.; Amirkhosravi, M.; Gong, X.; Gray, T.G.; Manas-Zloczower, I. Recycling epoxy by vitrimerization: influence of initial thermoset chemical structure. *ACS Sustain. Chem. Eng.* **2020**, doi:10.1021/acssuschemeng.0c04815.

227. Liu, T.; Hao, C.; Zhang, S.; Yang, X.; Wang, L.; Han, J.; Li, Y.; Xin, J.; Zhang, J. A Self-Healable High Glass Transition Temperature Bioepoxy Material Based on Vitrimer Chemistry. *Macromolecules* **2018**, *51*, 5577–5585, doi:10.1021/acs.macromol.8b01010.

228. Liu, T.; Hao, C.; Wang, L.; Li, Y.; Liu, W.; Xin, J.; Zhang, J. Eugenol-Derived Biobased Epoxy: Shape Memory, Repairing, and Recyclability. *Macromolecules* **2017**, *50*, 8588–8597, doi:10.1021/acs.macromol.7b01889.

229. Altuna, F.; Hoppe, C.; Williams, R. Epoxy Vitrimers: The Effect of Transesterification Reactions on the Network Structure. *Polymers (Basel).* **2018**, *10*, 43, doi:10.3390/polym10010043.

230. Han, J.; Liu, T.; Hao, C.; Zhang, S.; Guo, B.; Zhang, J. A Catalyst-Free Epoxy Vitrimer System Based on Multifunctional Hyperbranched Polymer. *Macromolecules* **2018**, *51*, 6789–6799, doi:10.1021/acs.macromol.8b01424.

231. Lu, L.; Pan, J.; Li, G. Recyclable high-performance epoxy based on transesterification reaction. *J. Mater. Chem. A* **2017**, *5*, 21505–21513, doi:10.1039/c7ta06397k.

232. Yu, K.; Taynton, P.; Zhang, W.; Dunn, M.L.; Qi, H.J. Influence of stoichiometry on

the glass transition and bond exchange reactions in epoxy thermoset polymers. *RSC Adv.* **2014**, *4*, 48682–48690, doi:10.1039/C4RA06543C.

233. Cao, L.; Fan, J.; Huang, J.; Chen, Y. A robust and stretchable cross-linked rubber network with recyclable and self-healable capabilities based on dynamic covalent bonds. *J. Mater. Chem. A* **2019**, *7*, 4922–4933, doi:10.1039/C8TA11587G.

234. Post, W.; Susa, A.; Blaauw, R.; Molenveld, K.; Knoop, R.J.I. A Review on the Potential and Limitations of Recyclable Thermosets for Structural Applications. *Polym. Rev.* **2020**, *60*, 359–388, doi:10.1080/15583724.2019.1673406.

235. Hedrick, J.; Yilgör, I.; Wilkes, G.; McGrath, J. Chemical modification of matrix Resin networks with engineering thermoplastics. *Polym. Bull.* **1985**, *13*, 201–208, doi:10.1007/BF00254652.

236. Sue, H.-J.; Puckett, P.M.; Bertram, J.L.; Walker, L.L. The Network Structure of Epoxy Systems and Its Relationship to Toughness and Toughenability. In *ACS Symposium Series*; 2000; Vol. 759, pp. 171–197.

237. Galy, J.; Sabra, A.; Pascault, J.-P. Characterization of epoxy thermosetting systems by differential scanning calorimetry. *Polym. Eng. Sci.* **1986**, *26*, 1514–1523, doi:10.1002/pen.760262108.

238. Tarifa, S.; Bouazizi, A. Glass transitions in crosslinked epoxy networks. *J. Therm. Anal.* **1997**, *48*, 297–307, doi:10.1007/BF01979273.

239. Osswald, T.; Rudolph, N. *Polymer Rheology*; Carl Hanser Verlag GmbH & Co. KG: Cincinnati, 2015; ISBN 978-1-56990-523-4.

240. Mezger, T. *The Rheology Handbook*; Vincentz Network, 2020; Vol. 59; ISBN 9783748603702.

241. Gottfried Wilhelm Ehrenstein; Gabriela Riedel; Pia Trawiel *Praxis der Thermischen Analyse von Kunststoffen*; 2003; ISBN 978-3-446-22340-0.

242. Sperling, C. Entwicklung und Charakterisierung ausgewählter Vitrimersysteme, University of Leoben, 2020.

243. Altuna, F.I.; Hoppe, C.E.; Williams, R.J.J. Epoxy vitrimers with a covalently bonded tertiary amine as catalyst of the transesterification reaction. *Eur. Polym. J.* **2019**, *113*, 297–304, doi:10.1016/j.eurpolymj.2019.01.045.

244. Kaiser, S.; Novak, P.; Giebler, M.; Gschwandl, M.; Novak, P.; Pilz, G.; Morak, M.; Schlögl, S. The crucial role of external force in the estimation of the topology

freezing transition temperature of vitrimers by elongational creep measurements. *Polymer (Guildf).* **2020**, *204*, doi:10.1016/j.polymer.2020.122804.

245. Yang, Y.; Zhang, S.; Zhang, X.; Gao, L.; Wei, Y.; Ji, Y. Detecting topology freezing transition temperature of vitrimers by AIE luminogens. *Nat. Commun.* **2019**, *10*, 1–8, doi:10.1038/s41467-019-11144-6.

246. Giebler, M.; Radl, S.; Ules, T.; Griesser, T.; Schlögl, S. Photopatternable epoxy-based thermosets. *Materials (Basel).* **2019**, *12*, 2350, doi:10.3390/ma12152350.

247. Giebler, M.; Radl, S.V.; Ast, M.; Kaiser, S.; Griesser, T.; Kern, W.; Schlögl, S. Dual-Responsive Polydimethylsiloxane Networks. *J. Polym. Sci. Part A Polym. Chem.* **2018**, *56*, 2319–2329, doi:10.1002/pola.29206.

248. Oliver, W.C.; Pharr, G.M. An improved technique for determining hardness and elastic modulus using load and displacement sensing indentation experiments. *J. Mater. Res.* **1992**, *7*, 1564–1583, doi:10.1557/JMR.1992.1564.

249. Giebler, M.; Alabiso, W.; Wieser, V.; Radl, S.; Schlögl, S. Photopatternable and Rewritable Epoxy-Anhydride Vitrimers. *Macromol. Rapid Commun.* **2021**, *42*, 2170005, doi:10.1002/marc.202170005.

250. Giebler, M.; Sperling, C.; Kaiser, S.; Duretek, I.; Schlögl, S. Epoxy-anhydride vitrimers from aminoglycidyl resins with high glass transition temperature and efficient stress relaxation. *Polymers (Basel).* **2020**, *12*, 1–14, doi:10.3390/POLYM12051148.

251. Feigl, V. Einfluss des Katalysators auf Vitrimersysteme, Montanuniversitaet Leoben, 2021.

252. Camino, G.; Lomakin, S..; Lazzari, M. Polydimethylsiloxane thermal degradation Part 1. Kinetic aspects. *Polymer (Guildf).* **2001**, *42*, 2395–2402, doi:10.1016/S0032-3861(00)00652-2.

253. Deshpande, G.; Rezac, M.E. Kinetic aspects of the thermal degradation of poly(dimethyl siloxane) and poly(dimethyl diphenyl siloxane). *Polym. Degrad. Stab.* **2002**, *76*, 17–24, doi:10.1016/S0141-3910(01)00261-0.

254. Cichra, D.A.; Adolph, H.G. Relative rates of Hydrolysis of Nitro- and Fluoro-Substituted Esters. *Propellants, Explos. Pyrotech.* **1987**, *12*, 202–205, doi:10.1002/prep.19870120605.

255. Göpferich, A. Mechanisms of polymer degradation and erosion. In *The*

*Biomaterials: Silver Jubilee Compendium*; Elsevier, 1996; Vol. 17, pp. 117–128 ISBN 9780080451541.

256. RYDHOLM, A.; ANSETH, K.; BOWMAN, C. Effects of neighboring sulfides and pH on ester hydrolysis in thiol–acrylate photopolymers. *Acta Biomater.* **2007**, *3*, 449–455, doi:10.1016/j.actbio.2006.12.001.

257. Rutherglen, B.G.; McBath, R.A.; Huang, Y.L.; Shipp, D.A. Polyanhydride networks from thiol-ene polymerizations. *Macromolecules* **2010**, *43*, 10297–10303, doi:10.1021/ma102287v.

258. Shimomura, O.; Nishisako, T.; Yamaguchi, S.; Ichihara, J.; Kirino, M.; Ohtaka, A.; Nomura, R. DABCO- and DBU-intercalated α-zirconium phosphate as latent thermal catalysts in the copolymerization of glycidyl phenyl ether (GPE) and hexahydro-4-methylphthalic anhydride (MHHPA). *J. Mol. Catal. A Chem.* **2016**, *411*, 230–238, doi:10.1016/j.molcata.2015.10.035.

259. Lai, S.K.; Batra, A.; Cohen, C. Characterization of polydimethylsiloxane elastomer degradation via cross-linker hydrolysis. *Polymer (Guildf).* **2005**, *46*, 4204–4211, doi:10.1016/j.polymer.2005.02.051.

260. Pitt, C.G.; Shah, S.S. Manipulation of the rate of hydrolysis of polymer-drug conjugates: The secondary structure of the polymer. *J. Control. Release* **1996**, *39*, 221–229, doi:10.1016/0168-3659(95)00156-5.

261. Oku, A.; Huang, W.; Ikeda, Y. Monomer recycling for vulcanized silicone rubbers in the form of cyclosiloxane monomers. Role of acid buffers. *Polymer (Guildf).* **2002**, *43*, 7289–7293, doi:10.1016/S0032-3861(02)00714-0.

262. Brook, M.A.; Zhao, S.; Liu, L.; Chen, Y. Surface etching of silicone elastomers by depolymerization. *Can. J. Chem.* **2012**, *90*, 153–160, doi:10.1139/v11-145.

263. Zhao, Y.; Zhou, W.; Tan, H.; Fu, R.; Li, Q.; Lin, F.; Yu, D.; Walters, G.; Sargent, E.H.; Zhao, Q. Mobile-Ion-Induced Degradation of Organic Hole-Selective Layers in Perovskite Solar Cells. *J. Phys. Chem. C* **2017**, *121*, 14517–14523, doi:10.1021/acs.jpcc.7b04684.

264. Tazuke, S.; Tanabe, T. Functionality and Structure of Polymers. 3. Synthesis and Thermal Properties of Polymers Having a Dianthracene Main Chain. *Macromolecules* **1979**, *12*, 848–853, doi:10.1021/ma60071a012.

265. Barzynski, H.; Sänger, D. Zur Photolyse von makromolekularen o-

Nitrobenzylderivaten. *Angew. Makromol. Chemie* **1981**, *93*, 131–141, doi:10.1002/apmc.1981.050930112.

266. Rajasekharan Pillai, V.N. Photoremovable Protecting Groups in Organic Synthesis. *Synthesis (Stuttg).* **1980**, *1980*, 1–26, doi:10.1055/s-1980-28908.

267. Radl, S.; Roppolo, I.; Pölzl, K.; Ast, M.; Spreitz, J.; Griesser, T.; Kern, W.; Schlögl, S.; Sangermano, M. Light triggered formation of photo-responsive epoxy based networks. *Polymer (Guildf).* **2017**, *109*, 349–357, doi:10.1016/j.polymer.2016.12.070.

268. Sampieri, R.H. *Chemistry and Technology of Epoxy Resins*; Ellis, B., Ed.; Springer Netherlands: Dordrecht, 1993; ISBN 978-94-010-5302-0.

269. Gerbase, A.E.; Petzhold, C.L.; Costa, A.P.O. Dynamic mechanical and thermal behavior of epoxy resins based on soybean oil. *J. Am. Oil Chem. Soc.* **2002**, *79*, 797–802, doi:10.1007/s11746-002-0561-z.

270. Hosseini Nejad, E.; van Melis, C.G.W.; Vermeer, T.J.; Koning, C.E.; Duchateau, R. Alternating Ring-Opening Polymerization of Cyclohexene Oxide and Anhydrides: Effect of Catalyst, Cocatalyst, and Anhydride Structure. *Macromolecules* **2012**, *45*, 1770–1776, doi:10.1021/ma2025804.

271. Liu, D.-F.; Zhu, L.-Q.; Wu, J.; Wu, L.-Y.; Lü, X.-Q. Ring-opening copolymerization of epoxides and anhydrides using manganese( <scp>iii</scp> ) asymmetrical Schiff base complexes as catalysts. *RSC Adv.* **2015**, *5*, 3854–3859, doi:10.1039/C4RA08969C.

272. Pan, X.; Webster, D.C. Impact of Structure and Functionality of Core Polyol in Highly Functional Biobased Epoxy Resins. *Macromol. Rapid Commun.* **2011**, *32*, 1324–1330, doi:10.1002/marc.201100215.

273. Radl, S. V.; Schipfer, C.; Kaiser, S.; Moser, A.; Kaynak, B.; Kern, W.; Schlögl, S. Photo-responsive thiol–ene networks for the design of switchable polymer patterns. *Polym. Chem.* **2017**, *8*, 1562–1572, doi:10.1039/C7PY00055C.

274. Zhao, H.; Sterner, E.S.; Coughlin, E.B.; Theato, P. o -Nitrobenzyl Alcohol Derivatives: Opportunities in Polymer and Materials Science. *Macromolecules* **2012**, *45*, 1723–1736, doi:10.1021/ma201924h.

275. Scherzer, T. Depth Profiling of the Degree of Cure during the Photopolymerization of Acrylates Studied by Real-Time FT-IR Attenuated Total Reflection

Spectroscopy. *Appl. Spectrosc.* **2002**, *56*, 1403–1412, doi:10.1366/000370202260377698.

276. Varma, I.K.; Gupta, V.B. Thermosetting Resin—Properties. In *Comprehensive Composite Materials*; Elsevier, 2000; pp. 1–56.

277. Paramarta, A.; Webster, D.C. Curing kinetics of bio-based epoxy-anhydride thermosets with zinc catalyst. *J. Therm. Anal. Calorim.* **2017**, *130*, 2133–2144, doi:10.1007/s10973-017-6704-7.

278. Mauri, A.N.; Riccardi, C.C. The effect of epoxy excess on the kinetics of an epoxy-anhydride system. *J. Appl. Polym. Sci.* **2002**, *85*, 2342–2349, doi:10.1002/app.10867.

279. Chen, J.; Soucek, M.D. Ultraviolet curing kinetics of cycloaliphatic epoxide with real-time fourier transform infrared spectroscopy. *J. Appl. Polym. Sci.* **2003**, *90*, 2485–2499, doi:10.1002/app.12898.

280. Trappe, V.; Burchard, W.; Steinmann, B. Anhydride-cured epoxies via chain reaction. 1. The phenyl glycidyl ether/phthalic acid anhydride system. *Macromolecules* **1991**, *24*, 4738–4744, doi:10.1021/ma00017a002.

281. Barabanova, A.I.; Lokshin, B. V; Kharitonova, E.P.; Afanasyev, E.S.; Askadskii, A.A.; Philippova, O.E. Curing cycloaliphatic epoxy resin with 4-methylhexahydrophthalic anhydride: Catalyzed vs. uncatalyzed reaction. *Polymer (Guildf).* **2019**, *178*, 121590, doi:https://doi.org/10.1016/j.polymer.2019.121590.

282. Couture, G.; Granado, L.; Fanget, F.; Boutevin, B.; Caillol, S. Limonene-based epoxy: Anhydride thermoset reaction study. *Molecules* **2018**, *23*, 1–16, doi:10.3390/molecules23112739.

283. Corcuera, M.A.; Mondragon, I.; Riccardi, C.C.; Williams, R.J.J. Polymer networks derived from the anhydride curing of tetraepoxides. *J. Appl. Polym. Sci.* **1997**, *64*, 157–166, doi:10.1002/(SICI)1097-4628(19970404)64:1<157::AID-APP14>3.0.CO;2-1.

284. Musto, P.; Abbate, M.; Ragosta, G.; Scarinzi, G. A study by Raman, near-infrared and dynamic-mechanical spectroscopies on the curing behaviour, molecular structure and viscoelastic properties of epoxy/anhydride networks. *Polymer (Guildf).* **2007**, *48*, 3703–3716, doi:10.1016/j.polymer.2007.04.042.

285. Naar, N.; Lamouri, S.; Jeacomine, I.; Pron, A.; Rinaudo, M. A Comprehensive

Study and Characterization of Colloidal Emeraldine-Base. *J. Macromol. Sci. Part A* **2012**, *49*, 897–905, doi:10.1080/10601325.2012.714688.

286. Zhang, B.; Yuan, C.; Zhang, W.; Dunn, M.L.; Qi, H.J.; Liu, Z.; Yu, K.; Ge, Q. Recycling of vitrimer blends with tunable thermomechanical properties. *RSC Adv.* **2019**, *9*, 5431–5437, doi:10.1039/C9RA00015A.

287. Kaupmees, K.; Trummal, A.; Leito, I. Basicities of Strong Bases in Water: A Computational Study. *Croat. Chem. Acta* **2014**, *87*, 385–395, doi:10.5562/cca2472.

288. Pratt, R.C.; Lohmeijer, B.G.G.; Long, D.A.; Waymouth, R.M.; Hedrick, J.L. Triazabicyclodecene: A Simple Bifunctional Organocatalyst for Acyl Transfer and Ring-Opening Polymerization of Cyclic Esters. *J. Am. Chem. Soc.* **2006**, *128*, 4556–4557, doi:10.1021/ja060662+.

289. Ham, Y.R.; Kim, S.H.; Shin, Y.J.; Lee, D.H.; Yang, M.; Min, J.H.; Shin, J.S. A comparison of some imidazoles in the curing of epoxy resin. *J. Ind. Eng. Chem.* **2010**, *16*, 556–559, doi:10.1016/j.jiec.2010.03.022.

290. Merighi, S.; Mazzocchetti, L.; Benelli, T.; Giorgini, L. Evaluation of Novel Bio-Based Amino Curing Agent Systems for Epoxy Resins: Effect of Tryptophan and Guanine. *Processes* **2020**, *9*, 42, doi:10.3390/pr9010042.

291. Merighi, S.; Mazzocchetti, L.; Benelli, T.; Giorgini, L. Adenine as epoxy resin hardener for sustainable composites production with recycled carbon fibers and cellulosic fibers. *Polymers (Basel).* **2020**, *12*, 1–21, doi:10.3390/polym12123054.

292. Dell'Erba, I.E.; Williams, R.J.J. Homopolymerization of epoxy monomers initiated by 4-(dimethylamino)pyridine. *Polym. Eng. Sci.* **2006**, *46*, 351–359, doi:10.1002/pen.20468.

293. Jang, Y.H.; Goddard, W.A.; Noyes, K.T.; Sowers, L.C.; Hwang, S.; Chung, D.S. p K a Values of Guanine in Water: Density Functional Theory Calculations Combined with Poisson−Boltzmann Continuum−Solvation Model. *J. Phys. Chem. B* **2003**, *107*, 344–357, doi:10.1021/jp020774x.

294. Bender, M.L. Mechanisms of Catalysis of Nucleophilic Reactions of Carboxylic Acid Derivatives. *Chem. Rev.* **1960**, *60*, 53–113, doi:10.1021/cr60203a005.

295. Meyer, J.L.; Bakir, M.; Lan, P.; Economy, J.; Jasiuk, I.; Bonhomme, G.; Polycarpou, A.A. Reversible Bonding of Aromatic Thermosetting Copolyesters for

In-Space Assembly. *Macromol. Mater. Eng.* **2019**, *304*, 1800647, doi:10.1002/mame.201800647.

296. Ji, F.; Liu, X.; Sheng, D.; Yang, Y. Epoxy-vitrimer composites based on exchangeable aromatic disulfide bonds: Reprocessibility, adhesive, multi-shape memory effect. *Polymer (Guildf).* **2020**, *197*, 122514, doi:10.1016/j.polymer.2020.122514.

297. Ruskowitz, E.R.; Deforest, C.A. Photoresponsive biomaterials for targeted drug delivery and 4D cell culture. *Nat. Rev. Mater.* **2018**, *3*, doi:10.1038/natrevmats.2017.87.

298. Ghosh, B.; Kulkarni, S.S. Advances in Protecting Groups for Oligosaccharide Synthesis. *Chem. - An Asian J.* **2020**, *15*, 450–462, doi:10.1002/asia.201901621.

299. Batchelor, R.; Messer, T.; Hippler, M.; Wegener, M.; Barner-Kowollik, C.; Blasco, E. Two in One: Light as a Tool for 3D Printing and Erasing at the Microscale. *Adv. Mater.* **2019**, *31*, 1904085, doi:10.1002/adma.201904085.

300. Soliman, S.M.A.; Nouvel, C.; Babin, J.; Six, J.-L. o -nitrobenzyl acrylate is polymerizable by single electron transfer-living radical polymerization. *J. Polym. Sci. Part A Polym. Chem.* **2014**, *52*, 2192–2201, doi:10.1002/pola.27232.

301. Schumers, J.-M.; Fustin, C.-A.; Can, A.; Hoogenboom, R.; Schubert, U.S.; Gohy, J.-F. Are o -nitrobenzyl (meth)acrylate monomers polymerizable by controlled-radical polymerization? *J. Polym. Sci. Part A Polym. Chem.* **2009**, *47*, 6504–6513, doi:10.1002/pola.23693.

# 6   List of tables

# 7   List of figures

# 8 Abbreviations

| | |
|---|---|
| CANS | Covalent adaptable networks |
| CD | Critical dimension |
| DA | Diels Alder |
| D | Diffraction limit (d) |
| DCM | Dichlormethane |
| DMBA | Dimethylbenzylamine |
| DMA/DMTA | Dynamic Mechanical Analysis |
| DOF | Depth of focus |
| DSC | Differential scanning calorimetry |
| DSSA | Dodecenylsuccinic anhydride |
| $E_a$ | Activation energy |
| ECC | 3,4-Epoxycyclohexylmethyl-3',4'-epoxycyclohexane carboxylate |
| epoxy-NBE | (2-Nitro-1,4-phenylene) bis(methylene) bis(2-(oxiran-2-yl)acetate) (epoxy-NBE) |
| ePSI | Extended phase shift interferometry |
| *et al.* | *et alii* |
| *etc.* | *et cetera* |
| EUV | Extreme ultraviolet lithography |
| FT-IR | Fourier-transform Infrared |
| HHMPA | Hexahydro-4-methylphthalic anhydride |
| HHPA | hexahydrophthalic anhydride |
| GA | Glutaric anhydride |
| γ | Contrast |
| GME | Glycidyl 2-methylphenyl ether |
| HOMO | Highest occupied molecular orbital |
| ISC | Intersystem crossing |
| LCD | Liquid crystal display |
| LUMO | Lowest unoccupied molecular orbital |

| | |
|---|---|
| MHHPA | Methylhexahydrophthalic anhydride |
| NIL | Nanoimprint lithography |
| MNR | Molecular network rearrangements |
| NA | Numerical aperture |
| NMR | Nuclear magnetic resonance |
| NBE | Nitrobenzylester |
| *o*-NBE | *ortho*-Nitrobenzylester |
| OLED | Organic light emitting diode |
| R | Rayleigh equation |
| ROMP | Ring-opening metathesis polymerization |
| RT | Room temperature |
| PBS | Poly(2-butane sulfone) |
| PDMS | Polydimethylsiloxane |
| PI | Photoinitiator |
| PMMA | Poly(methyl methacrylate) |
| PTFE | Polytetrafluoroethylene |
| S | Sensitivity |
| Si | Silicon |
| $T_g$ | Glass transition temperature |
| $T_V$ | Topology- freezing transition temperature |
| TBD | 1,5,7-Triazabicyclo[4.4.0]dec-5-ene |
| TGA | Thermogravimetric |
| THF | Tetrahydrofurane |
| TPP | Triphenylphosphine |
| UV | Ultraviolet |
| UV-Vis | Ultra-violet - visible |
| WLF | Williams–Landel–Ferry model |
| WLI | Wight light interferometer |
| wt% | Weight percent |
| $Zn(acac)_2$ | Zinc acetylacetonate |
| $Zn(OAc)_2$ | Zinc acetate |

# 9   Appendix

## Curriculum Vitae

| Personal details | |
|---|---|
| **Name** | Michael Giebler |
| **Birth** | 18.08.1987 in Graz |

| Education | |
|---|---|
| 01/2020 – 05/2021 | **EMBA at the California Lutheran University** |
| 02/2016 – 05/2021 | **PhD at the Chair of Chemistry of Polymeric Materials  at the Montanuniversitaet Leoben** |
| 10/2013 - 09/2016 | **Master Chemistry at the Graz University of Technology**<br><br>**Master thesis:** Supercritical fluid impregnation of polycarbonate with copper nanoparticles in carbon dioxide at the Institute of Chemical Engineering and Environmental Technology, TU Graz, under the supervision of Assoc.Prof. Dipl.-Ing. Dr. Thomas Gamse |
| 02/2014 - 07/2014 | **Exchange semester at the Deakin University in Melbourne**<br>Attending courses in microbiology, ecology and sociology |
| 10/2008 – 09/2013 | **Bachelor Chemistry at the Graz University of Technology**<br><br>**Bachelor thesis**: bioBOOOST: Hydrierende Verflüssigung von bioCHAR, Hydrodeoxygenierung von entwässerten Pyrolyseöl at the Institute of Chemical Engineering and Environmental Technology, TU Graz, under the supervision of Univ.-Prof. Dipl.-Ing. Dr.techn. Siebenhofer |
| 1998 **–** 2007 | **Wirtschaftskundliches Bundesrealgymnasium Graz** |

**Professional Experience**

| | |
|---|---|
| 02/2016 – 04/2021 | **Researcher at the Polymer Competence Center Leoben GmbH** |
| | Participation in scientific and industrial projects, supervision of Bachelor and Master students in the course of a dissertation. |
| | |
| 11/2015 - 11/2016 | **Student trainee OMV Refining & Marketing** |
| | Department for Project Management und Portfoliomanagement in Schwechat |
| | |
| 08 - 09/2015 | **Internship OMV Refining & Marketing** |
| | Department for Project Management und Portfoliomanagement in Schwechat |
| | |
| 09 - 10/2014 | **Internship OMV Refining & Marketing** |
| | Department for R&D in Schwechat |

## Publications

### Peer-viewed journals

| | |
|---|---|
| 2021 | <u>Giebler, M</u>.; Alabiso, W.; Wieser, V.; Radl, S.; Schlögl, S. Photopatternable and Rewritable Epoxy-Anhydride Vitrimers. *Macromol. Rapid Commun.* **2021**, *42*, 2170005, doi:10.1002/marc.202170005. |
| 2020 | Kaiser, S.; Novak, P.; <u>Giebler, M</u>.; Gschwandl, M.; Novak, P.; Pilz, G.; Morak, M.; Schlögl, S. The crucial role of external force in the estimation of the topology freezing transition temperature of vitrimers by elongational creep measurements. *Polymer.* **2020**, *204*, doi:10.1016/j.polymer.2020.122804. |
| 2020 | <u>Giebler, M</u>.; Sperling, C.; Kaiser, S.; Duretek, I.; Schlögl, S. Epoxy-anhydride vitrimers from aminoglycidyl resins with high glass transition temperature and efficient stress relaxation. *Polymers.* **2020**, *12*, 1–14, doi:10.3390/POLYM12051148. |
| 2019 | <u>Giebler, M</u>.; Radl, S.; Ules, T.; Griesser, T.; Schlögl, S. Photopatternable epoxy-based thermosets. *Materials (Basel).* **2019**, *12*, 2350, doi:10.3390/ma12152350. |
| 2018 | <u>Giebler, M</u>.; Radl, S.V.; Ast, M.; Kaiser, S.; Griesser, T.; Kern, W.; Schlögl, S. Dual-Responsive Polydimethylsiloxane Networks. *J. Polym. Sci. Part A Polym. Chem.* **2018**, *56*, 2319–2329, doi:10.1002/pola.29206. |
| 2018 | Romano, A.; Roppolo, I.; <u>Giebler, M</u>.; Dietliker, K.; Možina; Šket, P.; Mühlbacher, I.; Schlögl, S.; Sangermano, M. Stimuli-responsive thiol-epoxy networks with photo-switchable bulk and surface properties. *RSC Adv.* **2018**, *8*, 41904–41914, doi:10.1039/c8ra08937j. |

### Patents

| | |
|---|---|
| 2020 | <u>Giebler M</u>., Schlögl S., Wanghofer F., Wolfberger A.: Aushärtbare Zusammensetzung zur Herstellung eines Vitrimers und daraus erhältliches Vitrimer und Verfahren zu dessen Herstellung; filed at the Austrian Patent Office A50332/2020 |

**Poster presentations**

| 2018 | <u>Giebler M.</u>, Radl S.V., Ast M., Kaiser S., Griesser T., Kern W., Schlögl S.: Comparison of the photolytic versus the hydrolytic degradation of dual-responsive polydimethylsiloxane networks; at ESPS 2018, Mulhouse, France |
| 2017 | <u>Giebler M.</u>, Radl S.V., Ast M., Griesser T., Kern W., Schlögl S.: Study of photocleavable epoxy-anhydride networks using photosensitive *o*-nitrobenzyl ester links; at DVSPM 2017, Vienna, Austria |